DEVELOPMENT OF BULK-SCALE AND THIN FILM

MAGNETOSTRICTIVE SENSOR

Except where reference is made to the work of others, the work described in this dissertation is my own or was done in collaboration with my advisory committee. This dissertation does not include proprietary or classified information.

_____
Cai Liang

Certificate of Approval:

_____   _____
Bryan A. Chin   Barton C. Prorok, Chair
Professor   Associate Professor
Materials Engineering   Materials Engineering

_____   _____
Aleksandr Simonian   ZhongYang (Z.-Y.) Cheng
Professor   Associate Professor
Materials Engineering   Materials Engineering

_____   _____
Stuart Wentworth   George T. Flowers
Associate Professor   Interim Dean
Electrical & Computer Engineering   Graduate School

DEVELOPMENT OF BULK-SCALE AND THIN FILM

MAGNETOSTRICTIVE SENSOR

Cai Liang

A Dissertation

Submitted to

the Graduate Faculty of

Auburn University

in Partial Fulfillment of the

Requirements for the

Degree of

Doctor of Philosophy

Auburn, Alabama
December 17, 2007

DEVELOPMENT OF BULK-SCALE AND THIN FILM

MAGNETOSTRICTIVE SENSOR

Cai Liang

_____

Signature of Author

_____

Date of Graduation

VITA

Cai Liang, son of Shuoqing Liang and Daihe Chen, was born on February 27, 1964, in Macheng city, Hubei Province, China. He graduated from Macheng No. 1 high school in July 1982, and then studied at the Central South University (Changsha, China) for four years where he received the Bachelor of Science degree in Metallurgy Engineering in July 1986. He then worked with Baosteel (Shanghai China) as a Production, Research, and Design Engineer from August 1986 to February 1994. While working with Baosteel, he attended a Master of Engineering program in Northeastern University (Shenyang China) from September 1992 to February 1994. He then worked with the Singna Private Limited (Singapore) as a Production Engineer until December 1995. From December 1995, he worked at the Singapore Institute of Manufacturing Technology (SIMTech) as a Research Associate, working in the areas of thin film and microelectronics packaging technology. Five years later, in December 2000, he joined to the Focus Interconnection Technology Corporation (Austin, TX, USA) as a Principal Engineer, working in wafer bumping flip chip packaging process till June 2001. Prior to enrolling in the Ph.D. program in Materials Engineering at Auburn University in Fall 2003, he was a Packaging Engineer with Cirrex Corporation (Alpharetta, GA), working in optoelectronics packaging and assembly. He received his M.S. in Materials Science and Engineering from National University of Singapore in 2003. He was married to Rui Shao on February 8, 1995. He and Rui are blessed with their daughter, Susanna, and son, William.

DISSERTATION ABSTRACT

DEVELOPMENT OF BULK-SCALE AND THIN FILM

MAGNETOSTRICTIVE SENSOR

Cai Liang

Doctor of Philosophy, December 17, 2007
(M. S. National University of Singapore, 2003)
(M. E. Northeastern University, China, 1994)
(B. S. Central South University, China, 1986)

258 Typed Pages

Directed by Bart Prorok

Three key areas were investigated in this research. These are: (1) finite element modeling using modal analysis to better understand the mechanics of longitudinal vibration system, (2) thin film material Young's modulus measurement in a nondestructive manner by a magnetostrictive sensor, and (3) optimization of a deposition process for sputtering magnetostrictive thin films from Metglas 2826 MB ribbon and machining them into useful sensor platforms.

We have verified the principle of operation for the longitudinal vibrating system through experimentation and comparison with numerical simulations of cantilevers, bridges, and beams. The results indicated that the governing vibration equation should use the plane-stress or biaxial modulus. Furthermore, the Poisson's ratio for Metglas 2826 MB was found to be 0.33. A resonating mechanical sensor was constructed from

commercially available Metglas 2826 MB strip material and was used to measure Young's modulus of sputter deposited thin film material, e.g. Cu, Au, Al, Cr, Sn, In, SnAu (20/80 eutectic), and SiC, with a proposed measurement methodology. The determined Young's modulus values were comparable to those found in the literature. In addition, a finite element modeling analysis was employed to verify the Young's modulus determined by experimentation. Glass beads (size of ~425 μm) were attached to freestanding (free-free ended) magnetostrictive sensors in order to simulate the attachment of target species. These mass-loading results indicated that the frequency shifts are sensitive to the location of the mass on the sensor's surface. Finite element analysis was conducted and ascertained that when a particle comparable in size to *E. Coli O157* cell (mass in pico-gram range) attaches to sensor of 250 x 50 x 1.5 microns in size, a significant resonant frequency shift results, indicating that the sensor has the potential to detect the attachment of a single bacterium. These simulations also confirm that the resonant frequency shift is dependent on the location of the mass attachment along the longitudinal axis of the sensor.

Finally, a process for depositing magnetostrictive thin film material from directly sputtering of Metglas 2826 MB ribbon was developed. Microscale sensors were fabricated with this film material. Dynamic testing of these microscale sensors was carried out on freestanding particles of the size 500 x 100 x 3 microns. The resonant frequency of these microfabricated particles was found to increase significantly in both magnitude and amplitude after the particle was annealed. A model was employed to explain why the magnetoelastic sensor behavior changed after annealing.

ACKNOWLEDGEMENTS

DEDICATED

To the memory of my parents and my eldest sister,

whose love and encouragements led me on the road of scientific research

and

To my wife, daughter, son, and other family members,

for their love, unconditional support, and encouragements.

Style Manual or J. used: <u>IEEE Transaction on Components and Packaging Technology</u>

Computer software used: <u>Microsoft Office, Matlab, SAS, Sigmaplot 8.0, and CAD</u>

TABLE OF CONTENTS

LIST OF TABLES

xvi

LIST OF FIGURES

xxiii

xxv

1. INTRODUCTION

1.1. Motivation for Research

1.1.1. Development of Mechanical Sensor for Thin Film Property Measurement

For decades, researchers and engineers have extensively applied thin film materials in microelectronics for very- to ultra-large-scale-integrated (VLSI/ULSI) circuit and microelectromechanical systems (MEMS) or microsystems technology (MST). The mechanical properties such as Young's modulus of thin film materials are commonly unknown and assumed to be similar to their bulk values. However, the mechanical properties of thin films may differ from their bulk counterparts due to differences in operating deformation mechanisms, material texture, and other microstructural issues. Although many techniques have been explored to assess this issue, most are destructive, time consuming, and expensive to perform. Most require the tests to be conducted on the thin film materials constructed by microfabrication processes that increase the measurement cost. Furthermore, the additional microfabrication process may influence the thin film properties [1]. A standard method for measuring thin film mechanical properties that is nondestructive, quick, easy, and cost effective to perform does not yet exist.

1.1.2. Development of Biosensors

Since September 11, 2001, security monitoring has become a growing concern in virtually every country, which in turn has driven the research and development of advanced devices and technologies to protect, detect, and trace biological species by unintentional biological attack. The area of food safety is included in these new security concerns, and a way to monitor food production from the farm through production process and the supply chain to customers is in growing demand. In the United States, it has been estimated that nearly 76 million people suffer from food-borne illnesses each year, accounting for 325,000 hospitalizations and more than 5,000 deaths [2, 3]. Recently it was reported that lettuce and spinach contaminated with *E. Coli O157:H7* caused sickness in twenty-eight people and one death [4, 5], which further indicates that food safety is extremely important to human lives. The development of an advanced device that can simply and quickly detect any harmful bio-agent threats in food products is becoming an important challenge. The development of mesoscale and microscale sensor platforms based on MEMS/MTS technology has shown great promise and represents a paradigm shift in homeland security and anti-terrorism efforts. In addition, MEMS sensors offer the advantages of vastly reduced sample consumption and little to no by-products, as are typically produced in chemical and biochemical analyses.

1.2. Objectives of This Research

The objectives of this work had two main themes (1) to study and improve magnetostrictive strip fashioned from Metglas 2826 MB ribbon as sensors platforms and

(2) to develop a deposition process for constructing magnetostrictive thin film from Metglas 2826 MB for MEMS and sensors applications. In accomplishing these goals this work was divided into three areas where experimental and numerical interrogation were employed in the design and characterization of these sensors. These are:

1). Finite element modeling using modal analysis to better understand the mechanics of actuation of magnetostrictive forms.

The proof-of-principle of a sensor designed in resonating cantilever, bridge, and freestanding forms in their longitudinal mode will be studied by experimentation and simulation. The analytical solution for predicting the resonant frequency of a magnetostrictive sensor will be verified, and if necessary, be modified to express the correct state of strain on the magnetostrictive form. The approach will involve combining experimentally determined behavior that will be verified by FEA study. This will include characterizing the resonant frequency shift of a sensor due to deposition of a thin film material, a single and multiple bimolecular cells attached to its surface, and their position, or orientation, on the sensor.

2). Developing a highly accurate magnetostrictive sensor for measuring the elastic modulus of a thin film and detecting a concentrated mass on the sensor's surface.

Here, a bulk scale magnetostrictive sensor will be constructed from Metglas 2826 MB ribbon and used to measure the elastic properties of sputter deposited Cu, Au, Cr, Sn, Sn-Au, etc. thin films. An improved methodology of determining Young's modulus of a thin film material was introduced, which is more similar but also more accurate than existing techniques. The results will be compared with many popular but complicated techniques, such as the membrane deflection experiments, and will be verified by finite

element modeling analysis. A glass bead as a concentrated mass will be attached to a bulk-scale sensor to determine the sensor's response to this unevenly distributed mass. Simulation will be employed to study the effect of a mass compatible to an *E. Coli* cell on the sensor.

3). Developing a deposition process for sputtering thin films from Metglas 2826 MB ribbon and micromachining them into useful sensor platforms. A feasibility study of directly sputtering magnetostrictive target material (Metglas 2826 MB) to form a magnetostrictive thin film will be the primary focus of this area. The sputter target will be fabricated from Metglas 2826 MB ribbon. A systemic study will be applied to the process of deposition towards obtaining optimized thin film properties. Finally, microscale sensors will be fabricated from the sputtering deposited magnetostrictive thin film, and will be characterized for their potential application in detection of chemical and biochemical agents.

1.3.   An Overview of the Contents

This dissertation consists of seven sections, including the introduction. The second section gives a general overview of the principles of magnetostrictive sensors and the potential applications of such sensors in measuring Young's modulus of thin film and biochemical agents. Details of the magnetostrictive sensors' resonant frequency measurements are discussed in this section as well. The third section is a more detailed discussion the fundamentals and advantages of a sensor vibrating in the longitudinal mode over the transverse mode. The strategy of sensor design for detecting a single biomolecule is discussed. Section four reports the finite element simulation results of

magnetostrictive sensors for the two applications mentioned above. In conjunction with experimental data, the Poisson's ratio of Metglas 2826 MB is determined and its influence on the theoretic calculation of resonant frequency is discussed. The proof-of-principle of a cantilever and bridge sensor operated in longitudinal mode is verified by both experimentation and simulation.

Section five details the methodology of determining Young's modulus and investigates sensor response to the unevenly loaded masses on its surface. Eight thin film materials that include very soft solder indium, tin, and hard Cr and SiC were deposited and their Young's moduli were measured. Both crystalline (BCC and FCC) and non-crystal materials are covered. Refinements in the ease of testing and data reduction as well as reduced measurement error are addressed. A simulating experiment was also conducted to determine the elastic modulus of Cr and Cu to verify the results obtained by the magnetostrictive sensor. As a biosensor, the test of a concentrated mass (glass bead) attached to the sensor at various locations was conducted. The simulation results of its response to single and multiple biomolecule are also elucidated.

Section six describes the thin film magnetostrictive material synthesis and its properties, as well as the performance of microscale sensors that were fabricated with such thin film material. Resonant frequency of freestanding particles with and without annealing is tested and the Q value before and after annealing is compared. The overall conclusions and suggestions for future study are described in section seven.

2. MAGNETOSTRICTION AND MAGNETOSTRICTIVE SENSORS

2.1. Fundamentals of Magnetostrictive Materials

2.1.1. Magnetic Properties of Materials

From the atomistic point of view, most solid matters exhibit the phenomenon of magnetism as a result of electrons orbiting about the nucleus and the electrons spinning on their own axes. There are several categories of magnetic materials based on the degree and type of their mutual interactions. We generally distinguish them as Diamagnetism, Paramagnetism, Ferromagnetism, Antiferromagnetism, and Ferrimagnetism.

Ampere postulated that orbiting valence electrons (inner atomic current) in solids create an intrinsic magnetic moment [6] as seen in Fig. 2-1, which may be understood by moving a bar magnet toward (or backward) a looped wire, which induces a current in the loop, and the current causes, in turn, a magnetic moment as illustrated in Fig. 2-2. The magnetic moment (m) in Fig. 2-1 can be written as Equation (2-1) according to the Bohrs model.

$$m = IA \qquad (2\text{-}1)$$

where I is the current of orbiting electron in Fig. 2-1, A is the area, which directly relates to the radius (r) of the orbiting electron. Current I is carried by one electron orbiting about the nucleus at the distance r with the frequency $v = \omega/2\pi$ can be expressed
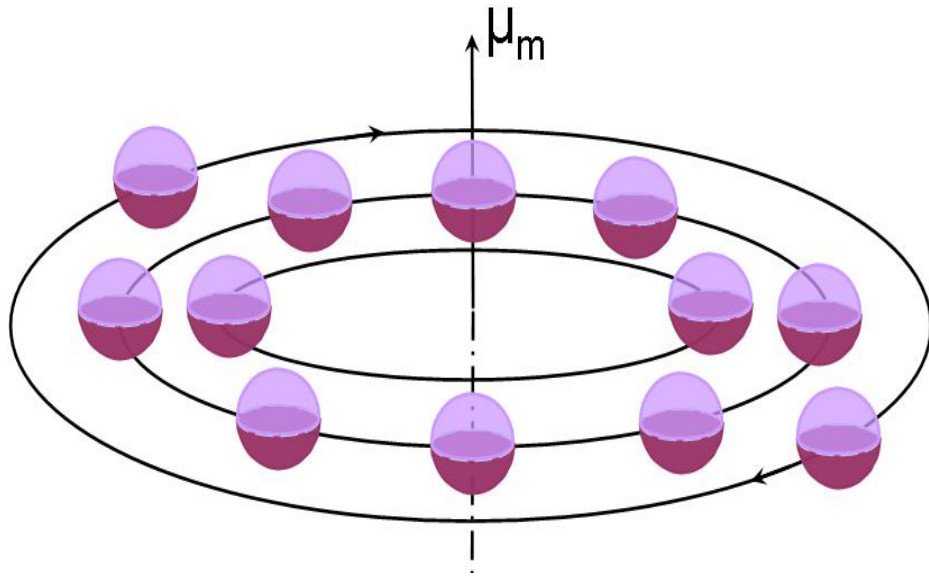
Fig. 2-1   Schematic showing the electrons orbiting around the nucleus to generate

magnetic moment.
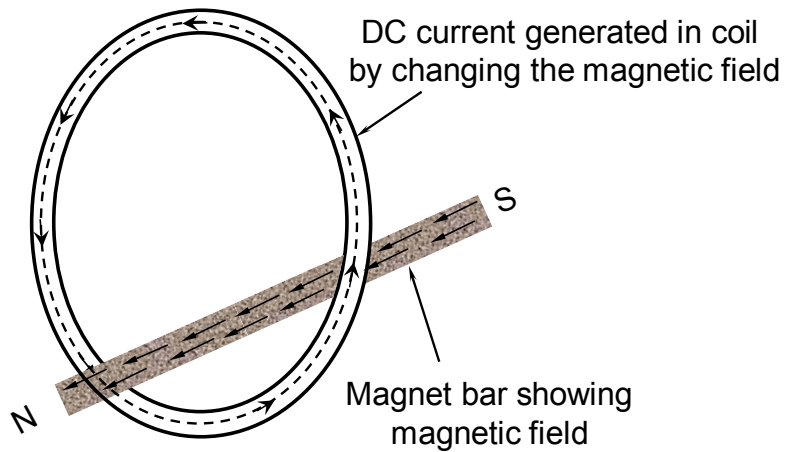
Fig. 2-2   Schematic depicting the DC current generated in a closed circuit by moving

magnetic field.

as:

$$I = e\frac{\omega}{2\pi}$$

(2-2)

where ω is the angular frequency. The orbiting magnetic moment is thus obtained via Equation (2-3)

$$m_{orb} = e\frac{\omega}{2\pi}\pi r^2 = \frac{1}{2}e\omega r^2$$

(2-3)

By a combination of the quantum mechanics and Bohrs model, the orbiting magnetic moment must have the same value as Bohrs model, i.e.

$$m_{orb} = m_{Bohr} = 9.274 \times 10^{-24}(J/T)$$

(2-4)

This inner atomic current (electrons bound to their respective nuclei) can be influenced by the external magnetic field, i.e. the applied magnetic field may accelerate or decelerate the orbiting electrons. In addition, free electrons in metals are forced to move in a magnetic field in a circular path, a so-called induced magnetic field. This induced field tends to oppose the applied magnetic field. Diamagnetism is the characteristic of these interactions of a matter with external magnetic field. All materials exhibit diamagnetic response to an external magnetic field, but the magnitude and degree of such response is generally very weak. An electron spinning on its own axis as a built-in angular momentum with the value ħs also results in magnetic moment as illustrated in Fig. 2-3. Here S is spin quantum number +/- 1/2, and ħ is the Planck constant with value of 6.626×10^{-34} (J·S). In order to maintain the lowest energy state, based on Pauli principle, the fully filled state, electrons spin in opposite directions in one electron state (one spins up, another spins down), then the overall spin magnetic moment is zero as a result of their canceling effect on each other, and diamagnetism is the only mannerism.
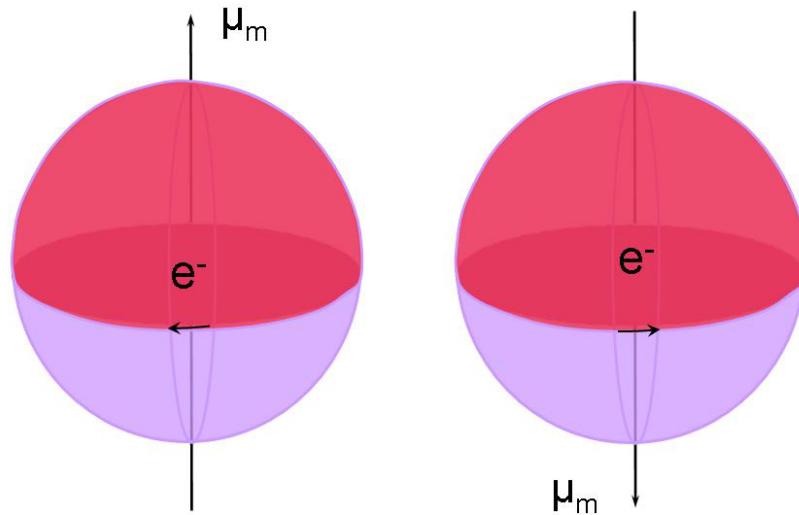
Fig. 2-3　Spin electrons result in a magnetic moment.

In the case of unpaired (partially filled) atomic/molecular electron state, the spin magnetic moment is not canceled out, which gives rise to a permanent magnetic moment or dipole in solid materials. These kinds of materials are often called paramagnetic materials. Generally, the net magnetic moment in paramagnetic materials is zero due to the orientation of dipoles being arranged randomly with the thermal energy. If an external magnetic field applied to this type material, the magnetic moment (dipoles) will align to the applied field. Such interaction is known as paramagnetism.

The magnetic flux density or magnetic induction B of a material under external magnetic field H has the following relationship with the applied Magnetic field

$$B = \mu_0 \mu_r H \tag{2-5}$$

where μ_0 is constant and μ_r is the relative permeability of the material. Equation (2-5) can be rewritten in terms of magnetization M and H:

$$B = \mu_0(M + H)$$

In the extreme cases, many unpaired 3d and even 4f electrons, as depicted in Fig. 2-4 for Fe, spin in the same direction (parallel) and spontaneously align in a small region (also called domain) below Curie temperature T_C without the presence of an external magnetic field. These individual domains are magnetized to a saturation state. The spin directions in individual domains differ from one another, resulting in a zero net magnetic moment. Materials like Fe, Co, Ni, etc. that possess such characteristics are referred to as ferromagnetic material. When an external magnetic field is applied to ferromagnetic materials, the domains whose spins are parallel or nearly parallel to the field will grow at the expense of the unfavorably aligned domains, hence a net magnetic moment will be produced.

3d shell electron spin
Fe 26: $1s^2 2s^2 2p^6 3s^2 3p^6 3d^6 4s^2$
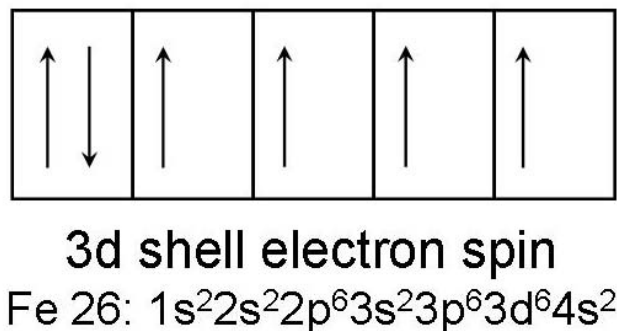
Fig. 2-4   Spin alignment of 3d electrons in Fe element.

Antiferromagnetic materials possess the same characteristics of spontaneous alignment of moments below a critical temperature (Néel temperature) as do

ferromagnetic materials. However, the neighboring atoms (sublattices) in antiferromagnetic materials are aligned in antiparallel fashion, which results in a no net magnetic moment. Cr, MnFe, and most ionic compounds, e.g. MnO, exhibit antiferromagnetic properties. No particular applications of antiferromagnetic materials have been found by employing the antiferromagnetism. In ferrimagnetic materials, the magnetic moments are antiparallel like antiferromagnetic materials. The electrons of neighboring atoms (sublattices) are arranged in the opposite direction, but the magnetic moments are not equal or not completely cancelled out; consequently, a net magnetic moment is produced.

2.1.2. Magnetostrictive Behavior and Magnetoelastic Interactions of Magnetic Materials

Most ferromagnetic materials exhibit the magnetostrictive phenomenon, that is, the material changes in dimension as a result of the domains aligning to an applied external magnetic field. This effect was first observed with Ni and Fe material in 1842, by James Joule [7, 8]. In fact, with this change in dimension, the magnetization state in the material is hence changed, which interacts with the external field and results in magnetoelastic behavior.

As discussed in the previous section, ferrimagnetic and antiferromagnetic materials also possess the same magnetostriction behavior as ferromagnetic materials. Ferromagnetic materials generally are Fe, Ni, and Co metals or their alloys. Ferrimagnetic materials, however, are ceramics and anisotropic and usually exhibit the hard magnetic properties of large remanence and coercive field. Antiferromagnetic

11

materials are most commonly found among ionic compounds and have no particular applications. So far, ferromagnetic materials have been demonstrated to be a good candidate for magnetostrictive sensors because of their soft magnetic properties (low remanence and coercive field) in general. Moreover, ferromagnetic material can be made in amorphous (non-crystalline) metallic alloys by rapidly spinning and cooling of a liquid alloy [9]. For example, Metglas 2826 MB [10], consisting of Fe, Ni, Mo, and B, is a typical amorphous ferromagnetic material having the advantages of nearly magnetic isotropic structure, considerable high permeability, low coercivity, and low hysteresis loss. Therefore, in this research, we are interested in the ferromagnetic materials including Fe, Ni, Co and their alloys, in particular, Metglas with $Fe_{40}Ni_{38}Mo_4B_{18}$ in ribbon and sputtered film forms. Metglas 2826 MB is used as the prototype material for fabrication of sensors in bulk-scale and as the sputtering target for deposition of magnetostrictive thin films that are used to fabricate microscale sensor platforms.

The most common and well developed magnetostrictive sensors are designed to measure the linear displacement and strain [11, 12], which is based on the magnetostrictive behavior of magnetostrictive material. The application of magnetostrictive sensors to measure chemical or biochemical agents as a mass sensor has only been conducted in recent years [13-25]. The operation principle of such sensors is completely different from that which is used as a mechanical sensor to measure the linear displacement or strain. If a magnetostrictive material is exposed to an alternating magnetic field, it is subjected to compression and extension in the longest axis; subsequently the applied field will be interacted by such a change of inner state of magnetization. When the frequency of the alternating magnetic field is equal to the

12

magnetostrictive material's resonant frequency, the largest oscillation will occur. As a result, the highest magnetic flux density is produced, and the resonant frequency can be detected by analysis of the signal in a close loop circuit. This is the basis for antitheft sensor tags currently used Electronic Article Surveillance (EAS) system [26, 27] and sensors used to measure chemical and biochemical species.

This study will further extend the applications of the magnetostrictive phenomena to measuring Young's modulus of thin film material and detecting mass loaded on magnetostrictive sensors.

2.2.   Magnetostrictive Sensor Operation in the Longitudinal Vibration Mode

When the alternating magnetic field is applied to a sensor that is made of magnetostrictive material in a rectangular shape, with the easy magnetization axis aligned with the longitudinal direction, it can cause the sensor to oscillate in its resonant frequency. Here, the magnetic energy is transferred to mechanical energy to cause the sensor to change its shape (dimension) as a result of switching domains in the magnetostrictive sensor. Fig. 2-5 illustrates the sensor response to an applied magnetic field. When the external field H=0, domains inside the sensor remain randomly placed and the sensor reveals zero magnetic moment, but they will align to the applied field when the external magnetic field is turned on.
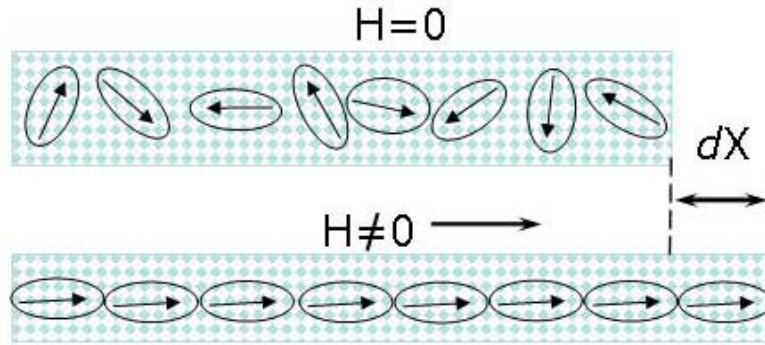
Fig. 2-5   Schematics of a magnetostrictive sensor's response to the applied magnetic field.

For a sensor under the magneto-mechanical interaction, a magnetoelastic force is produced in a longitudinal direction, which is x in this case. The unit mechanical force analysis is explained in Fig. 2-6. The total force in the unit is equal to the product of unit mass and acceleration speed base on the Newton's 2nd law, as expressed in Equation (2-7) [28, 29]

$$-\frac{\partial}{\partial x}(A\sigma_x)dx = m\frac{\partial^2 u}{\partial t^2} \tag{2-7}$$

where u is the elastic body deformation (longitudinal displacement from the position of equilibrium) in the x direction, σ_x is the stress in x direction, and $\frac{\partial^2 u}{\partial t^2}$ is body deformation acceleration speed. In applying Hooke's law, Equation (2-8), to this, a general equation for a uniform cross section rectangular sensor is then obtained, Equation (2-9)

$$\sigma_x = -E\varepsilon_x = -E\frac{\partial u}{\partial x} \tag{2-8}$$

14

$$\frac{\partial^2 u}{\partial t^2} = \left(\frac{E}{\rho}\right)\frac{\partial^2 u}{\partial x^2} \tag{2-9}$$

where u is the elastic body deformation (displacement) in x direction, and $\frac{\partial u}{\partial x}$, $\frac{\partial^2 u}{\partial x^2}$ are

the strain and strain rate, respectively. E and ρ correspondingly denote the Young's

modulus and density of the sensor material. Young's modulus E expressed here is

dependent on the state of strain in the structure. The elastic body deformation

(displacement) u should be such a function of x and (time) t as to satisfy the partial

differential of Equation (2-9).
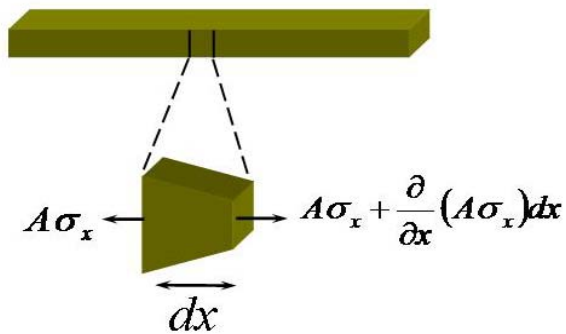
Fig. 2-6   Mechanical force analysis in a unit of sensor.

2.2.1. Fix-Free Ended Cantilever Sensor

When a fix-free ended structure sensor (Fig. 2-7), thereafter called cantilever, is actuated in the longitudinal vibration mode, the natural frequency can be obtained by applying the boundary conditions of

$$(u)_{x=0} = 0$$

and

$$\left(\frac{\partial u}{\partial x}\right)_{x=L} = 0$$

to Equation (2-9), and the resonant frequency in longitudinal vibration mode without considering the damping effect is obtained as following equation

$$f = \frac{2n-1}{4L}\sqrt{\frac{E}{\rho}} \qquad (2\text{-}10)$$

where n is integral, equals to 1, 2, 3…., for the first mode, n = 1. L is the length of the sensor.
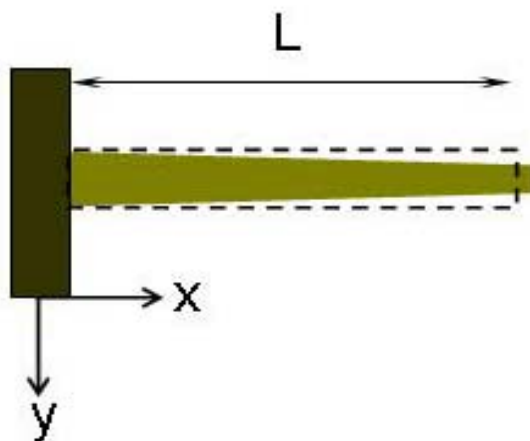
Fig. 2-7   Schematic showing a fix-free ended cantilever with L(length)>W(width).

16

2.2.2. Fix-Fix and Free-Free Ended Sensors

Fix-fix ended (thereafter-called bridge) and free-free ended (thereafter-called beam) sensor structure can be represented as in Fig. 2-8 (a) and (b), respectively. They both possess identical general governing equations for vibrating in longitudinal mode, which is found by applying individual boundary conditions, i.e. for fix-fix ended bridge:

$$(u)_{x=0} = 0 \text{ and } (u)_{x=L} = 0$$

and for free-free ended beam:

$$\left(\frac{\partial u}{\partial x}\right)_{x=0} = 0 \text{ and } \left(\frac{\partial u}{\partial x}\right)_{x=L} = 0$$

More details can be found in the reference [19, 28-30]. The resonant frequency of these two types of sensors is expressed in Equation (2-11)

$$f = \frac{n}{2L}\sqrt{\frac{E}{\rho}} \tag{2-11}$$

where n= 1, 2, 3 ….

(a)   (b)
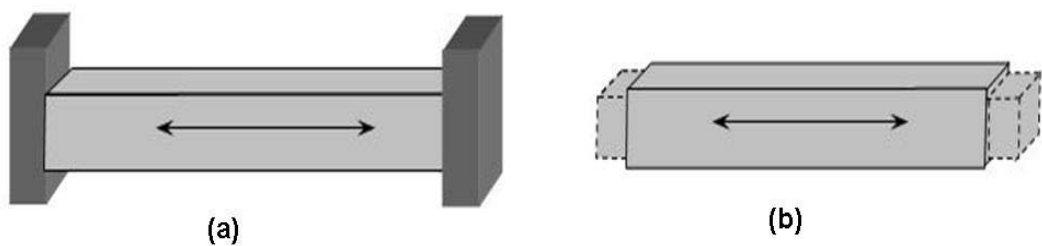
Fig. 2-8   Schematics of sensors structure in (a) bridge and (b) beam.

One can see that the resonant frequency magnitudes for the bridge and beam type sensor are twice that of the cantilever type. Additionally, the frequency is only dependent on the material's intrinsic properties and geometry of length.

2.3. Application of Magnetostrictive Sensors

Assuming that there is a solid, continuous thin film firmly deposited onto the sensor's surface, the resonant frequency of the sensor will consequently be shifted up or down, dependent on the shifts of elastic modulus and density. The change in frequency for any type of sensor described above can be approximately estimated by the first order Taylor expression

$$\Delta f = \frac{1}{2}\left(\frac{\Delta E}{E} - \frac{\Delta \rho}{\rho} \right) f_0 \qquad (2\text{-}12)$$

where Δf, ΔE and $\Delta \rho$ are the change of frequency, effective Young's modulus, and effective density of the sensor due to the thin film coating deposition, respectively. f_0 is the frequency of a sensor without any coating. In the case of no coating, the effective modulus and density will be the sensor material itself. When a sensor is deposited with a thin film coating, the effective modulus and effective density will be determined from both sensor and film materials.

It is possible to measure the thin film's Young's modulus by knowing the sensor material's properties. Grimes and his coworkers demonstrated this possibility of measuring the elastic modulus of Ag and Al thin films [31, 32]. If the coating has the same Young's modulus and density as the sensor does, there will be no change in

frequency. However, if the film coating is evenly deposited on the surface without change the elastic modulus of this structure, Equation (2-12), can be written as

$$\Delta f = -\frac{1}{2}\left(\frac{\Delta\rho}{\rho}\right)f_0 \tag{2-13}$$

This equation can be further written as Equation (2-14) if there is a mass evenly distributed on the sensor surface.

$$\Delta f = -\frac{1}{2}\left(\frac{\Delta m}{m_0}\right)f_0 \tag{2-14}$$

This is the foundation of employing a resonated sensor in detecting the presence of a chemical or biochemical mass attaching to its surface.

2.3.1. Mechanical Sensor for Measuring Young's Modulus of Thin Film Material

The bridge and beam type sensors are taken as examples to examine the prospects of their applications. The first order (n = 1) frequency is typically used because it has the largest amplitude of resonant frequency [28]. Fig. 2-9 depicts a sensor that is coated with a thin film material. Assuming that the film and substrate have the same strain during the vibration process, the overall (also called effective) Young's modulus and density of the sensor/thin film composite can be found in the following equations,

$$E = \frac{t}{t+\Delta t}E_{sen} + \frac{\Delta t}{t+\Delta t}E_{film} \tag{2-15}$$

$$\rho = \frac{t}{t+\Delta t}\rho_{sen} + \frac{\Delta t}{t+\Delta t}\rho_{film} \tag{2-16}$$

19

where subscripts sen and film denote the sensor and thin film, respectively. parameters t
and Δt are the thickness of sensor and the film, respectively.
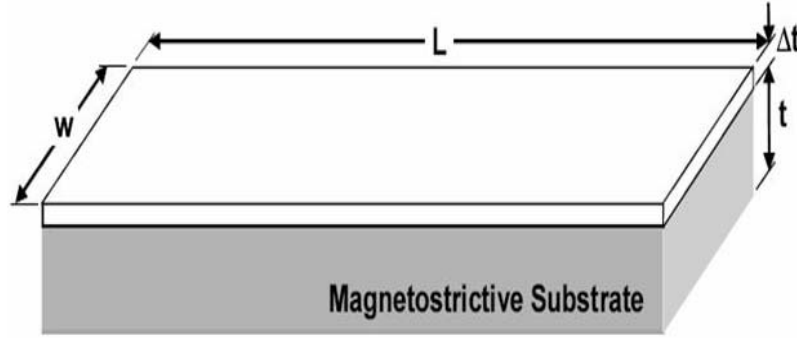
Fig. 2-9   Representation of sensor with thin layer of coating [33].

2.3.1.1.   Determining Young's Modulus in Terms of Mass

Applying Equations (2-15) and (2-16) to Equation (2-11) with n = 1, one can obtain
Equation (2-17) that establishes the relationship of thin film Young's modulus with other
parameters. The masses (m_{sen} and m_{film}) of the sensor and film are used here instead of
their densities. By measuring both the mass and resonant frequency of a sensor before
and after thin film deposition, and knowing the Young's modulus of the sensor material,
the Young's modulus of the thin film material, according to Grimes et al [31, 32], can
therefore be determined

$$\left(\frac{f}{f_0}\right)^2 = \frac{m_{sen}}{m_{sen} + m_{film}}\left(\frac{\Delta t}{t} \times \frac{E_{film}}{E_{sen}} + 1\right) \qquad (2\text{-}17)$$

where f and f_0 are the frequency of the sensor with and without thin film coating,
respectively.

2.3.1.2.   Determining Young's Modulus in Terms of Density

Applying Equations (2-15) and (2-16) to Equation (2-12), one can rewrite Equation (2-12) as

$$\left.\begin{array}{c} \dfrac{\Delta f}{f_0} = \dfrac{1}{2}\left(\dfrac{\Delta t}{t + \Delta t}\right)\left(\dfrac{E_{film}}{E_{sen}} - \dfrac{\rho_{film}}{\rho_{sen}}\right) \\[2em] \Delta f = f_0 - f \end{array}\right\} \qquad (2\text{-}18)$$

As it can be seen, if assuming the thin film Young's modulus and its density are thickness independent under the micro scale regime, the relative resonant frequency shift $\dfrac{\Delta f}{f_0}$ is a linear function of the relative film thickness change $\dfrac{\Delta t}{t + \Delta t}$. The thin film Young's modulus can therefore be determined. This method requires the measuring density of thin film that is typically identical to its bulk value and has the potential to provide more accurate results.

2.3.1.3.   Error Analysis

Two methodologies of determining the Young's modulus of thin film coating have been described, which theoretically should give an identical result. However, the resolution for each instrument may vary; hence, a relative measurement error may occur. The error can be derived from Equations (2-17) and (2-18) and expressed in Equations (2-19) and (2-20). The error in measuring mass is eliminated in the second equation.

21

$$\left| \frac{dE_{film}}{E_{film}} \right| \leq \left| \frac{d(\Delta t)}{\Delta t} \right| + 2 \times \left(\left| \frac{df}{f} \right| + \left| \frac{df_0}{f_0} \right| \right) + \left| \frac{dm_{sen}}{m_{sen}} \right| + \left| \frac{dm_{film}}{m_{film}} \right| \qquad (2\text{-}19)$$

$$\left| \frac{dE_{film}}{E_{film}} \right| \leq \left| \frac{d(\Delta t)}{\Delta t} \right| + \left| \frac{df}{f} \right| + \left| \frac{df_0}{f_0} \right| + \left| \frac{d\rho_{film}}{\rho_{film}} \right| \qquad (2\text{-}20)$$

2.3.2. Mass Sensor for Analyzing Chemicals or Biochemical Agents

A mass sensor, e.g. for biochemical species detection, is depicted in Fig. 2-10, where the antigen is selectively bonded to an antibody as an example. It is supposed that the chemical or biochemical agent does not alter the sensor's mechanical property, e.g. Young's modulus, physical geometry, e.g. thickness, and the attached mass is relatively much smaller than that of the sensor ($\Delta m << m_{sen}$). Equation (2-13) therefore, can be written in the following fashion

$$\frac{\Delta f}{f_0} = -\frac{1}{2} \left(\frac{\Delta m}{m_{sen}} \right) \qquad (2\text{-}21)$$

where Δm is the mass of chemicals or biomolecule uniformly adsorbed on the sensor surface.
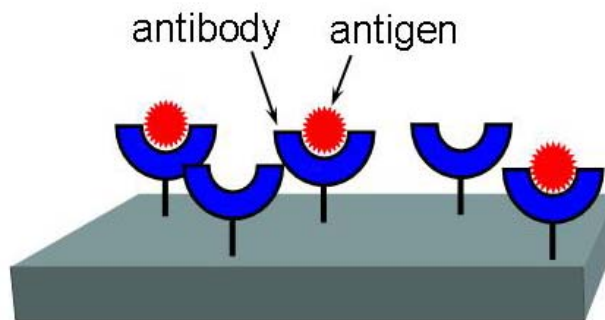
Fig. 2-10 Schematic diagram illustrating the attachment of antibodies bonded with antigens onto the sensor surface.

Sensor sensitivity, which is a key characteristic of a mass sensor, is defined as "the resonant frequency change per mass change", written as

$$S = \left| \frac{\Delta f}{\Delta m} \right| = \frac{f_0}{2 m_{sen}} \tag{2-22}$$

This is the general equation for all types of sensors discussed previously. From this it is clear that a higher sensitivity can be obtained by reducing the sensor's mass and making it more comparable to the target mass, e.g. constructing micro scale sensor platforms.

2.3.2.1. Mass Sensor with Uniformly Distributed Mass Attachment

The first order natural frequency of a cantilever sensor found from Equation (2-10) is expressed in Equation (2-23)

$$f_0 = \frac{1}{4 L} \sqrt{\frac{E}{\rho}} \tag{2-23}$$

The change in resonant frequency due to a uniformly distributed mass load on the sensor is stated as

$$\Delta f = -\frac{1}{2} \left(\frac{\Delta m}{m_{sen}} \right) f_0 = -\frac{1}{8L} \left(\frac{\Delta m}{m_{sen}} \right) \sqrt{\frac{E}{\rho}} \tag{2-24}$$

Similarly, the first order natural frequency for the bridge and beam sensor is obtained from Equation (2-11) and is given by Equation (2-25)

$$f_0 = \frac{1}{2 L} \sqrt{\frac{E}{\rho}} \tag{2-25}$$

The change in the resonant frequency due to a uniformly distributed mass load on the sensor is expressed in Equation (2-26).

$$\Delta f = -\frac{1}{2}\left(\frac{\Delta m}{m_{sen}}\right)f_0 = -\frac{1}{4L}\left(\frac{\Delta m}{m_{sen}}\right)\sqrt{\frac{E}{\rho}} \tag{2-26}$$

For a sensor of the same size, a bridge or beam sensor yields a value of frequency and sensitivity two times greater than that for a cantilever sensor. One may see the higher sensitivity is attainable from the benefits of using

- Bridge and beam type sensors, and

- Microscale geometry, as a result of reduction of the sum of mass.

2.3.2.2. Mass Sensor with a Concentrated Mass Attachment

The resonant frequency shift of a sensor due to a uniform mass distribution on the sensor surface was described in Equations (2-24) and (2-26). However, if the mass is not evenly loaded on the sensor surface, e.g. a single biomolecule cell, the sensor's response to such concentrated mass will be different. Fig. 2-11 depicts a cantilever sensor with a concentrated mass attached at the free end. Recall the differential Equation (2-9),

$$\frac{\partial^2 u}{\partial t^2} = \left(\frac{E}{\rho}\right)\frac{\partial^2 u}{\partial x^2}$$

The boundary conditions for the case of a concentrated mass attached to the free end of a cantilever are [29]:

at x = 0,

$$u = 0 \tag{2-27}$$

and at x = L,

$$\Delta m\left(\frac{\partial^2 u}{\partial t^2}\right) = -(EA)\frac{\partial u}{\partial x} \tag{2-28}$$

24
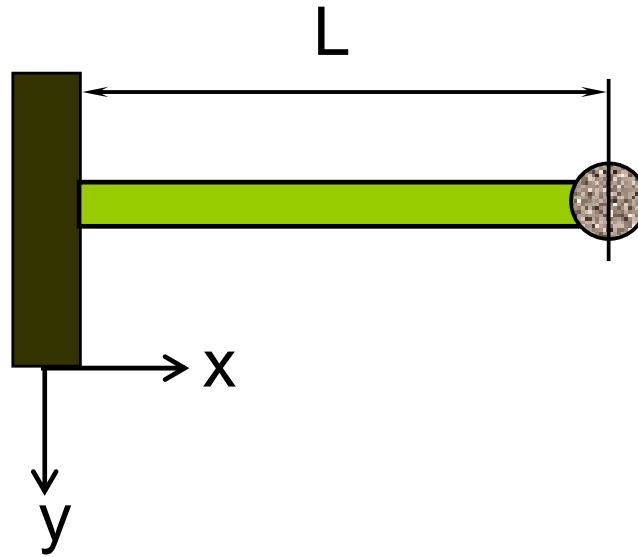
Fig. 2-11   Schematic diagram showing the concentrated mass attached to the free end of a cantilever.

Assuming that the cantilever performs one of the principal modes of vibration, the u, therefore, can be expressed as a function of x and t in Equation (2-29)

$$u(x,t) = f(x)\left[A\cos(\beta t) + B\sin(\beta t)\right] \tag{2-29}$$

in which A and B are constants, f(x) is a certain function of x alone, and β is the angular frequency of this vibrating system. By submitting Equation (2-29) to Equation (2-9), one can obtain,

$$f''(x) + \frac{\beta^2 \rho}{E} f(x) = 0 \tag{2-30}$$

The boundary conditions of Equations (2-27) and (2-28), therefore, become

$$f(0) = 0 \tag{2-31}$$

and

$$f'(L) - \left(\frac{\Delta m}{EA}\right)\beta^2 f(L) = 0 \tag{2-32}$$

25

Let η be the ratio of the attached mass (Δm) to the mass of the cantilever ($m_{sen} = AL\rho$), and inserting

$$\eta = \frac{\Delta m}{m_{sen}} = \frac{\Delta m}{AL\rho}$$

into Equation (2-32), we have

$$f'(L) - \eta L \left(\frac{\rho \beta^2}{E} \right) f(L) = 0 \tag{2-33}$$

The standard solution to Equation (2-30) is

$$f(x) = C \cos(\beta \sqrt{\frac{\rho}{E}} x) + D \sin(\beta \sqrt{\frac{\rho}{E}} x) \tag{2-34}$$

To satisfy the boundary condition: $f(0) = 0$, C must vanish and β must be real. Equation (2-34) therefore becomes

$$f(x) = D \sin(\beta \sqrt{\frac{\rho}{E}} x) \tag{2-35}$$

To meet the boundary condition of Equation (2-33), Equation (2-35) becomes

$$\cos(\beta L \sqrt{\frac{\rho}{E}}) = \eta(\beta L \sqrt{\frac{\rho}{E}}) \sin(\beta L \sqrt{\frac{\rho}{E}}) \tag{2-36}$$

Let $k = \beta \sqrt{\frac{\rho}{E}}$, then Equation (2-36) can be written as

$$\tan(kL) = \frac{1}{\eta kL} \tag{2-37}$$

It is clear that the solution to Equation (2-37) is directly related to the value of η. If $\eta = 0$, it means there is no mass attached on the free end, the solution for Equation (2-37) will be kL = (2n-1)π/2, n = 1.2,3…, in fact, this is the case of fix-free ended cantilever. The

resonant frequency of this cantilever system can be obtained and expressed in Equation (2-38), which is the same as Equation (2-10).

$$f = \frac{\beta}{2\pi} = \frac{\frac{(2n-1)\pi}{2L}\sqrt{\frac{E}{\rho}}}{2\pi} = \frac{2n-1}{4L}\sqrt{\frac{E}{\rho}} \tag{2-38}$$

where n = 1, 2, 3,…

Similarly, if η is infinitely large, which means the mass attached on the free end is too large, the system, therefore, corresponds to a fixed end at x = L, or fix-fix ended bridge. In such case, the solution for Equation (2-37) is

kL = nπ, n = 0, 1, 2, 3,…

Then the resonant frequency of such system is expressed in Equation (2-39), which is equivalent to Equation (2-11)

$$f = \frac{\beta}{2\pi} = \frac{\frac{n\pi}{L}\sqrt{\frac{E}{\rho}}}{2\pi} = \frac{n}{2L}\sqrt{\frac{E}{\rho}} \tag{2-39}$$

where n = 1, 2, 3,…

The general resonant frequency for a cantilever with a concentrated mass attached at the free end is expressed as following,

$$f = \frac{\beta}{2\pi} = \frac{k\sqrt{\frac{E}{\rho}}}{2\pi} = \frac{k}{2\pi}\sqrt{\frac{E}{\rho}} \tag{2-40}$$

Now we consider the case of attaching a small amount of mass on the free end, for example, if η = 0.0005, the approximate solution to Equation (2-36) is kL = 1.570019. The resonant frequency for this case is

27

$$f = \frac{\beta}{2\pi} = \frac{k\sqrt{\dfrac{E}{\rho}}}{2\pi} = \frac{\dfrac{1.570019}{L}\sqrt{\dfrac{E}{\rho}}}{2\pi} = \frac{1.570019}{2\pi L}\sqrt{\frac{E}{\rho}} \qquad (2\text{-}41)$$

The resonant frequency shift due to this concentrated mass ($\Delta m = 0.0005 m_{sen}$) attached to the free end can be obtained as the following:

$$\Delta f = f - f_0 = \frac{1.570019}{2\pi L}\sqrt{\frac{E}{\rho}} - \frac{1}{4L}\sqrt{\frac{E}{\rho}} = \left(\frac{1.570019}{\dfrac{\pi}{2}} - 1 \right)\left(\frac{1}{4L}\sqrt{\frac{E}{\rho}} \right) = \left(\frac{3.140038}{\pi} - 1 \right)f_0 \qquad (2\text{-}42)$$

The relative frequency change is then

$$\frac{\Delta f}{f_0} = \left(\frac{3.140038}{\pi} - 1 \right) = -4.94861607 \times 10^{-4}$$

If we consider that this amount of mass (Δm) is uniformly distributed on the sensor's surface, then the relative frequency change can be obtained from Equation (2-21) and is,

$$\frac{\Delta f}{f_0} = -\frac{1}{2}\left(\frac{\Delta m}{m_{sen}} \right) = -\frac{1}{2} \times 0.0005 = -2.5 \times 10^{-4}$$

We can see that the concentrated mass attached on the free end has much higher frequency change than the uniformly distributed one. Similarly, it is easy to determine that there will be no change in resonant frequency if the concentrated mass is attached to the fixed end of a cantilever or bridge.

For different ratios (η values) of the concentrated mass to the mass of this cantilever sensor, the solution (kL value) of Equation (2-37) can be either mathematically or graphically obtained. Table 2-1 lists the kL values for some particular η values for the fundamental mode (n = 1).

Table 2-1 Calculated the roots (kL values) for Equation (2-37) at different η values.

η	0	0.0005	0.005	0.01	0.05	0.5	1	∞
KL	π /2	1.570019	1.562969	1.55219	1.496119	1.076869	0.860332	π

The general equation for the change in resonant frequency due to a concentrated mass attached to the free end cantilever can be expressed as,

$$\Delta f = \frac{kL}{2\pi L}\sqrt{\frac{E}{\rho}} - \frac{1}{4L}\sqrt{\frac{E}{\rho}} = \left(\frac{2kL}{\pi} - 1\right)\frac{1}{4L}\sqrt{\frac{E}{\rho}}$$

(2-43)

and the relative frequency shift is,

$$\frac{\Delta f}{f_0} = \frac{2kL}{\pi} - 1$$

(2-44)

Table 2-2 lists the relative resonant frequency shift obtained by Equation (2-44) for concentrated mass and Equation (2-21) for an evenly distributed mass at different ratios of the attached mass to the cantilever mass. Based on the results in Table 2-2, it can be concluded that there is a large difference of relative frequency shifts between the concentrated and evenly distributed mass loaded on the cantilever sensor surface.

Similarly, if this concentrated mass attached on one of the free ends of a free-free ended beam, the boundary conditions will be

at x = 0,

$$\frac{\partial u}{\partial x} = 0$$

(2-45)

and at x = L,

$$\Delta m \left(\frac{\partial^2 u}{\partial t^2}\right) = -\left(EA\right)\frac{\partial u}{\partial x}$$

(2-46)

29

Table 2-2 Calculated relative resonant frequency changes for a concentrated mass attached to the free end and an evenly distributed mass with the same amount as a concentrated one at a different ratio of this attached mass to the sensor mass (η).

η		0	0.005	0.005	0.01	0.05	0.5	1	∞
$\dfrac{\Delta f}{f_0}$	Con.	0	-0.00049486	-0.00498303	-0.00991683	-0.04754106	-0.31444390	-0.045229596	1
	Even	0	-0.00025	-0.0025	-0.005	-0.025	-0.25	-0..5	-∞

Note: con. represents concentrated mass loaded on the free end, and even represents the mass evenly distributed on the sensor's surface.

Submitting Equations (2-45) and (2-46) to Equation (2-29), we obtained a new set boundary conditioning equations as follows:

$$f'(L) - \eta L \left(\frac{\rho \beta^2}{E} \right) f(L) = 0$$

(2-47)

Applying these two boundary conditions to Equation (2-34), we have D = 0 and

$$\eta \left(L\beta \sqrt{\frac{\rho}{E}} \right) = -\tan \left(L\beta \sqrt{\frac{\rho}{E}} \right)$$

or

$$\eta(kL) = -\tan(kL)$$

(2-48)

If there is no concentrated mass attached (η = 0), kL must be 0, π, 2π, 3π…, to satisfy Equation (2-48), therefore, the resonant frequency for this fee-free ends system is

$$f = \frac{\dfrac{n\pi}{L}\sqrt{\dfrac{E}{\rho}}}{2\pi} = \frac{n}{2L}\sqrt{\frac{E}{\rho}}$$

where n = 1, 2, 3,….

30

If η is infinitely large, the solution to Equation (2-48) is kL = $\pi/2$, $3\pi/2$, $5\pi/2$, and the resonant frequency of this system is

$$f = \frac{\frac{(2n-1)\pi}{2L}\sqrt{\frac{E}{\rho}}}{2\pi} = \frac{2n-1}{4L}\sqrt{\frac{E}{\rho}}$$

In fact, this system is identical to fix-free ended cantilever in this case.

The general resonant frequency equation for this free-free ended beam with a concentrated mass attached to one of its ends is actually the same as the case of the cantilever attached with a concentrated mass on the free end as stated by Equation (2-40). The difference is that the k value is different due to boundary conditions different in particular case. However, the relative frequency shift for the free-free ended beam system is as following:

$$\frac{\Delta f}{f_0} = \frac{kL}{\pi} - 1$$

(2-49)

Table 2-3 lists the solution of kL value for Equation (4-48) and the relative resonant frequency shift for some particular η values. If there is no concentrated mass attached on the end, there is no frequency change. If the attached mass is infinitely large, the resonant frequency is reduced to the half of that for the free-free ended beam system, which is identical to the case of fix-free ended cantilever. It can be seen that the relative frequency shift for a concentrated mass attached to one end of the freestanding beam is also higher than that of evenly distributed mass on the sensor surface.

Table 2-3 Calculated kL values from Equation (2-48) and relative resonant frequency shift from Equation (2-49) at a different ratio (η) of attached mass to the free-free ended beam mass.

η	0	0.0005	0.005	0.01	0.05	0.5	1	∞
kL	π	3.1400225	3.1259645	3.1104975	2.9930425	2.2889295	2.0287575	$\pi/2$
$\dfrac{\Delta f}{f_0}$	0	-0.00049978	-0.0049746	-0.0098979	-0.047285	-0.02714111	-0.03542264	-0.5

Although the discussion above is based on the case of a concentrated mass attached to the free end of a cantilever or beam. One can anticipate that if the concentrated mass is not attached at the end of a cantilever, beam or bridge, it will likely result in a different resonant frequency change even if the mass has the same amount value. This is because the acceleration speed will be different at the location where there is a concentrated mass attached, which results in the system having a different resonant frequency.

Considering the case of vibrating free-free ended beam, regardless of the amount of an attached concentrated mass, by inserting Equation (2-34) with D = 0 to Equation (2-29), the body deformation amplitude of this sensor can be expressed as a function of x and time (t) and rewritten as,

$$u(x,t) = C\cos(\beta\sqrt{\frac{\rho}{E}}x)\left[A\cos(\beta t) + B\sin(\beta t)\right] \tag{2-50}$$

or

$$u(x,t) = C\cos(kx)\left[A\cos(k\sqrt{\frac{E}{\rho}}t) + B\sin(k\sqrt{\frac{E}{\rho}}t)\right] \tag{2-51}$$

in which, k is related to the η. If η = 0, and kL = π for the first mode, the displacement u(x.t) of a position at x = L/2 will be zero at any given time t. This is the neutral position of a free-free ended beam vibrating in the first longitudinal mode. When a concentrated mass is attached to the middle of this sensor, there will be no effect on the frequency of this system. Note that if there is any concentrated mass loaded at a location other than the middle on this sensor, the middle of the beam is no longer the natural position. When the mass is attached at the natural position, it will result in no resonant frequency change.

2.4.   Methodology of Detecting the Resonant Frequency of a Magnetostrictive Sensor

The test setup consists of three key units, a HP8751A network analyzer (a), a custom made read coil that serves as a A/C magnetic field generator and sensor's signal pick up (b), and a permanent magnetic bar that serve as a magnetic bias field (c), as shown in Fig. 2-12. Note that the read coil is directly connected to port 1 of the network analyzer and both the read coil and magnetic bar are not in scale. They are enlarged for better observation. The characteristics of a magnetostrictive sensor can be characterized through this set up. The basics can be described as follows: when the analyzer sends a RF swept signal (exciting signal) or power, through the coil, which generates an A/C magnetic field in the coil, a magnetostrictive sensor inside the coil will alternatively change its shape or vibration as a result of response to this A/C magnetic field. Such change in shape of the sensor will produce a second; an alternative magnetic field that will interacts with the read coil (also called pick up) to generate a second, an alternatively signal at the same frequency as the applied RF signal. When the frequency of the applied RF swept signal reaches the resonant frequency of the magnetostrictive strips, oscillation occurs, and the

strips are deformed, therefore, reaching its maximum. Consequently, this is the largest interaction between the magnetostrictive strips and the pick-up coil. This largest interaction results in the largest power change in the device under test (DUT) and network, which is analyzed by the network analyzer through measuring either the transmitted or the reflected signal.
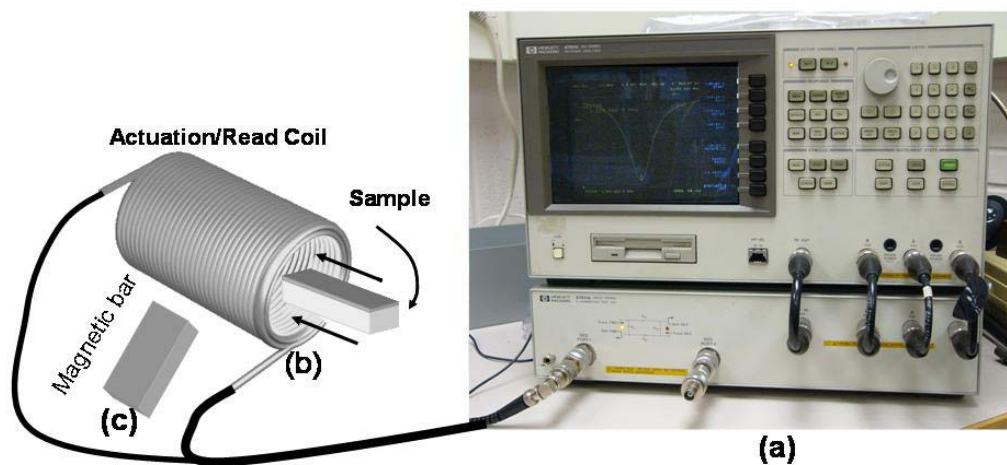
Fig. 2-12 Resonant frequency detection setup. Actuation/read coil, and magnetic bar are not to scale.

In this measurement setup, we measured the reflected signal (S_{11} parameter). Fig. 2-13 is the representation of the S-parameters of a two-port device signal flowchart. The signal reflected from the DUT is measured as a ratio with the incident signal, and it is expressed as a reflected coefficient, or a return loss. It is mathematically defined as [34].

$$reflection\ coefficient = \frac{reflected\ power}{incident\ power}$$

$$= S_{11}\quad or\quad S_{22}\quad (magnetitude\ or\ phase)$$

(2-52)

34

In our case, port 2 was terminated; therefore, S_{11} is the input reflection coefficient, is defined as

$$S_{11} = \left(\frac{b_1}{a_1}\right)_{a_2=0} \tag{2-53}$$
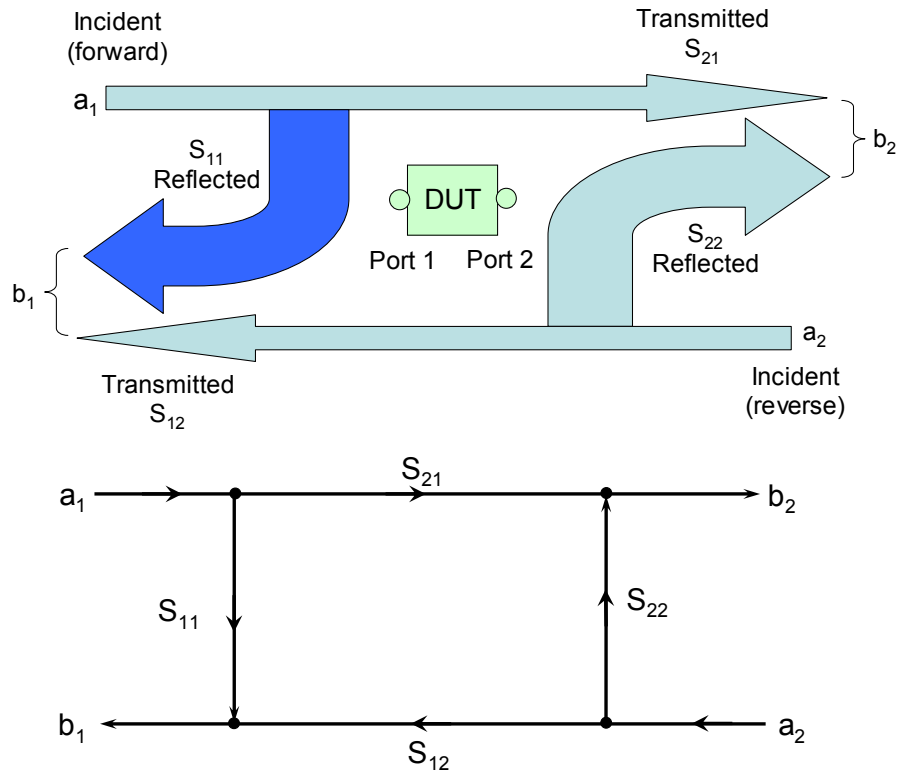
Fig. 2-13 S-parameters flow diagram.

Fig. 2-14 is the frequency response of S_{11} parameters displaced in log magnitude and phase of the DUT, the size of the sensor is 5mm by 1mm. The HP8751A network analyzer can display S_{11} data linear magnitude, log magnitude, or phase. The linear magnitude and log magnitude have similar frequency response patterns. Either one can be used to determine the corresponding frequency at the S_{11} peak. Here, the S_{11} in magnitude

format was more convenient to use instead of phase to determine the sensor response to the incident frequency.
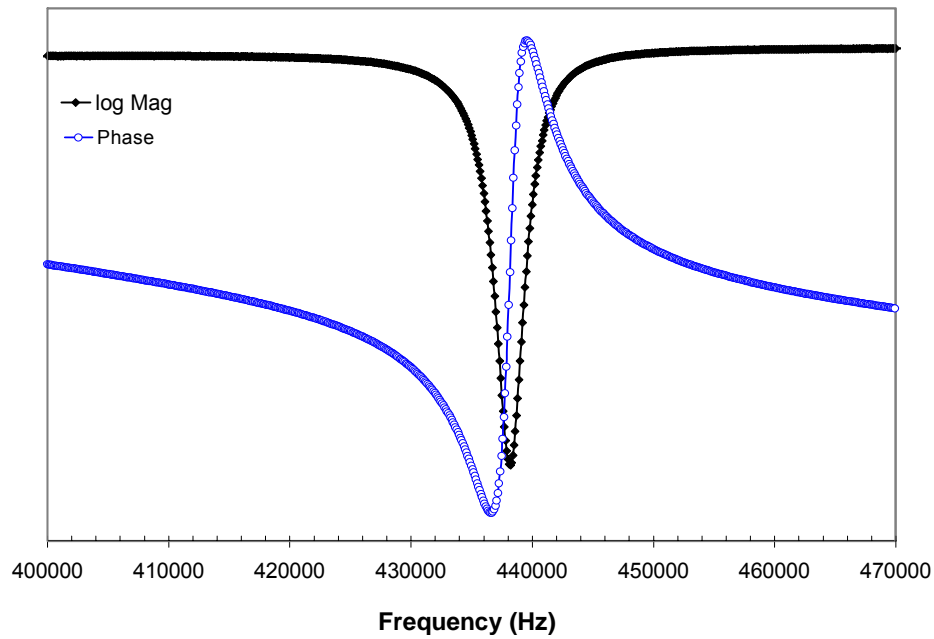
Fig. 2-14 S_{11} change with the swept frequency.

The amount of power reflected from the device under test is directly related to impedances of both the device and the measuring system. The largest power reflection corresponds to the oscillation of the sensor occurring at this swept frequency point, therefore, the resonant frequency of the sensor under test can be determined though this test. The conversion of S_{11} data to the equivalent complex impedance (Z_R) can be done through the Equation (2-54) [34]

$$Z_R = Z_0 \frac{1 + S_{11}}{1 - S_{11}} \qquad (2\text{-}54)$$

36

where Z_0 is the impedance of the network, we set it at its default value 50 Ω. One can

convert S_{11} data to the impedance as a function of incident RF swept frequency or

directly measure impedance through the analyzer. Fig. 2-15 shows the measured

impedance (magnitude and phase) change as a function of the swept frequency. One can

find the largest S_{11} magnitude change occurs at the frequency 438400 Hz in Fig. 2-14,

and the minimum and maximum impedances occur at frequencies 435700 Hz and 439300

Hz in Fig. 2-15, respectively. The differences between them are

$$\frac{438400 - 435700}{438400} = 0.62\% \text{ and } \frac{438400 - 439300}{438400} = -0.21\%$$
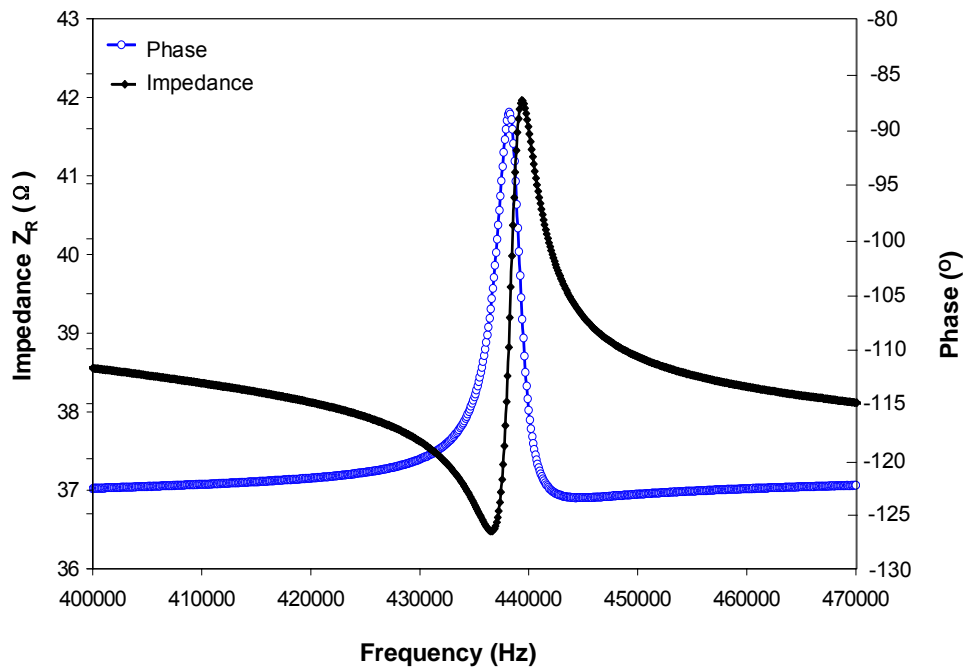
Fig. 2-15 Impedance change as a function of the swept frequency

This clearly indicates that using the log magnitude format of S_{11} will not result in

significant error in determining the resonant frequency of a sensor. The resonant

37

frequency of the magnetostrictive sensor is therefore determined where the smallest S_{11} signal magnitude (largest amplitude change) occurs through this study.

3. FUNDAMENTALS AND ADVANTAGES OF A SENSOR VIBRATING IN THE LONGITUDINAL MODE

Before magnetoelastic sensors were developed for mass detection, researchers often relied on the cantilever- or bridge-based mass sensors that operated in transverse mode. In fact, sensors fabricated in the cantilever or bridge structure can be actuated in either transverse vibration (out of plane) or longitudinal vibration (in plane) modes, depending on the exciting method applied. Microcantilever sensor operation in the transverse mode is typically driven by an actuation element, and the response is detected by the sensing element. Electrostatic, thermomechanic and piezoelectric actuation are common techniques used for actuation, while optical reflections, piezoelectric and piezoresistive sensing read-out are common techniques for signal detection. The following reviews the actuation and detection techniques.

3.1. Comparison of the Fundamentals of Vibrating a Cantilever, Bridge, or Beam System

3.1.1. The Transverse Mode

3.1.1.1. Actuation Techniques

Electrostatic actuation utilizes an electrostatic force that is generated by a charge from applying a high voltage (>100v) with very little current. A cantilever beam or

diaphragm can be excited to vibrate if an A/C electric field is applied. Thermomechanical actuation is based on the joule resistive heating effect. When a composite beam is electrically heated (~5-10 v with small mA current), the thermal stress will cause a larger extension for the higher CTE material, while the counterpart with a lower CTE component will extend less. As a result, the beam is bent. This method only works at very low frequencies due to the time necessary for the heat to radiate/diffuse away. Piezoelectric actuation, on the other hand, is based on the electromechanical coupling effect exhibited by certain materials. When voltage is applied across two parallel surfaces, a piezoelectric material will undergo mechanical distortion, i. e. a change in shape, and vice/versa if mechanical deformation is applied. This method currently drives the majority of applications needing a resonator or transducer. An earphone, for example, uses an electrical input to generate a mechanical output. As mentioned above, piezoelectric materials also exhibit the effect that a voltage drop can be produced when they are subjected to applied mechanical stress, which has been employed in strain gauges, microphones, microbalances, and others. Ferrari et al. [35] reported in 1996, employing the piezoelectric effect to both actuate and sense cantilever resonance and changed thereof. The mass sensitivity is the range of 280 to 1200 Hz/mg for this type of mass sensor.

3.1.1.2. Sensing Techniques

Optical reflection, piezoresistance, and electrostatic measurement methods are commonly used to detect cantilever bending in the static mode [36-44]. Optical reflection of a focused laser beam on a cantilever can be detected either by a position

sensitive detector [44] or by interference of a reference laser beam with the one reflected by the cantilever [45]. The electrostatic method involves monitoring the capacitance change due to a bending cantilever or bridge. Optical reflection and piezoresistance are commonly used for detecting the resonate frequency in the dynamic mode [46, 47]. Pinnaduwage and coworkers [43] reported that the bending signal is much clearer and easier to measure than the resonant frequency signal. However, when it is operated in a liquid, especially in an opaque liquid, the laser undergoes refraction in the liquid and significantly loses intensity in both bending and dynamic modes. In such cases electronic measurements are more prudent; however, if the cantilever bending is less than 50 nm, the signal may not be detected by the piezoresistive elements [48] and the large damping effects of liquid environments may limit the application of the piezoresistive technique. The magnetostrictive effects to drive and sense cantilever sensors [25, 49-51] in the transverse mode have been widely studied as well.

3.1.2.   The Longitudinal Mode

Longitudinal vibration, the counterpart of the transverse mode, involves resonance along the structure's longest axis (in plane vibration). In the past, there were no actuation techniques available to excite a cantilever or bridge into longitudinal vibration. However, magnetostrictive materials offer great promise in this mode of actuation. In this method, magnetic domains respond and switch in the direction of an applied field. This phenomenon is exhibited in all ferromagnetic materials and will be very useful as a means to drive a sensor platform in the longitudinal mode (under an externally modulated magnetic field). The details of the fundamental mechanism and inducing resonance by

external magnetic fields with a close loop circuit (pick-up coil) were discussed in section 2.

3.2. Advantages of Vibrating a Cantilever, Bridge, and Beam in the Longitudinal Mode Over the Transverse Mode

3.2.1. Comparison of the Resonant Frequency Magnitude for the Two Vibration Modes

The first order natural frequency for a cantilever and bridge vibrating in the transverse mode without damping can be found in Equations (3-1) and (3-2)

$$f_0 = \frac{1}{2\pi}\left(\frac{1.875}{L}\right)^2\sqrt{\frac{EI}{A\rho}} = \frac{t}{2\pi\sqrt{12}}\left(\frac{1.875}{L}\right)^2\sqrt{\frac{E}{\rho}} = \frac{0.1615 \times t}{L^2}\sqrt{\frac{E}{\rho}} \qquad (3\text{-}1)$$

$$f_0 = \frac{1}{2\pi}\left(\frac{4.730}{L}\right)^2\sqrt{\frac{EI}{A\rho}} = \frac{t}{2\pi\sqrt{12}}\left(\frac{4.73}{L}\right)^2\sqrt{\frac{E}{\rho}} = \frac{1.028 \times t}{L^2}\sqrt{\frac{E}{\rho}} \qquad (3\text{-}2)$$

where E is Young's modulus in an isotropic material, ρ is the density of the cantilever or bridge material, and L and t, respectively, denote the length and thickness of the cantilever or bridge.

If a sensor of a fix-free ended structure, a cantilever, is vibrating in either the transverse or longitudinal modes, the relationship of first order resonant frequency can be obtained by combining Equations (3-1), for transverse mode, and (2-10), for longitudinal mode, as,

42

$$f_L \approx \frac{1.55\,L}{t} f_T \qquad\qquad (3\text{-}3)$$

where f_L and f_T are the resonant frequencies of the longitudinal and transverse modes respectively. A similar relationship of first order frequency for a fixed-fixed ended structure, a bridge, between the transverse and longitudinal modes is expressed as Equation (3-4) by combining Equations (3-2) and (2-11)

$$f_L \approx \frac{0.49\,L}{t} f_T \qquad\qquad (3\text{-}4)$$

again, f_L and f_T represent the resonant frequency of longitudinal and transverse mode, respectively.

For a sensor 250 μm long, 50 μm wide and 5 μm thick, its first order frequency in the longitudinal vibration mode will be 77.5 times that of the transverse mode for a cantilever structure, and 24.5 times that of the transverse mode for a bridge structure. It is worth noting that the resonant frequency for a bridge is approximately 6.4 times greater than a cantilever if both are operated in transverse mode and is 2 times greater if both are operated in longitudinal mode. Figs. 3-1 and 3-2 compare resonant frequencies of cantilever and bridge structures under various operating modes. In both cases, the resonant frequency drops very fast as the size (length) increases, but more so in the transverse mode. Large discrepancies in the magnitude of frequency between the longitudinal mode and the transverse mode can be observed, even for lengths down to 10 μm. We expect that the higher frequency of the longitudinal mode will result in higher frequency shift and mass sensitivity when mass is attached to it.
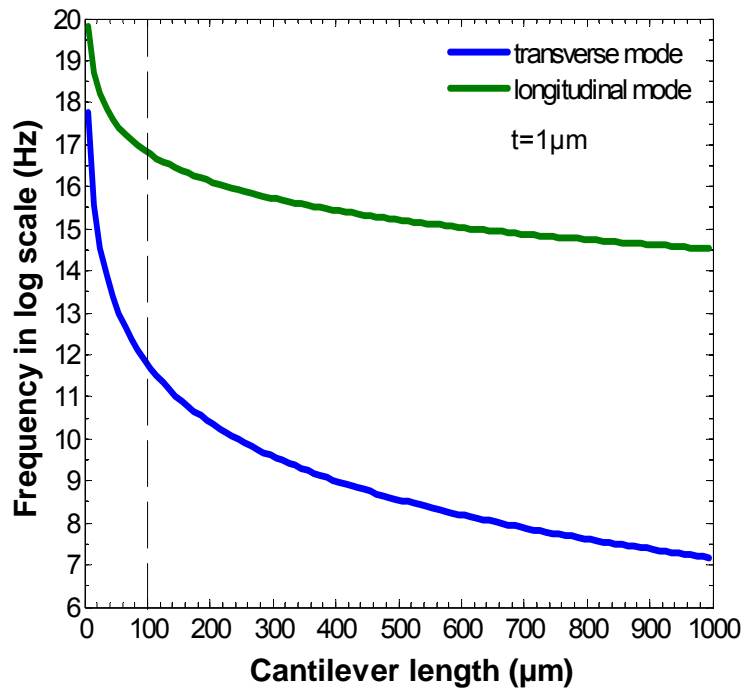
Fig. 3-1　Comparison of cantilever resonant frequency operated in different modes.
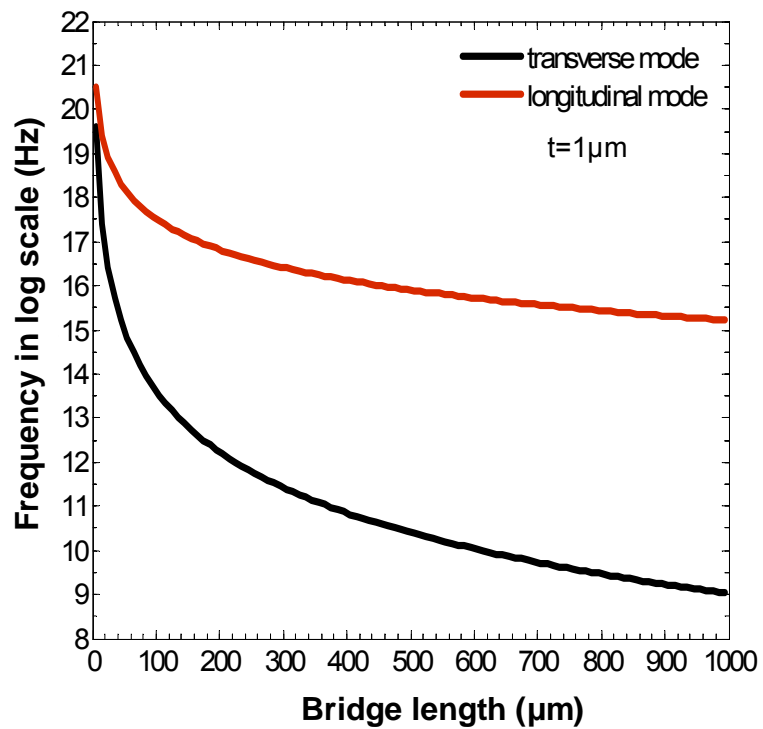
Fig. 3-2　Comparison of bridge resonant frequency operated in different modes.

3.2.2. Comparison of Sensitivity for Two Vibration Modes

A mass sensor working in either of the vibration modes will have a sensitivity expression in the same manner as stated by Equation (2-22), which is

$$S = \left| \frac{\Delta f}{\Delta m} \right| = \frac{f_0}{2m_{sen}}$$

(3-5)

Assuming the sensor has an aspect length to width ratio of at least 5, then the sensitivity for a cantilever working in transverse mode (S_{CT}) and longitudinal mode (S_{CL}) is expressed as

$$\left. \begin{aligned} S_{CT} &\approx \frac{0.40375 \; \upsilon}{\rho L^4} \\ S_{CL} &= \frac{0.625 \; \upsilon}{\rho L^3 t} \end{aligned} \right\}$$

(3-6)

Obviously, a cantilever in the longitudinal vibration mode has a much higher sensitivity than that in the transverse mode, e.g. for a 250 μm x 50 μm x 5 μm cantilever, ρ = 7.9 g/cc. $S_{CT} \approx 1.28\%$ S_{CL}. This is also true for a bridge with the same size $S_{BT} \approx 4.11\% S_{BL}$, where S_{BT} and S_{BL} are the sensitivities of bridge operated in the transverse mode and longitudinal mode, respectively. The relationship of the sensor's sensitivity for the transverse mode and the longitudinal mode can be derived and expressed in Equations (3-7) and (3-8) for cantilever and bridge, respectively.

$$S_T \approx 0.641 \left(\frac{t}{L} \right) S_L$$

(3-7)

$$S_T \approx 2.056 \left(\frac{t}{L} \right) S_L \qquad\qquad (3\text{-}8)$$

where S_T, S_L are the sensitivity of transverse and longitudinal mode respectively.

By comparing the sensitivity of a cantilever sensor vibrating in transverse and longitudinal modes one can plot the ratio of S_T to S_L as a function of length under a variety of sensor thickness, (see Fig. 3-3). As seen in this figure, the sensitivity of a cantilever sensor operated in the transverse mode is only a fraction of that when operated in the longitudinal mode. The value of 10% is achievable when the sensor thickness is rather large, for instance, 15 μm or 28 μm. However, in such case the sensitivity for the longitudinal mode itself is relatively low. A similar trend is seen for a sensor configured as a bridge that is operated in the transverse or longitudinal modes (see Fig. 3-4). In both configurations, it is clear that a sensor operating in the transverse mode has a significantly lower sensitivity compared with one operating in the longitudinal mode. From this, we can draw two conclusions: (1) the longitudinal mode is the preferred resonance mode for maximum sensitivity and (2) the performance of the transverse mode becomes even poorer in comparison as thickness is decreased. The second becomes more important when considering thin film devices, which will be covered in later sections.
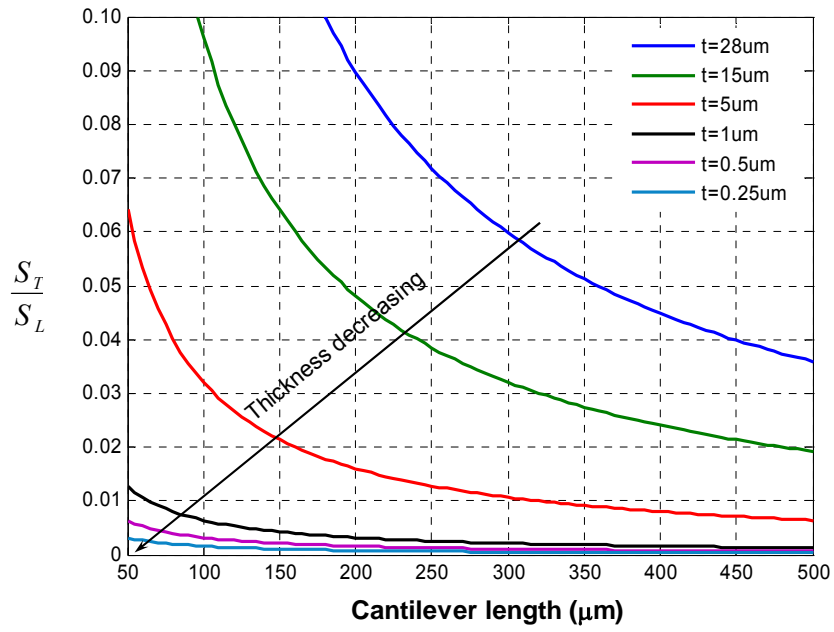
Fig. 3-3 The sensitivity ratio $\left(\frac{S_T}{S_L}\right)$ of a cantilever sensor as a function of sensor geometry.
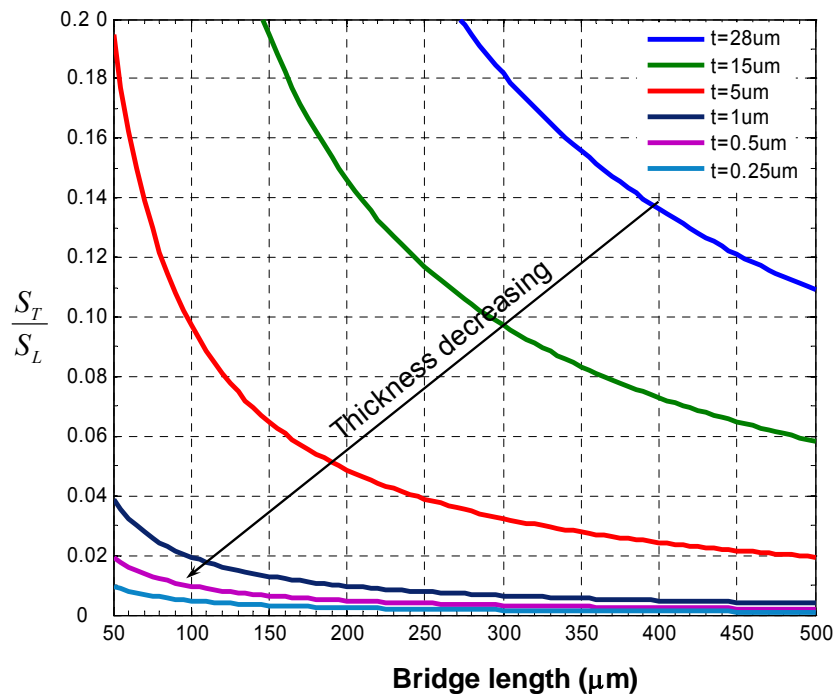
Fig. 3-4 The sensitivity ratio $\left(\frac{S_T}{S_L}\right)$ of bridge sensor as a function of sensor geometry.

47

3.3. Minimum Sensor Geometry Required for Detection of a Single Biomolecule

One of the goals of Auburn's Detection and Food Safety Center is developing the ability to detect the attachment of a single biological species, particularly for those agents with a very low pathogenic limit. In order to detect a single biomolecule, e.g. with a mass of approximately 1pg, under the in-house instrument's resolution of 25 Hz, the sensor must have a sensitivity better than 25 Hz/pg, or 2.5E+16 Hz/kg. By using Equation (3-5) and assuming a standard aspect ratio of length to width of five, one can plot the trends of device sensitivity with size. Figs. 3-5 and 3-6, respectively, illustrate how the sensitivity of a cantilever (made of Metglas with ρ = 7.9 g/cc) working in the transverse or longitudinal mode changes with sensor size (geometry). It should be noted that in the transverse mode, and according to Equation 3-6, the sensitivity is not a function of the sensor thickness. Thus, there is only one curve in Fig. 3-5. In the case of longitudinal mode, the sensitivity is a function of both the sensor length and thickness. In order to achieve the same sensitivity, a cantilever operated in the transverse mode has to be made in a much smaller size, but a variety of cantilever sizes can be used for it operation in the longitudinal mode. This is important to a magnetostrictive sensor, since the signal of such type of sensor is directly related to the volume of magnetostrictive material employed, sensor made in large will produce stronger signal. This is another outstanding feature of a sensor operated in the longitudinal mode.

The size required to detect a single biomolecule for a sensor operated in the longitudinal mode is relatively large. For example, if the sensor has a thickness of 1μm, the necessary cantilever length is about 242 μm. The length required for detection of a single biomolecule for some particular thickness of a cantilever, bridge or beam is at least
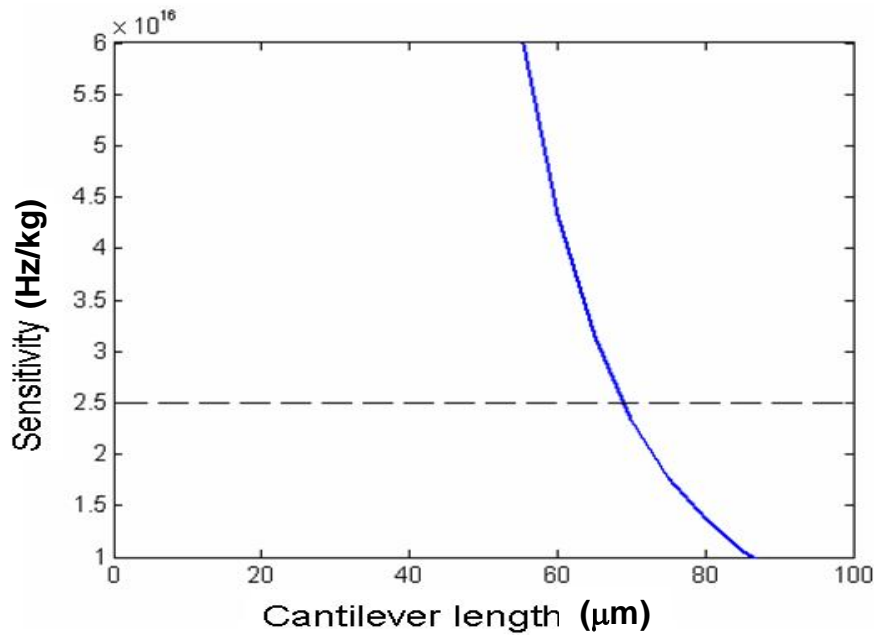
Fig. 3-5   Change in sensitivity of a cantilever in the transverse mode by size.
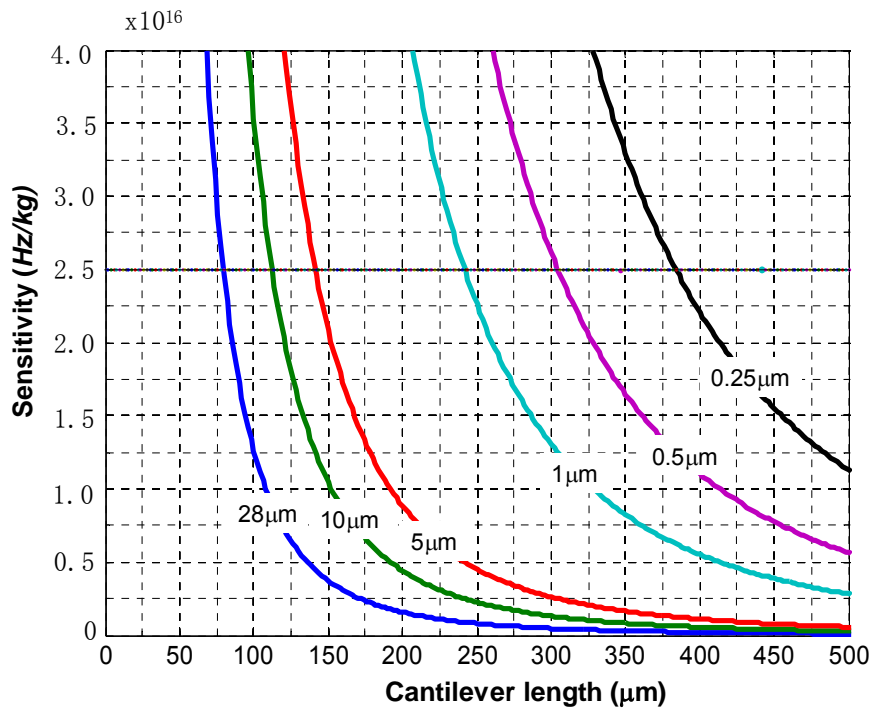
Fig. 3-6   Change in sensitivity of a cantilever in the longitudinal mode by size.

smaller than the size summarized in Table 4-3. It is clear that longitudinal mode actuation combined with a bridge structure yields the best solution when considering that the larger the sensor is the easier it is to fabricate, handle and operate.

Table 3-1 Essential geometry of a cantilever and bridge sensor designed for detecting a single biomolecule.

Sensor thickness t (µm)		28	10	5	1	0.5	0.25
Cantilever	Width w (µm)	16	22	28	48	61	76
	Length L (µm)	79.6	111.7	140.7	242.8	305.9	383.6
Bridge or beam	Width w (µm)	20	28	35.5	61	76	96.7
	Length L (µm)	100.3	140.7	177.4	305.9	383.6	483.3

Note: the material properties used for these calculations are for Metglas 2826 MB and are given earlier in the text. Furthermore, in reality, a thin layer of Au is necessary to facilitate attachment of the capture layer and is not considered here.

It should also be noted that the discussion above is based on the mass being evenly distributed on a sensor's surface. For a concentrated mass on a sensor, the resonant frequency change, however, is different from the evenly loaded case, which was discussed in section 2.

3.4. Summary

The sensitivity of a sensor that is constructed in a fix-fix ended bridge and a free-free ended beam doubles the value for a fix-free ended cantilever. The advantages of a

mass sensor operated in the longitudinal mode as opposed to the conventional transverse mode were discussed by a comprehensive comparison of frequency and mass sensitivity for cantilever and bridge operation in both the transverse and longitudinal modes. The mass sensitivity of a sensor operated in the transverse was found to possess only a fraction of the sensitivity when operated in the longitudinal mode.

The fundamental size requirement of a miniaturized sensor, it is fabricated in the structure of cantilever or bridge, and operated in both vibrating modes was addressed, so that sensors can be optimized to detect mass attachments on the order of a single spore or cell. It was found that a cantilever sensor operated in the transverse mode must be designed as small as 70 μm in length so that it is possible to detect a single spore, while a cantilever sensor operated in the longitudinal mode can detect the same mass at a significantly larger sensor size. This is important for easier fabrication, operation and handling of the sensors.

4. CORRECTION TO THIN, SLENDER BEAM VIBRATING IN THE
LONGITUDINAL MODE PRINCIPLE AND VALIDATION OF PROOF-OF-
CONCEPT EQUATIONS

The potential applications of a resonated sensor for measuring thin film Young's modulus and mass detection have been discussed in the preceding sections. To better understand the mechanism of a sensor operated in the longitudinal vibration mode finite element analysis was employed to numerically simulate the magnetostrictive sensors. This section reports on these results and details the modification and verification of the operation principle of a thin slender beam vibrating in the longitudinal mode. In addition to the finite element analysis, proof-of-principle for this modification was also verified by experimentation. Metglas 2826 MB and its material properties were used as the sensor material for both experimentation and simulation.

4.1. Introduction

Mass sensors based on a cantilever operating in the transverse mode have received extensive research interest over the past decade or so due to the ease and convenience of actuating and measuring resonance behavior. However, as demonstrated in the previous section, the sensitivity of this type of sensor is rather low in comparison to other vibrational modes for the identical structure. In recent years, magnetostrictive materials have enabled the longitudinal vibration mode to be considered as the resonance mode of a sensor platform. Unfortunately, most of the attention in this area has only been focused on the relationship between the relative resonant frequency shift and the relative mass

change of the sensor, which is prudent, but only in cases where mass is the only parameter influencing the resonant frequency change. To the best of the author's knowledge, little effort has been focused on addressing the fundamental aspects of cantilever/bridge operation in the longitudinal. For example, the geometry causes other parameters to influence behavior. It is important to have a clearer understanding of these issues so that device design may be improved and optimized.

The first step in the numerical simulations was the assumption that the cross-section of the bar remains in-plane during longitudinal vibration. In reality, when a slender bar, such as a cantilever, bridge or freestanding beam, vibrates in the longitudinal mode, the lateral strain induced by the longitudinal stress is small and negligible since the longitudinal wave is much larger in comparison to the cross-sectional dimensions of the bar. In such case, the first order resonant frequency can be obtained by

$$f = \frac{1}{4L}\sqrt{\frac{E}{\rho}}$$

and

$$f = \frac{1}{2L}\sqrt{\frac{E}{\rho}}$$

for a cantilever and bridge/freestanding beam respectively [28, 30, 52], as discussed in section 2. These equations are the general reflections of bars configured in their respective structures. These equations hold for general dimensions where length, width and thickness are comparable in magnitude. However, as one or more dimensions become significantly different in magnitude, say a sufficient reduction in size, geometrical effects begin to play a role in the form of the Poisson Effect, whereby the reduced dimensions cause a different response to straining governed by the materials

53

dimensions and Poisson's ratio. In the case of Metglas tape with a thickness of 28μm, the dimensions are on the order of L>w>>t. This defines a plate-like situation where cantilever, bridge or beam structures subjected to the elastic deformation in the longitudinal direction will be under a state of plane-stress rather than uniaxial-stress. As such, Poisson's ratio would play a different role in resonance behavior. In general, Landau [30] suggested replacing Young's modulus E with the plane-strain modulus $E/(1-v^2)$ for deformation of plate-like structures. Harris [52] and Timoshenko [28], however believed the above equations still hold true for the plate case. These arguments are contradictory to some extent, but the extensive experimental work with cantilevers in the transverse mode has demonstrated that geometry influences which modulus to use, i.e. the plane-strain, plane-stress or uniaxial modulus. This issue has yet to be studied and the early work in applying Metglas strips in longitudinal mode resonance employed the plane-strain modulus in accordance with Landau [14, 53, 54]. However, when one experimentally measures the resonant frequency of a cantilever or beam in longitudinal vibration, the measured values are much higher than the calculated values predicted by the equations cited above. For example, a freestanding beam with a dimension of 8 mm x 1.6 mm x 28 μm that is made of Metglas with a density of 7.9 g/cc and Young's modulus of 105 GPa [10] has a measured resonant frequency of 274,700 Hz in the longitudinal mode. If we assume Poisson's ratio of this material is 0.33, which is typical for an amorphous glassy metal, the calculated frequencies will be 227,856 Hz and 241,378 Hz by Timoshenko and Landau's equations, respectively. Either case is lower, whereas real-life damping effects should cause the measured value to be lower then the calculated one.

Equation (4-1) is the widely cited form adopted by many papers [13, 14, 17, 19, 53-57] that deal with Metglas operated in longitudinal vibration.

$$f = \frac{1}{2L}\sqrt{\frac{E}{\rho(1-\nu^2)}}$$

(4-1)

For this equation if Poisson's ratio 0.5 is used, and the results seem to agree. However, Poisson's ratio for Metglas was measured to be 0.33 by Chou et al. [58], and should be the values employed. Additionally, a metal should not posses a Poisson's ratio 0.5. Table (4-1) lists the resonant frequencies obtained from different equations and experimental tests for different geometries vibrated in the longitudinal mode. In the calculation, Poisson's ratio 0.33 was used.

Table 4-1 Comparison of resonant frequencies calculated by using E and plane-strain modulus $E/(1-\nu^2)$ with experimental test for freestanding beam cantilever and bridge at different lengths.

L(mm)	Structure	(kHz)		
		Uniaxial E	Plane Strain $E/(1-\nu^2)$	Experimental
8	Freestanding	227.9	242.7	274.7
9	Cantilever	101.3	107.3	123.7
14.4	Bridge	126.6	134.1	153.9

The discrepancy in the values of the calculated resonant frequencies that are lower than the measured values must relate to the chosen state of strain in the structure, which manifests from the three-dimensional combination of elastic extension and contraction strains. Since the bars are more plate-like they are likely to be in a state of plane-stress. In such a case, the elastic modulus should be replaced by the plane-stress modulus $E/(1-v)$. Given that the effect of the different dimensions on the state of strain are uncertain, it is possible that for the given dimensions the effect lies between plane-stress and plane-strain, the difference being the operating power of Poisson's ratio.

In order to investigate this hypothesis we began by assuming that the importance of Poisson's ratio influence is variable and denoted as n. This enables us to investigate the potential for plane-stress conditions [$E_{plane-stress} = E/(1-v)$] [59] or a mixture of plane-strain and plane-stress conditions. Therefore, the first order longitudinal vibration frequency for a thin, slender, cantilever can be expressed as Equation (4-2)

$$ f = \frac{1}{4L}\sqrt{\frac{E}{\rho(1-v^n)}} \tag{4-2} $$

Similarly, the first order longitudinal vibration frequency for the fix-fix ended bridge or free-free ended beam can be expressed by Equation (4-3).

$$ f = \frac{1}{2L}\sqrt{\frac{E}{\rho(1-v^n)}} \tag{4-3} $$

$$ \upsilon = \sqrt{\frac{E}{\rho(1-v^n)}} \tag{4-4} $$

where ν is Poisson's ratio, and υ is often referred to as the acoustic wave propagation speed, which is an intrinsic material property. Both experimentation and simulation were conducted to assess the state of strain present in the cantilever and bridge structures.

4.2. Determination of the Correct Analytical Solution for Thin Slender Beams

In order to determine the value of n in Equation (4-3) it was important to first measure the acoustic wave propagation speed experimentally, which can then be plugged into Equation (4-4) to determine the relationship between Poisson's ratio and operation number n. The wave speed measurement was accomplished by measuring the resonant frequency of thin strips of several different lengths and then plotting frequency vs length, the signature of which can be fitted with regression to extract the wave speed. This will enable the exponent n to be expressed in terms of Poisson's ratio via Equation 4-4. In turn, numerical simulations employing modal analysis will be performed to determine resonant frequency as Poisson's ratio is systematically varied and consequently yield values of n that satisfy Equation 4-3. When the acoustic wave speed of the experiments and the simulations is equal, the true Poisson's ratio and the value of its exponent can be identified.

To investigate these issues several samples of magnetostrictive strips were prepared and tested in order to determine the wave propagation speed in the medium. Rectangular strips of commercially obtained Metglas 2826 MB 28 μm thick were cut with a dicing saw to the sizes and aspect ratios listed in Table 4-2. Followed cutting, all specimens were cleaned and prepared for testing. The strips were subjected to a modulated external magnetic field in order to drive them to resonance while their time-dependent response

was monitored with a pickup coil. A complete methodology for these procedures was described in section 2. Specimens were clamped at one end for a cantilever or at two ends for bridge, as illustrated in Fig. 4-1.

Table 4-2 Specimen's size and aspect ratio.

L/W \ L (mm)	2	4	6	8	10	v (m/s)
2	2x1	4x2	6x3	8x4	10x5	4427.8
4	2x0.5	4x1	6x1.5	8x2	10x2.5	4455.4
5	2x0.4	4x0.8	6x1.2	8x1.6	10x2.0	4498.4
8	2x0.25	4x0.5	6x0.75	8x0.5	10x1.25	4496.4
10	2x0.2	4x0.4	6x0.6	8x0.8	10x1.0	4445.8
Ave.						4464. 7

a   b
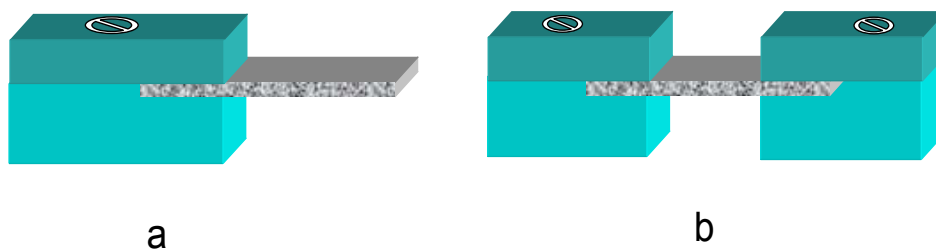
Fig. 4-1   Schematic diagram of setup for resonant frequency testing in (a) cantilever and (b) bridge.

Figs. 4-2 and 4-3 show the data obtained for length to width ratios of 4 and 10 and reveal that the data points fell on top of one another. This was true for all aspect ratios tested, which implies that width did not influence the resonant frequency, whereas it does in transverse modes. By applying a power regression fit to the data and using Equation (4-4), the wave propagation speed can be determined, (see Table 4-2). By this method, the average wave propagation speed for Metglas 2826 MB was found to be 4464.7 m/s. Using Equation 4-4, one can express Poisson's ratio as a function of the exponent n, the solid line in Fig. 4-4.

$$\text{Ratio} = 4 \quad y = 2227.7x^{-1.01}$$
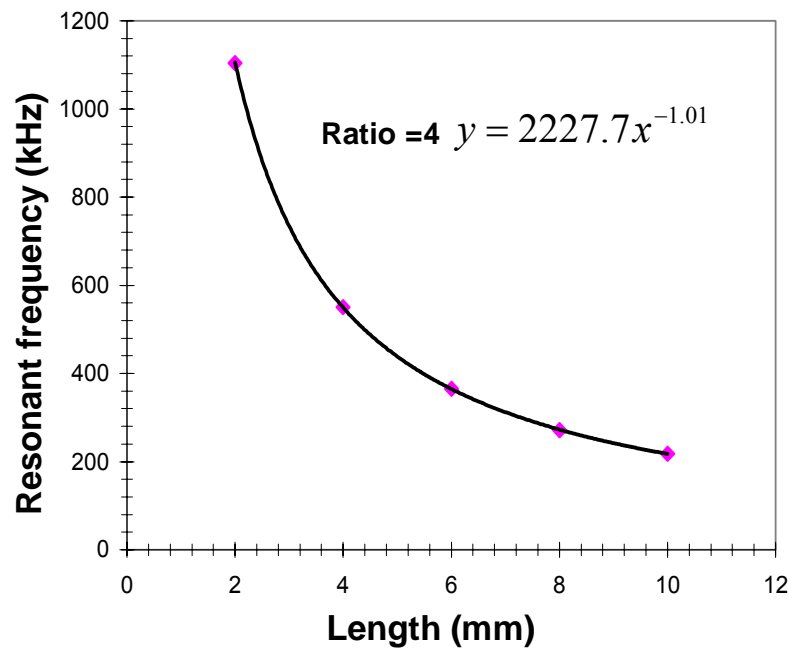
Fig. 4-2   Measured resonant frequency of sensor vs. sensor's length at aspect ratio = 4
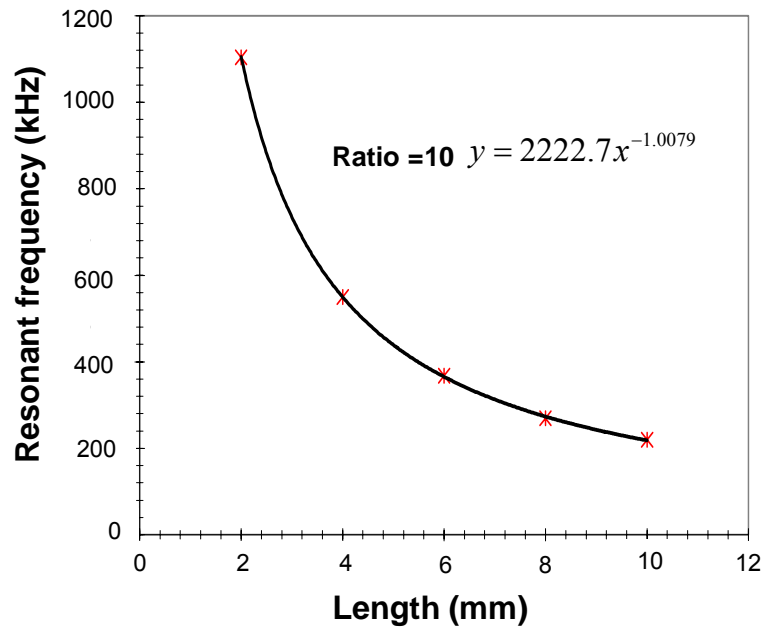
Fig. 4-3 Measured resonant frequency of sensor vs. sensor's length at aspect ratio = 10.
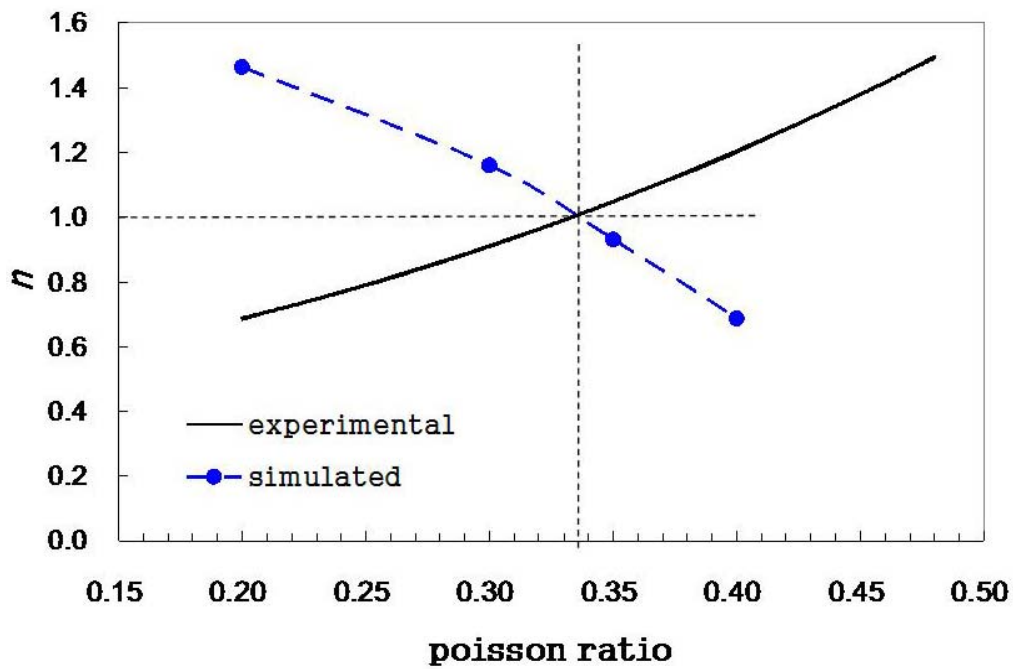
Fig. 4-4 Operator number (n) as a function of Poisson's ratio (ν) obtained by

experiments and simulations.

In order to pinpoint Poisson's ratio for Metglas 2826 MB and the corresponding state of strain, finite element simulations were carried out using commercially available software from CoventorWare [60]. Specifically, the simulations involved modal analysis on an undamped, free-free slender bar with oscillations in the longitudinal mode. A magnetostrictive sensor with 8 mm x 1.6 mm x 28 μm size was used for simulation. The selected mesh type was Manhattan brick, the element order was set to parabolic, and element size was 160 x 160 x 5.6 μm^3, see Fig. 4-5. The material properties employed in the simulations were identical to those in the experimental analysis above. Poisson's ratio was systematically varied and the corresponding influence on resonant frequency was recorded as listed in Table 4-3 . One can then plug this information into Equation 4-3 to obtain Poisson's ratio exponent n, (see Table 4-3). These results essentially identify how the acoustic wave velocity is influenced by Poisson's ratio. When comparing them with the experimental results, consensus should be reached when the acoustic wave velocities match. Fig. 4-4 shows the overlie of the experimental data and simulation results, dashed line with circles, that reveals the velocities match at a Poisson's ratio of 0.33. This agrees with values tested by the supplier and published in 1979 [58]. Moreover, this corresponds to Poisson's ratio exponent of one clarifying that plane-stress/biaxial-modulus conditions dominate behavior for the geometry and dimensions used. Thus, the natural frequency relationship for a freestanding strip, bridge or cantilever should be modified using the plane-stress or biaxial modulus per Equation (4-5) for a cantilever and (4-6) for a bridge or freestanding beam,

$$f = \frac{2n-1}{4L}\sqrt{\frac{E}{\rho(1-\nu)}}$$

(4-5)

$$f = \frac{n}{2L}\sqrt{\frac{E}{\rho(1-\nu)}}$$

(4-6)

where n = 1, 2, 3.... Using Equations 4-5 and 4-6 as well as 2-11 and 4-1 and Poisson's ratio of 0.33, the resonant frequency for the different structures can be compared to measured values, see Table 4-4. In the case of a freestanding strip, the uniaxial and plane strain values are far below the experimental value, but the plane-stress value is just above. As mentioned before, the calculated value should be slightly larger due to some dampening effects in the experiments. The same follows for cantilever and bridge structures. This is a clear indication that for the longitudinal resonance of thin slender beam geometries, plane-stress dominates and the Poisson's ratio for Metglas is indeed 0.33.
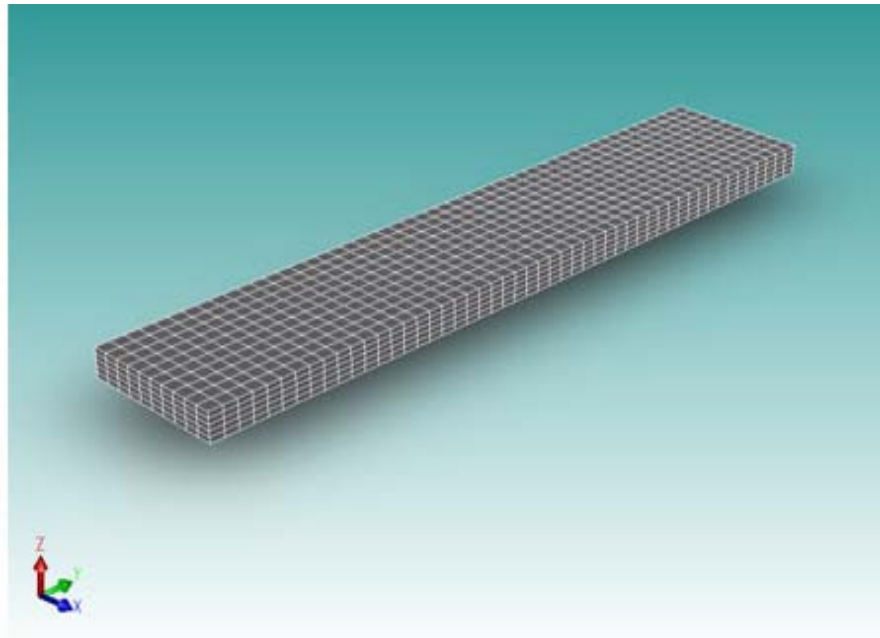
Fig. 4-5   Result of an 8 mm x 1.6 mm x 28 μm sensor meshed with 160 μm x 160 μm x 5.6 μm element size.

Table 4-3 Simulated results of resonant frequencies for different Poisson's ratio inputs, where n was calculated based on Equation (4-3).

ν	0.2	0.3	0.35	0.4
f (Hz)	240181.7	264367.8	288662.4	333547.5
n	1.43	1.13	0.93	0.69

Table 4-4 Comparison of the measured and calculated resonant frequencies (kHz) for three structures.

L(mm)	Structure	(kHz)			
		Uniaxial E	Plane Strain $E/(1-\nu^2)$	Plane Stress $E/(1-\nu)$	Experiment
8	Freestanding	227.9	242.7	278.4	274.7
9	Cantilever	101.3	107.3	125.7	123.7
14.4	Bridge	126.6	134.1	154.7	153.9

4.3. Experimental Test and Numerical Analysis to Verify the Longitudinal Mode Proof-of-Principle

4.3.1. Experimental verification of the Proof-of-Principle Equations

In order to verify that the mode equations given above are appropriate, additional experimental and numerical analysis will be performed using the first and second resonate state of the cantilever and bridge structures. The corrected resonant frequency relationships were stated in Equations (4-5) and (4-6). A series of experimental tests were carried out in the fashion of cantilever, bridge and cantilever array. The first two resonant states of a 14.4 mm long cantilever were recorded and are shown in Fig. 4-6. The second state was approximately three times that of the first state, and on examining Equation 4-5 the 2n-1 portion becomes 2 x 2 - 1 = 3, which confirms that the frequency magnitude of the second mode is 3 times that of the first mode. Fig. 4-7 is the resonant frequency record for a fixed-fixed ended bridge 14.4 mm long. The second mode is approximately 2 times the first mode which is verified with Equation 4-6 where n = 2. Thus, the analytical solutions in Equations 4-5 and 4-6 are correct.
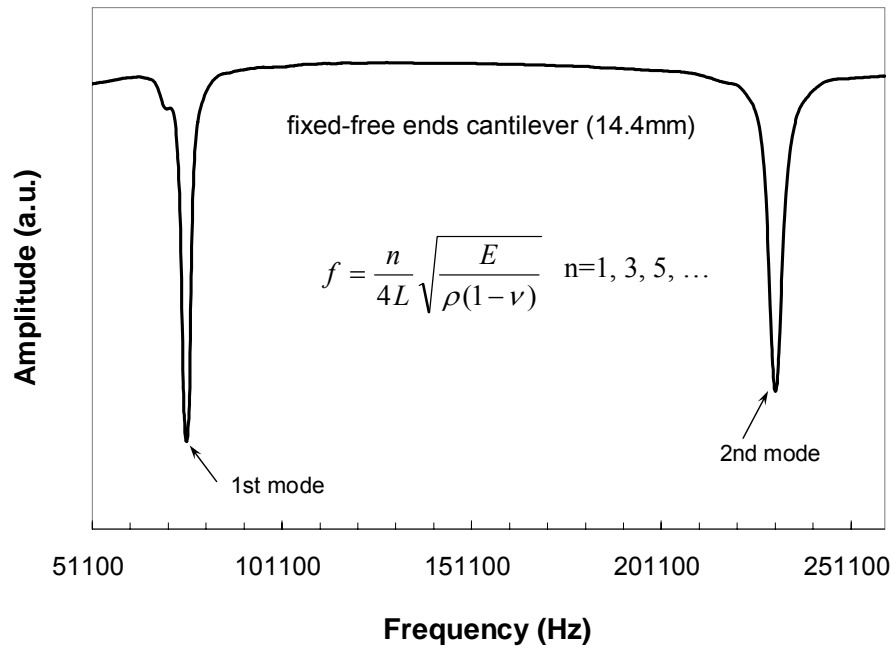
Fig. 4-6 Resonant frequency of the first two modes for a 14.4 mm cantilever.
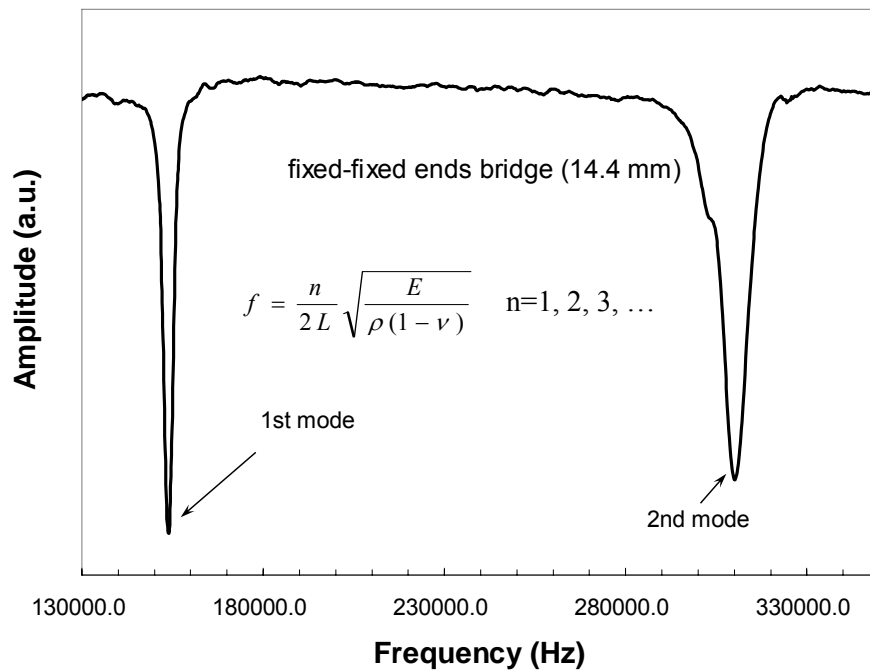
Fig. 4-7 Resonant frequency of the first two modes for a 14.4 mm bridge.

To further verify the analytical solutions, cantilevers of two different lengths, 14.4 mm and 9.0 mm, were constructed and tested simultaneously. Their resonant frequency spectrums were recorded and are shown in Fig. 4-8. Both sensors show that their resonant frequency in the second mode was 3 times that of their first mode. In addition, it demonstrates the possibility of making a sensor array for an application that could detect two different targets. All of these experiments confirmed that the concept-of-principle is valid, although the resonant frequency peaks are not perfect, which could be attributed to clamping effects. The signals are strong enough and their magnitudes are very near the value from the equations proposed above. It can then be concluded that magnetostrictive sensors made of Metglas 2826 MB follow the longitudinal vibration operation principle. These experimental results show that Equations (4-5) & (4-6) are valid.
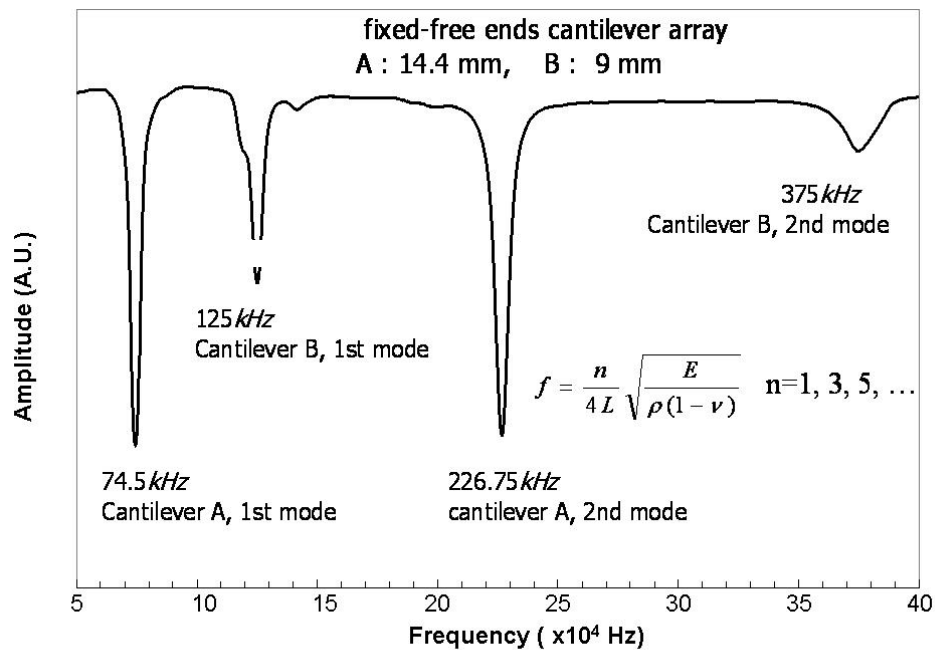
Fig. 4-8 Resonant frequency of the first two modes for cantilever array.

4.3.2. Numerical verification of the Proof-of-Principle Equations

Numerical analysis was also applied to the proof-of-principle to provide a final verification. A series of experiments by simulation were conducted to confirm the validity of Equations (4-5) and (4-6) for cantilever, bridge and beam. Table 4-5 lists the results of a cantilever of 80 μm x 20 μm x 1.0 μm. One can see the relationship of resonant frequency between the higher order mode and the first order mode is 1, 3, 5, 7 and so on. Fig. 4-9 shows the sensors' shapes under a different order of modes. Tables 4-6 and 4-7 summarize the simulation results of a bridge made of Metglas with 14.4 mm x 3.0 mm x 28 μm and a beam made of Au with 8 mm x 2 mm x 28 μm, respectively. The same relationship of the resonant frequency between the higher order mode and the first order mode is 1, 2, 3, and so on regardless of the materials and configurations in bridge or beam. These simulation results confirmed the validity of the general equations of the longitudinal vibrating cantilever, bridge and beam proposed before.

Table 4-5 Resonant frequency obtained by simulation for a cantilever (80 μm x 20 μm x 1.0 μm) made of Metglas.

Mode domain	Frequency	Generalized Mass	Damping	Order of mode
1	14433122.0	1.77E-12	0	1st
2	43299372.0	1.77E-12	0	2nd
3	51870192.0	4.43E-13	0	
4	58838872.0	7.76E-13	0	
5	66210624.0	1.04E-12	0	
6	72165688.0	1.77E-12	0	3rd
7	75480456.0	1.30E-12	0	
8	85564432.0	1.30E-12	0	
9	95646120.0	8.18E-13	0	
10	101032256.0	1.77E-12	0	4th
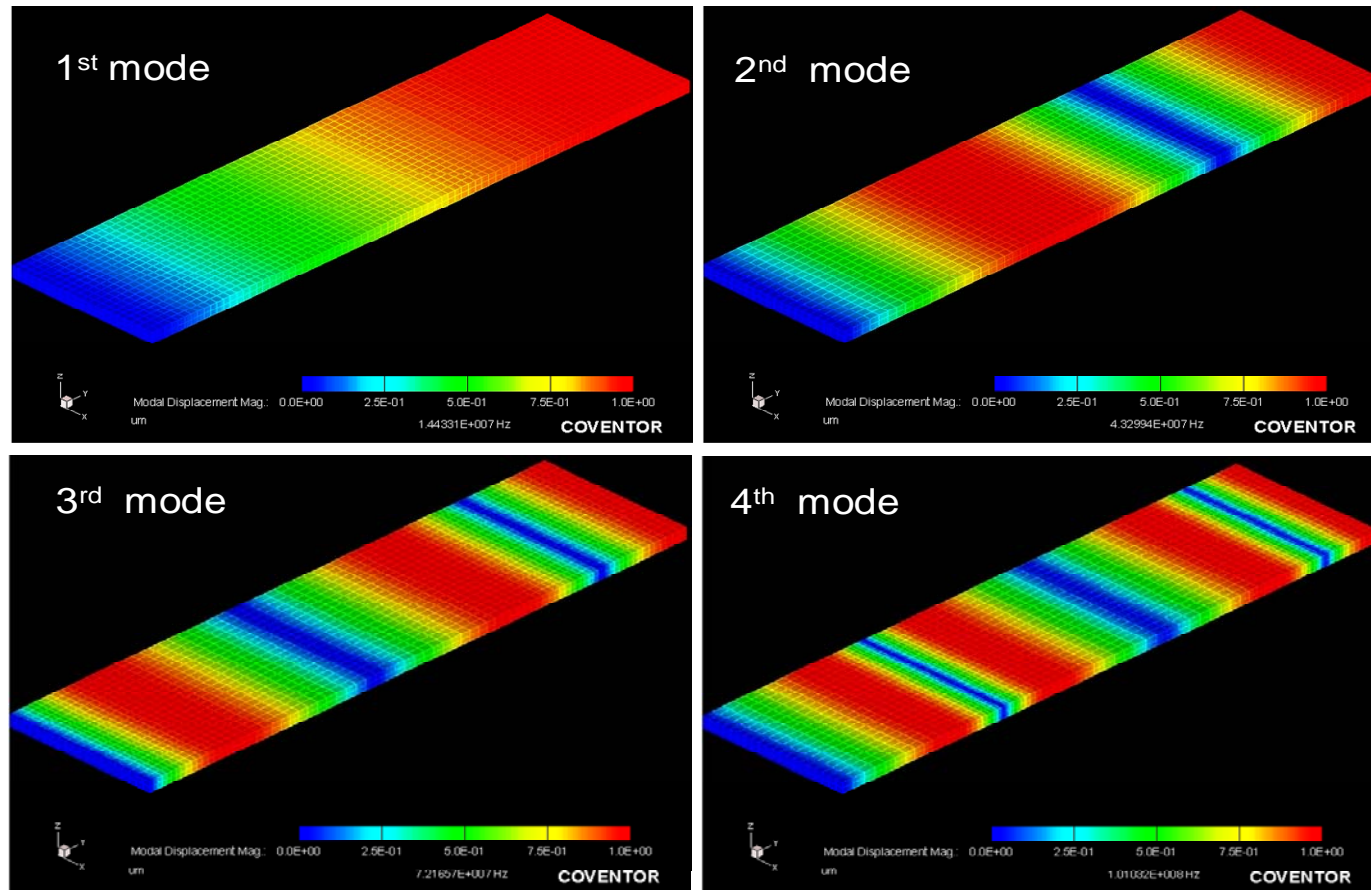
Fig. 4-9 Typical mode shapes at different orders of mode for a cantilever in longitudinal vibration.

Table 4-6　　Resonant frequency obtained by simulation for a bridge (14.4 mm x 3.0 mm x 28 µm) made of Metglas.

Mode domain	Frequency (Hz)	Generalized Mass	Damping	Order of Mode
1	160368.0	2.55E-06	0	1st
2	320736.1	2.55E-06	0	2nd
3	481104.1	2.55E-06	0	3rd
4	641472.1	2.55E-06	0	4th
5	698189.8	1.21E-06	0	NA
6	712483.9	1.27E-06	0	NA

Table 4-7 Resonant frequency obtained by simulation for a beam (8 mm x 1.6 mm x 28 µm) made of Au.

Mode Domain	Frequency (Hz)	Generalized Mass	Damping	Order of mode
1	68035.9	2.47E-07	0	1st
2	204107.6	2.47E-07	0	2nd
3	305598.7	4.98E-08	0	
4	338259.4	1.05E-07	0	
5	340179.4	2.47E-07	0	3rd
6	366239.5	1.32E-07	0	
7	404214.9	1.58E-07	0	
8	448299.4	1.85E-07	0	
9	476251.2	2.47E-07	0	4th
10	495718.7	1.91E-07	0	

4.4. Discrepancy Analysis of the Resonant Frequency Obtained by Experimental Measurement, Finite Element Simulation, and Numerical Calculation

Sensors with various materials, sizes and configurations as listed in Table 4-8 were used for either simulation or experimentation. Their first order resonant frequency obtained by three methods, namely experimentation, simulation and modification of Equations (4-5) and (4-6), and the resonant frequency differences between the proposed equation and experimental data or simulation data are presented in Table 4-9. The subscripts of c, e and s respectively represent calculation, experiment and simulation. $\Delta f_{cs}/f_c$ and $\Delta f_{ce}/f_c$ are the relative frequency differences obtained by simulation and experiment with respect to the data by calculation. The relative differences of resonant frequency between these three techniques are less than 3.3%. Such comprehensive analysis further confirms that the proposed equations and techniques are valid. Fig. 4-10 presents the simulation result of the first mode for a free-free ended beam with a size of 8 mm x 1.6 mm x 28 μm. Color in red indicates that the largest displacement occurred in the longitudinal axis, e.g. the free ends of beam.

Table 4-8 Sensor size, materials, and type used for simulation and experiment.

No.	Material	Size	Structure	Simulation	Experiment
1	Metgals	9 mm x 2 mm x 28 μm	Cantilever	No	Yes
2	Metgals	9.8 mm x 2 mm x 28 μm	Beam	No	Yes
3	Metgals	14.4 mm x 3 mm x 28 μm	Cantilever	Yes	Yes
4	Metgals	14.4 mm x 3 mm x 28 μm	Bridge	Yes	Yes
5	Gold	8 mm x1.6 mm x 28 μm	Cantilever	Yes	No
6	Metgals	250 μm x 50 μm x 1 μm	Cantilever	yes	No

Table 4-9 Analysis of the differences of resonant frequency obtained by calculation, simulation, and experimentation.

No.	L(mm)	Structure	f_c (Hz)	f_s (Hz)	f_e (Hz)	$\Delta f_{cs}/f_c$ (%)	$\Delta f_{ce}/f_c$ (%)
1	9.0	Cantilever	125919.3	------	125687.5	------	0.18
2	9.8	Beam	230710.8	------	227500.3	------	1.39
3	14.4	Bridge	157011.6	160368	153925	-2.14	1.97
4	14.4	Cantilever	78505.8	80184	75987.5	-2.14	3.21
5	8.0	cantilever	67130.3	68035.9	------	-1.35	-----
6	0.25	Cantilever	4521933.1	4618599	------	-2.14	------

Notice: Poisson's ratio 0.36 of Au employed for simulation. f_c, f_s, and f_e are the frequencies of numerical calculation, finite elemental simulation and experimentation, respectively $\Delta f_{cs} = f_c - f_s$, and $\Delta f_{ce} = f_c - f_e$.
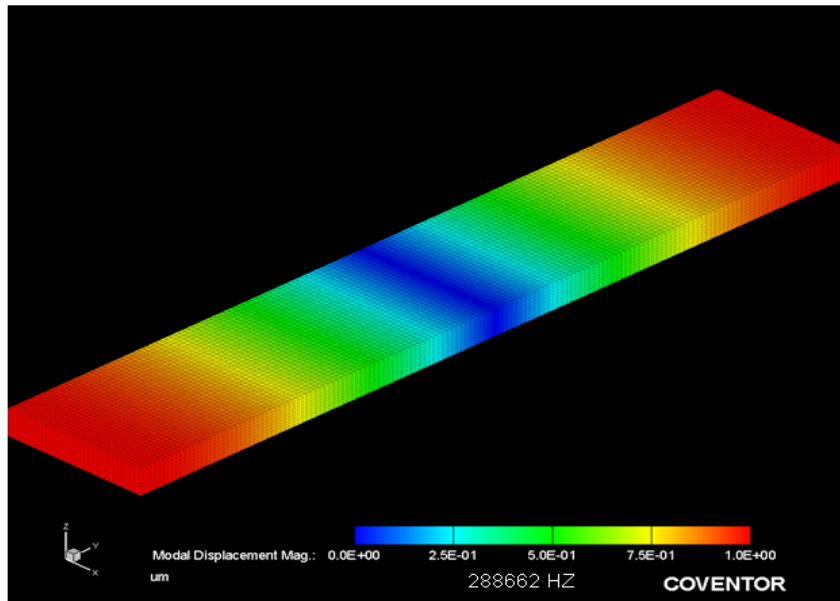
Fig. 4-10 Simulation results for freestanding Metglas beam with the size of 8 mm x 1.6

mm x 28 μm. Poisson's ratio of 0.35 was employed.

4.5. Summary

Simulation results have verified that experimental data obtained for magnetostrictive sensors constructed in cantilevers and bridges was indeed resonating in the longitudinal mode. In conjunction with simulation and experimental data, theoretical equations for predicting the resonant frequency of cantilever, bridge and beam were modified by replacing a plane-strain modulus with a plane-stress modulus (biaxial modulus). The proof-of-principal equations were validated. Poisson's ratio of Metglas 2826 MB was defined to be about 0.33, which is confirmed by the result of earlier study on Metglas and the supplier's claimed data.

5. BULK-SCALE MAGNETOSTRICTIVE SENSORS

The potential applications of a magnetostrictive sensor vibrated in the longitudinal mode to measure a thin film elastic modulus and detect mass deposited on the sensor's surface have been discussed in the earlier sections. In this section, the details of these applications will be discussed. Bulk scale, freestanding sensors 8 mm x1.6 mm were employed to determine the thin film elastic modulus, and 5 mm x 1 mm ones were used to detect the concentrated mass attached to the sensor's surface at different locations. Finite element simulations were employed to confirm the results from the thin film measurements and mass concentration experiments. In order to confirm the application of employing magnetostrictive sensors to measure a thin film Young's modulus, simulation experiments for freestanding beams with thin films of either Cu or Au were carried out to verify the experimental results and validate the technique. FEM was also performed to investigate the potential for Metglas sensors to detect the attachment of a single spore or cell on the surface and the response for multiple spores or cells attachments.

5.1. Thin Film Elastic Modulus Measurement

Thin film materials such as Al, Au, Cu, etc. have been widely employed in microelectronic and microelectromechanical systems (MEMS) as interconnecting and packaging materials. As these applications continue to develop, demands on material

75

performance are ever increasing, and there are many material issues associated with the miniaturization of electronic devices and the operation of MEMS and sensors that must be addressed [61, 62]. To better mitigate thin film material failure and improve device functionality and reliability, it is essential to first understand the intrinsic mechanical properties of the films involved. In addition, thin film mechanical properties are key inputs for numerical simulations designed to predict device life-cycle and reliability. In many cases, the mechanical properties of thin films may differ from their bulk counterparts due to differences in volume and size of the operating deformation mechanisms [63, 64].

To date, a variety of techniques has been employed to measure thin film Young's modulus, including both destructive and non-destructive methods. Destructive methods typically involve microfabrication processes to fashion the film material in freestanding structure, so that a microscale force can be applied to assess the properties. Examples of destructive techniques include the bulge test [65-67], microbend test [68, 69], microbeam tensile test [70], microbeam/microbridge bending, microbeam deflection test [71-76] and dynamic resonating [77-84]. In such testing methods, the thin films are deposited on a substrate (most cases are Si wafers) followed by a micromachining process to fabricate a freestanding diaphragm, cantilever beam, or fix-fix ended bridge, which is where the destructive technique name comes from. After the technique is applied, the continuous thin film or substrate is broken. Fig. 5-1 to Fig. 5-4 show the typical testing methods described here.
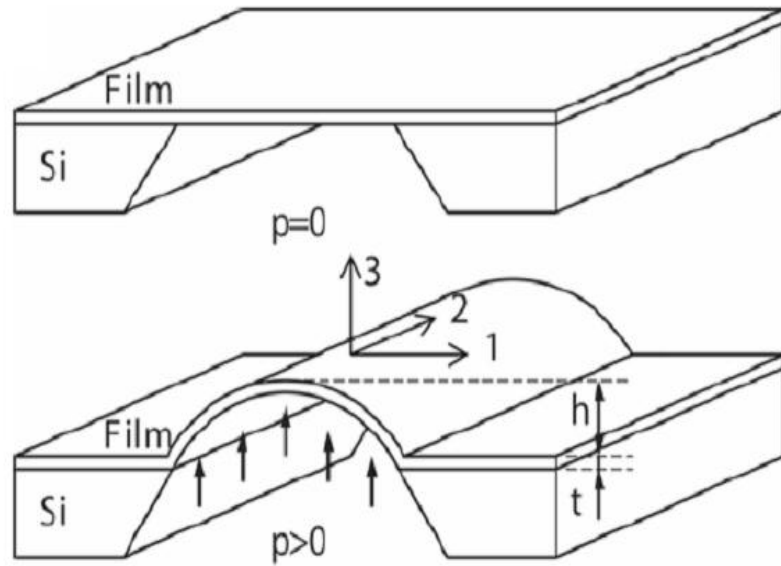
Fig. 5-1   Schematic diagram illustrating bulge test method [67].
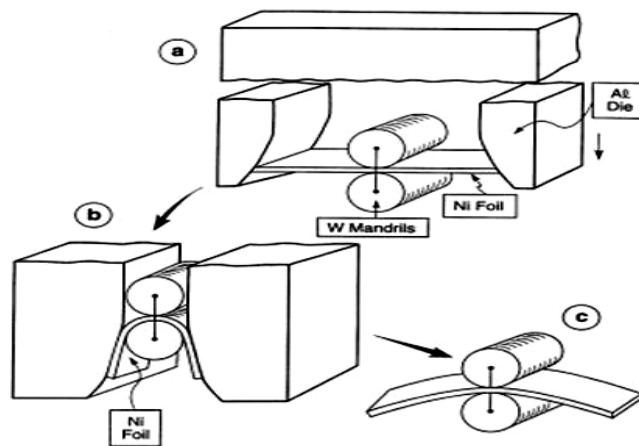
Fig. 5-2   Schematic of the microbend test [68].
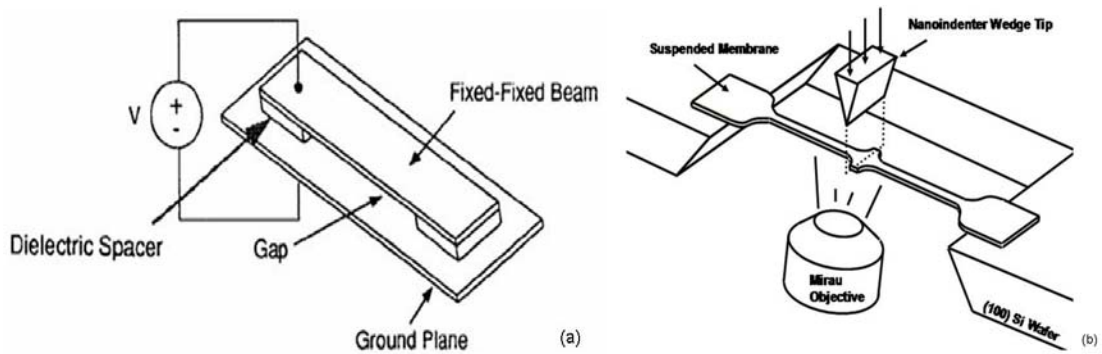
Fig. 5-3 Schematic of microbeam deflection test method in (a) deflection by electrostatic force [71], and (b) deflection by nanoindentation [72].
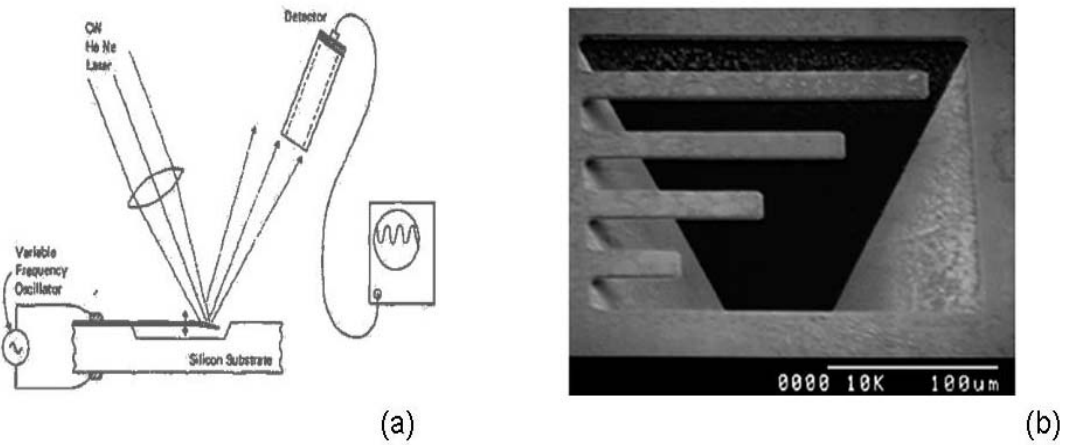
Fig. 5-4 Schematic depicting the method by dynamic vibrating cantilever in resonant frequency. (a) A laser detector is generally used to detect the frequency [77], and (b) a microfabricated SiO_2 cantilever array is used for the resonant frequency test [82].

In the bulge test [67] (Fig. 5-1), a pressurized gas is commonly used to deflect the thin film membrane, but an electrostatic force can be employed to load the film with an electric field between the film and ground plane. The microbend test [68] (Fig. 5-2) is based on the conventional three point bending measurement technique. The preferred samples are thin foils. When film thickness drops below 5 μm the test becomes difficult to perform. The microtensile test is realized by using a micro motor to stress the sample [70]. Such a test can be difficult to perform, but direct tension is the most desired technique. Furthermore, freestanding films tend to have residual stress and are often wrinkled causing error in the measurement. A considerable amount of effort has been focused on microbeam bending [71] or deflection [72] (Fig. 5-3) due to the ease of the test. In these techniques, exercising electrostatic force (Fig. 5-3 (a)) or nano-indentation to deflect/bend the cantilever or bridge are the most desirable choices. The dynamic resonating method (Fig. 5-4) involves the oscillation of a cantilever or bridge structure with its natural frequency. By detecting the frequency, a Young's modulus of film material is determined. In recent years, much more interest has been shown in this method [80, 82, 85]. Nevertheless, the resonant frequency detection technique is extremely complicated, normally involving many costly instruments and additional expenses in the microfabrication processes.

In contrast, non-destructive methods involve direct measurements that do not alter the films properties in any manner. These methods are dominated by acoustic wave based interrogation of Young's modulus [78, 86-91] and elastic constants [92-96]. Nano-indentation [59, 73, 97-109] that has been generally accepted for quick testing, is a technique in between these two testing methods.

In this acoustic wave based non-destructive technique for measuring thin film elastic properties, the film is examined in its deposited condition; no additional modification process, which has the potential to alter the film's physical properties, is required. Unfortunately, the apparatuses involved in such methods described in the references are often bulky and expensive. The nanoindentation technique also assesses the film properties directly without amending its condition in the macro scale, though it does result in local damage to the film as depicted in Fig. 5-5 [101].

The advantages of destructive techniques are that they typically provide more information on the material properties such as yield stress, fracture toughness, etc. However, they require relatively long and complex fabrication processes and expensive instrumentation to achieve their measurements. Moreover, thin film material properties may be influenced by the fabrication procedures employed to fashion the test structures, which has been observed during testing silver thin film mechanical properties [1].
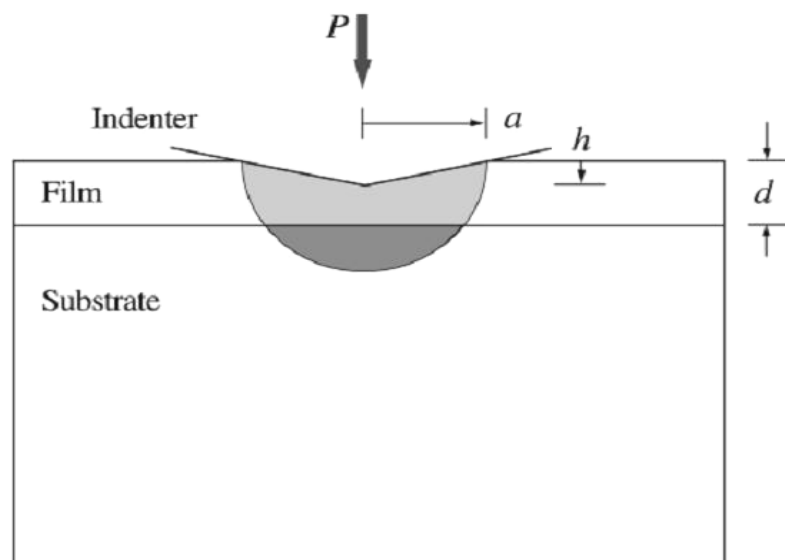
Fig. 5-5   Schematic depicting the nanoindentation test method [101].

On the other hand, non-destructive techniques are typically only adept at assessing elastic properties and require sophisticated instrumentation and data reduction procedures. Nanoindentation is able to provide both elastic and hardness properties that can be quickly extracted from the indentation data; however, the data may be influenced by the substrate's properties, the indentation depth and the film thickness. In the case of porous materials, this test may cause densification to occur, and the in other case, phase transformation can be induced due to large hydrostatic pressure. Although numerous reviews have been published discussing the influence of the techniques and the materials' size on their mechanical properties [59, 63, 100], there is no standard technique generally accepted by the thin film mechanics community that is simple, inexpensive and non-destructive in assessing mechanical properties. A little known technique that employs a magnetostrictive resonator, developed by Grimes and coworkers [31, 32], has been shown to be adept at assessing thin film elastic properties and may be the standard technique the community seeks, in terms of evaluating elastic properties. The technique is simple and inexpensive to perform, requires no post deposition fabrication, and is non-destructive in nature. This section is aimed at assessing the technique by measuring the elastic properties of several commonly employed thin film materials and offering a discussion of the error involved.

5.1.1. Experimental Details

Thin films of Au, Cu, Al, Cr, In, and Sn were DC sputter deposited onto a sensor cut from Metglas ribbon (smooth side) by a Discovery 18 sputter system from DENTON VACUUM, Inc. All targets were purchased from Kurt J. Lesker, Inc. with purity of 99.99% or better. The SiC thin film was obtained by directly sputtering from a SiC target with Ar plasma. More details can be found in Liang et al. [110]. The background vacuum was achieved at $3x10^{-6}$ torr or better for each deposition. Sputter power density of 4.5 w/cm^2 was used for the metallic films deposition, and an Ar flow rate of 25 sccm with the process pressure of 5 mT were employed for all sputtered films. A thin layer of 12 nm Ti was applied by RF sputter as an adhesion promoter prior to Cu or Au film deposition without breaking the vacuum. An Au rich lead-free solder AuSn (80/20 wt. %) thin film was obtained by co-sputtering of Sn and Au targets, simultaneously. A deliberated experiment was preformed to obtain the correct composition of AuSn (80/20) eutectic solder, which was examined by EDX. All targets were sputter cleaned for 15 minutes with shutter covered before deposition. Thin film thickness was controlled by sputtering time and measured by a TENCOR alpha-step 200 profilometer from TENCOR Instruments, Inc. A Rigaku X-Ray Vertical Diffractometer with Cu Kα radiation was employed to characterize the crystal structure of these thin films, and the surface morphology of the film was characterized by using a JEOL JSM 7000F field-emission SEM equipped with EDX capability.

Metglas 2826 MB ribbon was obtained from Metglas, Inc. and cut to sizes of 8 mmx1.6mm by a semiconductor ranked dicing saw and cleaned with acetone, methanol, IPA(Isopropyl Alcohol), DI (deionized) water and dried by nitrogen gas. The sensors

were dehydrated in a convection oven at 120°C for 20 minutes prior to use. In the case of measuring the Au film Young's modulus, the masses of the sensor before and after deposition were measured immediately by a Metter-Toledo AT-20 microbalance with a resolution of 2 μg. The method used of measuring the resonant frequency of the sensor with or without the thin film coating was described in section 2.

5.1.2.   Results and Discussion

This section details the characterization and results of deposited thin film. Parameters such as surface morphology, crystal structure, and sensor responses to various types of films, the determined thin films Young's moduli and error analysis are included.

5.1.2.1.   Surface Morphology of Deposited Thin Film Materials of Au, Cu, Al, Cr, In, Sn, AuSn (80/20), and SiC

All films deposited on the magnetostrictive sensor platform exhibited continuous surface coverage and excellent adhesion as no delimitation or pits were observed during SEM characterization. This is a good indication that the numerical solution can assume that film and sensor undergo the same amount of straining during vibration testing. Deposited Au and Cu films possessed very fine grain sizes/particles as shown in Fig. 5-6 (a) and (c). The grain size of the Cr exhibited sawfish likeness or star shapes with even morphology as shown in Fig. 5-6 (d), which have been commonly observed by other researchers [111]. The low-melting-temperature materials, the In, Sn, and Al films, exhibited considerable large grain sizes/particles and appeared somewhat porous, (Fig. 5-6 (b), (e) and (f)). Furthermore, indium and tin films possessed a random island texture

and relatively rough surface. The Sn film also had whiskers on its surface approximately 1.0 μm long as seen in the Fig. 5-7(h). These whiskers are often observed in electronic packaging and assembly but are also found by other researchers in sputter deposition processes [112] and are likely due to relief of compress stress in the film. Finally, the AuSn (80/20) eutectic solder yielded the most unusual of the microstructure, (see Fig. 5-6 g). No large islands were seen as in the pure Sn film, likely due to alloying with Au atoms. As was seen in the SEM image, the surface became flusher and developed into interlaced structures.

As deposited gold films of various thicknesses were examined under SEM. Uniform particle sizes of the Au coating were clearly developed on the sensor platform whose size scaled with the film thickness, (see Fig. 5-7). Complete surface coverage was observed even at film thickness as thin as 100 nm. The particle size increase with film thickness was likely a result from increased thermal energy induced and the large number of Au atoms available for aggregation for thicker film [113]. Also, note that the deposition of thicker Au film requires the longer processing time; consequently, a higher temperature on substrates may result from additional commission of ions and atoms. However, when the film thickness became thicker than 0.855 μm, the grain size remained relatively constant. The highest substrate temperature recorded during the sputtering process for different thin film thicknesses is listed in Table 5-1. Similar occurrences were observed for other materials during sputter deposition, but all exhibited lower temperatures than that for Au, likely a result from the sputter yield of Au being the highest among all films grown.
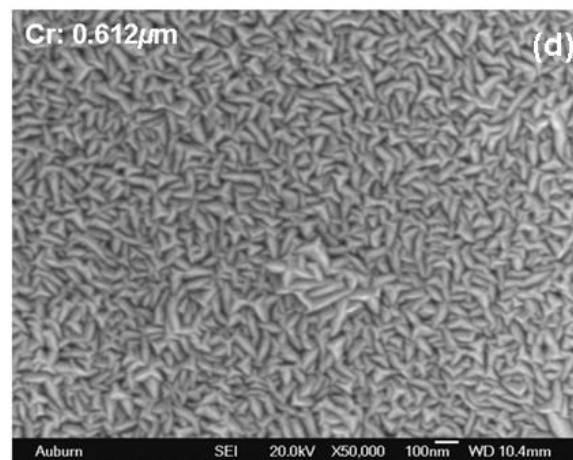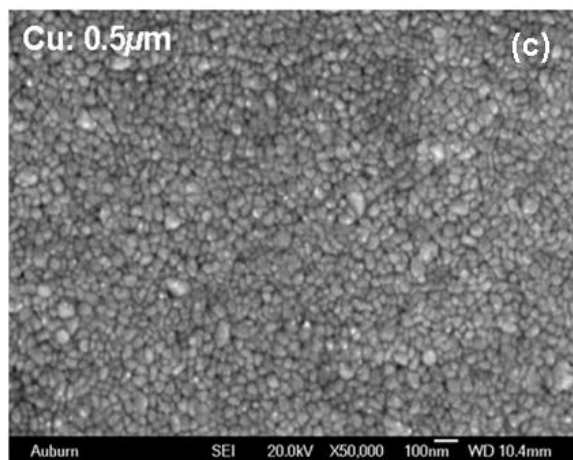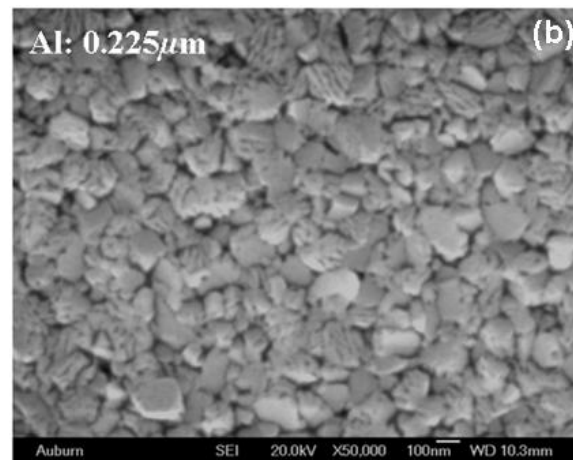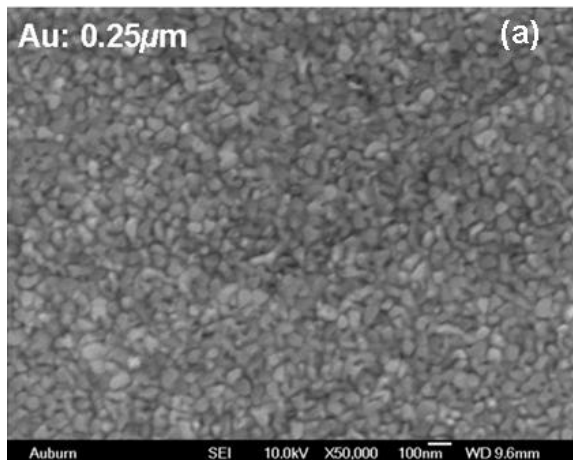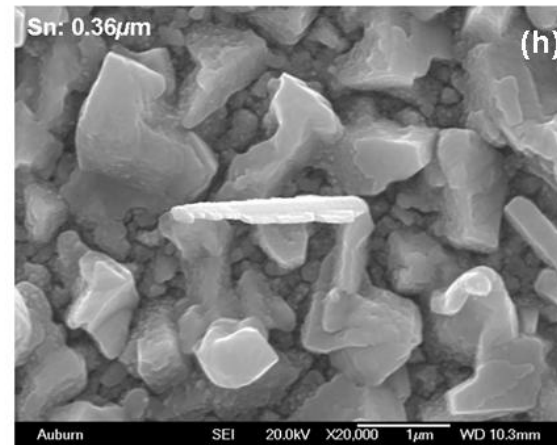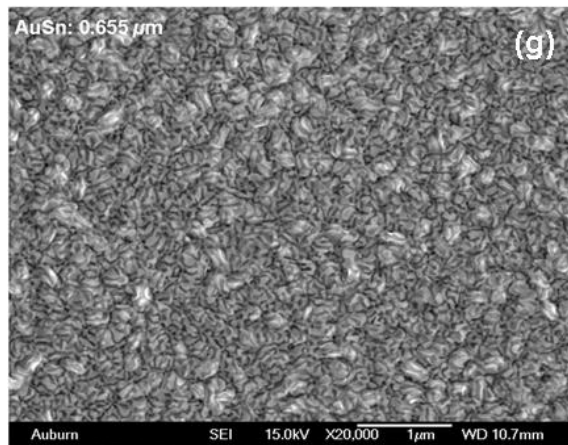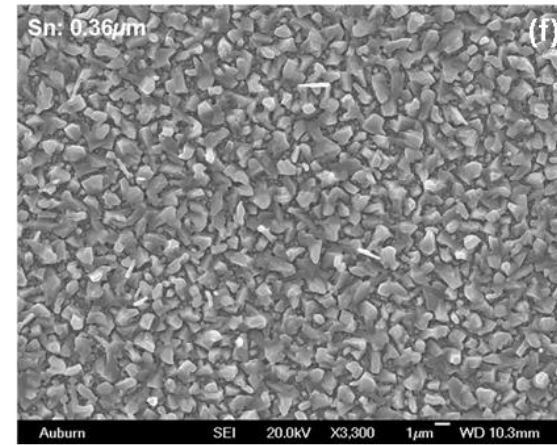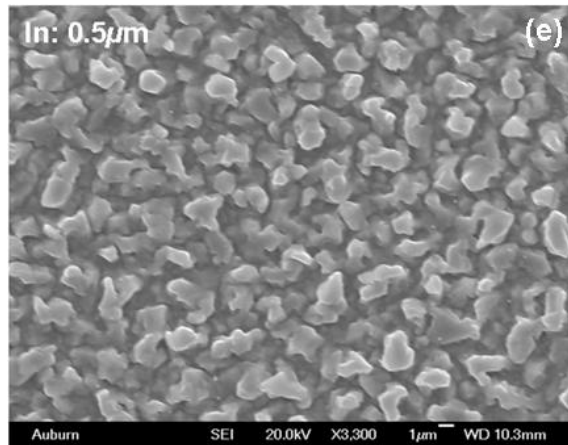
Fig. 5-6   SEM images of film surface morphology. The material of film and its thickness is indicated on each image.

Au: 0.10μm
Auburn   SEI   10.0kV   X50,000   100nm   WD 9.8mm

Au: 0.25μm
Auburn   SEI   10.0kV   X50,000   100nm   WD 9.6mm

Au: 0. 50μm
Auburn   SEI   10.0kV   X50,000   100nm   WD 9.5mm

Au: 0. 855μm
Auburn   SEI   10.0kV   X50,000   100nm   WD 9.8mm
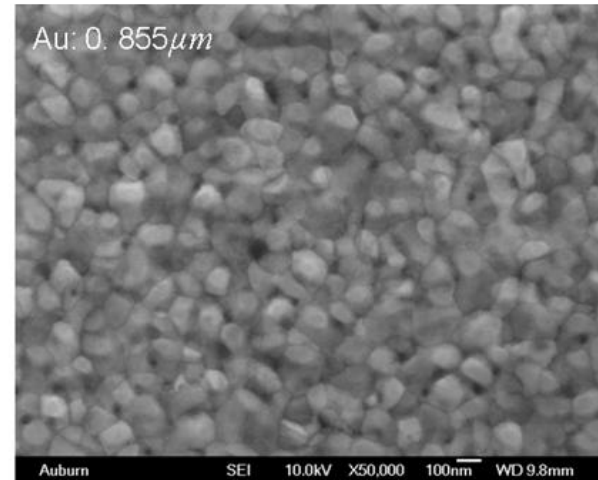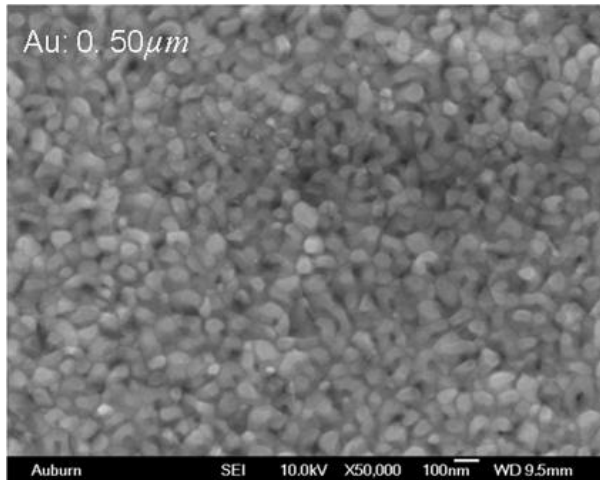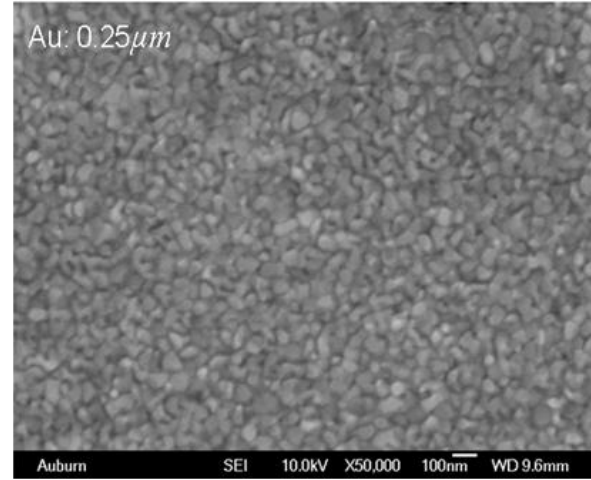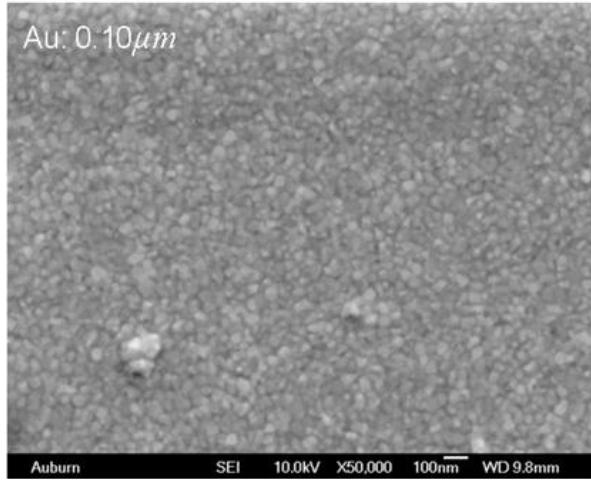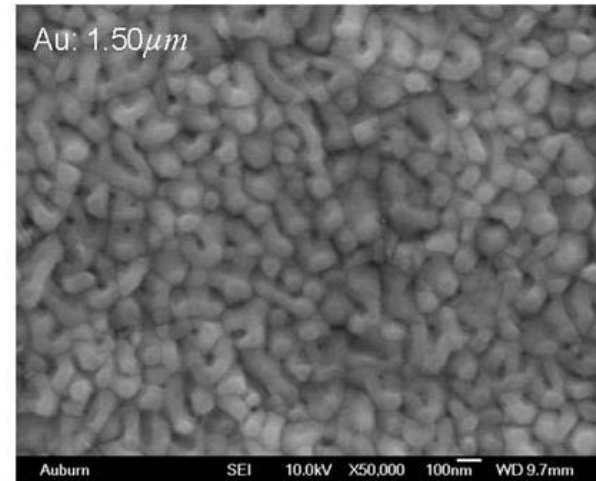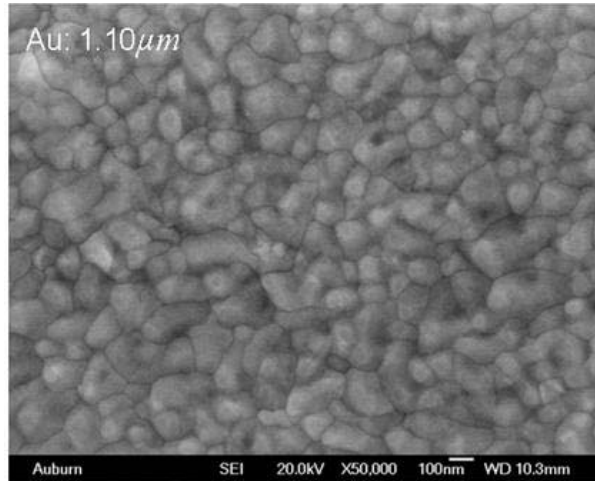
Fig. 5-7   SEM images of Au film with different thickness of 0.1 μm, 0.25 μm, 0.50 μm, 0.855 μm, 1.10 μm, 1.50 μm.

Table 5-1 Highest temperature of near substrate surface reached during deposition

Film thickness (μm)	0.25	0.50	0.855	0.89	1.00	1.10	1.50
Temperature (°C)	33	43	51	55	57	58	65

5.1.2.2.   Crystal Structure of Sputtering Deposited Thin Film

The crystal structure of the films was characterized by X-ray diffraction (XRD) technique, and typical patterns are shown in Fig. 5-8 and 5-9. All metallic films deposited by sputter deposition exhibited polycrystalline structure, except Au which had significantly (111) preferred orientation, shown in Fig. 5-9. The amorphous structure of SiC was also determined by XRD, but it is not shown here. The XRD result of the Metglas 2826 MB sensor substrate has confirmed its amorphous structure.

The eutectic AuSn (80/20) solder film exhibits a mixture of AuSn, Au_5Sn, and Sn phases; the existence of AuSn and Au_5Sn phases was expected from the Au-Sn phase diagram in Fig. 5-10 [114]. The single phase of Sn in this mixture was detected by XRD. The Sn may have been in an unstable phase owing to the eutectic AuSn mixture that was not reflowed. The composition of AuSn solder was analyzed by EDX, and the result was directly reflected back to modify the deposition process so that eutectic composition could be obtained. The best composition of Au rich AuSn eutectic solder achieved was 79.81/20.17 wt% as seen in Fig. 5-11 under the sputter circumstances of 44 w RF power for Au and 120 w DC for Sn with 5 millitorr sputtering pressure.
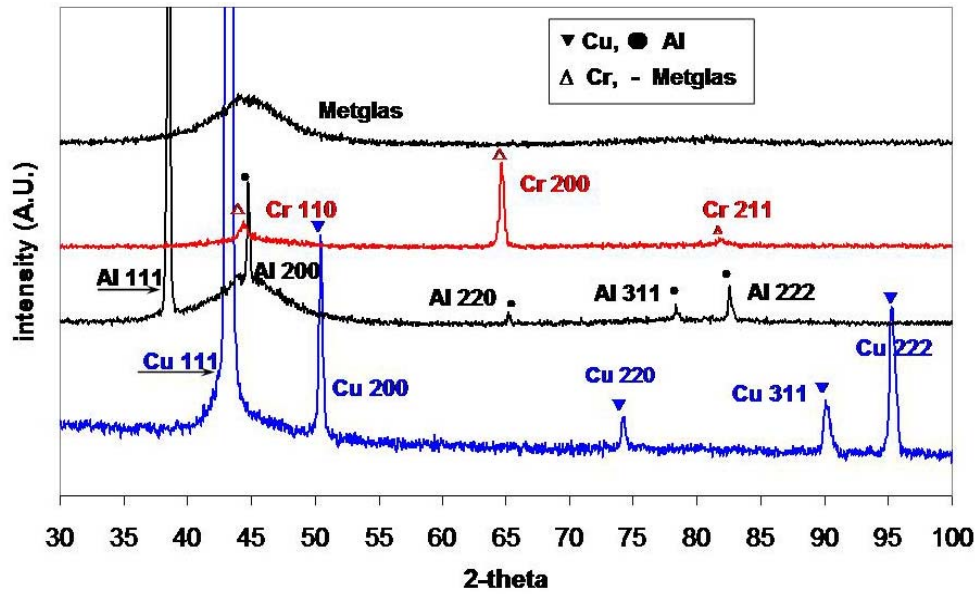
Fig. 5-8 XRD patterns for thin films deposition on Metglas sensors.
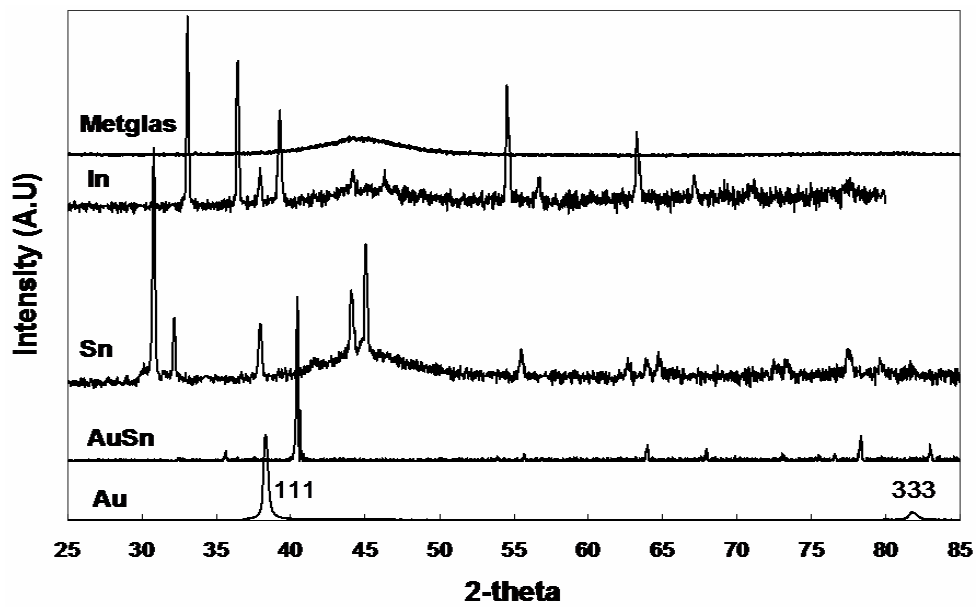
Fig. 5-9 XRD pattern for Au and solder thin film materials.
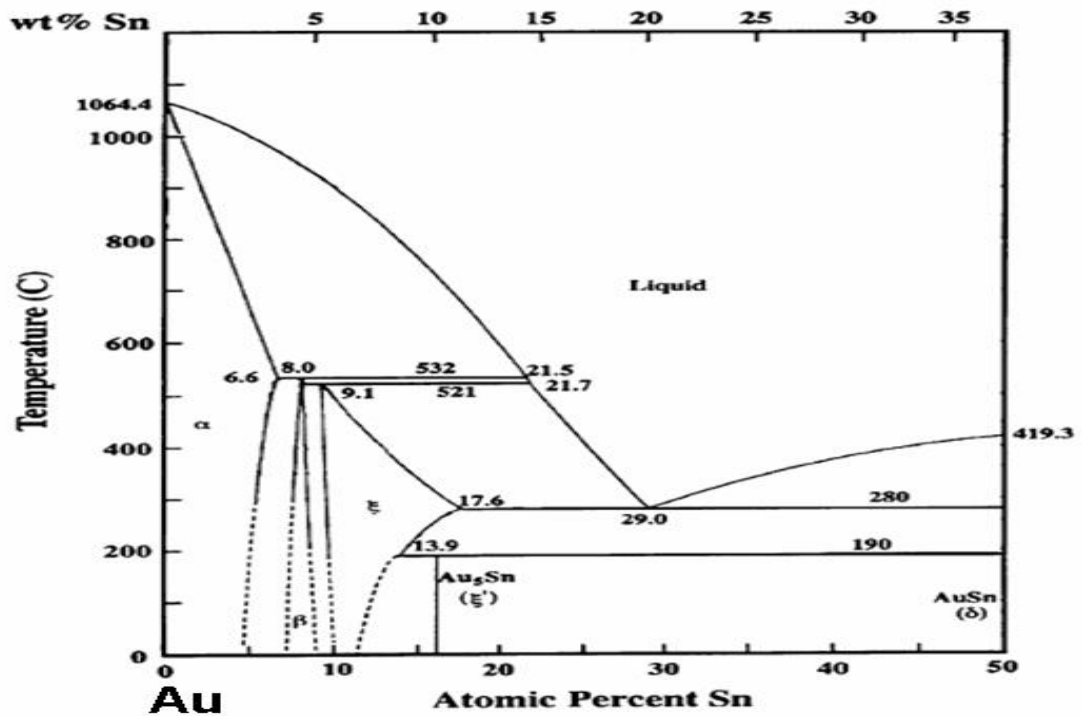
Fig. 5-10 Au rich portion of Au-Sn equilibrium phase diagram [114].

Element	keV	KRatio	Wt%	At%	At Prop	ChiSquared
Sn	3.443	0.1497	20.19	29.59	0.0	23.72
Au	2.121	0.7601	79.81	70.41	0.0	23.72
Total		0.998	100.00	100.00	0.0	16.79
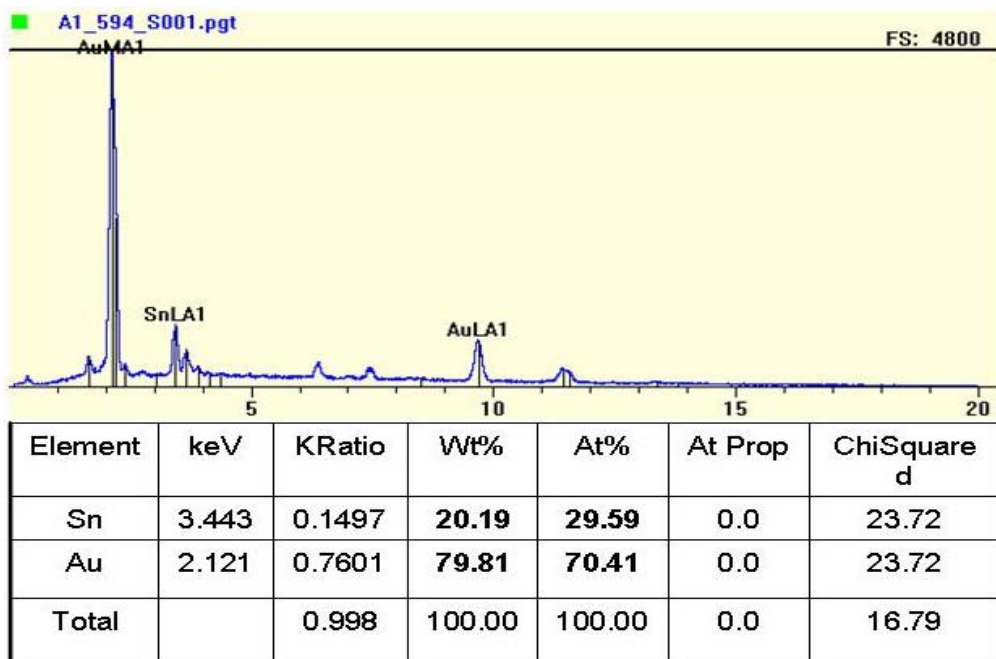
Fig. 5-11 EDX analysis of AuSn solders composition.

5.1.2.3. Sensor Response to Various Thin Film Coatings

The magnetostrictive sensor exhibits very different response to various thin film coatings described in the previous section. The resonant frequency of the sensor were found to shift up to higher values when an Al, Cu, Cr, or SiC thin film was deposited onto the sensor surface. In contrast, it was found to shift downwards when Au, In, Sn and AuSn materials were deposited. See Fig. 3-13 for frequency vs. amplitude plots for Cr and Au responses. This behavior will be detailed in the next section. Relative resonant frequency shift for all films exhibited a strong linear relationship with their relative thickness changes, as predicted by the analytical solution.

5.1.2.3.1. Frequency Shift before and after Thin Films Coatings on Sensors

In reviewing Equation (2-12):

$$\Delta f = \frac{1}{2}\left(\frac{\Delta E}{E} - \frac{\Delta \rho}{\rho}\right)f_0$$

the change in frequency can be positive, negative or zero, depending on the thin film properties of Young's modulus and density. Fig. 5-12 shows that Au film coating decreased the frequency, while the Cr film coating increased the frequency. In fact, in order to determine whether the film coating will provoke increasing or decreasing of the sensor's frequency, one can just compare the acoustic wave propagation speed:

$$\upsilon = \sqrt{\frac{E}{\rho(1-\nu)}}$$

for thin film material with that for the sensor material, Metglas 2826 MB. If both the acoustic wave speeds are the same, then no resonant frequency change will be observed. This was observed when a thin film of Metglas was sputtered onto the Metglas sensor platform. No appreciable change in resonant frequency was observed, which indicated that the sputtering deposited magnetostrictive thin film directly from Metglas 2826 MB target has identical wave propagation speed as the Metglas 2826 MB sensor platform.
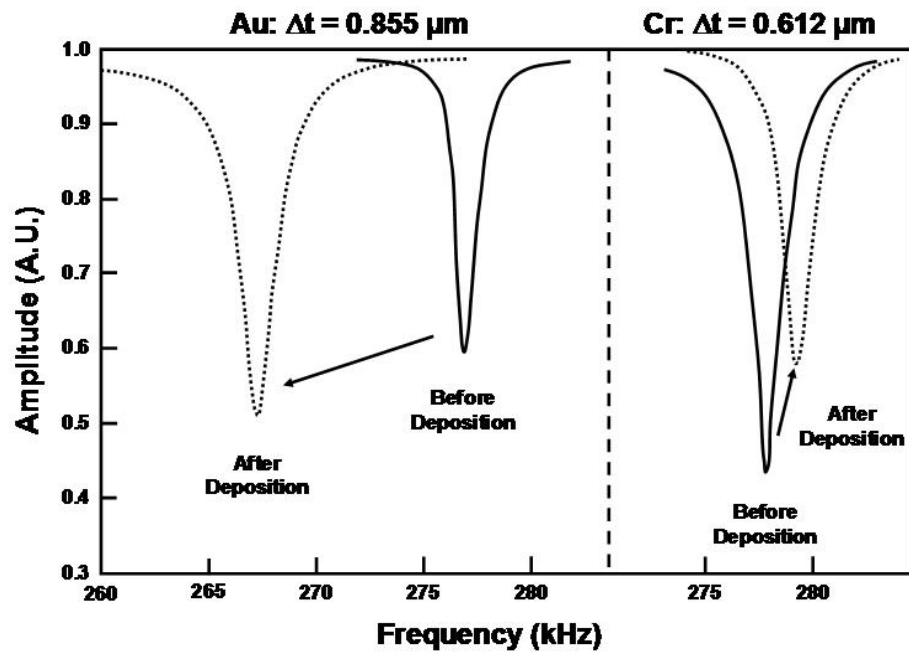
Fig. 5-12 Resonant frequency changes before and after thin film coating. The left panel shows the decrease in frequency after Au coating deposition, and the right panel shows increase in frequency after Cr coating deposition [33].

5.1.2.3.2. Relative Frequency Change with Relative Thin Film Thickness

As has been discussed in section 2.3.1, if Young's modulus and density of a film are independent of film thickness, then the relative frequency shift of ($\Delta f/f_0$) will change linearly with the relative thickness ratio of [$\Delta t/(t+\Delta t)$]. Fig. 5-13 plots all of the tested thin film materials that have resulted in the resonant frequency shift at a variety of thicknesses. An obvious linear relationship between the relative frequency shift and thickness ratio can be easily seen and indicates that the experimental data adheres well to the numerical solution. By determining the slope, the Young's moduli of those thin films were obtained by Equation (2-18). Section 5.1.2.5 will elaborate on the value of elastic moduli and Fig. 5-21 will graphically compare them. The data is presented here to illustrate the synergy between the numerical solution and experiments.
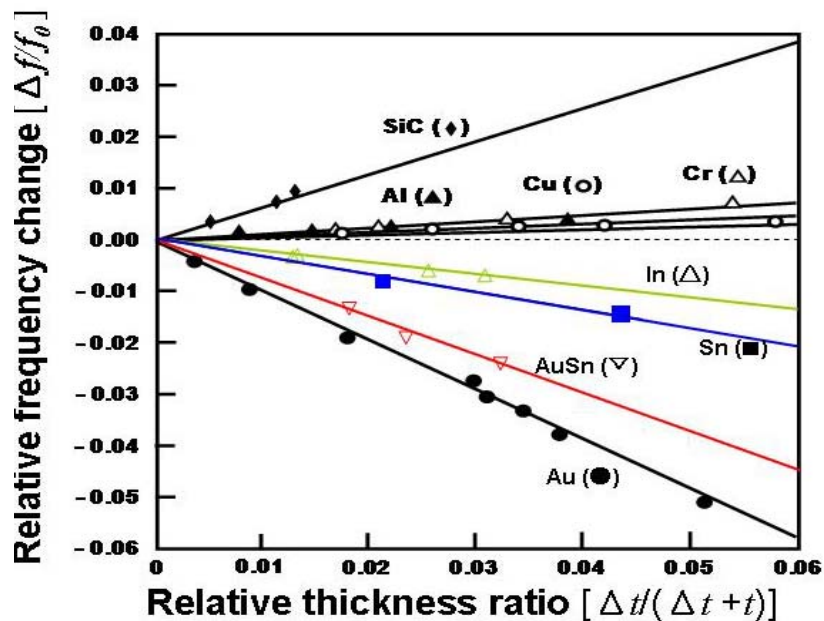
Fig. 5-13 Relative resonant frequency change as a function of relative thin film thickness ratio.

One can numerically examine the influence of the sensor thickness vs. film thickness on the relative frequency change $\Delta f/f_0$ of a longitudinal-mode resonator in order to determine the best ratio for maximizing sensitivity. The relationship is numerically described in Equation (2-18). In assuming material properties for an Au film, where frequency decreases with film deposition, one can plot the relative frequency shift verses film thickness for a sensor platform 1 to 28 micron thick, (see Fig. 5-14). This plot typically represents the group of thin film materials that result in a resonant frequency decrease. Similarly, Fig. 5-15 is the same plot for Cr film, representing film materials whose deposition causes a frequency increase. From both Figs., it is clear that in either case, when the sensor platform thickness decreases the relative frequency changes are larger for any thin film thickness. For example, when the platform has a thickness of 1 μm and 5 μm and is coated with 1 μm Au, the resonant frequency will shift downwards by about 0.5% of its uncoated frequency for the 1 μm platform and only 0.15% for the 5 μm platform. Thus, from Figs. 5-14 and 5-15, the following points can be easily observed:

- The thinner (or the lighter) the sensor is, the more sensitive the platform is to the thin film coatings regardless of the frequency shift up or down, and

- The thinner the film is, the more sensitive the sensor is regardless of the thickness of the sensor.
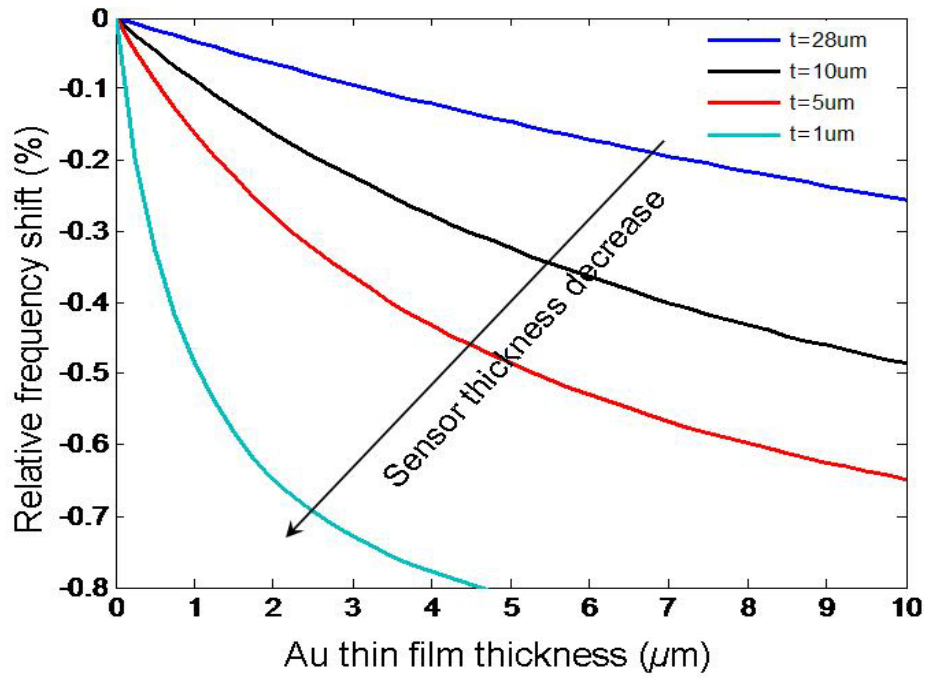
Fig. 5-14 Relative frequency changes vs. Au film for various sensor thicknesses based on
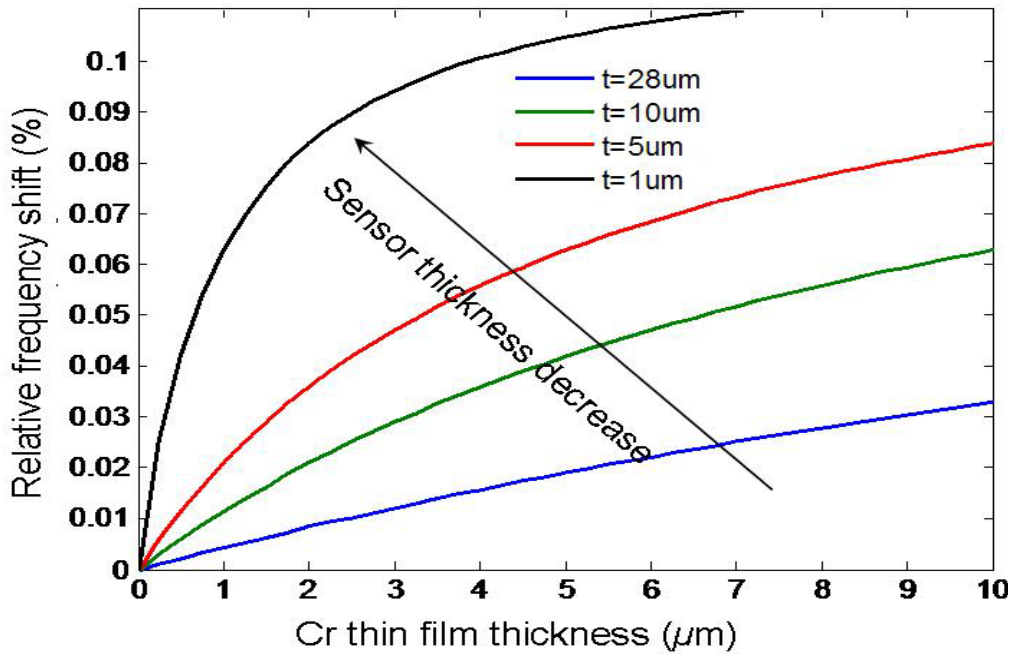
Equation (2-18).

Fig. 5-15 Relative frequency changes vs. Cr film for various sensor thicknesses based on

Equation (2-18).

5.1.2.4.   Sensor Response to the Applied Magnetic Field and Figure-of-merit Q Values

The principle behind the sensor vibration is the application of a modulated magnetic energy that drives the domains to switch direction with the field in an alternating manner. When the field is removed, stored elastic energy causes the domains to switch back to their original configuration. This switching process can be read with a sensing coil in close proximity. The coupling efficiency of such magneto-mechanical energy transfer can be influenced by many factors such as the strength of applied magnetic field, damping effects, internal stress of sensor, etc.

The oscillating frequency of a magnetostrictive sensor platform in response to an applied modulated magnetic field is a strong function of the applied field's strength. Typically, the sensor platform will exhibit its largest amplitude when the oscillating frequency matches the intrinsic resonant frequency of the sensor, at a particular narrow magnetic field strength range. This relationship can be seen by varying the strength of the applied field. Fig. 5-16 shows the amplitude versus frequency plot for a magnetostrictive sensor coated with 0.55 μm indium film. Although the same effect can be seen by interrogating the sensor platform without a deposited film, it seems more prudent to perform the characterization with a film since this is the objective of this work. When the applied field was very small and close to zero (0.73 Gauss), an oscillating frequency possessing a rather small amplitude was detected about 275.5 kHz. As the biased magnetic field (DC) strength was increased, the sensor's oscillating frequency was seen

to decrease somewhat while its amplitude increased rapidly. The sensor's amplitude was found to reach a maximum of 12.17 Gauss at an oscillating frequency of ~273 kHz, (see the left part of Fig. 5-16). When the applied field strength was increased further, from 12.17 to 25.27 Gauss, the sensor's amplitude began to drop while the frequency increased, (see the right-hand side of Fig. 5-16). The sensor's true oscillating frequency was then taken as the point where the sensor response had the maximum amplitude as described in section 2. Subsequently, reducing the applied field strength back to zero resulted in the sensor following the same process in reverse; this is seen best in Fig. 5-17 for a sensor platform without a thin film coating. The data is plotted by field strength versus oscillating frequency and response amplitude for an entire loop. The trends of Fig. 5-17 can be summarized as:

- The change of oscillation frequency with applied magnetic field strength through the loop cycle results in a "shoulder-head-shoulder"-like pattern.

- The amplitude of oscillation frequency change with applied magnetic field through the loop cycle results in a "m"-like pattern.

In the data in Figs. 5-16 and 5-17, the variation of the applied field was accomplished by moving the position of a permanent magnet relative to the sensor platform, whereby the distance of maximum response amplitude corresponded to the true oscillation frequency. Similar observation was reported by other researchers [115].
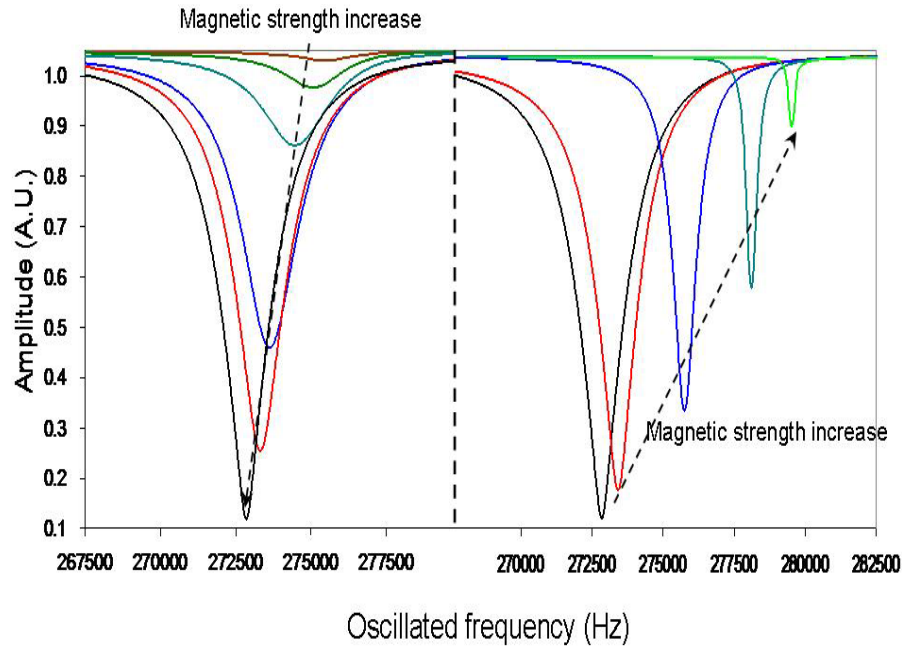
Fig. 5-16 Frequency response of sensor (8 mm x 1.6 mm x 28 μm) coated with 0.55 μm indium film to the applied DC magnetic field.
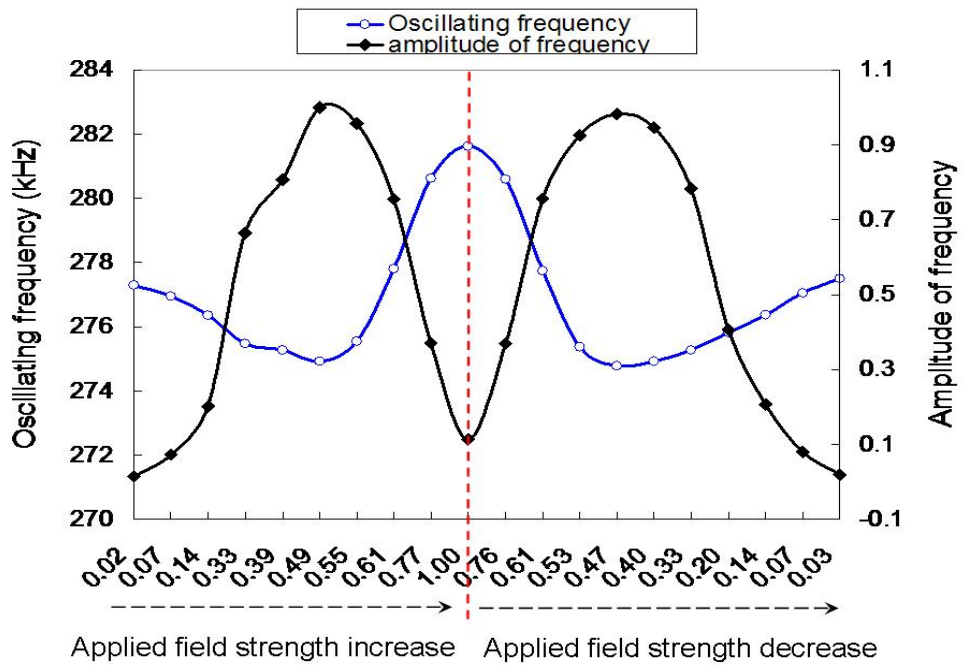
Fig. 5-17 Frequency and its amplitude change with normalized external field strength (DC bias).

The resonant frequency response peaks all exhibited different degrees of peak amplitude and sharpness. In order to determine the relative quality of these peaks it is necessary to use the quality factor (Q-factor), which is commonly used to examine the energy dissipation in microelectronics mechanical systems. Physically, the Q-factor represents the total energy lost per cycle of a vibration system and can be defined as [116, 117]:

$$Q = 2\pi \left(\frac{w_0}{\Delta w} \right) \tag{5-1}$$

where w_0 and Δw are stored vibration energy and total lost energy per cycle, respectively. This Q-factor can be calculated by analysis of the spectrum of resonant frequency. It is generally called as figure-of-merit, a numerical quantity based on one or more characteristics of a system or device that represents a measure of efficiency or effectiveness. Figure-of-merit can be experimentally determined as a ratio of the resonance frequency f_0 to the width (Δf) of the resonance peak at its half amplitude, and expressed as

$$Q = \frac{f_0}{\Delta f} \tag{5-2}$$

The Q-factor of a vibration system is dependent on many factors such as material properties, medium of operation, etc.

The Q-factor for the data in Fig. 5-16 and 5-17 can then be calculated bases upon Equation (5-2), which is plotted in Fig. 5-18 as Q-factor versus normalized applied field for a platform both with and without the indium film. The Q values for each sensor were found to be around 265 and to be very close to each other at their resonant frequency. At applied fields below the resonant frequency, the Q values were found to be 200, (see Fig.

5-18). At applied fields above the resonant frequency, the curves begin to differ with the uncoated platform possessing larger Q values. However, it is likely the Q-factor is a function of the type of film and its thickness, (see Fig. 5-19), where the Q value increases from 430 to 710 when the Cu thickness increases from 0.5 μm to 1.23 μm. A similar tendency is also seen in the case of the sensor with Cr coating, Fig. 5-20. Furthermore, Fig. 5-20 also indicates that films with higher Young's modulus seem to yield a higher Q value. As will be shown in next section, the Cu film material possessed a higher Young's modulus than the Cr film. Nevertheless, the Q value for a sensor with thin film coating is found to increase as film Young's modulus or film thickness are increased. In both cases the increase in effective elastic modulus of the vibrating system, when the film modulus was higher than that of the substrate, resulted in an increased Q-factor, which follow well with Equation (5-2). Furthermore, along with the Q-factor, the effective resonant frequency was found to increase as the film thickness increased. Such an increase in the Q-factor with increasing resonant frequency is mathematically confirmed for a cantilever vibrating in the transverse mode [116].
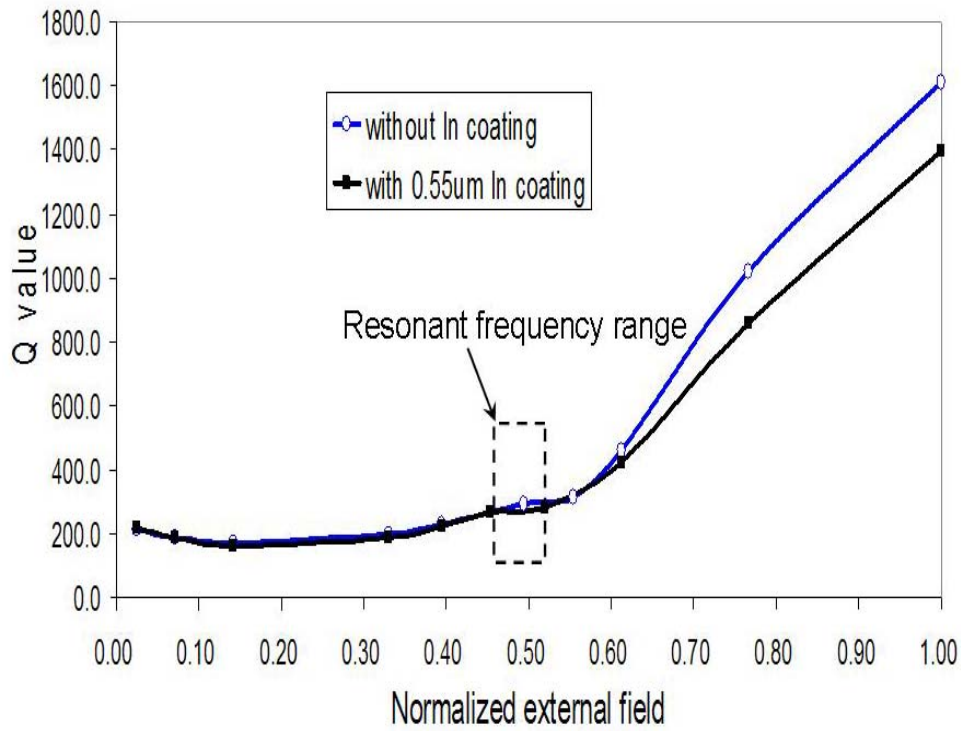
Fig. 5-18 Q value for sensors coated with and without 0.55 μm indium thin film.
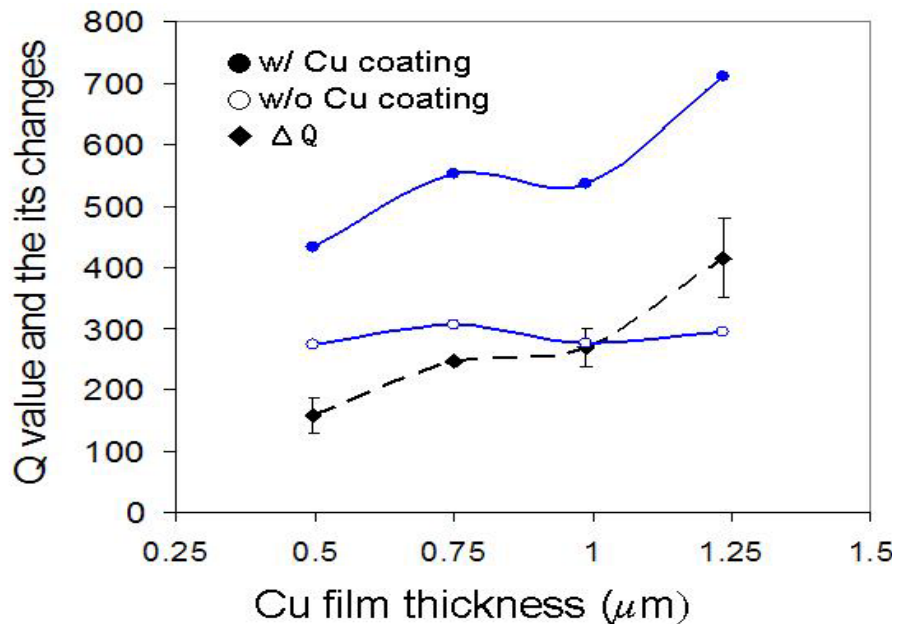
Fig. 5-19 Q values for a sensor without coating or with Cu coating of various thickness.
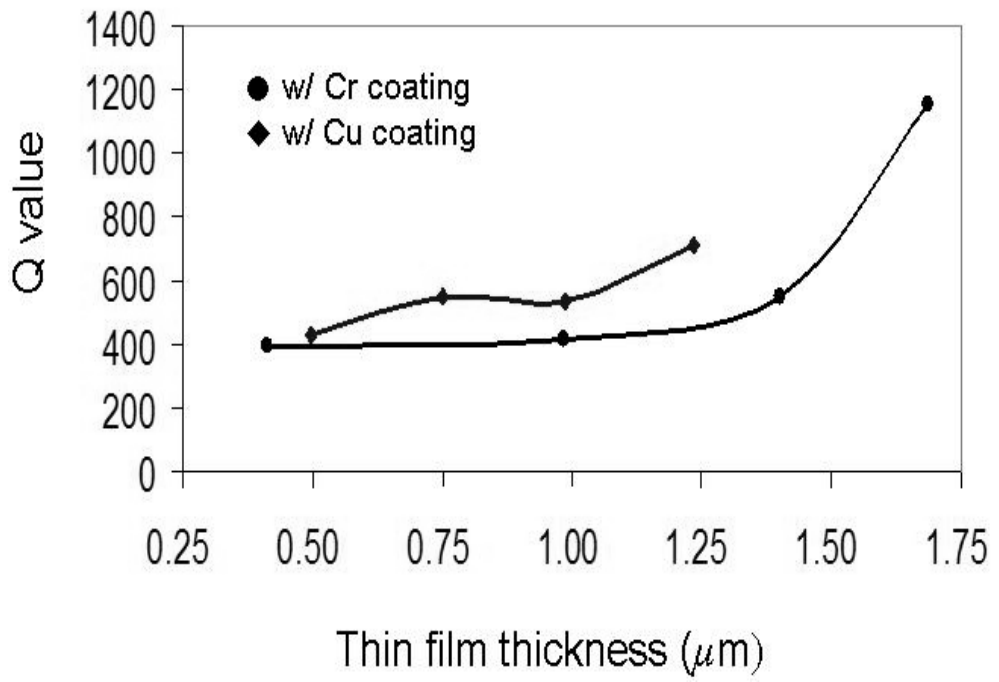
Fig. 5-20 Q value for sensors deposited with Cu and Cr film in different thickness.

5.1.2.5.   Determination of Young's Modulus for Thin Film Materials

The magnetostrictive sensor platforms were employed to determine the Young's modulus of various thin films deposited onto them, namely Au, Cr, Cu, Al, SiC, In, Sn and an AuSn alloy. The relative frequency change linearly relates to the relative thickness ratio for these materials as previously shown in Fig. 5-13, the Young's modulus of each film can be calculated by the linear regression fitting of each curve and using Equation (2-18). The calculation used the bulk material density, the material's bulk modulus and film modulus are listed in Table 5-2 for comparison. The measured values and bulk values are comparable for all the materials. Some significant disparities do exist. For example the Young's modulus of indium thin film material (23.9 GPa) measured during the course of this work showed a considerable difference from its bulk scale counterpart (12.7 GPa). This difference could be due to the error in film thickness measurement by profilometer. It was noted that scratches of the trace were produced due to the fact that film of indium was so soft, which resulted in the measure thickness less than its actual value. Consequently, a lower relative thickness ratio resulted. Additionally, the thin film microstructure can differ greatly from the bulk scale microstructure. In particular, many thin films exhibit a preferred texture due to minimization of surface tension during film growth. Furthermore, many thin films possess grain sizes in the nanoscale regime where they possess increased grain boundary volume ratios that can alter the elastic modulus. For the most part, thin film values measured here fall with in the range of thin film values measured by other researchers with other techniques, (see Fig. 5-21 and Table 5-3).

Table 5-2 Comparison of Young's modulus for thin film materials tested in this work and their bulk scale counterpart [118-121].

	Au	Cr	Cu	Al	SiC	In	Sn	AuSn	Metglas
Density (g/cc)	19.3	7.19	8.96	2.7	3.2	7.31	7.3	15.32	7.9
Young's modulus – bulk (GPa)	80	140	128	70	*	12.7	41.4	58	105
Young's modulus – thin film (GPa)	75.9	130.8	139.2	55.4	160.4	23.9	47.4	51.7	NA

* Young's modulus for SiC Varies from 100 to 460 GPa
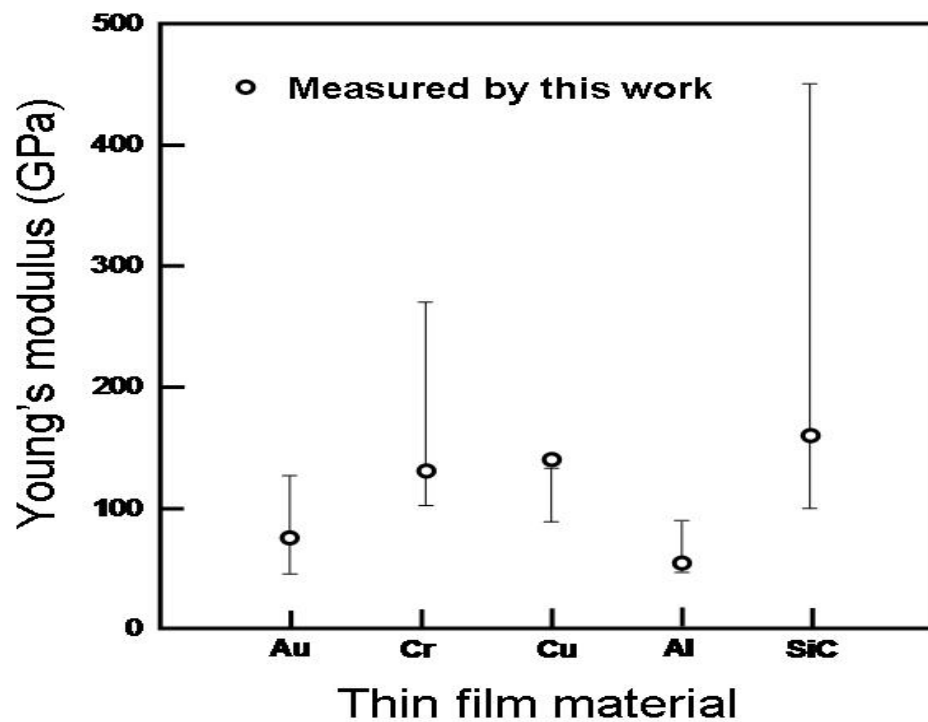
Fig. 5-21 Plot of Young's modulus determined in this work with other literature data.

Table 5-3 Summary of process, test method, and value for various thin film materials, methods in italics are non-destructive methods.

	Deposition Process	Test method (non-destructive)	Modulus (GPa)	Ref.
Au	E-beam	Micromembrane deflection	53 - 55	[122]
	Electroplated	Nanoindentation	72	[107]
	Sputter	Microcantilever Bending	107 - 130	[76]
		Nanoindentation	110 - 123	
	Sputter	Electrostatic Actuation	72 - 78	[123]
	Sputter	Micromembrane Deflection	68 - 78	[124]
		Magnetostrictive Sensor (this work)	66 - 77	
	unknown	Bulge Test (dynamic)	63 - 77	[125]
Cr	Sputter	Nanoindentation	107 - 234	[126]
	Sputter	Nanoindentation	157-172	[111]
	Sputter	3-Point Bending	275	[69]
Cu	E-beam	Laser Diffraction on Freestanding Films	102	[70]
	E-beam	Micromembrane Deflection	125 - 129	[127]
	Electroplating	Nanoindentation	99 - 123	[109]
		Microcantilever Bending	90 - 121	
	Electroplating	Microbridge Bending	115	[75]
Al	E-beam	Laser Diffraction on Freestanding Films	57	[70]
	E-beam	Micromembrane Deflection	65 - 70	[127]
	E-beam	*Magnetostrictive Sensor*	70	[32]
	Sputter	Stress-Temperature Plot	47 - 74	[128]
	Sputter	Nanoindentation	50 - 90	[99]
	Sputter	Electrostatic Actuation	75	[123]
	Sputter	Microcantilever Bending	77 - 81	[76]
		Nanoindentation	74 - 79	
	Sputter	Biaxial Bending	84	[129]
SiC	Sputter	Resonant Frequency	234-264	[88]
	APCVD	Nanoindentation	395	[107]
	CVD	Nanoindentation	324 - 384	[91]
		Acoustic Microscopy	351 - 452	
		Impulse Excitation	360 - 425	
	CVD	*Brillouin Light Scattering*	420 - 430	[90]
	PECVD	*High Frequency Acoustic Microscope*	196 - 273	[87]
	Laser Arc	*Laser-Induced Ultrasonic Surface*	100 - 150	[86]

5.1.2.6. Comparison of Au Film Young's Modulus Obtained by Different Methods and
Measuring Techniques

Young's modulus for Au film was determined by two methods, as described in
Equations (2-17) and (2-18). Fig. 5-22 shows the Young's modulus of Au that was
determined by the former method (Equation (2-17)). Fig. 5-23 shows the relative
frequency change as a function of relative Au film thickness change, which is the same
data plotted in Fig. 5-13, but with insertion of its corresponding modulus that was
determined by measuring the masses as shown in Fig. 5-22. When using this method, the
modulus varied from 66 GPa to 76 GPa in thickness ranging from 0.25 µm to 1.5 µm,
with an average of 71.5 GPa. The number of samples for each test is three. A mean
Young's modulus of 75.9 GPa for the same Au film was obtained with the assumption
that the Au film would have the same density as its bulk counterpart via Equation 2-18.
The average results of Young's modulus obtained by these two methods are fairly
comparable.

In order to verify the results of the thin film elastic modulus obtained by
magnetostrictive sensors, an MDE (Membrane Deflection Method) test was also
conducted on the same films' materials that were simultaneously deposited on both
sensors and MDE testing wafers. Details of MDE can be found elsewhere [130]. The
results of the Au film obtained through these two techniques are compared in Fig. 5-24,
where the method of measuring the masses of sensors before and after Au film deposition
was employed. Note that both techniques produced very similar modulus at a variety of
film thicknesses. Some difference was seen in the 0.25 µm thick film; it could be

attributed to the mass measurement error at the point when the film was very thin, and the

crystal structure different developed on different substrates [130].
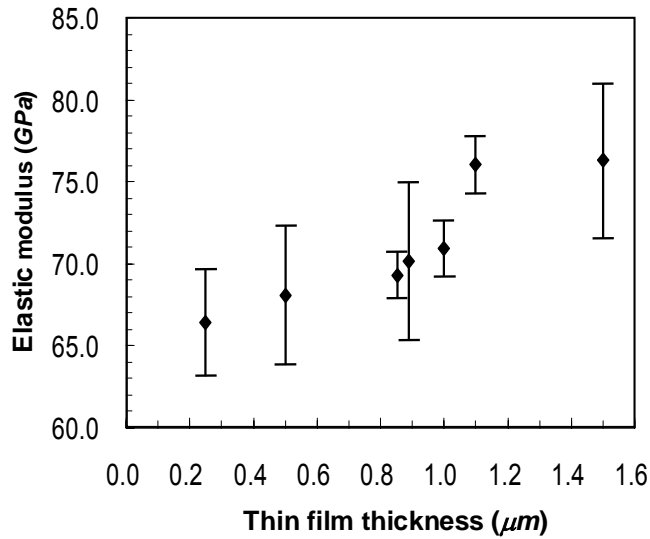
Fig. 5-22 Young's modulus of Au film obtained by measuring the masses of the sensors

and films.
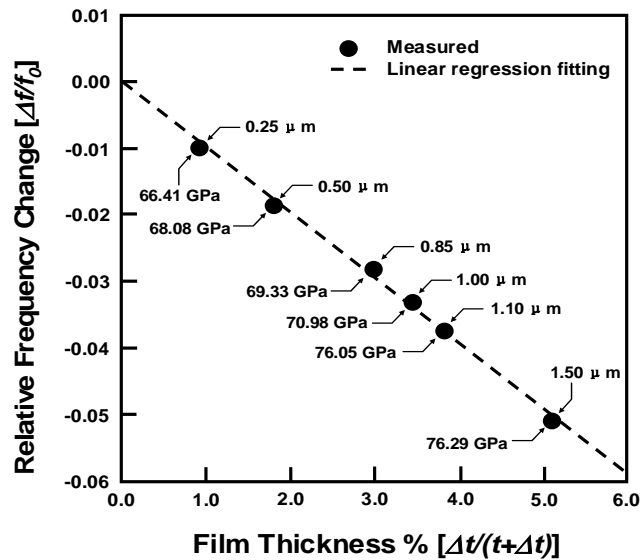
Fig. 5-23 Relative frequency change vs. relative Au thin film thickness change and its

corresponding Young's modulus obtained by measuring the masses of the sensor and film

[130].
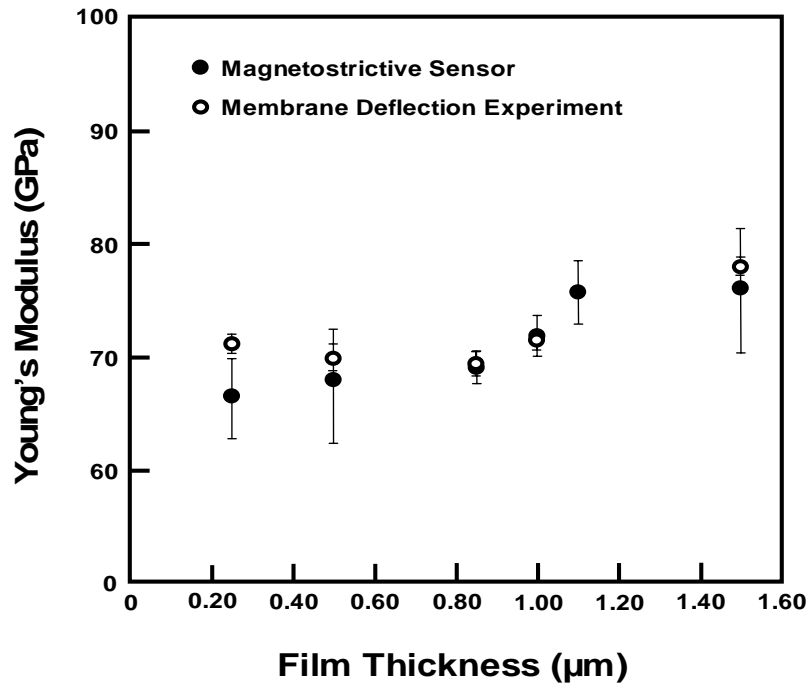
Fig. 5-24 Young's modulus of Au film measured at different thickness by magnetostrictive sensor and MDE [130].

5.1.2.7. Finite Element Analysis to Verify Thin Film Young's Modulus Measurement

The preceding sections demonstrated that a Metglas strip could be easily employed to measure the thin film Young's modulus. Although an alternative technique was used to verify the measurements, it is prudent to also perform numerical simulations as an additional counter check. In this regard, an element size of 160 μm x 160 μm x 5.6 μm was used for mode meshing 8 mm x 1.6 mm sensors. Fig. 5-25 represents the mesh model of a sensor with an Au coating on top. The materials' properties used in the simulation are listed in Table 5-4. Sensors coated with a Au film with the thicknesses of 0.25 μm, 0.40 μm, 0.50 μm, 0.855 μm, 0.89 μm, 1.00 μm, 1.10 μm and 1.5 μm were

analyzed. For the Cu, 0.497 μm, 0.74 μm, 0.99 μm, 1.23 μm, and 1.71 μm were used. These thicknesses of Cu or Au when used for simulation were identical to their experimental tests.

Simulations of the thin film Young's modulus measurement was performed for both the Au and Cu coatings and then compared to the experimental measurements presented in Fig. 5-26. The Young's modulus and density of all the materials used in the simulations are listed in Table 5-4. Using the same method described early, Equation (2-18) in particular; the relative resonance frequency change with the relative thickness ratio is presented in Fig. 5-26. By linear regression, Young's modulus of Au and Cu thin film was determined by simulation to be 79 GPa, and 143.5 GPa, respectively. These values are slight higher than that by experimentation, which is 75.9 GPa and 139.2 GPa, respectively. This disparity is not surprising, as the experimental tests possessed a small degree of dampening, such as friction of the specimen due to contact with the surface of the instrument, which influenced the tests. However, the values are close enough that this effect can be considered negligible.
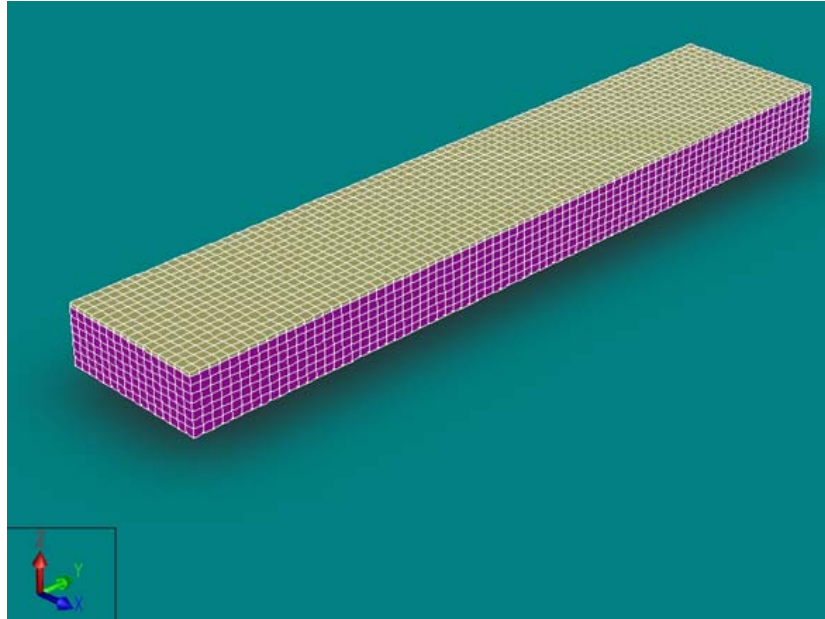
Fig. 5-25 Typical mesh model of a sensor coated with Au film.

Table 5-4 Materials properties used for finite element analysis.

Material	Young's modulus (GPa)	Density (g/cc)	Poisson's ratio (v)
Metglas™	105	7.9	0.33
Silicon nitride	222	2.7	0.27
Au film	73.5	19.3	0.36
Cu film	139.5	8.96	0.35
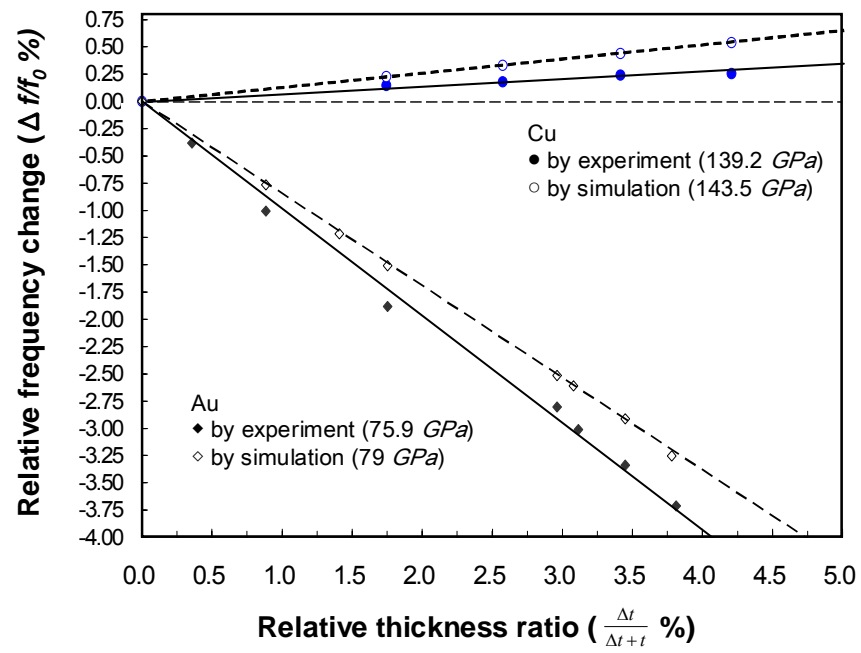
Fig. 5-26 Experimental and simulated results of the relative frequency change with the relative thickness.

5.1.2.8. Comparison of Error Resulting From Different Methodologies and for A Variety of Film Materials

Relative error can result from the resolution of instruments during measurement, e.g. resolution of frequency analyzer, microbalance, profilometer, and density measurement. The calculated relative error for Au thin film measurement in different methods is plotted in Fig. 3-27. The calculation was based on Equations (2-19) and (2-20) with $\Delta f = 25$ Hz, $\Delta m = 10$ μg, $\Delta t = 5$ nm, $\Delta \rho = 0.1$ g/cc and the other parameters were the measurement data. The results indicated that the method of weighting the masses of the sensor before and after the thin film coating appears to result in larger error. This is due to the additional error in the scale, which is not the complete error yet when you consider that moisture and other species can absorb onto the sensor surface after deposition and before post-deposition weighting. Thus, assuming the bulk density as the film density in measuring the film's Young's modulus results in less error and is more accurate. In this regard, one can also assess the effect of the material's density on the measurement error. Fig. 5-28 compares the relative error for several tested film materials of various thicknesses. A detailed error analysis can be found in reference [131]. There is a clear hierarchy of error which follows the trend that the lower the density the more error that will be associated with the measurement. Nonetheless, the largest relative error was less than 6.5% for Al in Fig. 5-28, which is much less than the technique of vibrating the cantilever in the transverse mode reported in the literature [78, 79, 88].
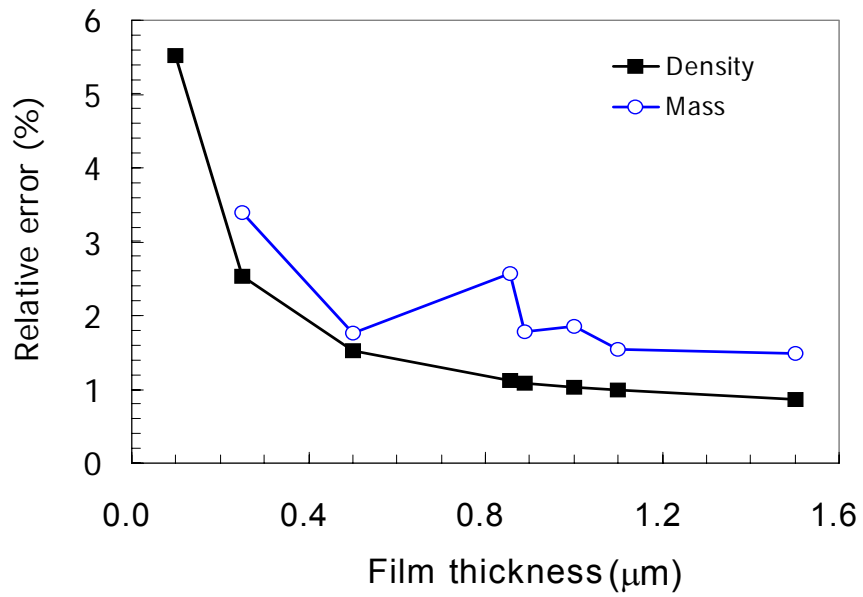
Fig. 5-27 Relative error of Young's modulus analysis for the methods applied in determining Au thin film material.
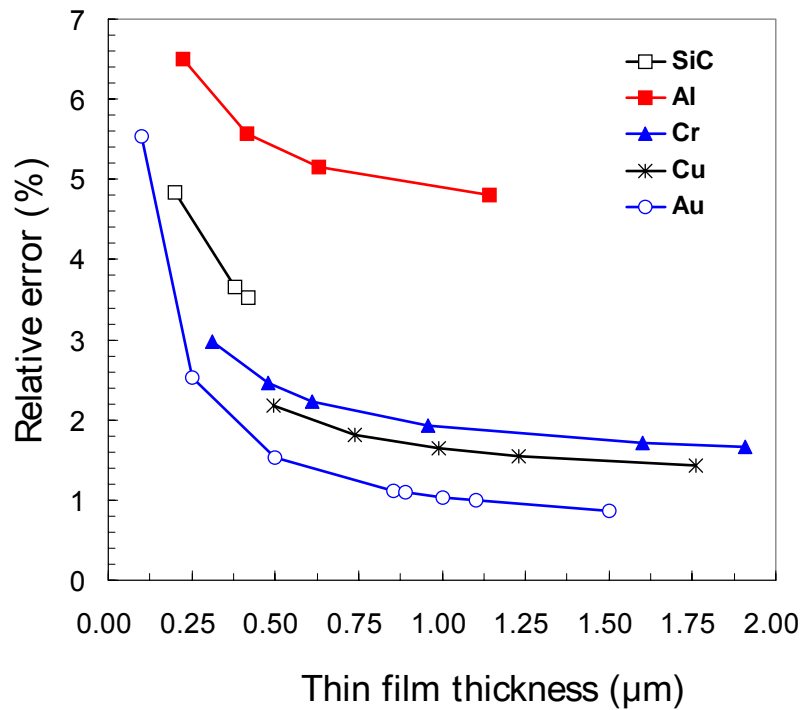
Fig. 5-28 Relative error of Young's modulus for various thin film materials.

5.2. Concentrated Mass Detection

There are four general sensor categories that are applied to chemical or biochemical analysis on the basis of the sensor's principal physics and operating mechanisms: chromatography & spectrometry, electrochemical sensors, optical sensors and mass sensors [132]. Overall, in comparing the advantages and drawbacks of these techniques, mass sensors tend to exhibit superior performance in the detection of biochemical molecules, via attachment to the sensor surface during/after reaction or absorption, by monitoring the sensor's resonant frequency change. The focus of this dissertation is mass sensors and, thus, only these will be reviewed. Types of mass sensors include the quartz-crystal microbalance (QCM), surface acoustic wave (SAW), flexural plate wave (FPT), and micro cantilever.

The QCM device operates via the electro-mechanical coupling effect of a piezoelectric material, in which the applied voltage results in shear deformation of the crystal. By modulating the electrical field, one can excite the device to vibrate at its resonant frequency. Consequently, when mass is attached or added to the surface it alters the device's resonant frequency a measured amount. This technique has long been employed as a mass sensor in monitoring thin film thickness during vacuum deposition [133, 134] and biochemical absorption [135, 136]. The SAW mode was first discovered by Lord Rayleigh in the nineteenth century and further developed by R. M. White who employed interdigitated electrodes to the device in the 1970s [137]. Many applications of SAW devices, such as chemical or biochemical sensor platforms, have been realized since then [138-142]. Detection of a chemical or biochemical molecule by a SAW device is similar to a QCM; both operate by monitoring a change in acoustic frequency. The

difference is that the SAW device generates an acoustic wave that travels along the sensor platform and is sensed at the other end. When it encounters any mass attached to the platform's surface the wave becomes slightly dampened. The operation frequency range for SAW devices is from a few tens of MHz to the GHz range [139, 143].

The FPW device is another acoustic wave sensor that is similar to a SAW device. It also employs interdigitated electrodes to generate and detect an acoustic wave in a thin flexural membrane and detects mass loaded onto its surface via its frequency change. Since the plate is only a few micrometers thick, the mass loading on the surface is comparable to the sensor platform and a higher mass sensitivity is achieved than with an SAW device [144]. In addition, the transverse vibrational mode of an FPW may be employed as an actuator to pump a liquid solution.

Both QCM and SAW devices operate in high to very high frequency ranges (a few MHz to 100 MHz) while the FPW only operates at a frequency of a few MHz or less. However, the mass sensitivities of the FWP's acoustic waves are on the order of SAW's and QCM's. Of the three, QCMs tend to possess higher Q values but are limited in their minimum size, whereas SAWs and FPWs can be made on the microscale and detect smaller amounts of mass. Table 5-5 compares the mass sensitivities of SAWs and FPWs in terms of lower minimum detectable concentrations of various species.

Table 5-5 Minimal detectable concentration for SAW and FPW [144].

Devices	Methanol (ppm)	Nitrous (ppm)	Helium (ppm)
FPW	75	80	250
SAW	535	2500	>10,000

Cantilever-based chemical and biochemical sensors have been studied for the past decade or so [36, 83, 145-156]. Two important developments in the area include: Cleveland et al. determined the spring constant of a cantilever by measuring the resonance frequency change due to mass added on the tip [83] and Gimzewski et al. [147] observed that chemical reactions taking place on the cantilever can be monitored via its deflection [147]. In 1995, Chen and Thundat [36, 38] demonstrated that cantilever resonant frequency shift was associated with the surface absorption of mass or molecules. Since then many researchers have explored the application of cantilever sensors in widespread areas for detection of chemical or biological agents [157]. Such detection is based either on the measurement of cantilever deflection [37, 46, 147, 158, 159] or on the resonant frequency shift [36, 153, 154, 160]. A very high mass sensitivity of 0.32 pg/Hz was reported by Sone [161] for the cantilever-based sensors.

By comparing the various types of mass sensors described above with their mass sensitivity and minimal detectable mass density in Table 5-6 reveals that the cantilever and FPW mass sensors both possess a similar order of detection level. However, Sone [161] reported that a mass sensitivity of 0.32 pg/Hz can be obtained, which inspired researchers to continue to work on cantilever sensors as an alternative technology.

Table 5-6 Comparison of mass sensors.

Techniques	Operation frequency (MHz)	S_m	S_m (cm^2/g)	MDMD	Reference
GCMS	NA	NA	~1 pg	~1 pg	[162]
QCM	6	$\propto \dfrac{1}{\rho t}$	14	10 ng/cm^2	[163]
SAW	112	$\propto \dfrac{1}{\rho \lambda}$	151	1.2 ng/cm^2	[163]
FPW	2.6	$\propto \dfrac{1}{\rho t}$	951	0.4 ng/cm^2	[163]
Cantilever	5~0.005	$\propto \dfrac{1}{\rho t}$	991~1363	0.67 ng/cm^2	[163]

Since 1998, Grimes' research group [164, 165] has been working on magnetoelastic materials, primarily Metglas strip, as a chemical sensor platform that is operated in the longitudinal vibration mode. Based on the resonant frequency change, the sum of mass (aggregated chemical molecules) absorbed on the sensor surface can be determined. Since then, numerous applications have been explored by Grimes' group including measurement of pressure, temperature, liquid viscosity, humidity, and fluid-flow velocity as well as environmental monitoring [54, 166-175]; pH value sensing [173, 176-178]; hydrogen, ammonia and other gas detection [18, 57, 179-181]; thin film Young's modulus measurement [32]; biomass/biomolecule detection [17, 53, 56, 182, 183]; and chemical reactions [184, 185]. An illuminating review of those applications can be found in the literature [13]. In recent years, Auburn University's Detection and Food Safety

Center (AUDFS) has dedicated much research effort by a similar principle, mainly based on freestanding beams and particles.

The most common method of binding biomolecule cells onto the sensor surface for mass detection is using a specific receptor recognizing only the agent of interest, which then, binds the antigen or spores to the sensor. As discussed above, the resonant frequency changes as a result of this process. The receptors employed by AUDFS in magnetostrictive sensors include antibodies and phage, more details of which can be found in [16, 20, 21]. These references describe sensors constructed of Metglas. These writings demonstrate it as a material of choice in detecting biological species. However, these works only deal with the mass evenly distributed on the sensor's surface; almost no one addresses unevenly distributed mass on a sensor, especially when the sensor vibrates in the longitudinal mode. In the following, details of measuring the concentrated mass attached to the sensor's surface are reported.

5.2.1.   Experimental Details

With consideration for the convenience of the test setup, the free-free ended beam was selected as the sensor platform for investigating the resonant frequency change due to a concentrated mass attachment. Sensors with dimensions of 5 mm length and 1 mm width were cut from a 28 μm thick Metglas 2826 MB strip. These specimens were prepared, by cleaning and drying, using the identical procedures described before. Glass beads [186] with a diameter about 425 μm were used to simulate the concentrated mass and were carefully loaded on to the sensor surface at different locations and secured with

glue. The average mass of a sensor and glass bead are 1066 μg and 181.5 μg, respectively. It should be noted that these experiments are aimed as assessing the position of the mass concentrations and not focused on demonstrating minimum sensitivity. Thus, significant sized beads were employed. The amount of glue employed for each bead was controlled to the best of our ability to minimize its influence. After a glass bead was loaded on the sensor surface, it was immobilized by drying at room temperature for at least two hours. The glass beads were randomly loaded onto the sensor surface, but their locations were characterized and reorganized afterwards. The resonant frequency of the sensor was measured before and after attachment of the glass bead in a manner identical to which is discussed in section 2.

5.2.2. Results and Discussion

Fig. 5-29 shows electron microscopic images of the glass beads attached to the sensors at various locations. In all cases, the measured resonant frequency of a free-free ended sensor with glass bead attached at different locations decreased relative to the frequency before attachment. Table 5-7 lists these results giving resonant frequencies before (f_0) and after (f) bead attachment. Note that x denotes the position for a single bead and x_1 and x_2 the positions when two beads were attached. Fig. 5-30 shows the recorded frequency spectrum for test case #2 where the glass bead was attached to the center of the sensor surface, with the neutral position in longitudinal direction; but slightly off-central line. No significant resonant frequency shift was observed for this position. As the bead was moved away from the neutral point towards the free ends the frequency shift increased. The shift reached a maximum when the glass bead was loaded at a position

120

closest to the free ends of the sensor, as in test case #7. Fig. 5-31 shows the result of test case #6 whose resonant frequency changed before and after glass bead attachment.
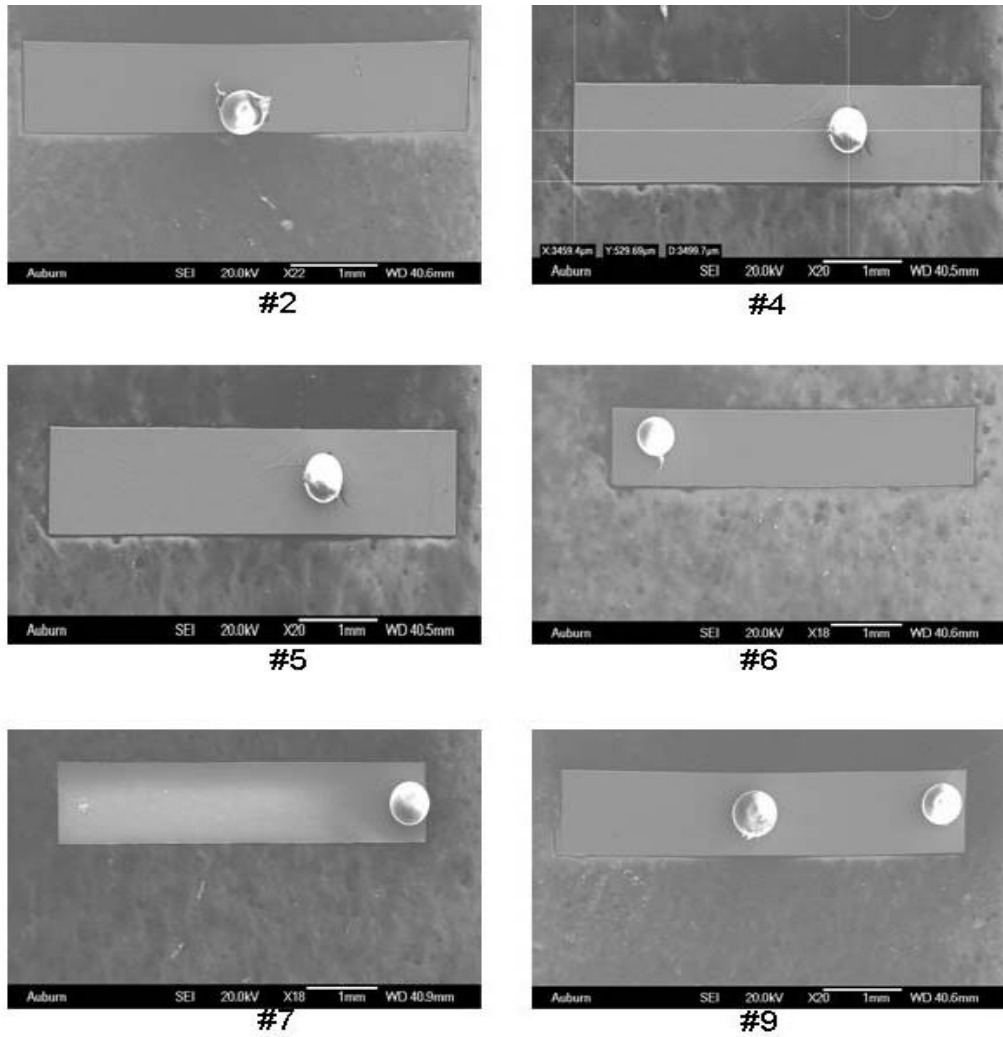
Fig. 5-29 SEM images showing glass beads attached to the sensor in various locations. The numbers correspond to the test numbers listed in Table 5-7.

Table 5-7 Test results of sensor (5 mm x 1 mm x 28 μm) attached with glass bead at different locations.

test	f_0 (kHz)	f (kHz)	Δf (kHz)	$\Delta f / f_0$	X (mm)	Glass bead location
1	443.334	443.268	−0.066	−0.00015	X=2.518	
2	438.400	438.468	0.068	+0.00016	X=2.482	
3	438.268	435.668	−2.600	−0.0059	X=3.010	
4	442.134	435.000	−7.134	−0.0161	X=3.460	
5	438.934	422.834	−16.100	−0.0367	X=3.682	
6	438.100	412.634	−25.466	−0.0581	X=4.392	
7	439.468	408.568	30.900	0.0682	X=4.942	
8	441.334	438.234	−3.100	0.0070	X1=2.668 X2=2.182	
9	437.668	411.634	−26.034	−0.0595	X1=4.818 X2=2.475	
10	441.200	397.900	−43.300	−0.0981	X1=4.908 X2=0.248	
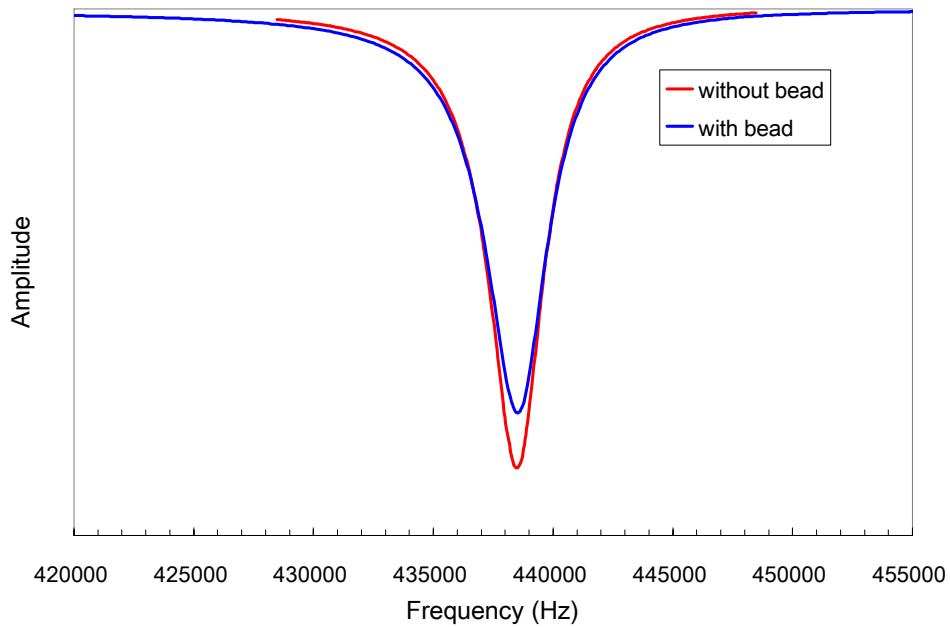
Fig. 5-30 Resonant frequency spectrum of a sensor (5 mm x 1 mm x 28 μm) with and without glass bead attached to its center.

122
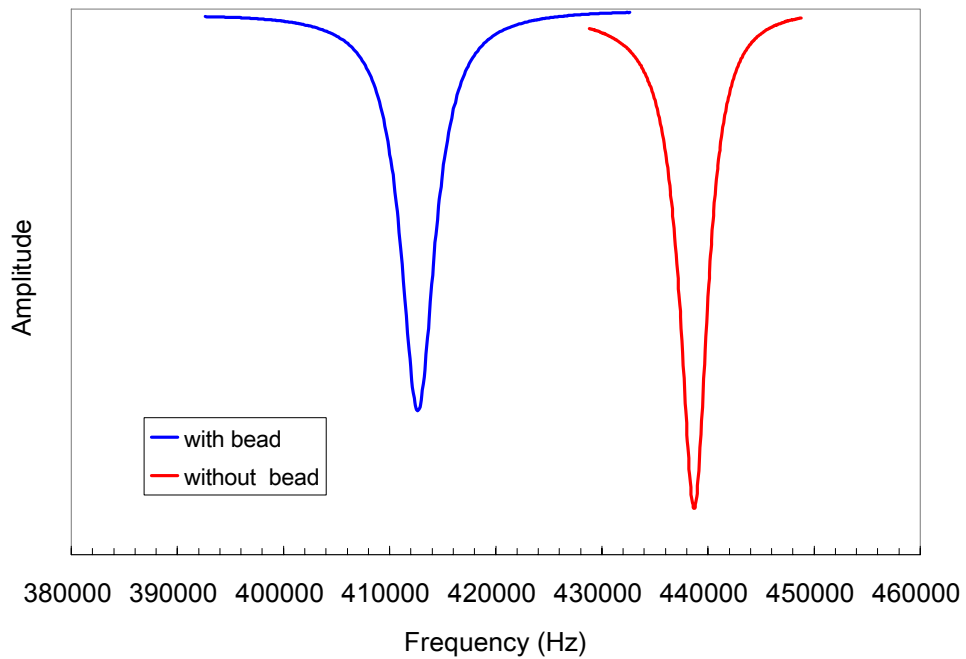
Fig. 5-31 Resonant frequency change due to glass bead attached to one of the free ends of a sensor (5 mm x 1 mm x 28 μm).

Fig. 5-32 plots the actual resonant frequency change due to glass bead position on the surface, and Fig. 5-33 is the same plot with relative resonant frequency shift. Note that the generated curve consists of the actual data to the right side of the neutral point, 0.5 normalized locations, and the left side is a mirror of the right side data. The data traces a curve with a maximum at the free ends and no change in the center. Thus, when species attach to the sensor, their position will determine their influence on the resonant frequency shift. The situation becomes more complicated when multiple mass concentrations attach to the surface.

The attachment of more than one mass concentration was investigated by placing two beads on the sensor surface, (test cases # 8, 9 and 10). When the second bead was

123

attached at the neutral point, there was no effect on frequency shift. However, when these two beads were placed at either end there was a significant shift in resonant frequency, beyond the 30 kHz of a single bead. A 43 kHz was the result in the test case #10. In this case, both sides reflected the acoustic wave at nearly the same speed and the neutral position was much nearer to the actual center of the sensor. As more mass concentrations were added the situation became more complex until a condition was reached where mass was evenly distributed across the sensor surface. These results indicate that detecting the attachment of a single attached mass, such as a spore or a cell, could be a difficult endeavor as these attachments will occur at random positions and may not be distinct from multiple attachments, if one is not located at the detectible position. A solution would be to place the capture layers near the ends of the sensor to better distinguish one or few attachments from multiple ones.
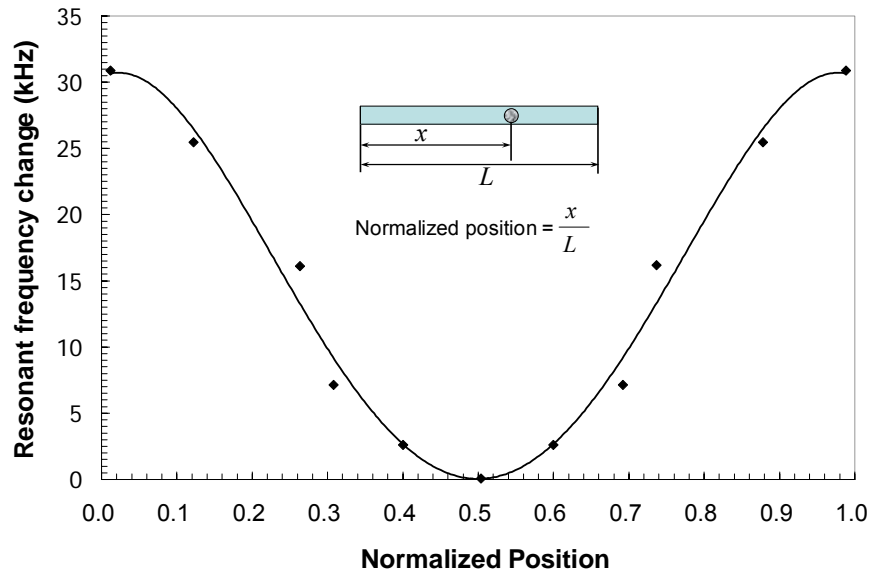
Fig. 5-32 Resonant frequency change as a function of the location of a glass bead

attached to the surface of a sensor of 5.0 mm x 1.0 mm x 28 μm.
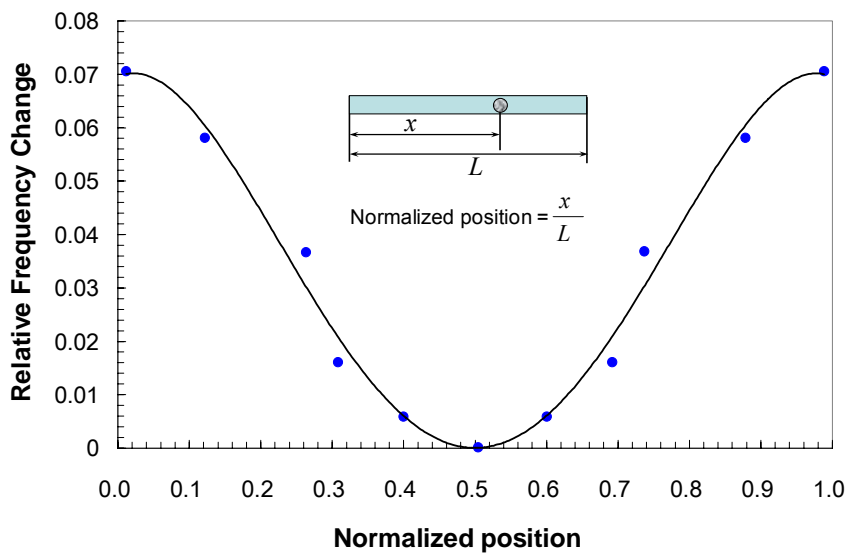
Fig. 5-33 Relative resonant frequency change as a function of the location of a glass bead

attached to the surface of a sensor of 5.0 mm x 1.0 mm x 28 μm.

5.2.3. Finite Element Simulation Analysis to Verify the Mass Detection for Mass Concentrations

In the preceding sections, experimental data were presented illustrating how the location of a mass concentration on a freestanding Metglas strip influenced its resonant frequency. In order to verify these results, numerical simulations were performed that mimicked the experimental conditions. The physical characteristics of the simulated sensors included a layered structure composed of 0.36 μm SiN, 1.0 μm Metglas 2826 MB and 100 nm of Au and dimensions of 250 μm x 50 μm. The chosen element size was 6.25 μm x 6.25 μm x 0.2 μm for model meshing. A mass of 1 pg with the size of 1.43 μm x 0.73 μm x 0.73 μm was used to simulate an *E. Coli O157: H7* cell [187]. The location of concentrated mass attached to the sensor surface was systematically varied and is depicted in Fig. 5-34, which is an 11x11 knot array where rectangles denote the simulated cells. In this regard, several aspects of location effect were investigated, which are (1) the influence of cell distance from the sensor neutral point (along the central line of the sensor), (2) the different orientations of the cells (length parallel or perpendicular to the longitudinal direction), (3) the off-centerline influence and (4) the randomly attached multiple masses.

The typical model meshing for testing single and multiple masses attached on the sensor surface are shown in Fig. 5-35. Fig. 5-35 (a) shows the single biomolecule loaded along the center axis, and (b) illustrates multiple cells loaded on the sensor surface. Test of three types of sensors (cantilever, bridge and freestanding beam) with the same testing circumstances were conducted in this simulation process.

126

Cell: 1 pg, 1.43 x 0.73 x 0.73
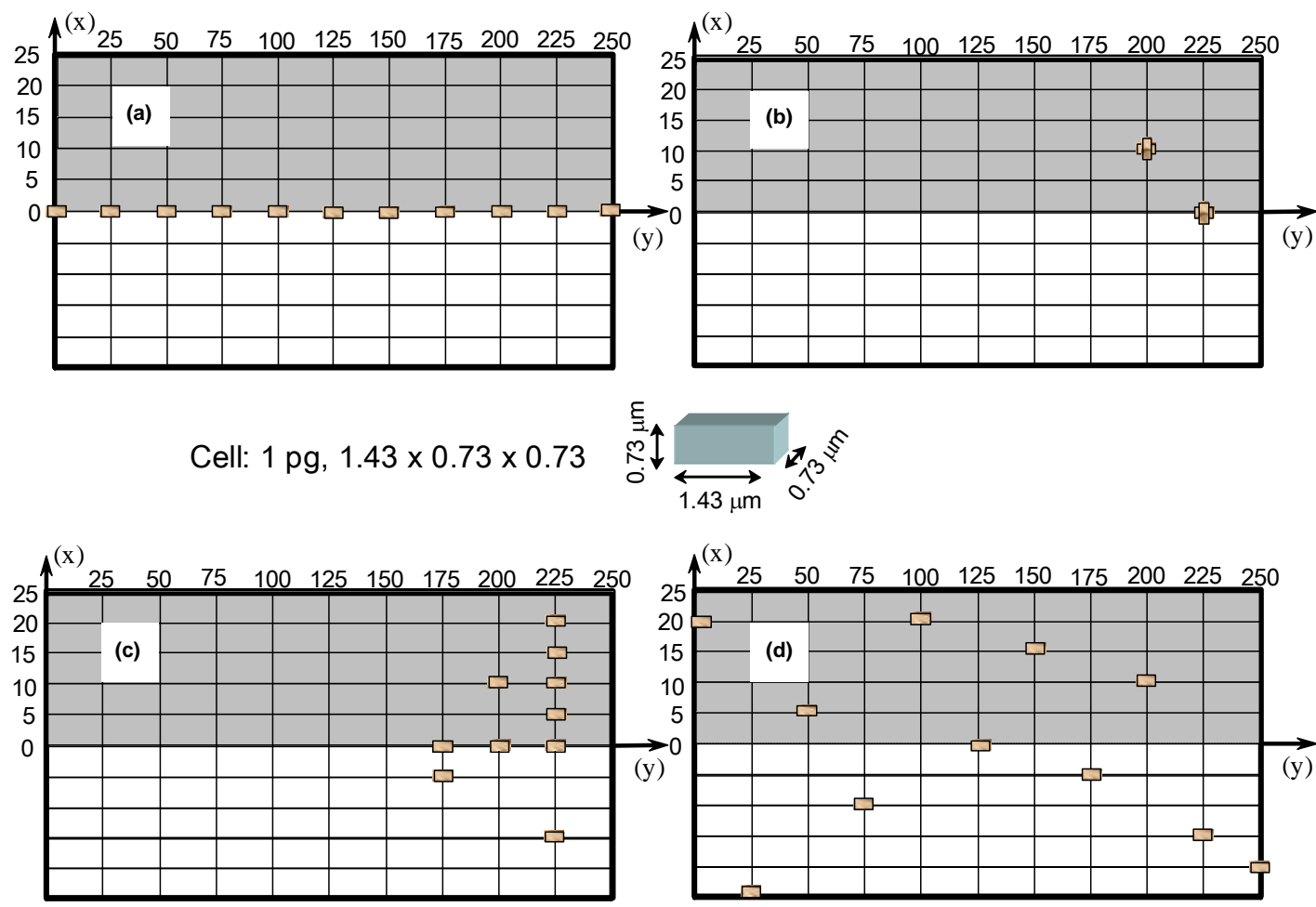
Fig. 5-34   Schematic diagram of the mass loaded on a sensor (250 µm x 50 µm) surface.
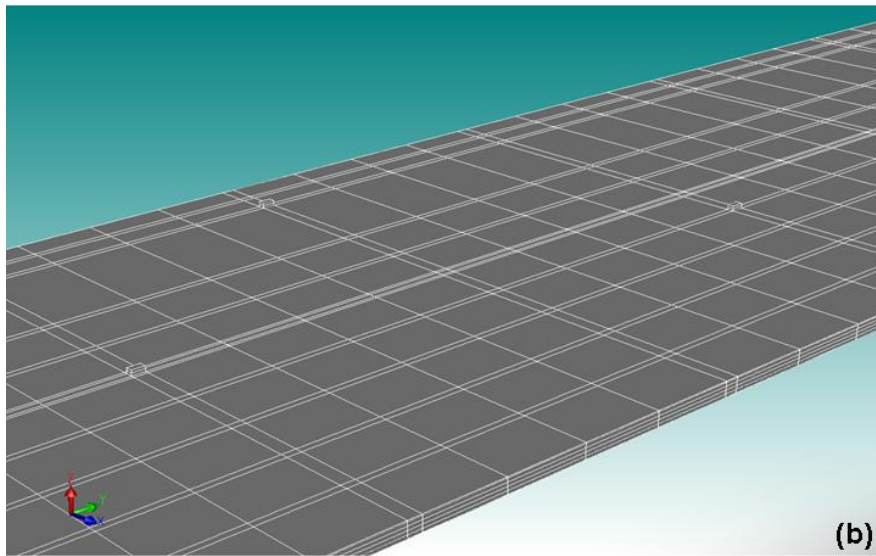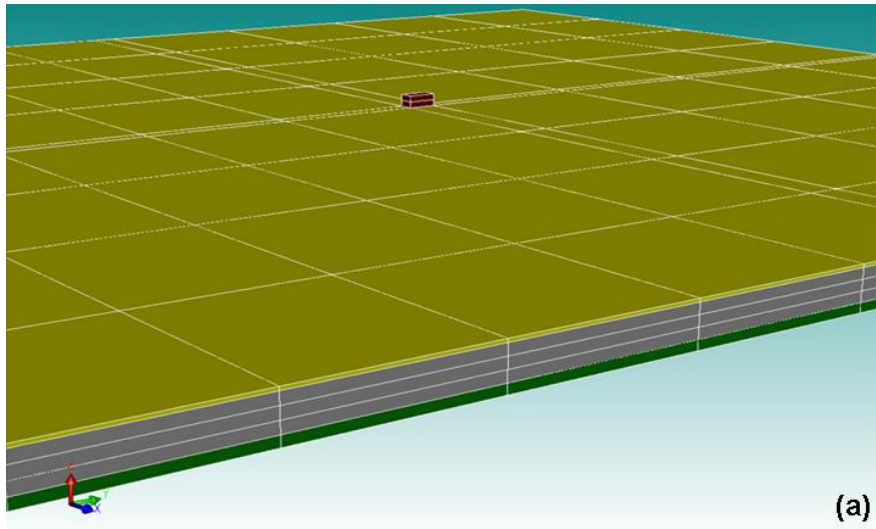
Fig. 5-35 Model meshing results for (a) a single cell and (b) multiple cells on a sensor.

5.2.3.1.   Results of Resonant Frequency Change Due to a Single Cell Attachment

A simulated single *E. Coli O157:H17* cell was attached to the sensor surface at the central line (along the y axis) at different locations with the same orientation as shown in Fig. 5-34 (a). The resonant frequency shifts of the first resonant state (sensitivity in this case for the mass is a unit) for a single bacterium mass with its location along the longitudinal direction are shown in Fig. 5-36 for sensors made in cantilever, bridge and beam configurations. It is clear that in all three cases the frequency change for a concentrated mass is a function of the location along the central axis. These results agree with experimental findings on the freestanding beams shown in Fig. 5-32. When these structures resonate in their first mode, the deformation is different depending on location as discussed in section 2. Here, the largest deformation occurs at the free ends for a cantilever or freestanding beam, while the largest deformation occurs at the center point of a fix-fix ended bridge, and no deformation occurs at the fixed ends of a cantilever or bridge and the middle of a freestanding beam. The positions of maximum deformation on each structure correspond exactly to the largest frequency shift in each case. The ability, then, to detect the attachment of a single cell will depend on whether it attaches to the areas where deformation occurs during resonance. For example, the largest frequency change on a cantilever of dimensions used in the simulations can be as high as 42.5Hz at the tip of the free end area but is close to zero if the mass is located near the fixed end. At the center of the cantilever, almost half of the largest change in value, about 21 Hz is possible. Only when the mass location is 125μm or further away from the fixed end, can the sensitivity reach the criteria for detecting a single bacterium as discussed in section 3.2. The average frequency shift is 21.3 Hz for the eleven positions investigated in the

simulations. In fact, the average value can be obtained by averaging the integrated area of each curve. It is noteworthy that the average value of 21.3 obtained by the simulation is slightly lower than the calculated criteria (25 Hz/pg). This may be a result of employing three layers in the structure and a slightly larger size (250 µm x 50 µm x 1.46 µm) in the simulation. In the calculation, the size of 242 µm x 48 µm x 1.0 µm with a single magnetostrictive layer was determined as shown in Table 4-3. Finally, it should also be noted that in Equation 3-6 of section 3.2.2, we assumed the attached cell mass is evenly distributed on the sensor surface. In reality, it is a concentrated point mass and cannot be considered an even distribution.
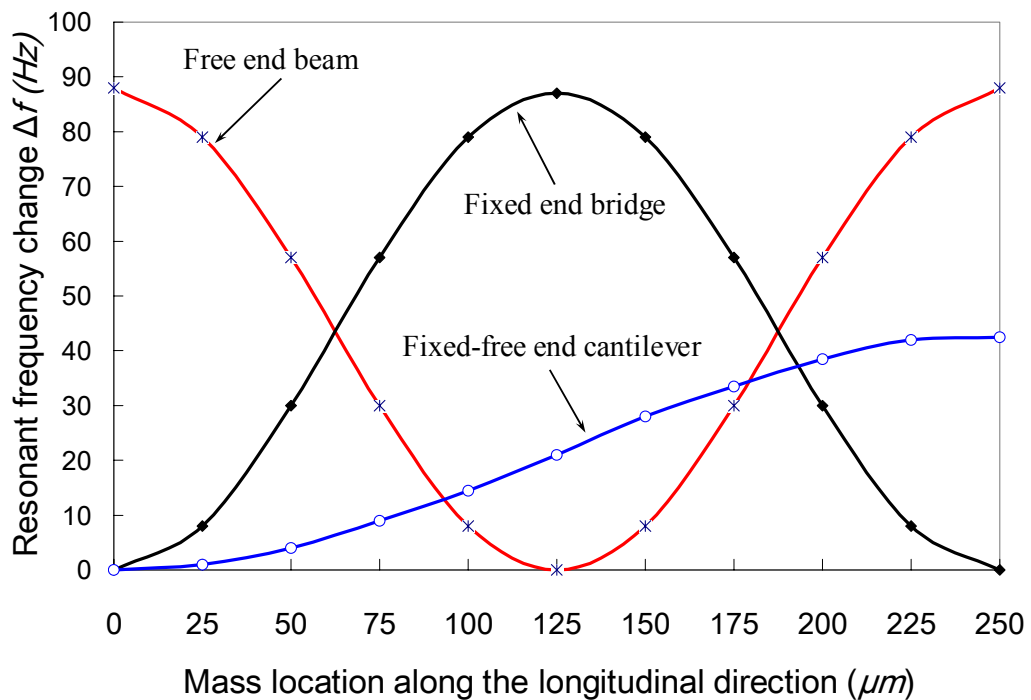
Fig. 5-36 Frequency shift of various structured sensors (sensitivity in this case) as a function of cell location along the central line

5.2.3.2.   Influence of Different Orientations of the Asymmetrical Cells

Simulations were conducted to assess whether cell orientation influences the resonant frequency shift. Here orientation means the long axis of the cell is parallel to the long axis of the sensor or perpendicular to it. This may cause some change in the sensor's behavior, but it is expected to be negligible. Figs. 5-37 and 5-38 illustrate these two orientations at position (x = 0, y = 225). The positions tested are (x = 0, y = 225) and (x = 10, y = 200) as shown in Fig. 5-34 (b). Simulation results indicated that for all three structures there was no effective change in resonant frequency between the orientations at different locations.
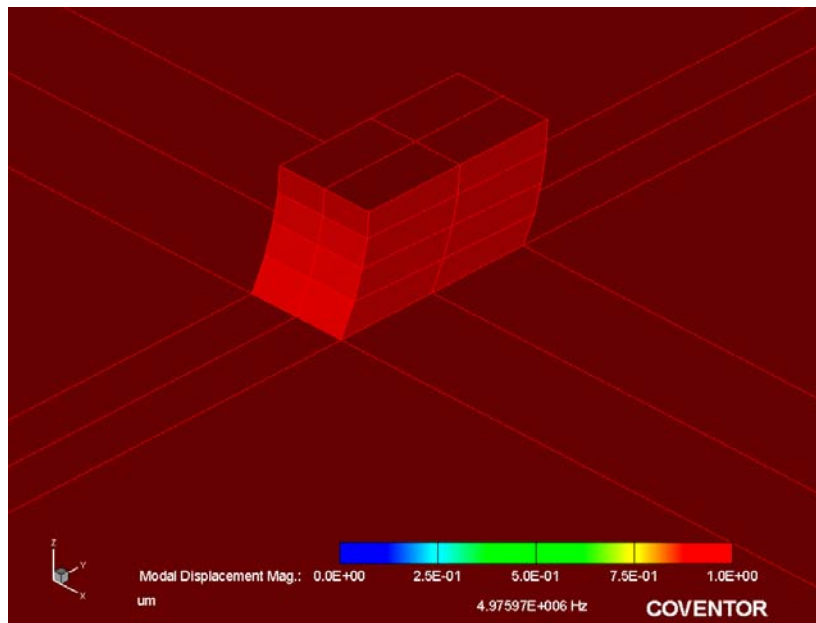
Fig. 5-37 An *E. Coli* cell orientated along the longitudinal axis at (x = 0, y = 225).
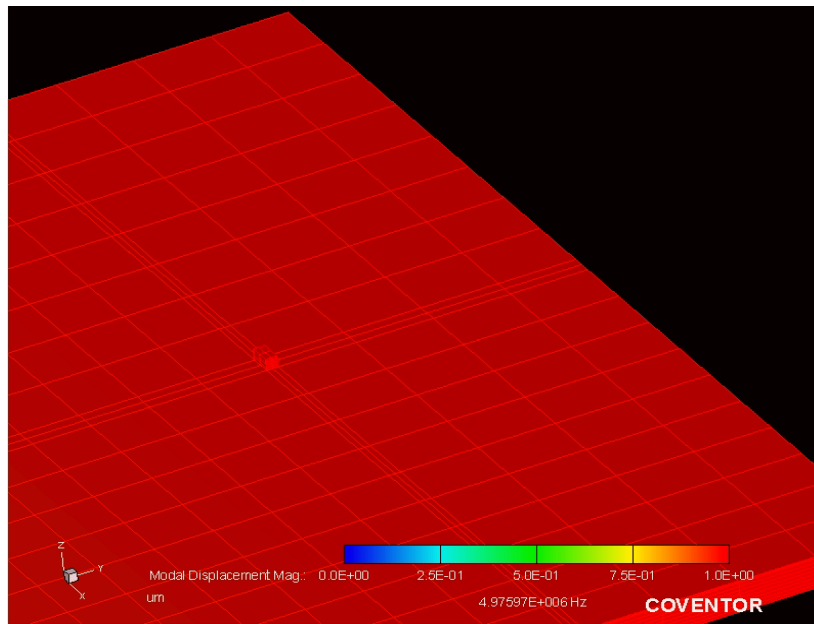
Fig. 5-38 An *E. Coli* orientated perpendicular to the longitudinal axis at (x = 0, y = 225).

5.2.3.3.   Influence of Off-Centerline Attachment

The influence of single mass attachments not on the centerline axis of the sensors was also investigated by numerical simulation. Fig. 5-39 illustrates an attached cell located at x = 20, y = 225, (see Fig. 5-34 c), on a cantilever, where the scale indicates displacement magnitude along the long axis of the device. The resonant frequency shift for this position was identical to the shift at position x = 0, y = 225 as shown in Fig. 5-37.
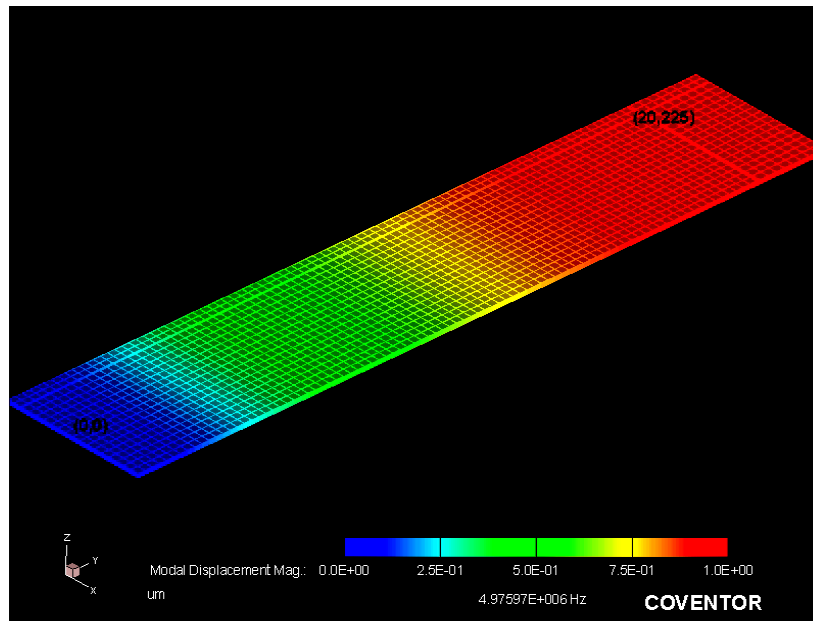
Fig. 5-39 Simulation results of an *E. Coli* cell orientated parallel to the longitudinal axis at (x = 20, y = 225).

Fig. 5-40 is the 3D plot of the simulated frequency change as a function of cell location on a cantilever surface. The resonant frequency change due to a single cell attachment was clearly longitudinal location dependent. The data for the freestanding beam and bridge are shown in Figs. 5-41 and 5-42 respectively and exhibit the same findings as the cantilever. Simulation results for all off-axis positions for the three structures indicated that resonant frequency shift was equivalent to the on-axis result. Thus, the shift is independent of position along the lateral axis direction in all cases. These results confirmed the experimental data presented in section 5.2.2, table 5-7, test #1 and #2 in particular. In these tests when the glass beads were attached in the same location at the longitudinal axis but a different location in the lateral axis, no significant frequency change resulted.

133
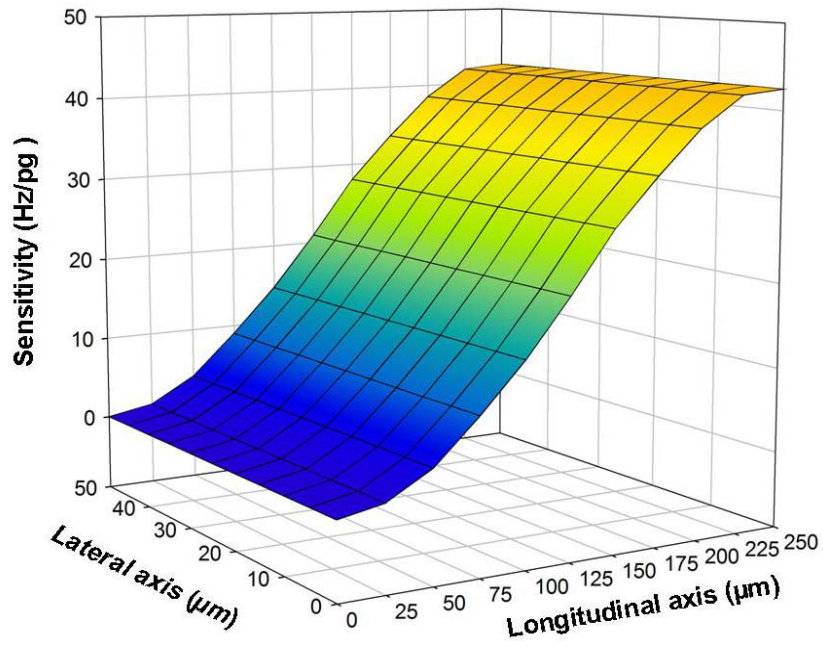
Fig. 5-40 Sensitivity of cantilever to biomolecule distribution on the surface.
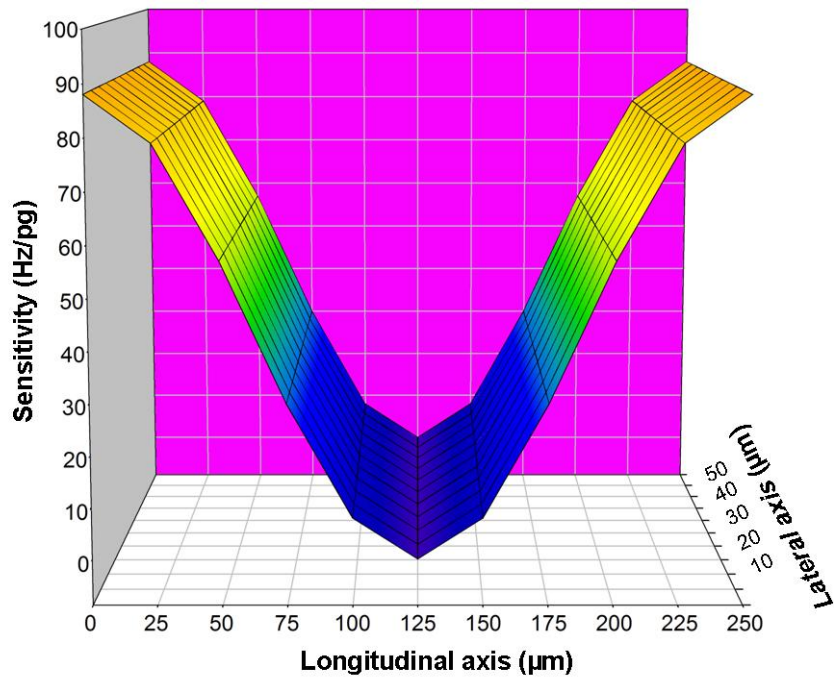
Fig. 5-41 Sensitivity of beam to biomolecule distribution on the surface.
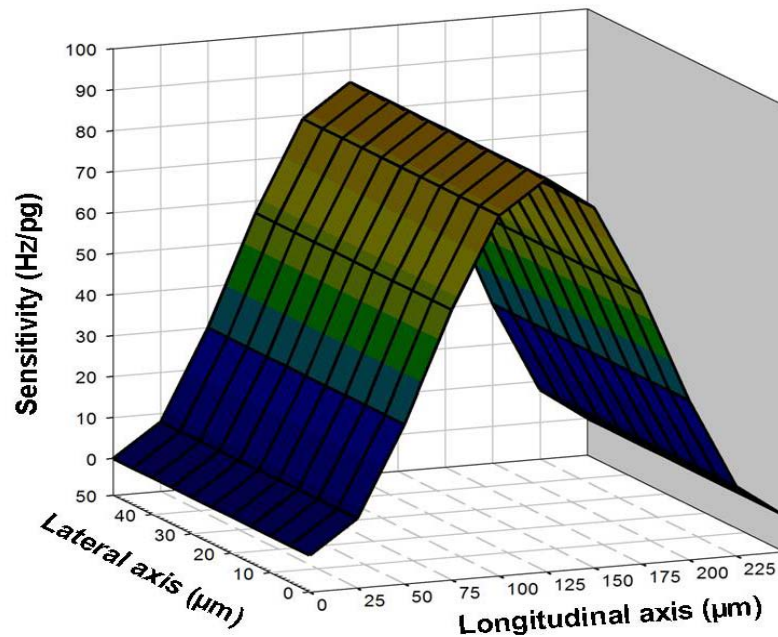
Fig. 5-42 Sensitivity of bridge to biomolecule distribution on the surface.

5.2.3.4. Influence of Randomly Attached Multiple Masses

A simulation analysis was carried out to investigate the influence of multiple mass attachments to each structure. Eleven positions were chosen at random, (see Fig. 5-34 d). Identical positions were used for all three structures and the frequency shifts were determined. The results are given in Table 5-8. The freestanding beam and bridge exhibited higher sensitivity, which can be explained by their higher resonant frequencies. When the beam and the bridge were compared, the beam had a higher sensitivity. However, theoretically, they should have the same sensitivity. This is likely due to one neutral position only on a freestanding beam, but two neutral positions on a bridge. Mass loaded at a location where it is neutral position has less sensitivity.

135

In comparing the cumulative frequency shift with the sum of frequency shifts for each individual position, it is interesting to note that they are nearly equivalent for all three structures, (see Table 5-8). Referring to Equations (2-21), (2-23) and (2-25), one can see that:

- The total resonant frequency decrease (233 Hz) as a result of eleven biomolecules attached on a cantilever surface is less than half the value of beam, but more than half the value of bridge with the same loads. It does not follow the theoretical prediction that cantilevers possess half the sensitivity of either bridge or beam.

- The total resonant frequency change (524 Hz) for eleven cells on a freestanding beam was higher than that for fix-fix ended bridge, due to more positions near the free end of the beam where there is higher sensitivity.

- Mass located at the middle of a freestanding beam may not be detectable, however, any mass located on a cantilever or bridge can be detected since there are no neutral positions on these sensors expect at the fixed ends where no deformations occur during vibration.

Even though on average the freestanding beam and bridge should yield the same performance for a given random attachment of multiple cells, in reality the bridge may have some out-of-plane deformation that would reduce its mass sensitivity. Furthermore, it would become more susceptible to dampening, as the out-of-plane displacement would push against the medium such as air, water, etc. Comparing the advantages and drawbacks of sensors made in different structures, the forms of bridge and cantilever

show that they are the preferred structure for detection of biological cell. Not only they can detect a mass anywhere on the surface, but they can also be integrated into a chip that can greatly reduce the problem of handling the device for end users.

Table 5-8 Summary of simulation results of frequency changes and sensitivities for the three types of sensors in response to *E Coli O157* cells bonded onto a (250 μm x 5 μm x 5 μm) sensor's surface

	Co-responses of eleven (11) E. Coli (Hz)	Sum of eleven (11) individual E. Coli (Hz)	Sensitivity (Hz/pg)
Cantilever	233	234	21.2
Bridge	435	438	39.5
Beam	524	524	47.6

5.3. Summary

The benefit of using a magnetostrictive sensor to measure the thin film Young's modulus was demonstrated. Such a technique offers a cost-effective, user-friendly and non-destructive test of thin film properties. The improved methodology of determining thin film Young's modulus by assuming film density being equivalent to bulk density significantly reduced the amount of error associated with the measurement. Magnetostrictive sensors respond differently to different thin film materials, and the

response depends on the combination of relative density and relative modulus change for the sensor and film composite. The same follows for the Q-factor.

The Young's modulus of Au film determined through the different methods, e.g. measuring the mass and assumed film density, is rather close each other. The results were also confirmed using the MDE technique. In addition, both simulation and experimentation determined the Au and Cu films' moduli are in good agreement. This longitudinal vibration mode technique showed less relative error than the transverse vibration mode for determining the thin film elastic modulus.

Glass beads were employed to simulate the attachment of a concentrated mass on sensors that were constructed as freestanding beams. For single bead attachments, the largest change was observed when the concentrated mass was loaded at the free end of the sensor, while no change in the resonant frequency occurred when it was attached to the middle of the sensor ($x = L/2$), the natural position of the free-free ended beam. The bead position was mapped out as a function of position on the sensor surface. Additionally, the influence of multiple mass concentrations was found to shift the neutral position of the beam due to different acoustic wave speeds on either side of the beam. It was determined then that single mass attachments would be difficult to discern from multiple one unless the capture areas were concentrated near the free ends of the beam.

Simulation results indicated that the sensor response to the attachment of a single cell/spore is also dependent on the location of the mass along the longitudinal axis only, but not the lateral axis. Cell orientation does not affect the sensors' response or sensitivity. The resonant frequency change for multiple biomolecules bonded on the sensor surface is equivalent to the value of the sum of the frequency changes induced in each individual

case. In the simulation, the freestanding beam showed higher sensitivity than bridge-structured sensors, but the mass located at the neutral position of a freestanding beam sensor will not be detectable. This drawback does not apply to a cantilever- or a bridge-structured sensor.

6.   DEPOSITION OF MAGNETOSTRICTIVE THIN FILM MATERIAL AND CHARACTERIZATION OF MICROFABRICATED MICROSCALE SENSORS

The operating principle of magnetostrictive sensors and their potential applications in the detection of biological species has been discussed in the preceding sections. From the results, it was clear that to improve the sensitivity for detecting very small quantities of a species, it is essential to reduce the sensor's mass (reduce its size relative to the biological species) and to increase the sensor's resonant frequency. To this end, it is desirable to reduce the sensor's size into the microscale size range. Thus, the sensors must be constructed from thin films of magnetostrictive material. Depositing these thin films as well as the microfabrication processes to machine them become critical factors in the sensors' performance. This section reports on investigating the optimum parameters for sputter deposition of Metglas 2826 MB magnetostrictive thin films, their micro-machining and corresponding characterization and testing as microscale sensors.

6.1.   Magnetostrictive/Magnetoelastic Thin Films

Engineers and scientists have employed magnetic materials in data storage devices for many years. Many applications of magnetic materials and their requirements can be found in Table 6-1 [188]. This study focused on the soft ferromagnetic materials with magnetostrictive properties that can be applied to resonating sensor construction. Giant magnetostrictive materials such as TbFeCo [189]

constituted of rare earth elements (Tb, Sm, Dy) and transition elements (Fe, Ni, Co) have large factors of magnetomechanical coupling. $TbFe_2$ shows the largest positive and $SmFe_2$ the largest negative magnetostriction [190]. As an example, Tb-Fe-Co thin films were studied for force measurement due to their large positive magnetostriction. Some criteria must be taken into account, though, when applying magnetostrictive materials in actuation and sensing devices such as mass sensors. These materials must have low magnetic anisotropy properties, so that noticeable differential responses or significant changes in strain as a result of a small change in the applied field can be obtained. In fact, such strain changes result from the magnetization of magnetostrictive materials under an applied external field. In addition, low to zero coercivity and remanence are essential to ensure that the magnetization process is dominated by moment rotation (switching). Giant magnetostrictive materials can be one of the candidates for mass sensor applications. Fe-Co-Si-B based magnetostrictive thin films can be used as stress sensors or high frequency RF devices [191, 192]. Other magnetic thin film materials including TbDyFe, CoFe, TbFeB, FeNi, CoNiFe, FeBSiC and FeB, have been the subjects of extensive research [193-201]. In most cases, a sputtering process is used for magnetic thin film deposition because sputtering provides more flexible control and better film quality. More information about thin film magnetostrictive materials deposition techniques and their application can be found in the literature [202].

Table 6-1 Magnetic materials and related criteria of their applications [188].

Field of application	Products	Requirements	Materials
Soft Magnet			
Power conversion electrical - mechanical	Motors, Generators, Electromagnets	Large MR Small HC Low losses, small conductivity, low ω	Fe based materials, e.g. Fe + (0.7 - 5)% Si or Fe + (35 - 50)% Co
Power adaptation	Transformers		
Signal transfer	Transformer	Linear M-H curve	Fe +~ 36% (Fe/Ni/Co) ≈ 20/40/40
	Low frequency to 100 kHz	Small conductivity and medium ω	
	High frequency up to 100 kHz	Very small conductivity and high ω	Ni-Zn ferrites
Magnetic field screening	"Mu"-metal	Large dM/dH for H ≈ 0 ideally Mr = 0	Ni/Fe/Cu/Cr ≈ 77/16/5/2
Sensor	Metglas		MetglasTM
Hard Magnet			
Permanent magnets	Loud speaker, Small generators, Small motors, Sensor	Large HC (and MR)	Fe/Co/Ni/Al/Cu ≈ 50/24/14/9/3, SmCo5, Sm2Co17 and Nd2Fe14B
Data storage analog	Video/Audio tapes	Medium Hc and MR, Hysteresis loop as rectangular as possible	NiCo, CuNiFe, CrO2 and Fe2O3
Data storage digital	Ferrite core memory, Drum		
	Hard/Floppy disc		
	Bubble memory	Special domain structure	Gd3Ga5O12
Specialties			
Quantum devices	GMR reading head	Special spin structure in multilayered materials	
	MRAM		

6.2.　Introduction to Physical Vapor Deposition and Sputter Deposition Technology

Physical Vapor Deposition (PVD), the counterpart of Chemical Vapor Deposition (CVD) is a widely employed thin film deposition process for many applications including surface coating for wear resist [203, 204] and decoration, optical coatings on lenses, thin film capacitor/resistors, metallization for microelectronic interconnections, packaging, and so on [205-208]. PVD processes are dominated by evaporation and sputter processes. Other PVD processes includes laser ablation and molecular beam epitaxy (MBE) which are used for the deposition of complex compound materials or high melting point materials. The sputter process is often preferred over evaporation in many applications because of its better step coverage, broader choice of materials, and better adhesion to the substrate. In addition, the sputter process enables deposited films to have the same chemical composition as the target source, which is the primary reason why sputtering is widely employed for metal alloy thin film deposition. Although the various components in the alloy can exhibit quite different sputtering yields, after a certain period of time the components with the higher sputtering rates are preferentially sputtered until the target surface becomes enriched in the other components and a so-called "steady state" surface composition is reached. In contrast, in evaporation deposition, source material is melted and evaporated by either thermal or electron beam heating. Due to the varying melting temperatures of the elements in an alloy, the thin film material subsequently loses its deposit stoichiometry. However, the use of a target material in sputter processing is remarkably low in comparison with the use of a target material in evaporation deposition process. Table 6-2 is the comparison of evaporation and sputter techniques from the book

of "Fundamentals of Microfabrication-The Science and Miniaturization" [206], where more details on the sputtering process in thin film deposition can be found.

Table 6-2 Comparison of evaporation and sputtering techniques [206].

	Evaporation	Sputtering
Rate	Thousand atomic layer per second (e.g. 0.5 µm *for* Al)	One atomic layer per second
Choice of materials	limited	Almost unlimited
Purity	Better (no gas inclusion, very high vacuum)	Possibility of incorporating impurities (low to medium vacuum range)
Substrate heating	Very low	Unless magnetron is used substrate heating can be substantial
Surface damage	Very low, with e-beam, x-ray damage possible	Ionic bombardment damage
In situ clean	Not an option	Easily done by sputtering etch
Alloy composition stoichiometry	Little or no control	Alloy composition can be tightly controlled
X-ray damage	Only with e-beam	Radiation and particle damage is possible
Change in source material	Easy	Expensive
Decomposition of material	High	Low
Scaling up	Difficult	Good
Uniformity	Difficult	Easy over large area
Capital equipment	Low cost	More expensive
Number of deposition	One deposition per charge	Many depositions can be carried out per target
Thickness control	Not easy to control	Several control possible
Adhesion	Often poor	Excellent
Shadowing effect	Large	Small
Film properties (e.g. grain size, step coverage)	Difficult to control	Controlled by bias, pressure and substrate heating

During sputtering process, a high electrical potential is applied between two parallel plates, ionization will take place if an inert gas (e.g. Ar) is introduced. The ionized Ar (Ar^+) is accelerated in the applied electrical field and gains high momentum energy. When the energized Ar ions are shot onto the target surface, the atoms of the target material are ejected from the target by bombardment and condensed onto the substrate, as depicted in Fig. 6-1, causing a thin film to be deposited. In modern sputter systems, the substrate can be plasma cleaned before the film deposition, which enhances the adhesion of the film on the substrate. The film properties can be modified by applying bias or heat during the deposition as well. High to ultra-high vacuum is often required for improved film quality. To do so, a turbo molecular pump or turbo pump is commonly used to replace the diffusion pump so that a better pumping efficiency and eradication of contamination caused by back stream oil from the diffusion pump can be achieved.

To facilitate higher sputtering yields (eventually higher deposition rate), a magnetron is implanted in the target electrode to confine the electron motion, hence stabilizing the plasma. The magnetron sputter electrode usually consists of a permanent magnetic material as shown in Fig. 6-2 (a & b). The magnetic field will restrict the electrons' motion toward the target surface, so that the electrons will not move onto the target surface or the chamber wall as a result of vanishing, which assures high plasma concentration and high sputter yields. The disadvantage of the magnetron sputter technique is that the efficiency of target usage is low.
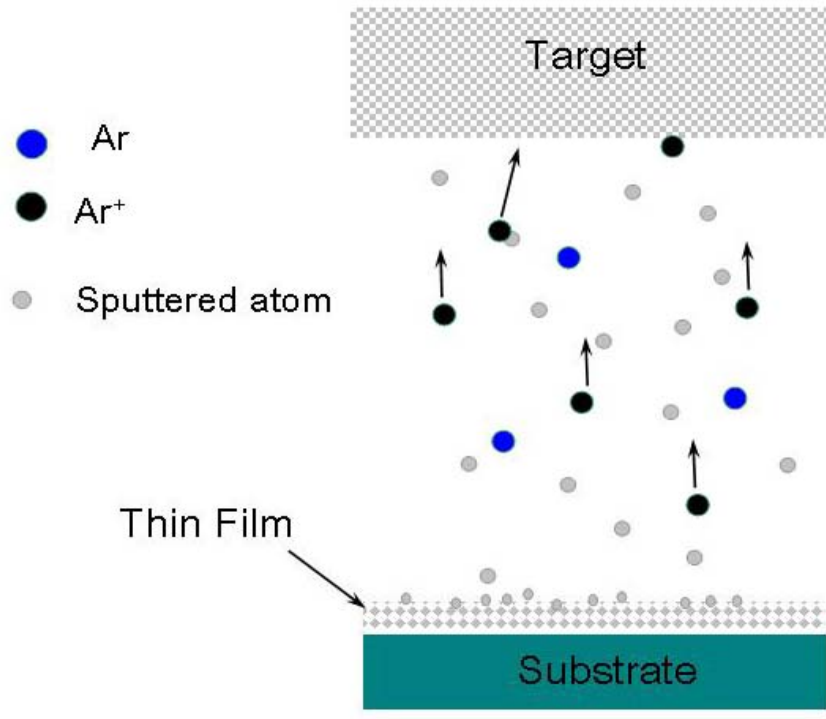
Fig. 6-1   Schematic depiction of sputter deposition process.
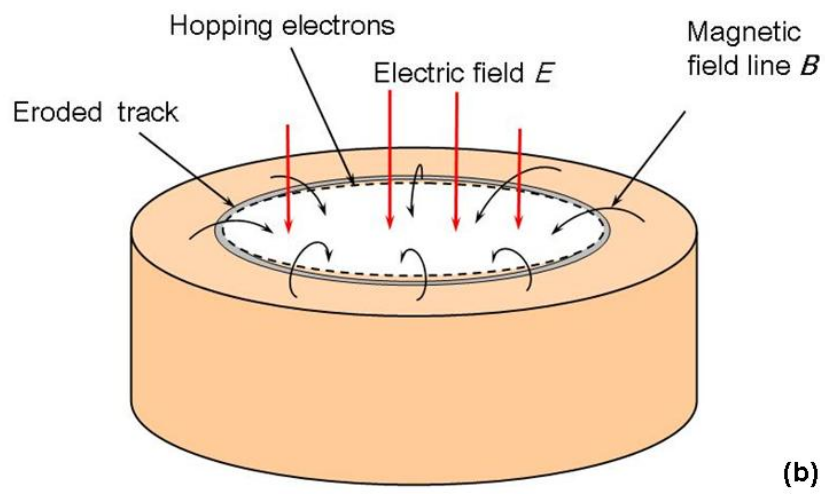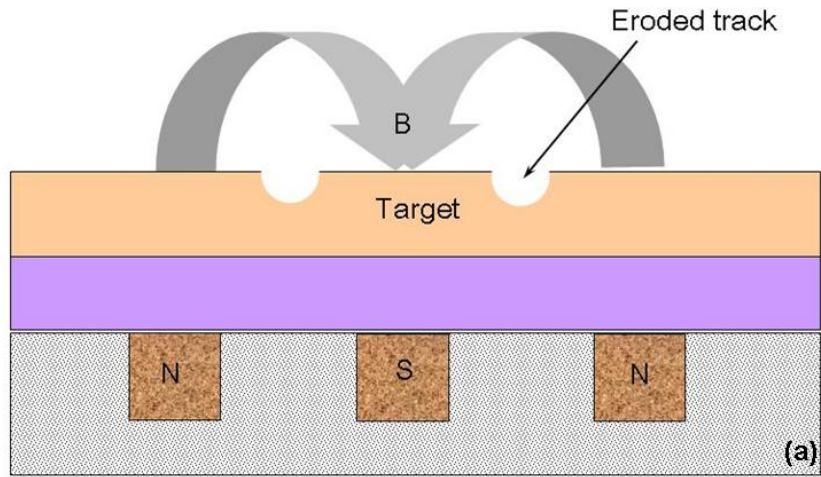
Fig. 6-2   Schematics of (a) a target assembly and (b) electrical and magnetic fields'
orientation related to a target.

In the case of sputtering magnetic materials, e.g. Ni, Fe, Co, and Metglas, the magnetic field integrated in the cathode must be stronger than the one for general nonmagnetic materials, in order to overcome the magnetic field effect of the target materials. Previous studies of sputtering Metglas 2605 SC strip material showed the facility of sputtering Metglas strip to form a thin film on a substrate [209].

In the sputtering deposition process, RF (radio frequency) and DC (direct current) are the two options for power supply. RF power is generally used for non-conductive targets, while DC is used for conductive target materials. RF power is delivered by a capacitively coupling discharge process, in which the total ion and electron flow to the target surface during an RF cycling must be zero. A negative self bias with respect to the plasma potential thus develops. Since the mobility of an electron and an ion, e. g. Ar, is different, a much larger current is drawn when the electrode is positive with respect to the floating potential than when it is negative. In order to achieve net zero current, it is essential to develop a DC bias so that the average potential is negative, as if there were a negative DC connecting to the target (cathode). Therefore, the DC bias is a measure of the RF sputter process. In the case of DC sputtering, as a DC is supplied to the target (cathode), the plasma discharge process is simple. More details on RF and DC plasma processes can be found in many books [210, 211].

Sputtering deposition is an intricate process, in which collisions occur between the sputtered atoms, ionized sputtering ions, neutral Ar species, radicals and electrons. Interactions take place between electrons, ions and radicals. The applied DC or RF power, the vacuum pressure, substrate temperature and bias are important factors that may affect the plasma discharge, sputter yield, and thin film properties. These parameters often

influence each other. For example, at higher vacuum pressure, many Ar molecules are present resulting in more collisions (hence, shorter mean free path). The frequent momentum transfer causes loss of energy of the Ar ion, which results in low sputter yield; consequently, the deposition rate is low. Moreover, the sputtered atom will suffer from many collisions that cause loss of the line-of-sight characteristic and energy as well. The overall effects will produce a different property of thin film. The collision of electrons also influences the electrical breakdown. The breakdown potential for a given sputter system is a function of the product of pressure (p) and electrodes' separation distance (d) as described in the Paschen curve in Fig. 6-3 [210]. One can see if the applied electrical potential is lower than the breakdown curve; under particular circumstances of pd value the plasma will not ignite. The product of pressure p and distance d is a critical parameter for the sputtering deposition process, and the minimum breakdown potential occurs at a particular pd value.

A variety of sputtering deposition processes are possible, including co-sputtering and reactive sputtering. Co-sputtering is a technique in which two or more target materials are simultaneously sputtered to produce an alloy or mixture of multi component film. For example, this process was used in deposition of the AuSn solder [212] and many others. However, exact control of the composition is often difficult, especially deposition with three and more elements such as Metglas 2826 MB that has four elements. This is not only due to its complicated control but also to the lack of system capability. In this case, direct sputtering from an alloyed target such as a Metglas strip to produce the similar compositional film materials is the primary choice. Fig. 6-4 shows the system used in this research (the plasma is on in the photo). Reactive sputtering deposition process is usually

by introduction of a reactive gas such as N_2, O_2, or CH_4 during the sputtering process. These reactive gases will decompose and react with the sputtered atoms, for example Ti [203, 204, 213, 214].
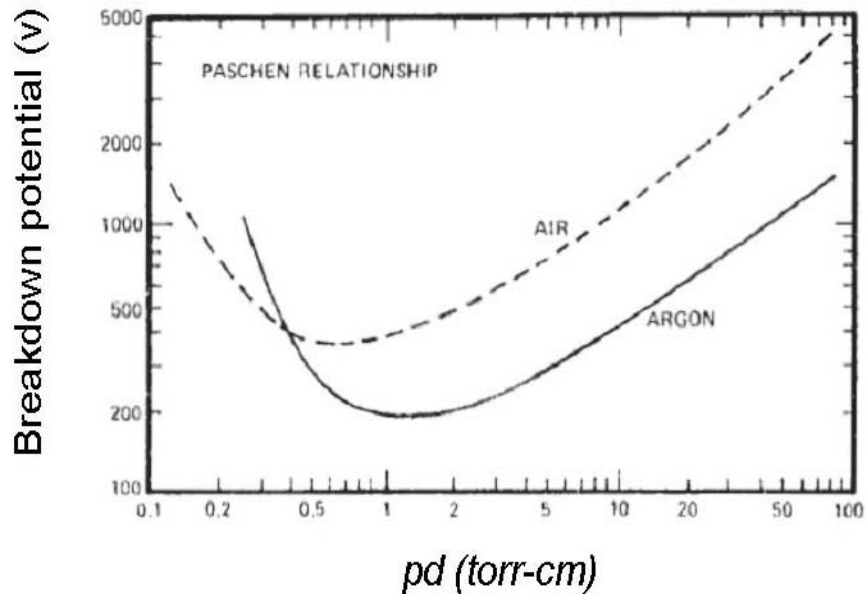
Fig. 6-3   Paschen curve for breakdown potential between parallel electrodes [210].

Fig. 6-4   Photo showing the sputter system with plasma on.

In this study, we deposited magnetostrictive thin film via direct sputtering Metglas 2826 MB ribbon. The study will focus on the following areas:

- Development of the process for deposition of magnetostrictive thin film material via directly sputtering Metglas 2826 MB.

- Characterization of magnetostrictive thin films.

- Fabrication of microscale magnetostrictive sensors with sputtering deposited magnetostrictive thin film, and

- Characterizations and testing the microfabricated sensors.

6.3.   Experimental Details

The Metglas 2826 MB strip with a composition $Fe_{40}Ni_{38}Mo_4B_{18}$ is a commercially available product. It has a standard ribbon size with widths of 12 mm and 50 mm, and a thickness of 28 microns. Metglas ribbon is made through rapid solidification and a thin thickness of the amorphous metal glass is therefore the typical product [9]. In order to produce a similar composition in thin film form, sputter deposition as discussed above is often employed. However, a Metglas target with the same composition as the ribbon is not available, and fabrication of a bulk form target has been unattainable by many leading target fabrication companies. In fact, it is not necessary to have a amorphous target to produce an amorphous thin film material, but the process parameter selection and study are of equal importance in deposition of this magnetostrictive thin film material. Our approach is to fashion a target from the commercially available ribbon.

6.3.1. Fabrication of Sputtering Target

A sputter target requires good thermal and electrical conduction when it is mounted onto the sputter cathode, including a Metglas sputter target. Solder, conductive silver paste and conductive adhesives can all be used to bond a Metglas ribbon onto a Cu backing plate. Conductive adhesive is the primary choice since the other two may introduce an air gap between the Metglas ribbon and the backing plate. This improper bonding may cause either poor electrical conduction or poor thermal conduction. The resulting local overheating can burn the target material and shorten a target's lifespan. One may think that using multilayer Metglas ribbon bonded onto the backing plate will make the target last longer. Capacitors, however, may develop between ribbons, and the bonding material may alter composition. Furthermore, as ribbon layers are removed by the energetic ions large pieces of the ribbon may fall and deposit onto the wafer. The criteria for making a Metglas target, therefore, can be summarized as:

- Cu baking plate should be smooth and thin enough to assure good thermal and electrical conducting,

- Bonding material should have high electrical and thermal conductivities plus good adhesion,

- Single layer of ribbon should be used to avoid compositional and large particle issues.

A 1.5 mm thick Cu backing plate was graded and polished to a near mirror finish, cleaned, and dehydrated before bonding with the Metglas ribbon. The ribbon was cut to the desired shape so as to completely cover the backing plate. The two were bonded

together with a adhesive. The target was subject to 110 $^{\circ}$C baking for 30 minutes to drive out any gases and organics that may have been trapped in the adhesive. Fig. 6-5 shows the erosion of targets surfaces after sputter for different times. The targets A, B and C were DC sputtered with a power of 30 watts and pressure of 5 millitorr for 1.0, 1.5 and 2.0 hours, respectively; the targets were obviously eroded after being sputtered for 2 hours. It was found that with a single ribbon layer a film 0.25 microns thick could be deposited. Thicker films require simultaneous deposition with multiple Metglas targets.
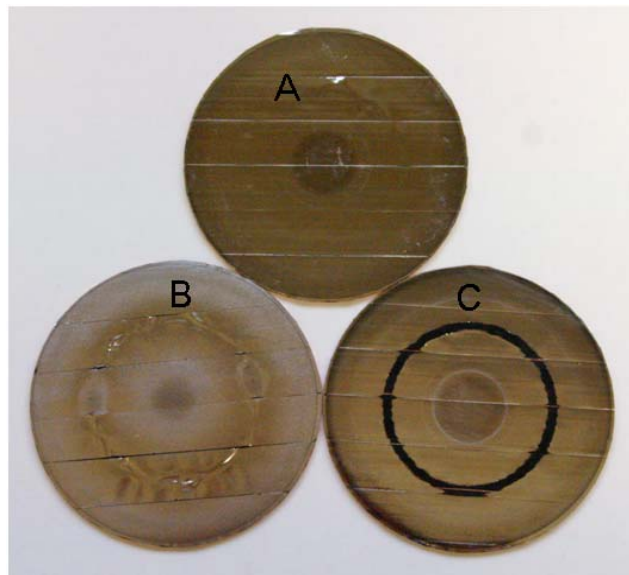
Fig. 6-5   Photo pictures of Metglas targets showing surface erosion after sputtering at different times.

6.3.2.   Design of the Sputter Deposition Process

As a magnetic thin film is sputter deposited on a Si wafer, the process parameters such as pressure, sputter power and substrate heating temperature are the key factors that

may influence the deposition rate and magnetic properties of the film. The deposition processes was conducted in two phases:

- Phase I

Magnetostrictive thin films were deposited at variable pressures ranging from 3 to 20 millitorr with constant sputter power at 30 watts.

- Phase II

Magnetostrictive thin films were deposited thorough a DOE (design optimal experiment) involving the sputter power, pressure and substrate heating temperature. The factors and variables are listed in Table 6-3.

The parameters for experiments were arranged according to the $L_4(2^3)$ matrix [215] as seen in Table 6-4. The outputs were the deposition rate, magntostrictive properties and microstructure of the films.

Table 6-3 DOE parameters and variables

Level	Sputter power (w)	Sputter pressure (mT)	Substrate heating temperature (setting) (ºC)
level (+1)	30	6	200
level (-1)	15	3	400

Table 6-4 $L_4(2^3)$ matrix for DOE

Expt.	Factors/variables			Outputs
	power	pressure	temperature	
1	-1	-1	-1	Deposit rate Microstructure Magnetic Properties • coerce force • energy loss • others
2	-1	+1	+1	
3	+1	-1	+1	
4	+1	+1	-1	

6.3.3.   Characterization of Magnetostrictive Thin Film

The magnetostrictive thin film thickness was measured by a stylus profilometer, the microstructure was examined by XRD and SEM, and the chemical compositions were analyzed by XPS. The magnetic properties were studied with a Digital Measurement System (DMS) Vibrating Sample Magnetometer (VSM) model 1660 at the Center for Materials for Information Technology, the Department of Physics and Astronomy, the University of Alabama, Tuscaloosa. All samples used for the tests were deposited on a Si wafer coated with a thin silicon nitride film. During the VSM test, the applied magnetic field was oriented parallel to thin film surface.

6.3.4.   Magnetostrictive Thin Film Annealing

Annealing of sputter deposited magnetostrictive thin film was conducted in a vacuum chamber (Isotemp vacuum oven model 281A, Fisher Scientific) at a temperature of 215 ^oC for two hours. The temperature of the chamber was naturally ramped up and cooled. It

typically takes an hour to ramp up from room temperature to 215 $^{\circ}$C. Samples were placed in the vacuumed chamber overnight for cooling to room temperature.

6.3.5. Microfabrication of Magnetostrictive Sensors

Three types of sensors were fabricated by bulk and surface micromachining processes in the Alabama Microelectronics Science and Technology Center (AMSTC) in the Electrical and Computer Engineering Department, Auburn University. Cantilever and bridge sensors were designed in various sizes. The process for fabrication of these types of sensor is relatively complex, and step-by-step procedures are depicted in Fig. 6-6. Note the deposition of SiC as an encapsulating layer to block the Au surfaces where it is not an actively required.

1. Si wafer with 300-500 nm nitride

2. Spin coating PR and patterning

3. PVD magnetostrictive thin film
With thin layer of Au

4. Remove PR and lift off

5. Nitride etch

6. Si wet etch
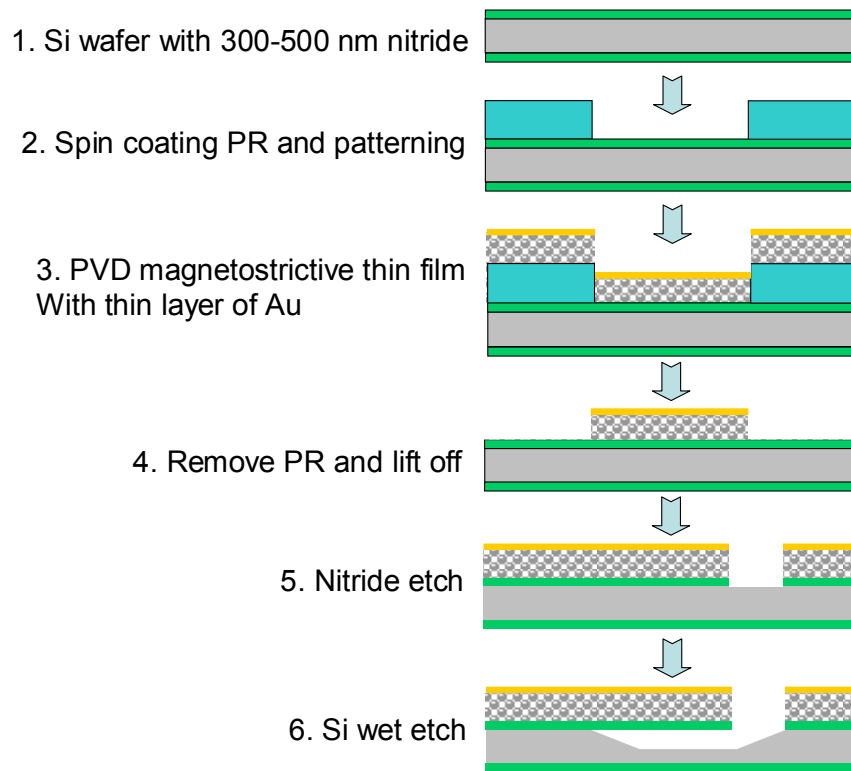
Fig. 6-6   Micromachining process for cantilever sensors (not to scale).

Freestanding beams (particles) were designed with the sizes of 500 μm x100 μm and 250 μm x 50 μm. The basic procedure for microfabrication of these particles is illustrated in Fig. 6-7. The most critical steps in this process are the PR (photoresist) coating and developing. The PR has to be thick enough, and it has to be completely removed where it is required.

Si wafer with 300-500 nm nitride

⬇

Clean and dehydration

⬇

Adhesion promoter application

⬇

Photoresist coating and baking

⬇

UV exposure and PR developing

⬇

Post baking

⬇

Deposition of magnetostrictive thin film

⬇
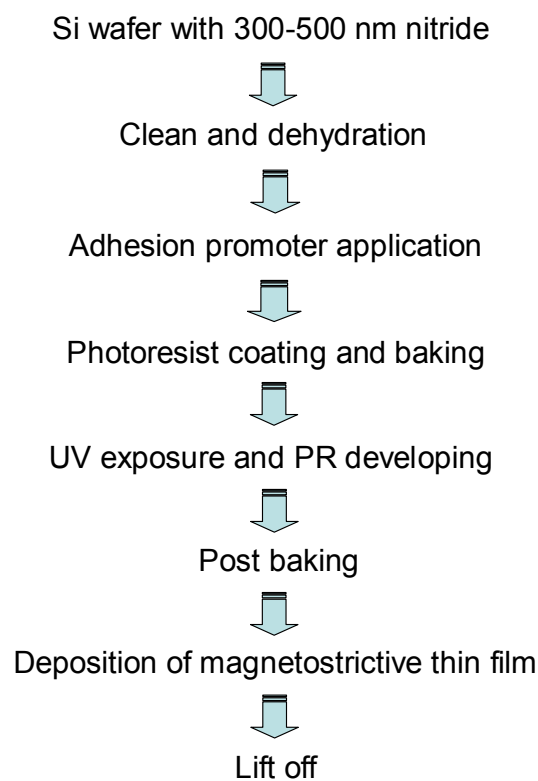
Lift off

Fig. 6-7   Basic procedure for lift-off sensors.

Since the target can only last for 90 minutes under a continuous sputter process, the deposition of the magnetostrictive thin film has to be repeated or performed with multiple targets simultaneously so that thicker film can be obtained. This repeating process

requires breakdown of the vacuum for target changes, which may result in slight oxidation and incoherence of the film.

6.4.   Results and Discussion

6.4.1.   Initial Approach of Deposition of Magnetostrictive Thin Film by Phase I

6.4.1.1.   Deposition Rate

The thin film deposition rate is often affected by the sputtering process parameters; in the process, pressure plays a key role over other parameters. Fig. 6-8 shows the deposition rates of sputtering Metglas as a function of deposition process pressure under a constant DC power of 30 w. The deposition rate increases as the process pressure increases in the high vacuum range, i.e. in the range of pressure less than about 10 millitorr. When the pressure exceeds this critical point, the deposition rate decreases with further increase in the pressure. A similar phenomenon was also observed for sputter deposition of Cr film [216]. The reason for this is that under high vacuum, the number of ionized Ar available is limited, and thus, the number of collisions decreases. Increasing the deposition pressure results in a increase in the number of Ar ions, hence more bombardment and greater sputter yields. However, when the pressure is too high, the collision and scattering of Ar ions dominate, which results in less sputtering efficiency, hence, lower sputter yield and lower deposition rates were observed. The optimum was a process pressure of approximately 10 millitorr.
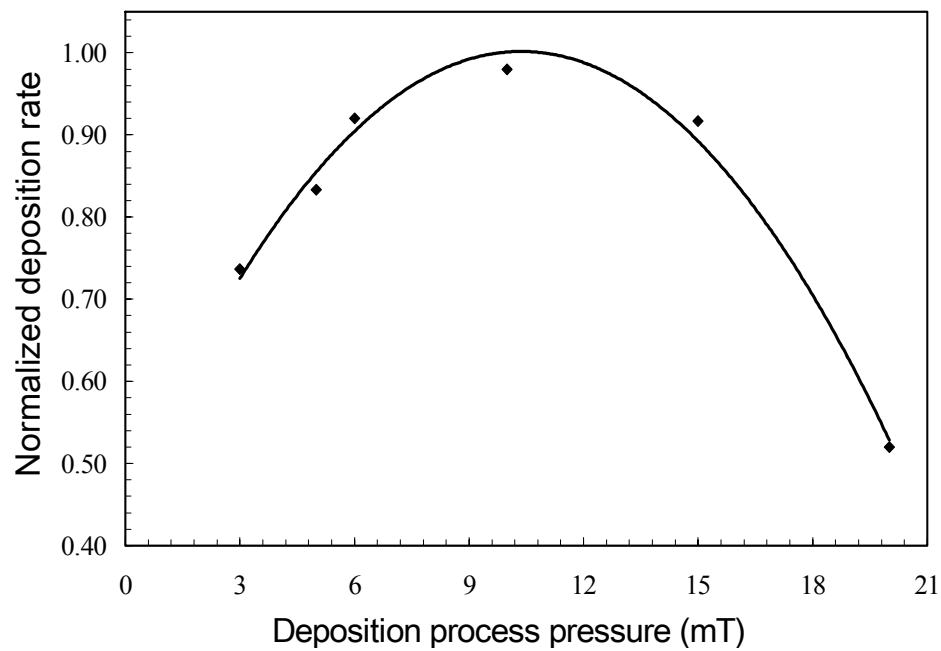
Fig. 6-8   Deposition rate as a function of process pressure change.

6.4.1.2.   Surface Morphology and Crystal Structure of Deposited Magnetostrictive Thin
            Films

Three samples deposited under 5 mT, 10 mT and 20 mT at a constant power of 30 watts were characterized using SEM, XRD and VSM. The surface images of those three samples are shown in Fig. 6-9, note the different magnifications employed in the imaging. It was evident that the surface roughness increases as the process pressure increases. Very fine particles are observed at the pressure of 5 mT. This result may be attributed to the collision and scatter effect. Sputtered atoms have higher energy under lower pressure; consequently, the film exhibits fine and dense particles. Additionally, in a higher vacuum, the higher kinetic energy of sputtered atoms may have
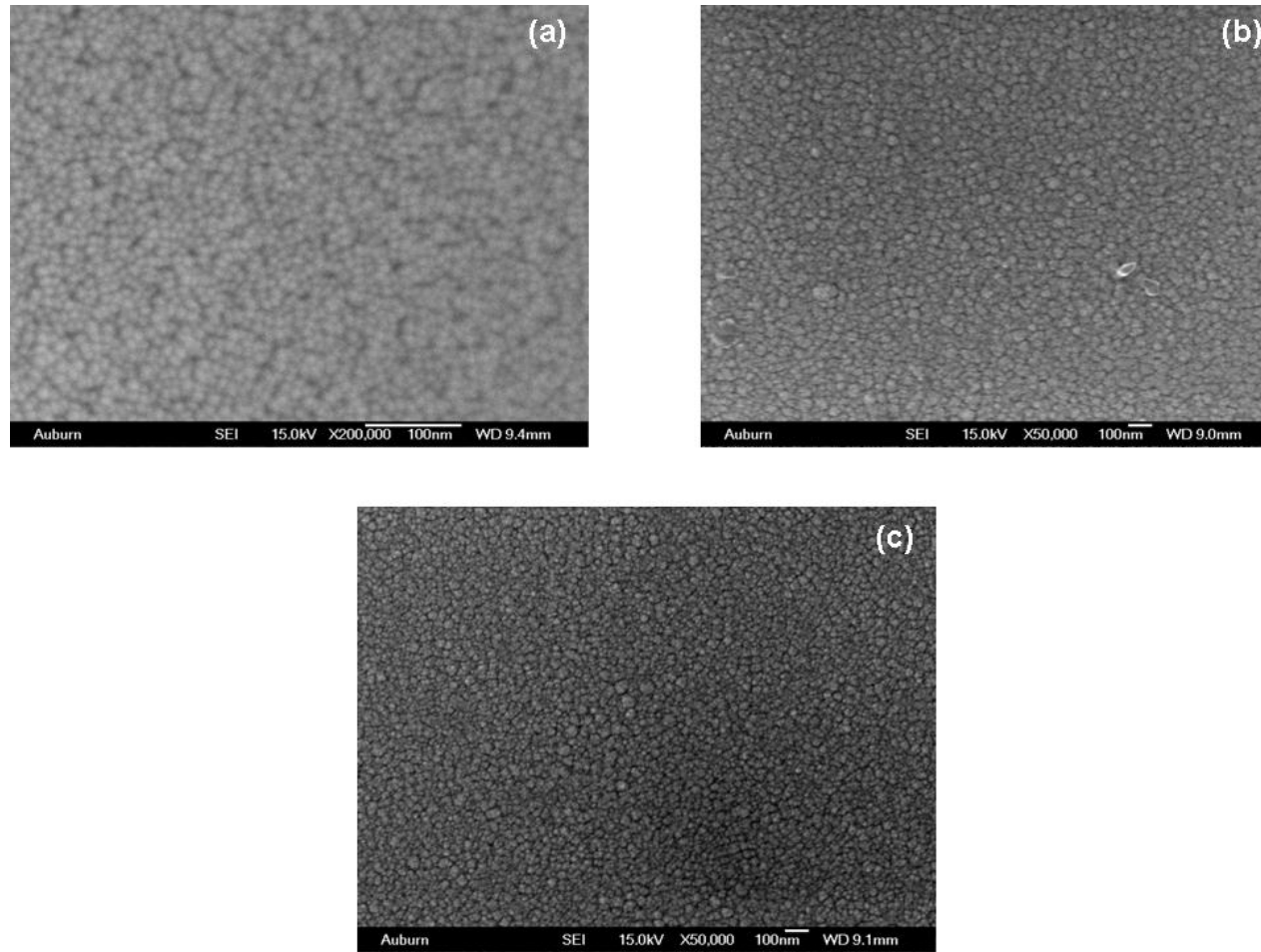
Fig. 6-9   SEM surface images for sputter deposited magnetostrictive thin film under different process pressure, (a) pressure = 5 *mT*, (b) pressure =10 *mT*, and (c) pressure = 20 *mT*. Note the difference in magnification between.

better surface absorption characteristics, which results in fine and smooth morphology. In contrast, in a low vacuum, since the sputtered atoms have low kinetic energy, deposition occurs in large cluster form, thus the film is rough and porous as seen in Fig. 6-9 (b) and (c).

Crystal structure transition was observed with X-ray diffraction of these samples. For the lower pressure (5mT) process, the magnetostrictive film exhibits a non-crystalline or amorphous structure. When the pressure is increased to 10 mT, Bragg reflections indicate that a crystal structure has developed, and the film exhibits crystalline FCC FeNi (111) and single Fe (200) phases. When sputter pressure is at 20 mT, weak Ni(200) and Mo(200) phases are also observed in addition to the FCC FeNi(111) and Fe(200) phases. The grain size of the FCC (FeNi) phase was determined by XRD via the Scherrer equation $B = \dfrac{0.9\lambda}{t\cos\theta}$ [217] (B is the FWHM, full width at half maximum of the broadened diffraction line on the 2θ scale, λ is the wavelength of copper k alpha, and t is the diameter of the crystallites) and was found to be approximately 25 nm and 39 nm for 10 mT and 20 mT, respectively. Fig. 6-10 shows the XRD spectrum of these three magnetostrictive films. This FCC (FeNi) phase was also observed by other researchers when annealing amorphous Metglas ribbon at a temperature over 500 ^{0}C [218] or when the Ni content is higher than 30 at. % [219]. One can see that both the Metglas 2826 MB ribbon and the low pressure sputter process deposited magnetostrictive film are of amorphous structure.
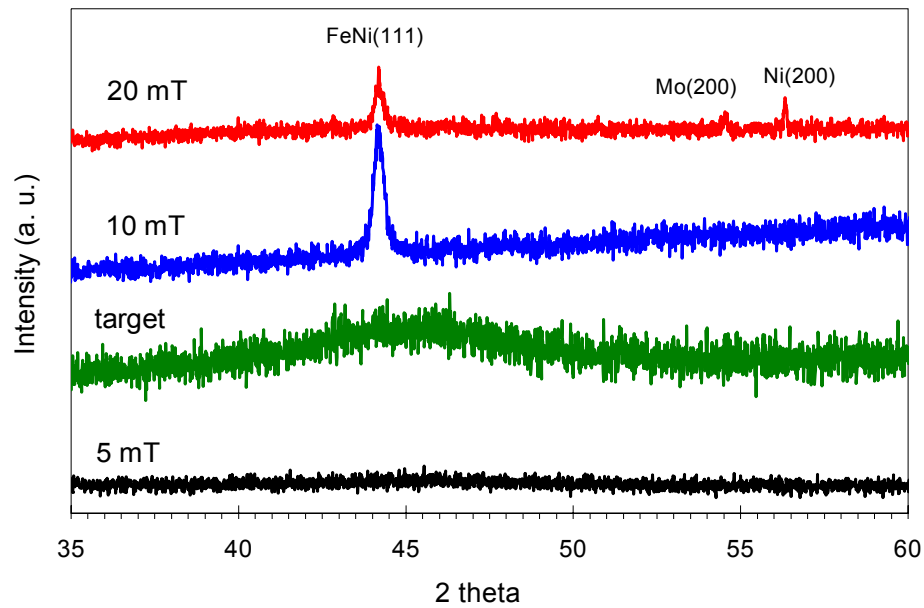
Fig. 6-10 XRD spectra for sputter deposited magnetostrictive films under different pressures.

6.4.1.3. Magnetic Properties of Deposited Magnetostrictive Thin Film

Magnetic properties are often directly related to the crystal structure of the magnetic material as well as grain size. In general, magnetostrictive properties can be improved by reducing the grain size to the nanoscale [220]. The thicknesses of the films deposited at 20 mT, 10 mT and 5 mT were 0.255 μm, 0.33 μm and 0.36 μm, respectively. Fig. 6-11 shows the Vibrating Sample Magnetometer (VSM) results of these films, which indicates that these sputter deposited films exhibited soft ferromagnetic behavior. Magnetic properties of the films show that they developed with a very low to high random uniaxial anisotropy at process pressures from 5 mT to 20 mT, which agreed very well with the random uniaxial anisotropy mode developed by Chi and Alben [221]. Moreover, thin film

163

deposited under 20 mT exhibited a residual stress with tension [222]. The key differences between soft and hard magnetic materials are the existence of large remanence (M_R) and coerce (H_C) of hard magnetic materials as seen in Fig. 6-12. Fig. 6-13 shows the coerce force, saturation force and energy loss change with the process pressure. Note that the energy loss is calculated by integration of the area of the H-M hysteresis loop shown in Fig. 6-11. Two mechanisms can account for the root cause of energy loss. One is the alternating change of magnetic field that induces Eddy currents traveling around in the material and the other is the movement of the domain walls, which require some energy and dominate the hysteretic loss.
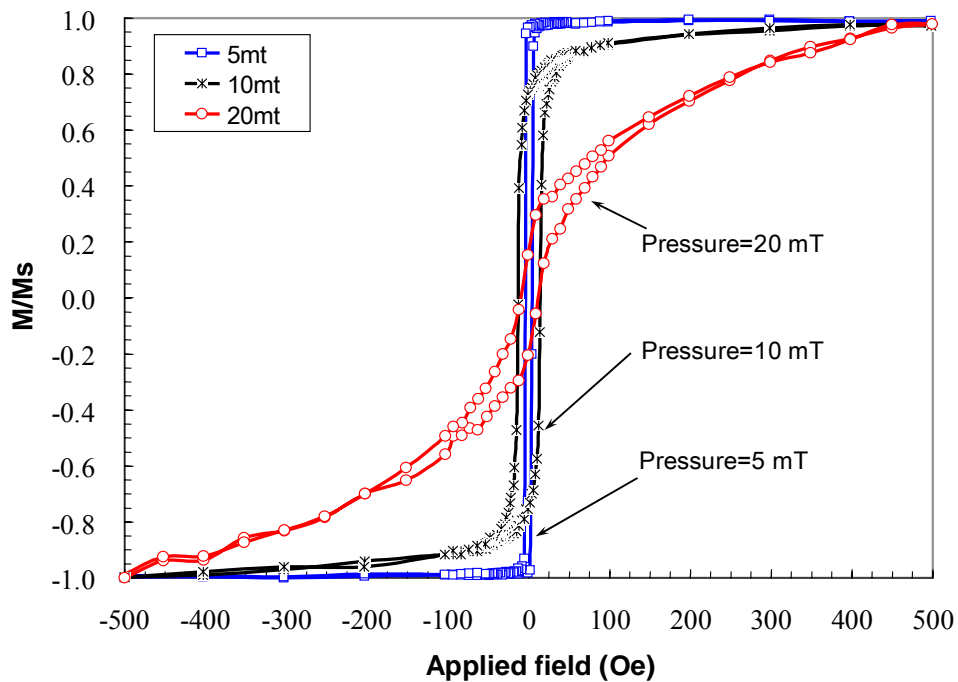
Fig. 6-11 Hysteresis loop for magnetostrictive films deposited under different pressures.
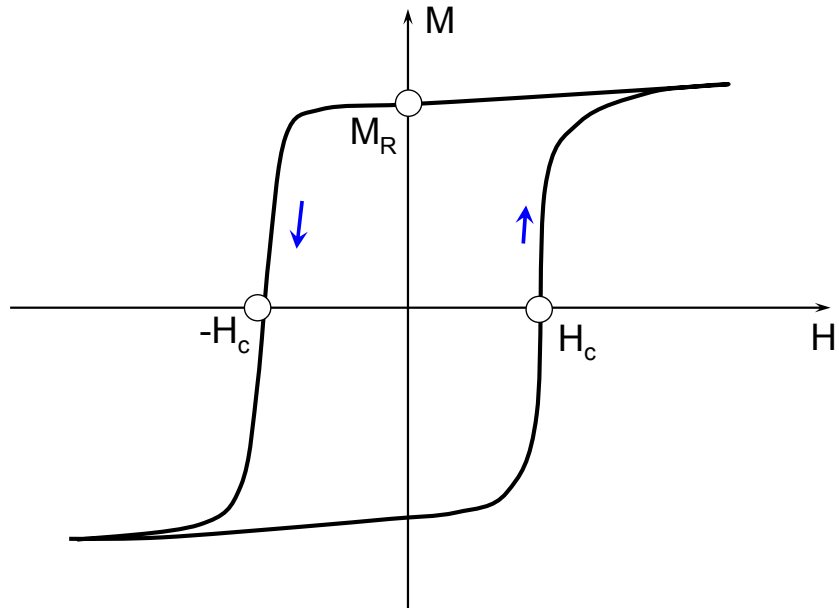
Fig. 6-12 General hysteresis loop of a hard magnetic material.
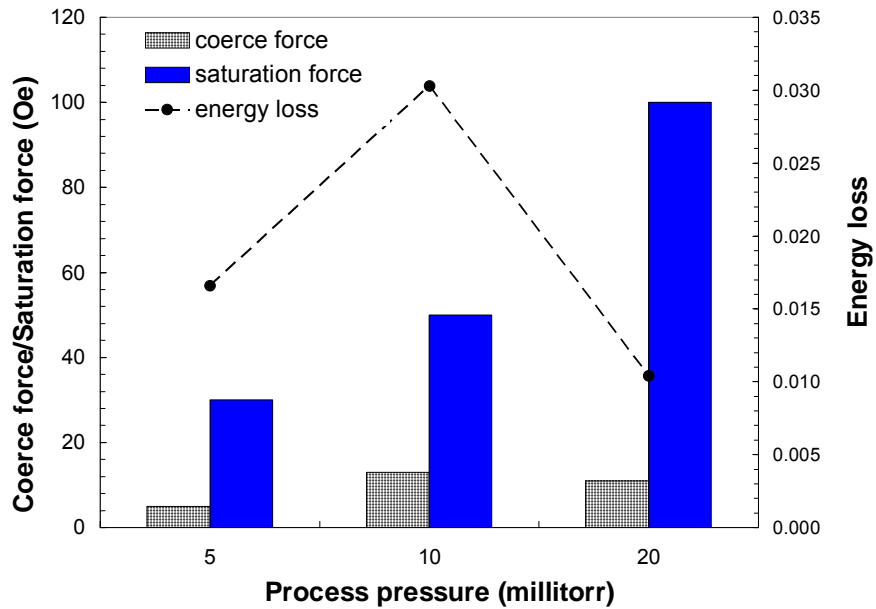
Fig. 6-13 Magnetic properties of magnetostrictive thin film as affected by deposition

pressure.

Based on the results, we can conclude that the lower deposition pressure results in improved film properties of both lower coerce and saturation forces. Although the energy loss is not the lowest one, it is still considerably small. Additionally, the H-B shape for the lower pressure deposited film material is comparable to as received Metglas 2826 MB ribbon, (see Fig. 6-14). It is notable that the coerce and the remanence are near zero, and the energy loss is very small for the Metglas 2826 MB strip. But it requires an appreciable field for saturation, which results from the presence of macroscopic easy axis and non-random uniaxial anisotropy associated with the production process [223].
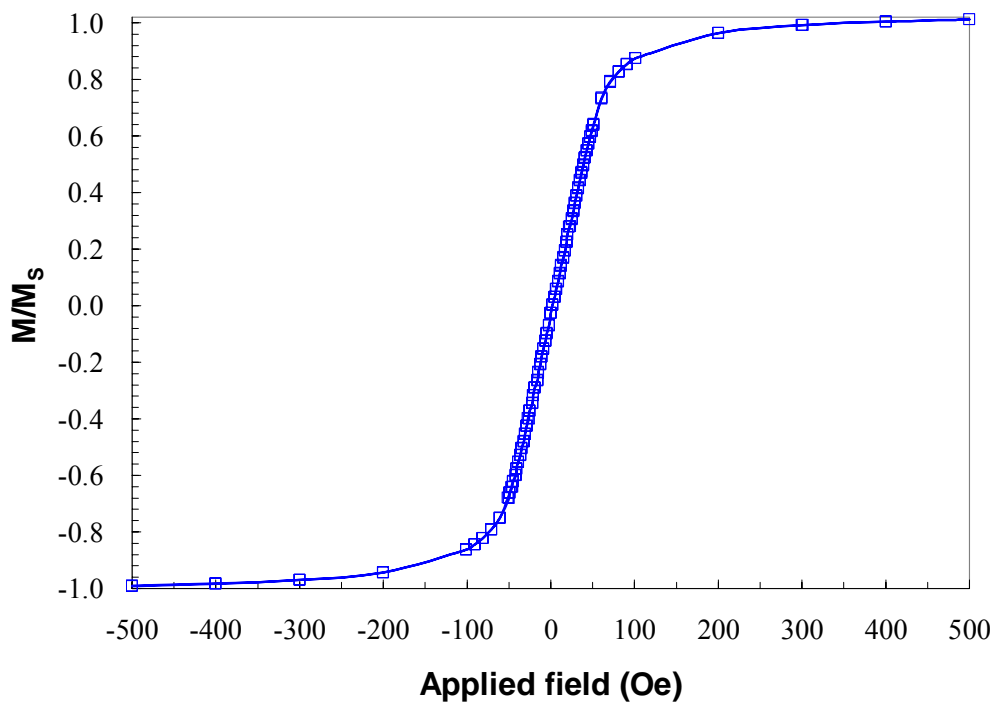
Fig. 6-14 Hysteresis loop for the Metglas 2826 MB ribbon.

At the lower deposition pressure of 5 mT, the sputtered magnetic film developed rather fine cluster/particle size relative to the higher pressures, (see Fig. 6-9), and a considerably smoother surface. Furthermore, this film exhibited an amorphous structure, which greatly reduced the anisotropy of magnetic properties. Consequently, less energy was required for the domains to switch under the applied magnetic field, i.e. they switched more easily. In contrast, the sputtered magnetic films that were deposited under higher pressure exhibited rough surfaces with considerably larger cluster/particle size as well as a degree of crystalinity. As a result, domain switching became more difficult, e.g. the domains underwent pining on the grain boundary when the films were exposed to an external magnetic field. Similar grain size effects were reported by other researchers [220, 224].

Moreover, the change in shape in the hysteresis curves may also be attributed to the internal stress level and its orientation to the external field that was observed with Ni, FeB and other materials [222, 225]. For example, Fig. 6-15 (a) shows the work of Foell [188] where the hysteresis loop of pure Ni is under tensile force that is parallel to the external magnetic field, while Fig. 6-15 (b) shows that the tensile force is perpendicular to the external field. Both exhibit significant changes in the remanence but not much in coercivity [188].
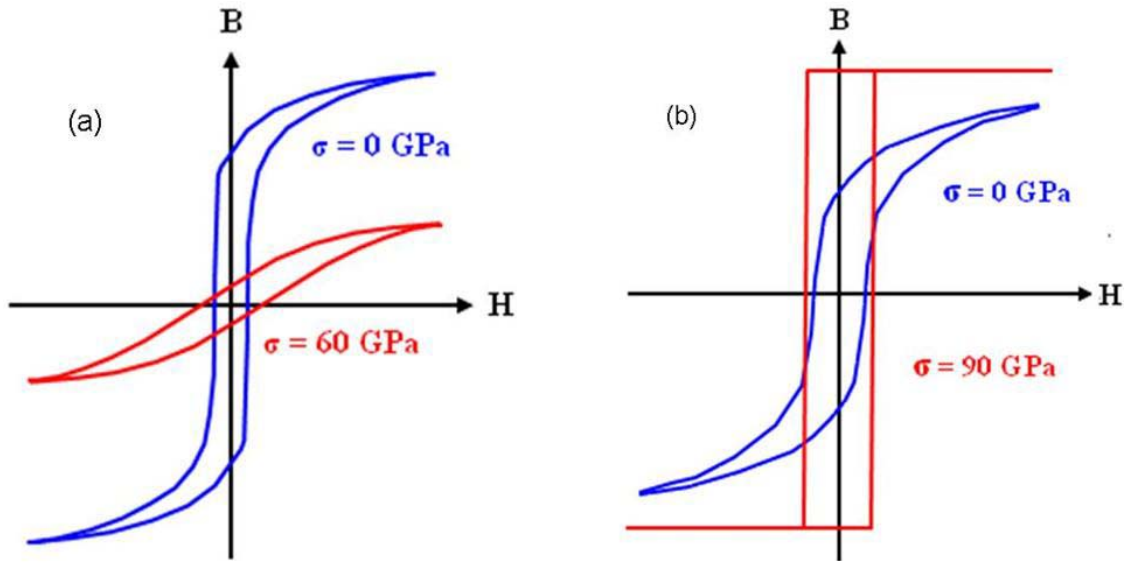
Fig. 6-15 B-H curves of pure Ni under different stress orientation to the external magnetic field, (a) tensile stress parallel to the applied field and (b) tensile stress perpendicular to the applied field [188].

6.4.1.4.   Thin Film Composition Analysis

The compositions of the magnetostrictive thin films deposited at 5 mT, 10 mT and 20 mT were analyzed by XPS (X-ray photoelectron spectroscopy). The analysis was conducted after sputter-etching of the specimen's surface for 10 minutes to sample the interior of the film. Table 6-5 summaries the XPS analysis results for the thin film and the target material as well. There is some difference in composition between the analyzed and supplier's specific data on the as received Metglas 2826 MB ribbon. The atomic composition of Fe, Ni, Mo, and B for the standard Metglas 2826 MB is 40, 38, 4 and 18, respectively. These differences between analyzed data and supplier's claimed data may be a result of experimental error. A variety of compositions of sputter deposited film

materials under different process pressures was observed. The discrepancy of films to the target material and divergence from film to film may be attributed to 1) the resolution and analysis error from XPS, 2) the target surface did not reach equilibrium, 3) the pressure influenced the surface adsorption of different components, and 4) the film surface did not reach the equilibrium state before the XPS analysis.

Table 6-5 Compositions of Metglas 2826 MB and magnetostrictive films.

XPS analysis	Composition (at%)			
	Fe	Ni	Mo	B
Metglas	35	40	5	20
5 mT	36	29	8	27
10 mT	28	37	13	22
20 mT	28	46	4	22

The Fe content was found to decrease with pressure while the Ni content increased as with pressure, (see Table 6-5). Mo content tended to vary and the B content increased for the 5 mT pressure. The most interesting change was the boron for the 5 mT pressure. This element was added to disrupt crystallization and form amorphous structures, which may play a role in why this film was amorphous. Furthermore, the increase in process pressure also imparts additional kinetic energy to depositing atoms, enabling them to diffuse into more favorable positions that leads to crystallization. The higher pressures also contain

more impurity oxygen atoms that would react with the Fe. These molecules, being larger, would have reduced speed and movement in the plasma and could be the mechanism behind the reduced Fe content and increased Ni content. It should be noted that there was a very small amount of oxygen and carbon content was detected the films and Metglas strip. Fig. 6-16 (a, b, c, d) shows the Auger electron spectroscopy (AES) results of surface analysis of the Metglas strip and films deposited at 5, 10 and 20 millitorr, respectively. and Fig. 6-17 is the results of analysis of the same specimens by X-ray photoelectron spectroscopy (XPS) after sputtering clean for 10 minutes. A higher oxygen content on the surface in both the target material and films was observed and is displayed in Fig. 6-16. The oxygen content in the Metglas target almost disappeared after sputter cleaning, but a small amount remained in the films as shown in Fig. 6-17. These results indicate that the oxygen content in Metglas ribbon was due to the surface absorption effect and the oxygen content in films were due to both surface absorption and deposition. In fact, oxygen is a unavoidable gas species in sputter deposition as a result of the low vacuum environment. Since the intensity of the XPS peak is related to the concentration of the element within the sampled area, and based on analysis of the O1s intensity in the XPS spectra in Fig. 6-17, one can further find that the oxygen residual in the film deposited at a lower pressure is less than the higher pressures, which is another factor in why the performance of the 5 mT film exceeds the others. The carbon content in the deposited films likely originated from the target material, as the C1s peaks in target and thin films analyzed by XPS all reminded similar.
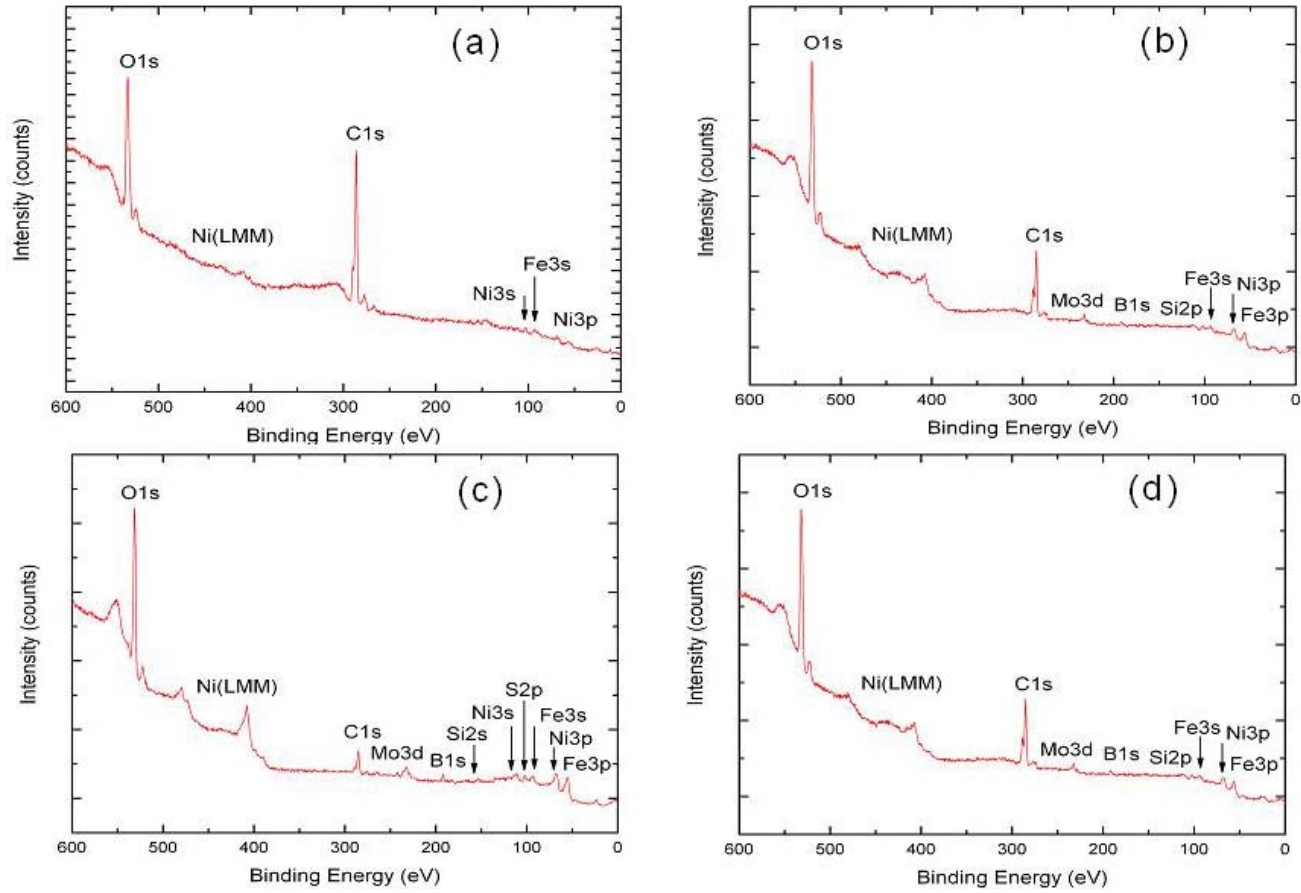
Fig. 6-16   AES spectra of Metglas^TM, and thin film deposited at various pressures. (a) Metglas^TM, (b) 5 millitorr, (c) 10 millitorr,
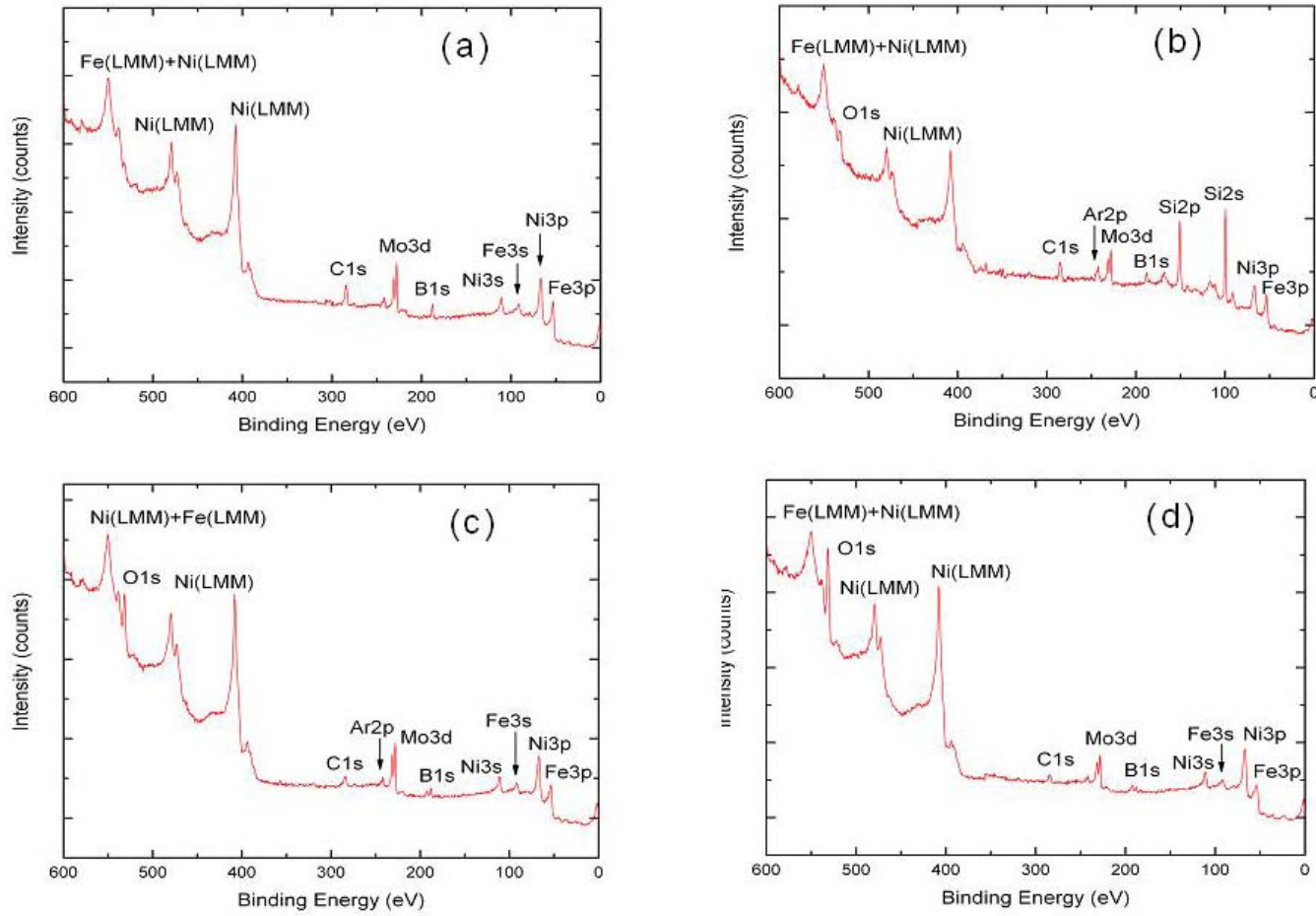
and (d) 20 millitorr.

Fig. 6-17   XPS spectra of Metglas^TM, and thin film deposited at various pressures. (a) Metglas^TM, (b) 5 millitorr, (c) 10 millitorr, and (d) 20 millitorr.

6.4.2.   DOE (Design of Experiment) Approach of Sputter Deposition by Phase II

6.4.2.1.   Deposition Rate and Surface Morphology Influenced by Various Factors

Thin film deposition rate is frequently manipulated by the sputtering power and sputtering pressure. Substrate heating temperature is another parameter that affects the deposition rate by altering the film properties, e.g. the density, crystallinity, composition, etc. Fig. 6-18 shows the deposition rate change with various factors. It is straight forward to understand that the deposition rate increases with increasing the sputtering power. The pressure effect follows the phenomenon observed and has been explained in section 6.4.1. When the temperature increases, there is more thermal energy available, which may promote film density. Hence, the deposition rate decreases with increasing temperature.

Fig. 6-19 shows the surface morphologies of the films examined by SEM. Note the different magnifications employed in the imaging. Very fine particles and a smooth surface were observed for films that were deposited under conditions of experiments (1) and (4) in Table 6-4, while larger particle and rough surface were developed in films that were deposited under conditions (2) and (3). It is clear that the higher temperatures of conditions (2) and (3) resulted in coarser clusters/particles and rougher surfaces.
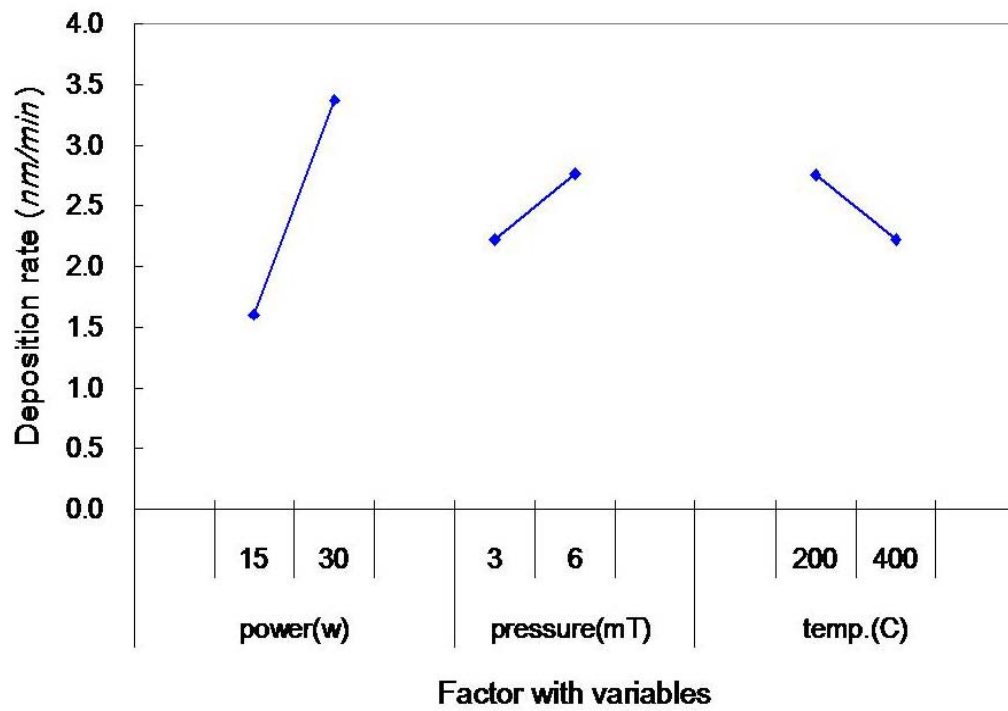
Fig. 6-18 Thin film deposition rate change with various deposition parameters.
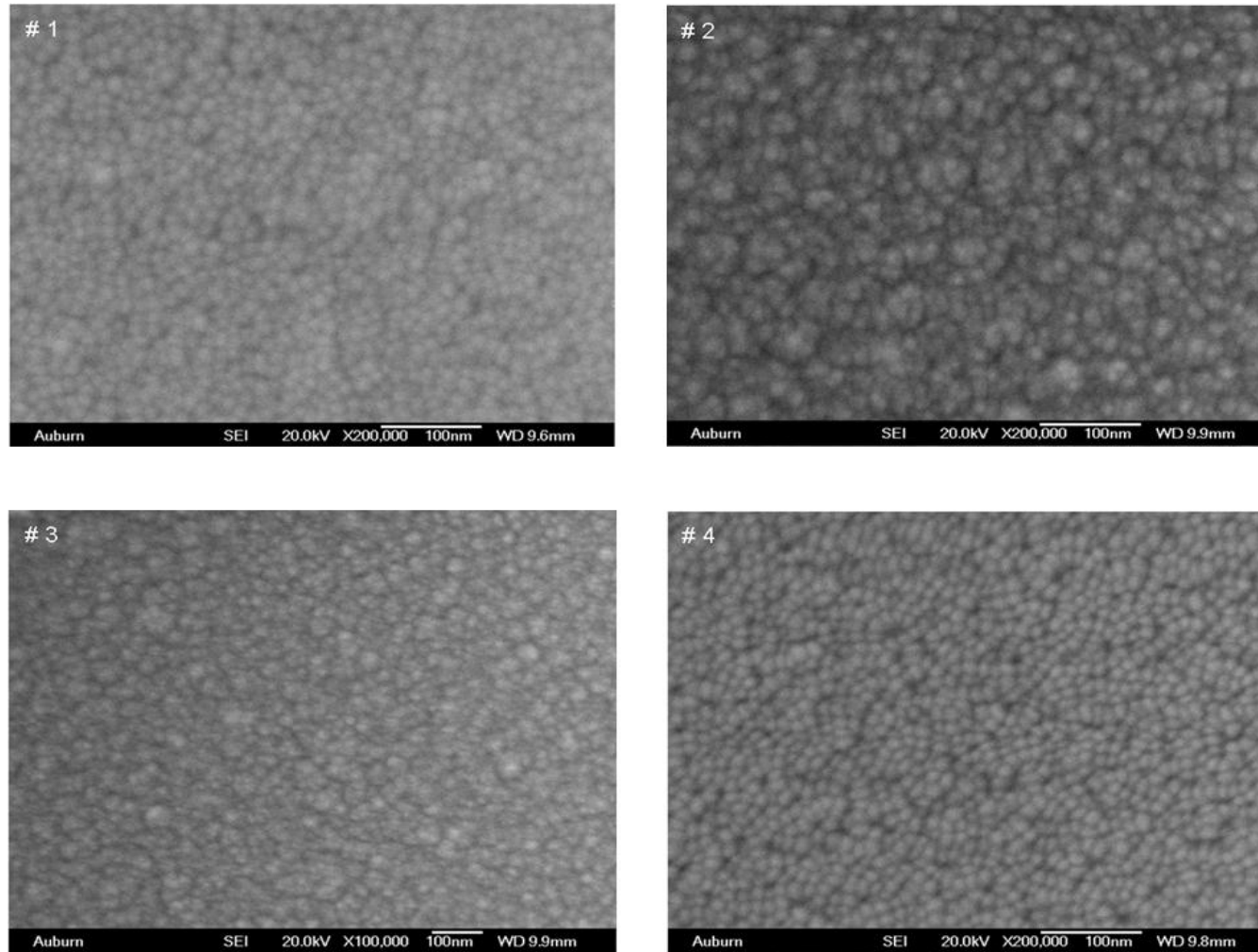
Fig. 6-19   Surface morphology of deposited films. (#1, #2, #3 and #4 correspond to the experiment of 1 to 4 in Table 6-4).

6.4.2.2.   Magnetic Properties Impacted by Various Factors

Evidently, the deposition pressure played a significant role in governing the magnetic properties of the thin film material. The effects of the sputtering power, substrate heating temperature and deposition pressure on the properties of the film materials were studied with the aid of the DOE as described in section 6.3.2. Fig. 6-20 presents the influence of these parameters on the film magnetic properties in terms of magnetization or hysteresis loop. All films deposited under the condition of the DOE exhibit soft ferromagnetic properties. The lowest coercity of these results was found to be about 5 Oe, and the highest was about 20 Oe.

The anisotropic magnetic characteristics of these films were examined by applying the in-plane magnetic fields in such a manner that they are perpendicular to each other, (see Fig. 6-21). All films exhibited a low anisotropic magnetic property. This low anisotropic magnetic property was most likely due to the rotation resolution of the substrate holder during the process of deposition.

Different deposition conditions can lead to significantly different magnetic properties. If we examine the shapes of hysteresis loop in Fig. 6-21 in microscale, one can see all samples show that tensile stress more or less was developed in these films, which were also observed by other researchers with Ni and FeB thin materials [222, 225]. The analysis of the DOE results for coerce force via each individual parameter is plotted in Fig. 6-22. The coerce force increases with both pressure and substrate heating temperature increasing, but coerce force decreases with increasing sputtering power. This pressure effect was observed to be similar to the initial deposition process developing step as discussed in section 6.4.1.3. From the above discussion, an optimal deposition

process can be obtained at pressure = 3 mT, power = 30 w, substrate heating temperature = 200 °C or less.
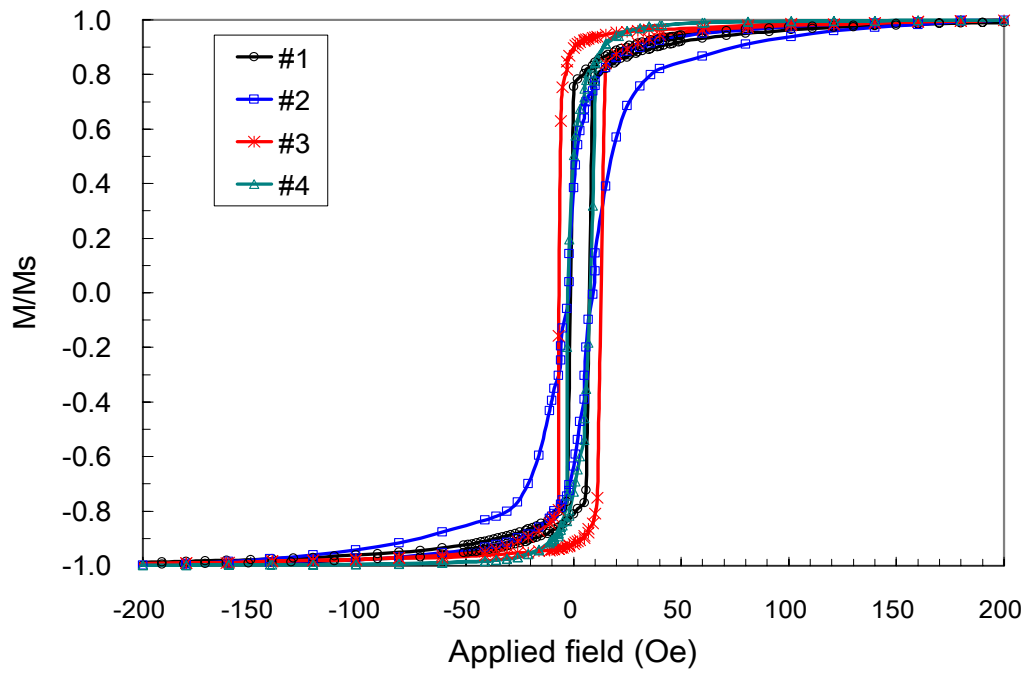
Fig. 6-20 Hysteresis loop for magnetostrictive film deposited under various conditions but with the same applied field orientation.
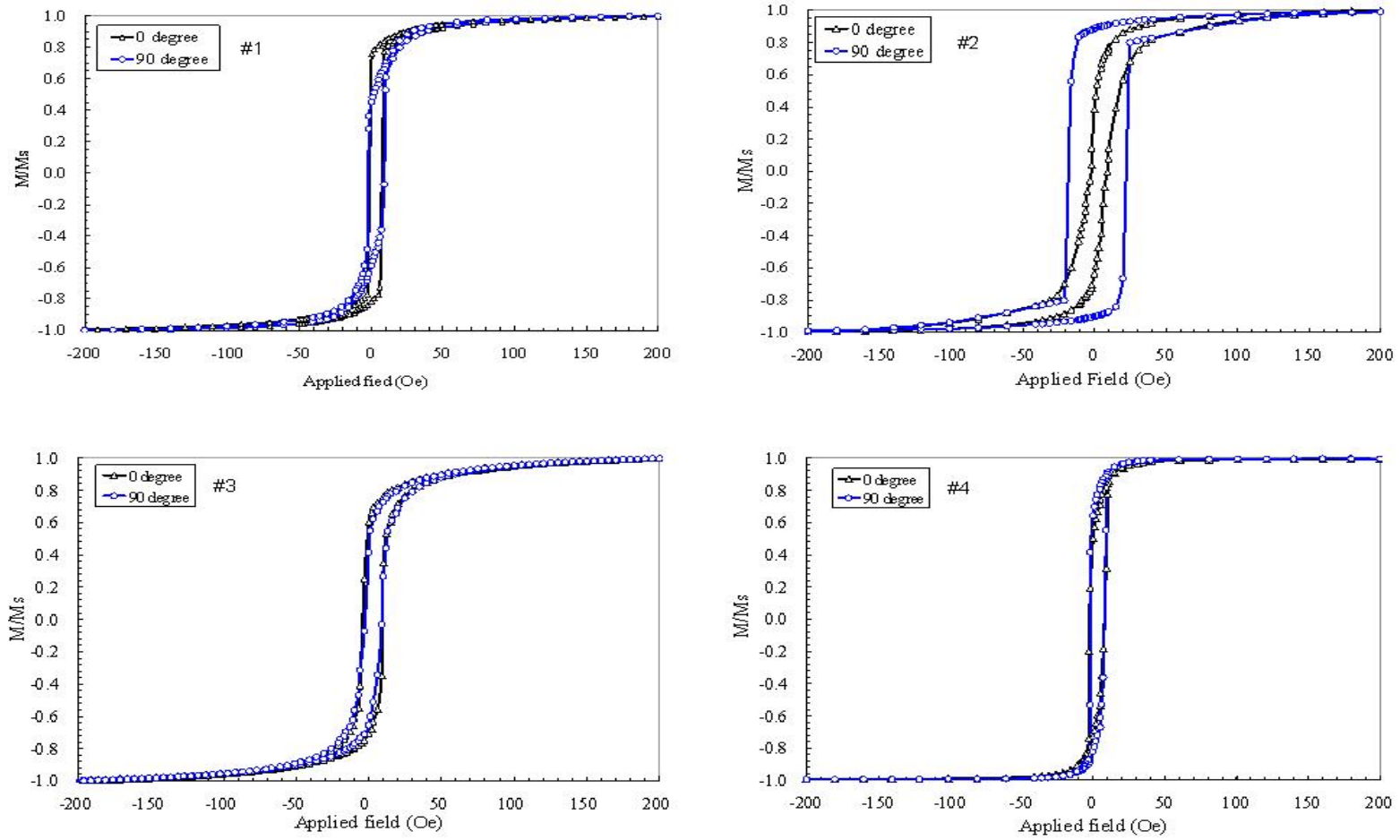
Fig. 6-21 Hysteresis loop for films deposited under conditions preset in the DOE. #1, #2, #3 and #4 refer to experiment run number set by the DOE in Table 6-4.
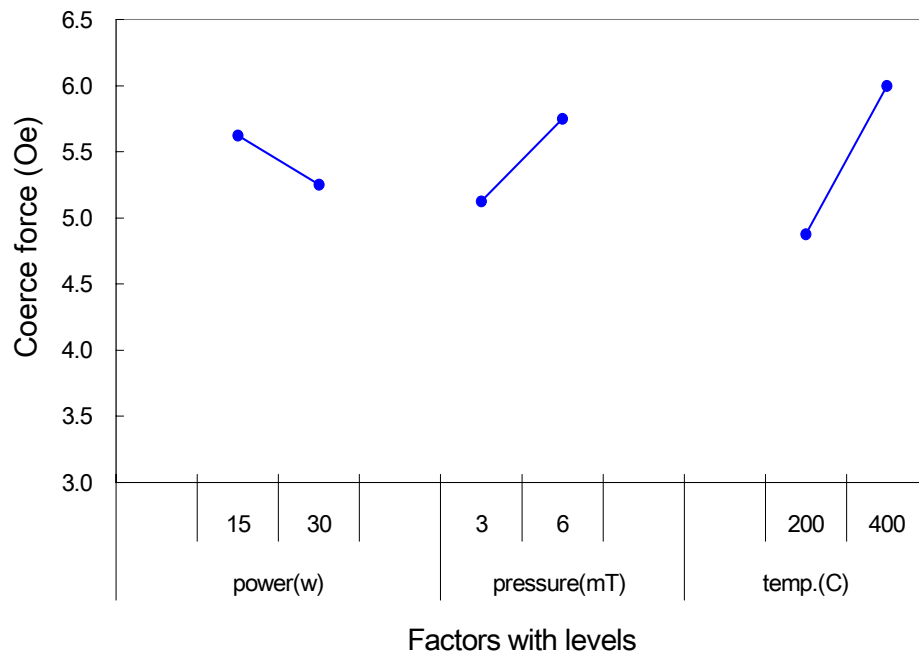
Fig. 6-22 Coercity change with each individual factor and variable.

6.5. Microfabrication and Functionality Test of Magnetostrictive Cantilever and Bridge Type Sensor

6.5.1. Microfabrication of Cantilever and Bridge Type Sensors

The microfabrication of sensors was carried out with a Si wafer coated with 0.35 μm LPCVD silicon nitride. A 0.2 μm Al film was coated on the nitride as a nitride etch mask followed by PR patterning and development. The Al was etched by the wet chemical method at room temperature. The opened Al windows for cantilever and bridge are shown in Fig. 6-23. After plasma etched off the silicon nitride layer, the KOH wet etch process was carried out to etch silicon. Fig. 6-24 shows the freestanding cantilevers and bridges. Note that some large bridges did not lift off at all because wet chemical etching of Si is anisotropic. SEM images of some final cantilevers and bridges are shown in Fig. 6-25. It is clear that there is no stress at all in the fabricated cantilevers or bridges. Otherwise, the cantilever or bridges would be bent.
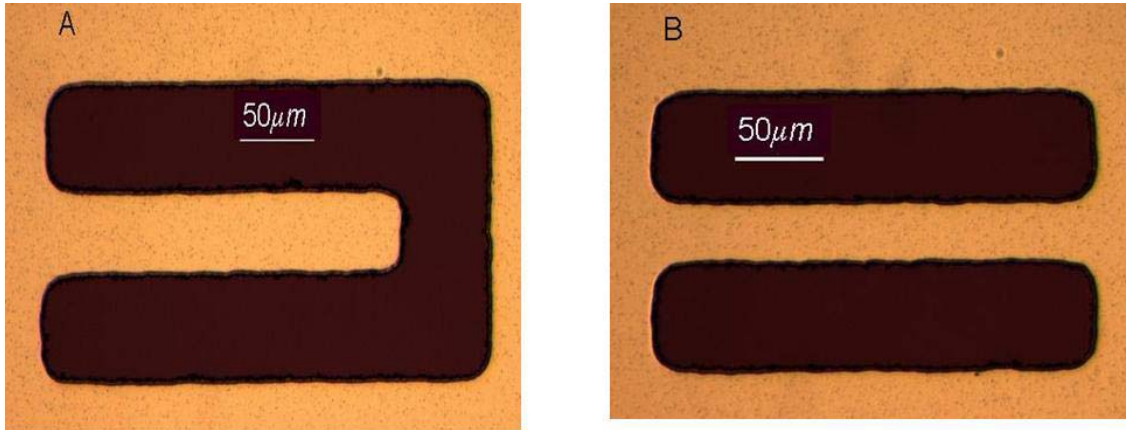
Fig. 6-23 Microscopic images of Al open windows for the etch SiN. (a) Cantilever (b) Bridge.
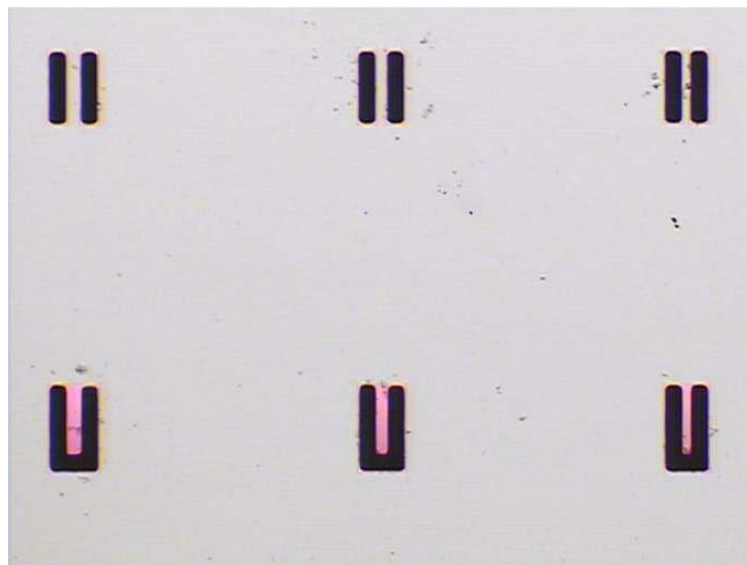
Fig. 6-24 Microscopic images of cantilevers and bridges after Si wet etching.

181
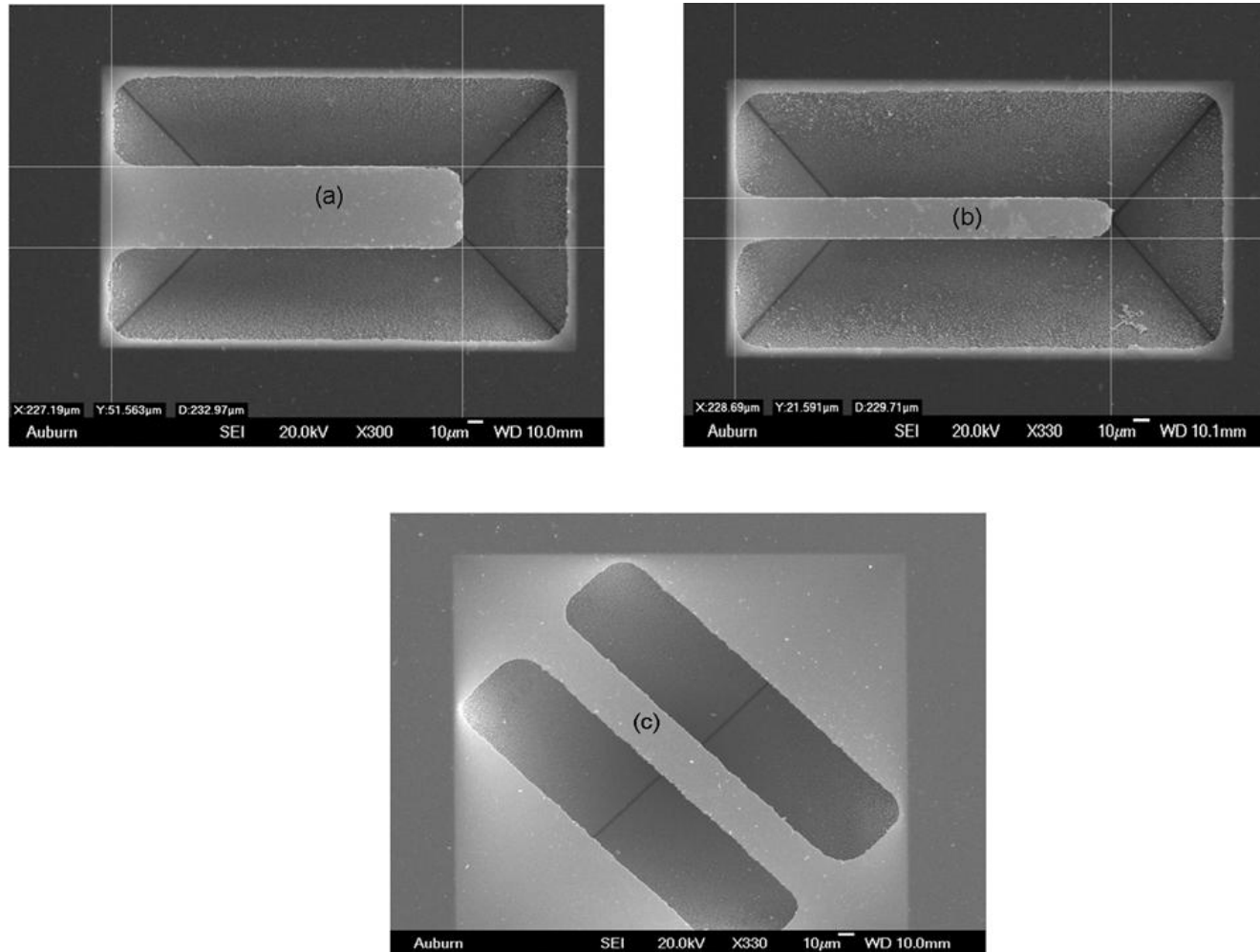
Fig. 6-25 SEM images for cantilevers and bridge. (a) and (b) are cantilevers with different aspect ratio, (c) is a fix-fix bridge.

6.5.2. Functionality Tests of Cantilever and Bridge Sensors

Cantilever and bridge type sensors that have been coated with 0.5 μm of sputtering Metglas or about 4 μm $Fe_{80}B_{20}$. These magnetostrictive thin films were subjected to a resonant frequency test. The details of deposition of $Fe_{80}B_{20}$ can be found elsewhere [200]. Fig. 6-26 shows the cantilevers and bridges coated with $Fe_{80}B_{20}$ thin film. It is notable that the $Fe_{80}B_{20}$ film was broken at the fixed end of some cantilevers, which can be attributed to the large stress developed in the magnetostrictive thin film.

A wafer fabricated with cantilevers and bridges was diced into small dies before magnetostrictive thin film deposition. Unfortunately, no resonant frequency was detected. This could have been caused by the following factors:

- The sensitivity of the detecting coil was not high enough to sense the response of the sensor.

- The relatively small magnetic material volume of the cantilevers and bridges resulted in the change in magnetic flux that was so small that the pick-up coil was not able to sense this induced magnetic field change.
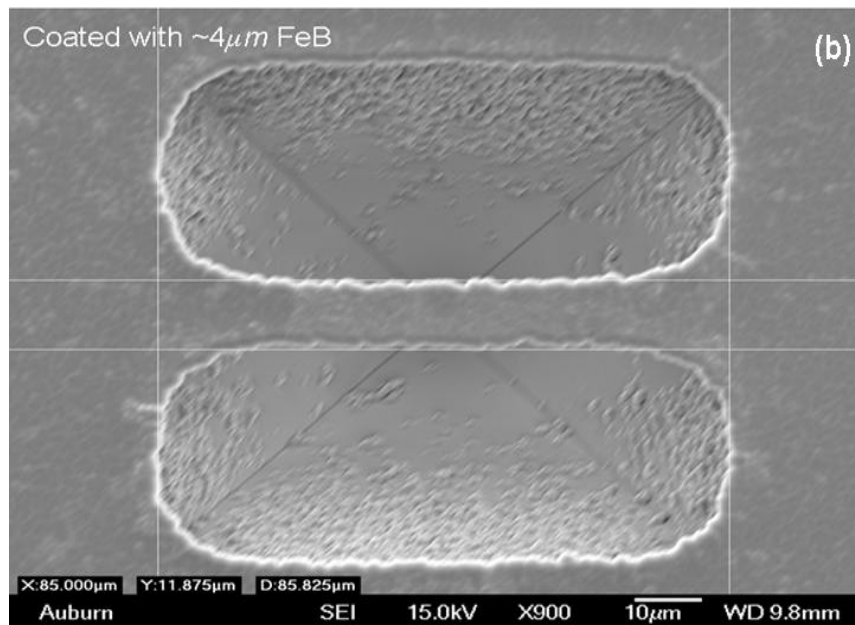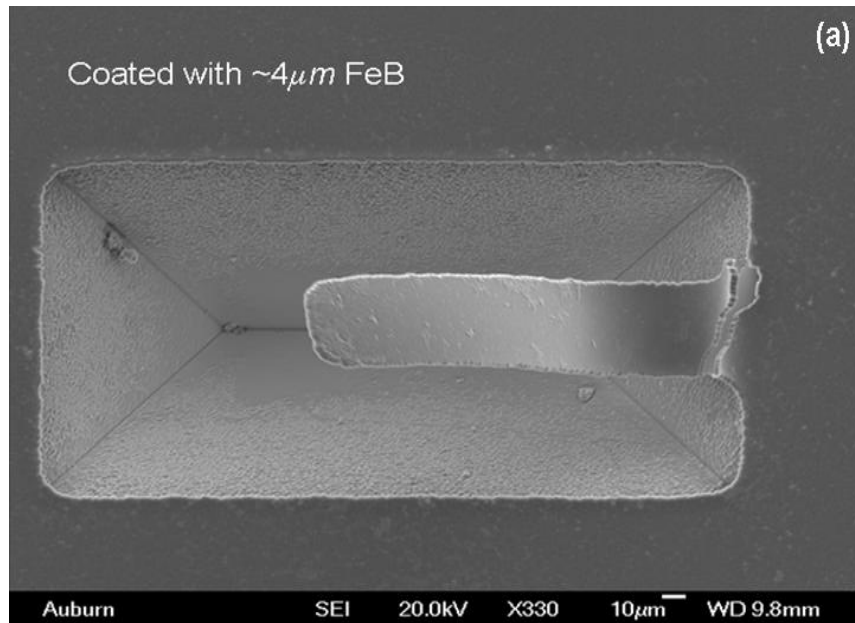
Fig. 6-26 SEM images for cantilevers and bridges coated with ~ 4 µm FeB thin films.

6.6. Microfabrication and Resonant Frequency Test of Magnetostrictive Freestanding Beam (Particle)

6.6.1. Free-free ended Beam (Particle) Fabrication

The process used for the fabrication of freestanding particles was described in Fig. 6-7. The specific process is to pattern photoresist into rectangular structures possessing the desired length and width of the freestanding beams. Fig. 6-27 illustrates these structures on the wafer. The Metglas film is then deposited and the PR dissolved so that the particles become freestanding and float off. In order to develop a functioning sensor, a 100 nm thin Au film was deposited before and after the deposition of magnetostrictive film to create a substrate for the capture film to adhere to. The process used for sputtering the Metglas film was the optimized one as discussed in section 6.4. Multiple sputtering processes were carried out to obtain a thicker magnetostrictive film material. The freestanding beams or particles before lift-off are shown in Fig. 6-28. Fig. 6-29 shows the freestanding beams before collection, from which one can see the free lift-off beams are bent. This observation indicates that tensile stress developed in the thin film materials, which confirms and explains the hysteresis loop shape with the measurement of magnetic properties by VSM as shown in Figs. 6-20 and 6-21.
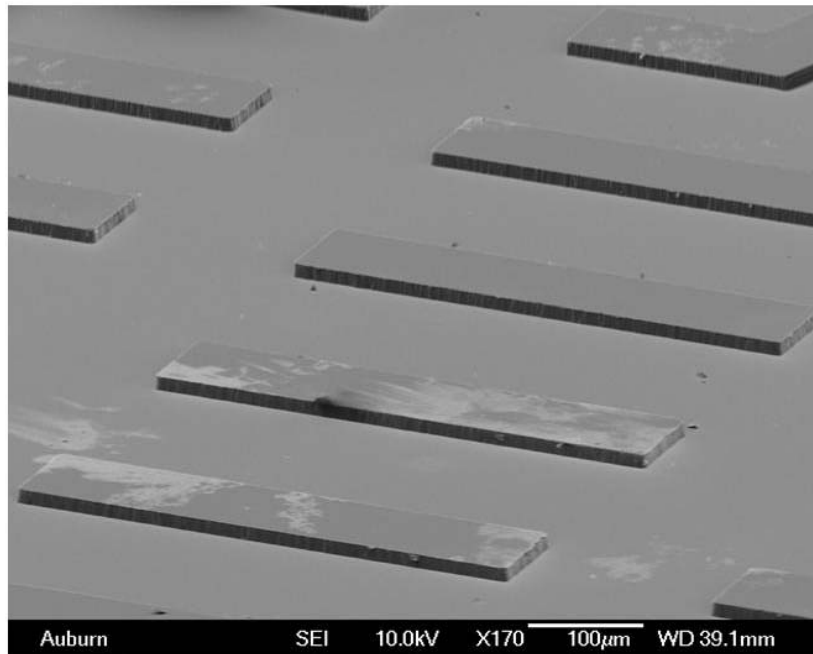
Fig. 6-27 SEM images of microfabricated photo resist templates for the fabrication of

freestanding sensors.
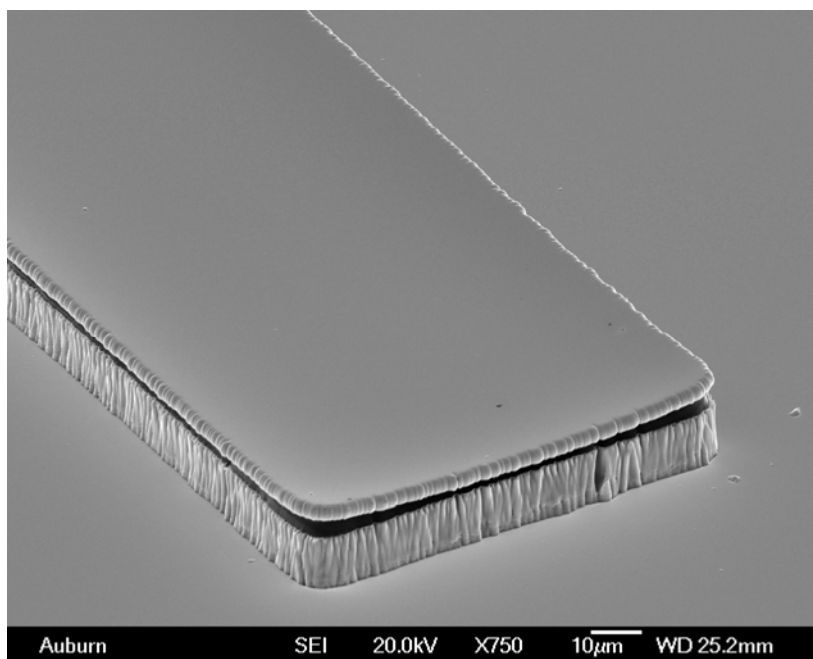
Fig. 6-28 SEM image of a freestanding beam (particle) on PR template.
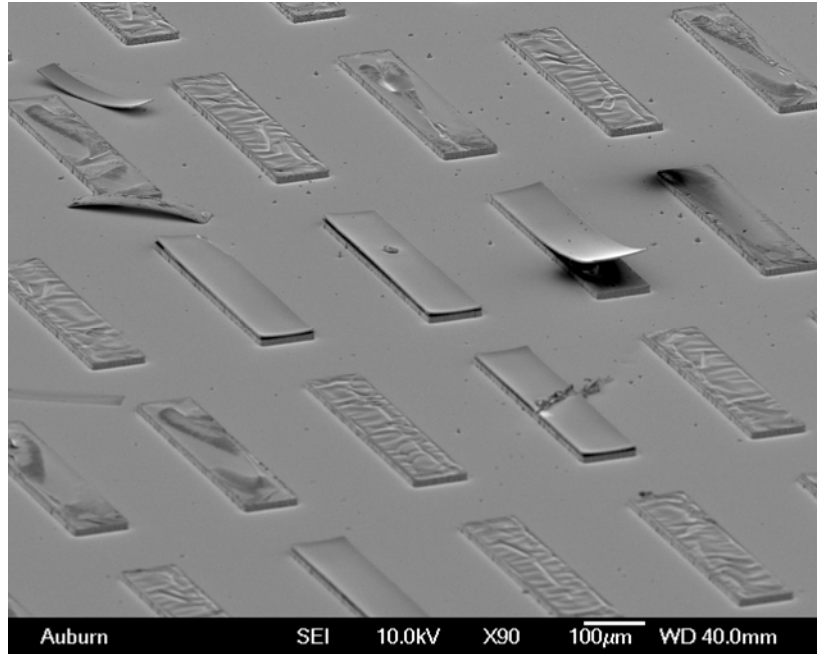
Fig. 6-29 SEM images of some uncollected, lift-off freestanding beams (particles). The bent particles appeared to be stressed.
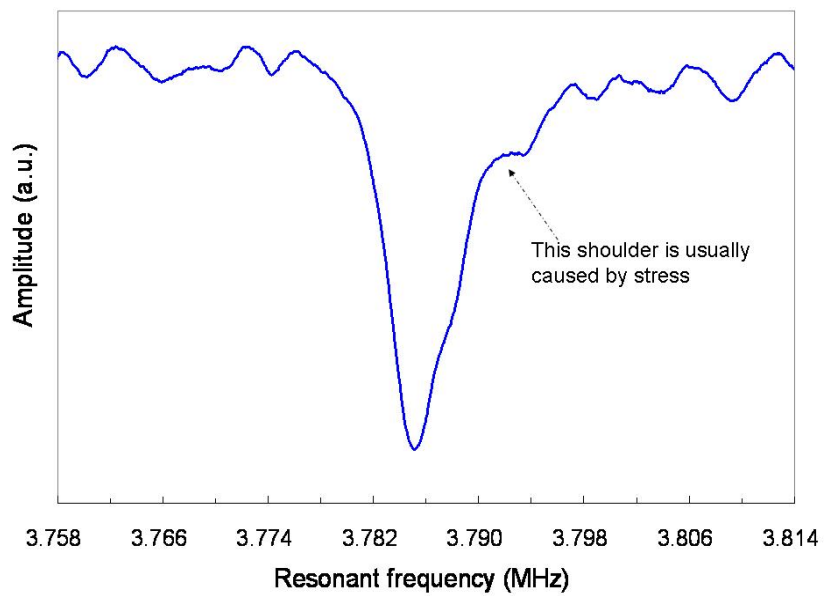
Fig. 6-30 Resonant frequency spectrum for a 500 μm x 100 μm beam (particle).

6.6.2. Results of Resonance Frequency Tests

The resonant frequency of the freestanding particles (beam) of 500 μm x 100 μm x 3 μm was measured by using the similar setup as the one used for large scale samples. Typical resonant frequency spectrum of a beam is as shown in Fig. 6-30. The amplitude of the resonant peak was usually weak but strong enough for testing, distinguishing and inspection. The calculated Figure-of-merit Q value is about 971.2 for this beam, which is much higher than the value of 265 for a large scale sensor made of Metglas strip.

6.6.3. Annealing Effect

The temperature profile for annealing was recorded and plotted in Fig. 6-31. The temperature ramp up was controlled by setting the electrical current that is directly linked to the target temperature (215 ^{o}C). Temperature cooling down was naturally controlled by the room environment. During cooling, the chamber was sealed and kept under vacuum.
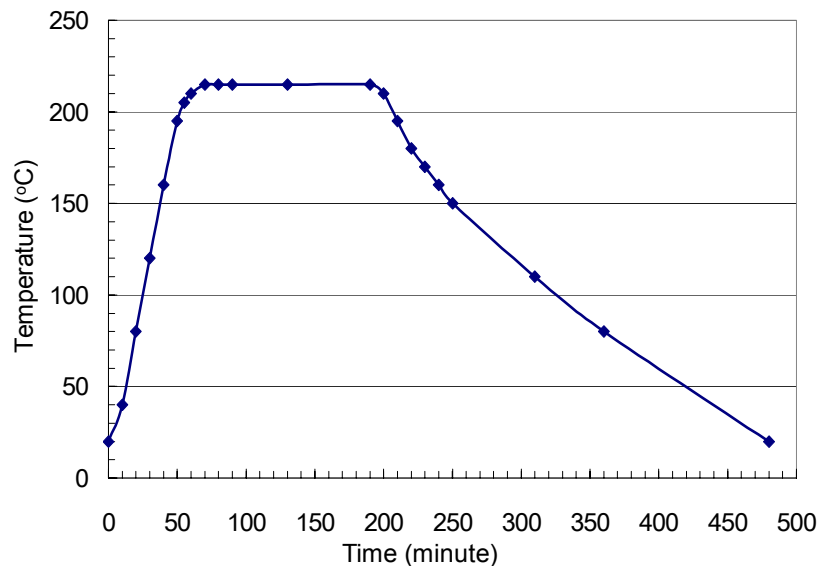
Fig. 6-31 Temperature changes with time during annealing/cooling process.

6.6.3.1. Effect of annealing on Magnetic Properties

The magnetic properties of annealed magnetostrictive film were also characterized by VSM. Fig. 6-32 indicates that after annealing, the coercity of the magnetostrictive film is slightly reduced to about 4 Oe, but the total energy loss is reduced significantly. The hysteresis loop starts to merge together right before the magnetization of the material gets saturated, which is desirable for our application in the dynamic vibration mode. For instance, when the applied field has so little change in the resonant frequency range that no resonant frequency jump occurs, a stable resonant frequency spectrum can be obtained.
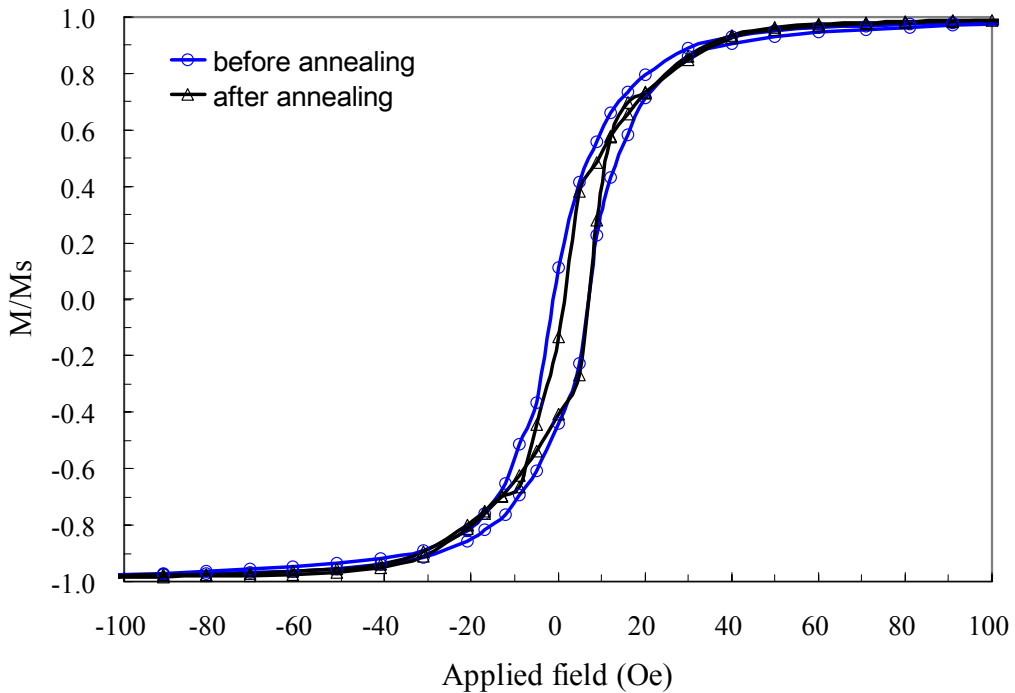
Fig. 6-32 Hysteresis loops of sputtering deposited films before and after annealing at 215°C for two hours in a vacuum chamber.

6.6.3.2.   Effect of annealing on the Resonance Frequency and Q-Factor of Sensor

Resonance frequency of the freestanding beam was significantly improved through annealing at 215 ^{o}C under vacuum condition. Fig. 6-33 shows a typical particle's resonant frequency shift before and after the heat treatment. After annealing, all particles tested exhibitd an increase in their frequencies by about 23 kHz (~0.6% of the original frequency), with an average resonant frequency of 4.019440 MHz. The annealing process also intensified the amplitude of the resonance frequency signal about 15 times as seen in Fig. 6-33. Additionally, the Figure-of-merit Q values for the annealed sensors were virtually increased by 180 in average from 971 to 1150.
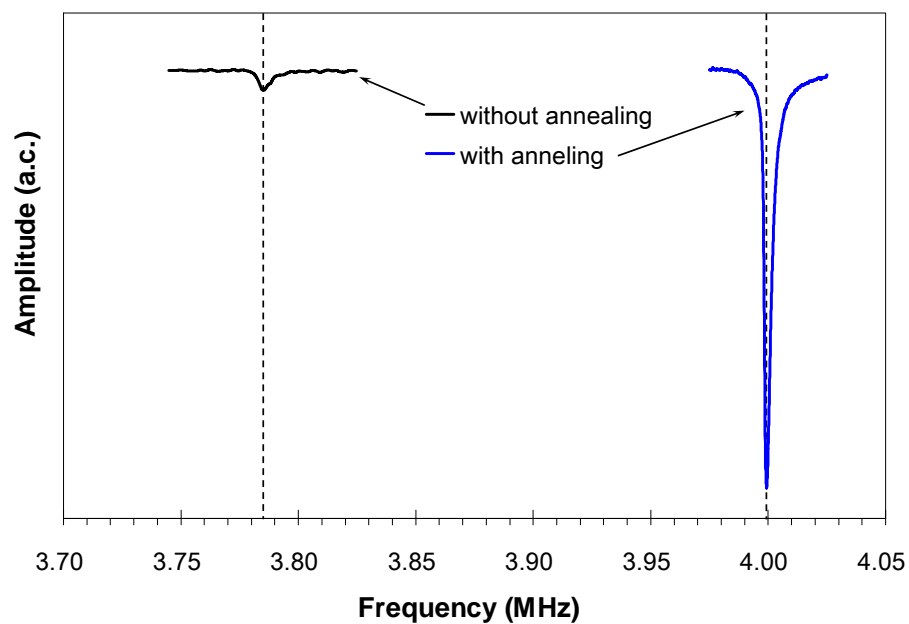
Fig. 6-33 Resonant frequency shift of a particle after annealing.

The Figure-of-merit Q value is an important measure of the sensor's quality, particularly for those applications for detecting a single or few biomolecule cells present

on the sensor surface. The higher the Q value, the sharper of the resonant frequency spectrum is; consequently, it is easier to locate the peak position of the spectrum. Fig. 6-34 (a) to (c) shows the profile of spectrum peak for the Q values varying from 930 to 1425. It can be seen that at lower Q values, the spectrum is rather broad, and the frequency peak is more difficult to determine. Such a flat spectrum at the peak position is not desirable, and may result in greater error of testing. As the Q value increases, the spectrum becomes sharper; and the peak position is therefore easy to distinguish. For example, in Fig. 6-34 (c) with Q value equal 1425, the frequency peak can be easily determined with an error of less than 50 Hz.
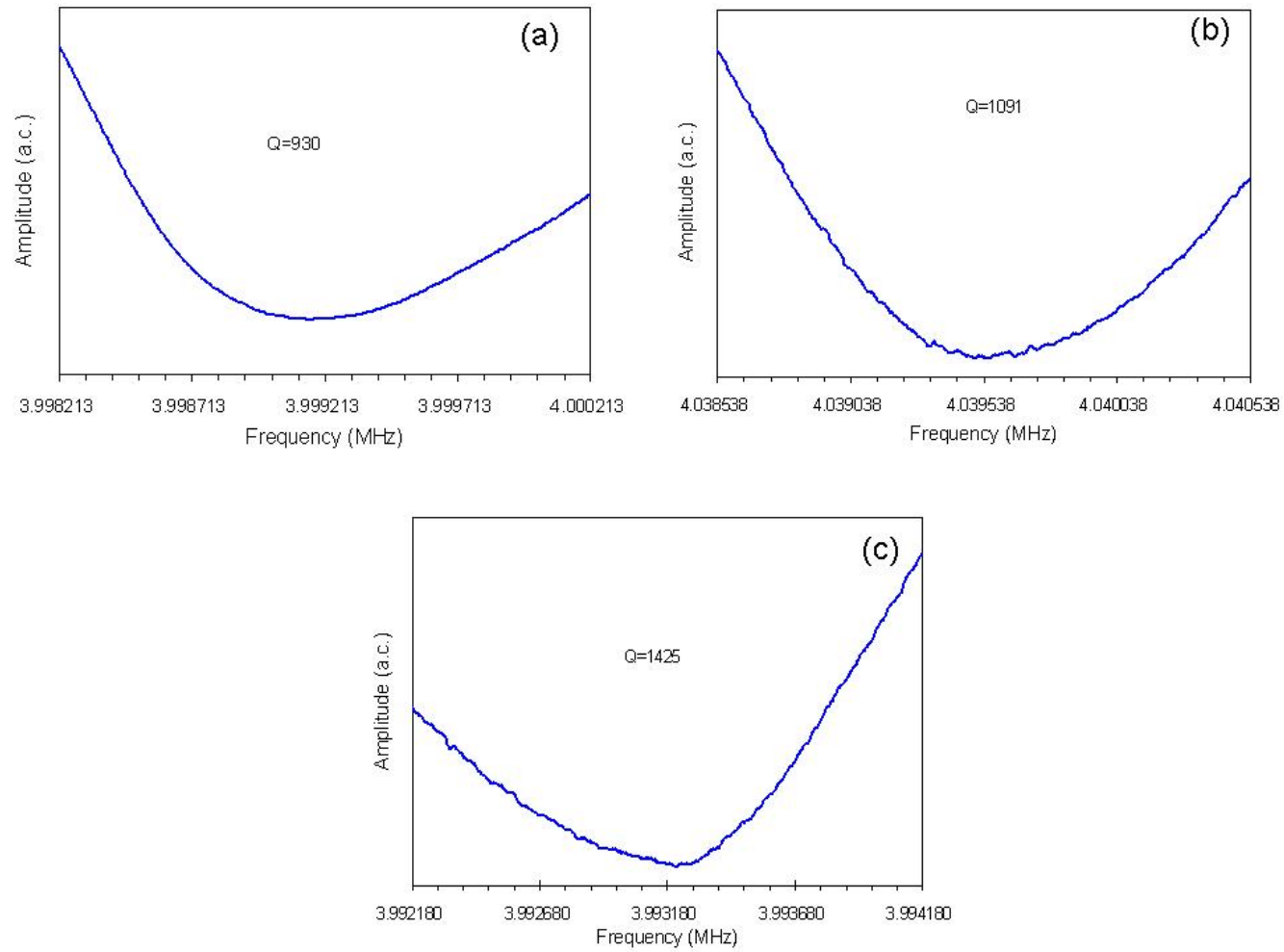
Fig. 6-34 Peak profiles of resonant frequency spectra for different sensors with various Q values.

6.6.3.3. Mechanisms on the Annealing Effects

The effect of annealing on the magnetic properties of magnetostrictive thin films and the sensor's performance may be attributed to an increase in the elastic modulus and a reduction in residual stress during the annealing process. The change in the elastic modulus of the film materials after annealing is most likely due to the defect healing. Furthermore, the annealing treatment also released the residual stress as it can be seen from Fig. 6-29, where the freestanding beams are bowed down due to stress developed in the magnetostrictive film. Fig. 6-35 shows that when the stress in the longitudinal direction of sensor is released, there is no curvature observed under SEM. However, we do observe that the sensor still has slight curvature in the width direction upon annealing. This effect of stress released in longitudinal direction greatly improves the sensor performance such as amplitude of the resonance frequency peak and Q value. The following model is suggested to elucidate the effects.
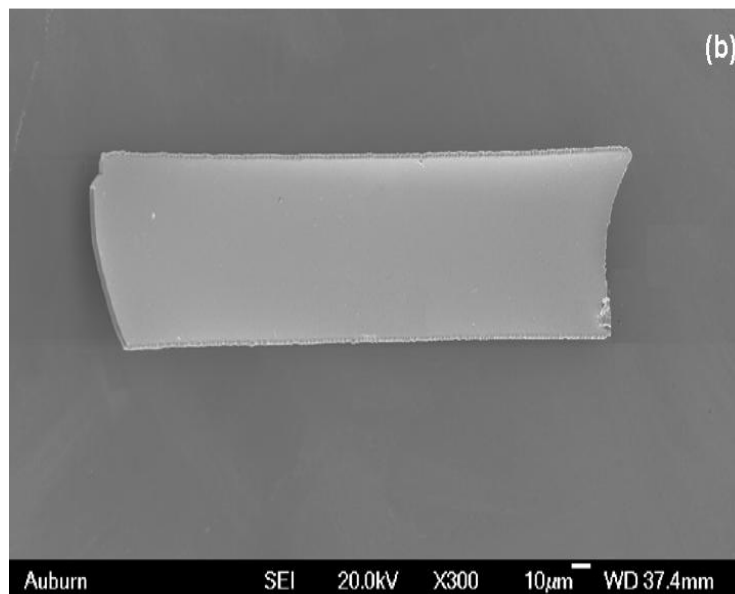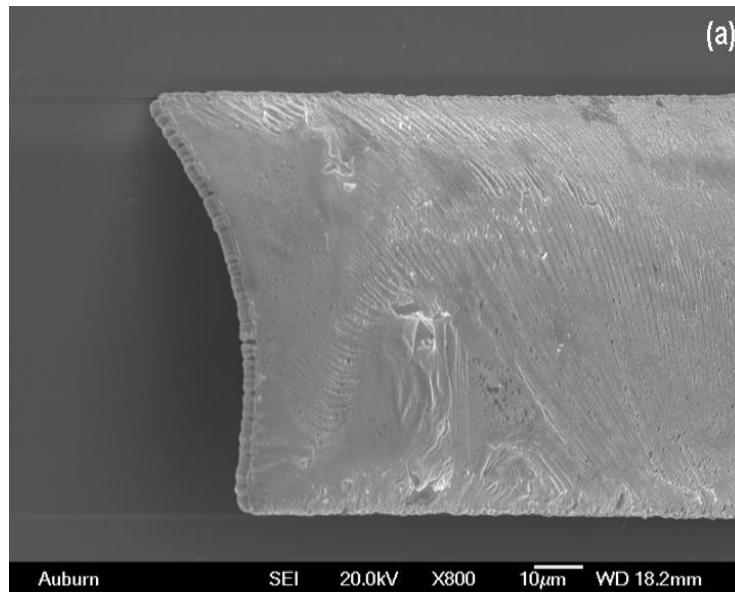
Fig. 6-35 SEM images of an annealed sensor. A slight curvature in the width direction

can be seen, but not in the longitudinal direction. (a) Bottom surface is up. (b) Bottom

surface is down.

When the bent sensor shown in Fig. 6-29 is subjected to an applied magnetic field (see model of Fig. 6-36) the magnetized domains will tend to align to the external filed. However, since there is bending in the longitudinal direction, many domains will impinge on the bent surfaces (top and bottom). In addition, the growth process of the domains will be confined by the bent surface. Such an effect is believed to significantly reduce the magnetized flux. Moreover, the direction of magnetized flux will follow the similar shape of the sensor, which is not parallel to the applied magnetic field, or the axis of read coil, but is a low angle to the them instead. Only the partial of magnetized flux whose direction is parallel to the read coil axis, M_{II} as shown in Fig. 6-36, will effectively interact with this read coil. Clearly, this interaction is less intense than the one that did not bend; therefore, the sensing coil detected a weaker signal during the sensor oscillating. One can compare this bent sensor with the unbent one shown in Fig. 6-37. In this case, magnetization took place perfectly aligned to the applied filed and the axis of the read coil in the longitudinal direction. Moreover, the formation of larger domains is possible in the longitudinal direction due to the lack of residual stress. This also helps to explain why this sensor's resonant frequency increased after annealing. Additionally, bent sensors exhibit tensile stress on one side and compressed stress on the other. The resonant frequency will be not the same as non-bent one, but it is lower due to the length of the side with tensile stress being longer than the one that does not bend. This causes different acoustic wave speeds and effectively widens the resonant peak. Likely this caused the sensor a very small amplitude and low Q values.

For the annealed sensor (Fig. 6-35), since the stress is released, there is no significantly bending in the longitudinal axis, although a small curvature was observed

195

with SEM in the lateral direction. The behavior of such sensors can be modeled as described in Fig. 6-38. The bending in the lateral direction would not significantly influence the magnetization of the sensor when the applied magnetic filed is parallel to the longitudinal direction. These out-of-plane effects likely only have negligible effects.
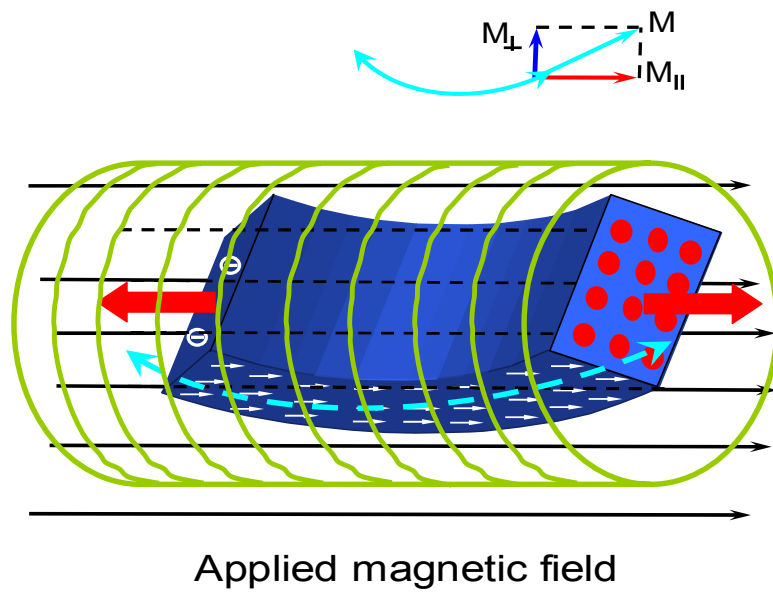
Fig. 6-36 Modeling of a sensor bent in longitudinal direction.

Applied H
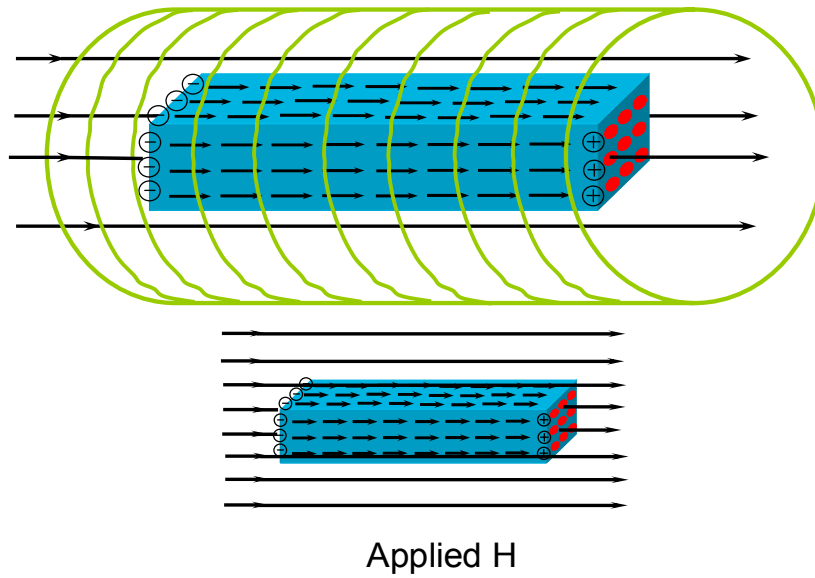
Fig. 6-37 Modeling of a perfect sensor without bending.

Applied H
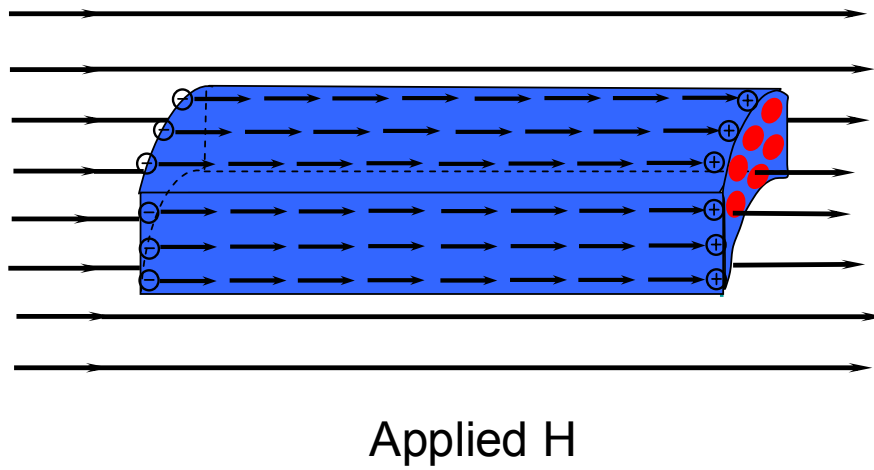
Fig. 6-38 Modeling of an annealed sensor that is only bent in the lateral axis, but not in

the longitudinal direction.

6.7. Summary

The fabrication of a Metglas sputtering target and deposition of a magnetostrictive thin film were demonstrated in this work. The film material exhibited soft ferromagnetic properties and low degrees of magnetic anisotropy. Deposition process studies indicated that the magnetic properties of thin film material are very much dependent on the process parameters, such as deposition pressure, sputtering power and substrate temperature. The optimal deposition parameters were found to be: pressure = 3 mT, power = 30 w, and substrate heating temperature = 200°C or room temperature.

Stress associated with the thin film during deposition was released by annealing at 215 $^{\circ}$C for 120 minutes, which resulted in increased resonant frequency and Q factor, aspects that are important in developing this material into a usable sensor. The resonant frequency of microfabricated magnetostrictive sensors in both cantilevers and bridges was not detectable by general detecting setup because the pickup coil wasnot sensitive enough. However, a successful detection of microscale freestanding beams was demonstrated. The sensor's performance was significantly improved by annealing and a model describing this effect was proposed.

7.   CONCLUSION AND FUTURE WORK

7.1.   Conclusions

This work focused on solving several issues in the development of magnetostrictive acoustic wave sensors. Magnetostrictive material has been shown to be an excellent material for actuation and sensing in sensors that are configured as a cantilever, bridge, and beam. These sensors are driven by an alternating magnetic field and mass changes are measured by monitoring changes in resonant frequency. The work addressed the benefits of the longitudinal vibration mode, provided more precise governing equations, and demonstrated that magnetostrictive sensors are a cheap and easy method for measuring the thin film Young's modulus. It also developed the optimum sputter deposition parameters for depositing magnetostrictive films from Metglas 2826 MB targets and illustrated how to microfabricate these structures into useful forms. Finally, it constructed and demonstrated operation of thin film microscale resonators.

In particular, the superiority of the longitudinal mode resonance over the transverse mode was discussed and proven. The governing equations for a thin slender beam resonating in the longitudinal mode was modified by replacing the plane strain modulus with the plane stress modulus for geometries associated with thin film resonators or bulk scale resonators where thickness is significantly less than length and width. This was accomplished through a combined experimental and numerical simulation approach

which not only found issues with the fundamental operation equation for the longitudinal mode, but also clarified and confirmed that the Poisson's ratio for commercial Metglas 2826 MB strip is 0.33. This work also aided in identifying that a cantilever sensor 250 microns in length 50 microns wide with a thickness one micron or less, should be able to detect small amounts of mass or even a single spore or cell attached to the sensor's surface.

Metglas resonators were constructed and used to measure the thin film Young's modulus of several materials commonly used in state-of-the-art devices. The results were confirmed using a second thin film measurement technique and demonstrated that this technique offers a cost-effective, user-friendly and non-destructive test for thin film properties. It also improved the methodology of determining the thin film Young's modulus by assuming that film density was equivalent to bulk density, which significantly reduced the amount of error associated with the measurement.

This research also successfully developed the optimum process parameters for magnetostrictive thin film deposition by directly sputtering a Metglas strip. The optimal deposition parameters were found to be pressure =3 mT, power = 30 w, and a substrate heating temperature of 200 $^{\circ}$C or room temperature followed by annealing at 215 $^{\circ}$C for 120 minutes. The deposited thin film material exhibited soft ferromagnetism and high isotropic magnetic properties. Freestanding beams or particles with the size of 500 μm x 100 μm x 3 μm were fabricated by standard microfabrication process and their resonant frequency was effectively detected. Annealing the sensors resulted in relieving residual stress, which significantly improved performance and Q factor.

7.2.   Future work

The successful deposition and microfabrication of thin film magnetostrictive sensors has the potential to revolutionize the MEMS and microdevices field by enabling remote/wireless powering and actuation of devices. Towards this goal, future work should focus on (1) better detection of small amounts of biological agents, (2) integrating these thin film actuators into actual devices or demonstrating their function and (3) developing small, on-chip read coils to detect their signals.

(1) Detection of Biological Agents

- develop a sensor with both bridges and freestanding beams of varying size to better assess attachment of biological species

- develop an algorithm that can distinguish between the number of spores or cells attaching and their position on the platform

(2) Integration as MEMS actuators would require the following tasks

- demonstrate that magnetostrictive films are compatible with many types of microfabrication processes

- demonstrate that magnetostrictive films retain their properties when subjected to typical MEMS microfabrication processes

(3) Development of a small, on-chip coils would require the following tasks

- develop a 2-dimensional magnetic coil capable of applying and reading the necessary fields

- examine employing giant magnetoresistive elements to detect fields generated by the films

REFERENCES

[1]   F. Qian, "Numerical Simulation and Mechanical Propeties of Free Standing Silver
        Thin Film," in *Materials Eng*. Auburn: Auburn University, 2006, pp. 111.

[2]   J. S. Bresee, V. Dietz, M. G. Patricia, L. F. Mccaig, P. S. Mead, C. Shapiro, L.
        Slutsker, and R. V. Tauxe, "Food-Related Illness and Death in the United States,"
        J. Environmental Health, vol. 62, 2000.

[3]   P. S. Mead, L. Slutsker, V. Dietz, L. F. McCaig, J. S. Bresee, C. Shapiro, P. M.
        Griffin, and R. V. Tauxe, "Food-Related Illness and Death in the United States.,"
        J. Environmental Health, vol. 62, pp. 9, 2000.

[4]   "Lettuce recalled over *E. Coli* concerns", presented at USA Today, San Francisco.
        11/29/2007, [Online] available:
        http://www.usatoday.com/money/industries/food/2006-10-09-lettuce_x.htm.

[5]   F. Pritzker, "CDC Detailed Report on Spinach and Escherichia coli Outbreak,"
        CDC, Mortality and Morbidity Weekly Report, No.55, September 27 2006.

[6]   R. E. Hummel, *Electronic Properties of Materials*, 3rd ed. Springer, New York,
        2000.

[7]   Iowa State University, "Magnetostrictive Transducers, Actuators, and Sensors",
        11/29/2007, [Online] available: http://www.public.iastate.edu/~terfenol/.

[8] Wikipedia, "Magnetostriction", 11/29/2007, [Online] available: http://en.wikipedia.org/wiki/Magnetostriction.

[9] G. E. Fish, "Soft magnetic materials," Proc. IEEE, vol. 78, pp. 947-972, 1990.

[10] Metglas Inc., 11/29/2007, " Magnetic Alloy 2826 MB, [Online] available: http://metglas.com/.

[11] P. Tayalia, D. Heider, and J. Gillespie, John W., "Characterization and theoretical modeling of magnetostrictive strain sensors," Sensors Actuators A: Physical, vol. 111, pp. 267-274, 2004.

[12] M. Formmberger and E. Quandt, *Magnetostrictive Sensors for Mechanical Properties*, vol. 5: American Scientific Publishers, 2006.

[13] C. A. Grimes, C. S. Mungle, K. Zeng, M. K. Jain, W. R. Dreschel, M. Paulose, and K. G. Ong, "Wireless Magnetoelastic Resonance Sensors: A Critical Review," *Sensors*, vol. 2, pp. 294-313, 2002.

[14] S. Wu, Y. Zhu, Q. Cai, K. Zeng, and C. A. Grimes, "A wireless magnetoelastic α-amylase sensor," *Sensors Actuators B*: Chemical, vol. 121, pp. 476-481, 2007.

[15] S. Wu, X. Gao, Q. Cai, and C. A. Grimes, "A wireless magnetoelastic biosensor for convenient and sensitive detection of acid phosphatase," *Sensors Actuators B*: Chemical, vol. 123, pp. 856-859, 2007.

[16] J. Wan, H. Shu, S. Huang, B. Fiebor, I.-H. Chen, V. A. Petrenko, and B. A. Chin, "Phage-based magnetoelastic wireless biosensors for detecting bacillus anthraces spores," *IEEE Sensors J*., vol. 7, pp. 470-477, 2007.

[17]   K. G. Ong, J. M. Leland, K. Zeng, G. Barrett, M. Zourob, and C. A. Grimes, "A rapid highly-sensitive endotoxin detection system," *Biosensors Bioelectronics*, vol. 21, pp. 2270-2274, 2006.

[18]   G. K. Mor, O. K. Varghese, M. Paulose, K. G. Ong, and C. A. Grimes, "Fabrication of hydrogen sensors with transparent titanium oxide nanotube-array thin films as sensing elements," *Thin Solid Films Proc. Fourth Int. Symp. on Transparent Oxide Thin Films for Electronics and Optics* (TOEO-4), vol. 496, pp. 42-48, 2006.

[19]   F. Cortes and M. J. Elejabarrieta, "Longitudinal vibration of a damped rod. Part I: Complex natural frequencies and mode shapes," *Int. J. Mechanical Sciences*, vol. 48, pp. 969-975, 2006.

[20]   R. Guntupalli, J. Hu, R. S. Lakshmanan, T. S. Huang, J. M. Barbaree, and B. A. Chin, "A magnetoelastic resonance biosensor immobilized with polyclonal antibody for the detection of Salmonella typhimurium," *Biosensors Bioelectronics*, vol. 22, pp. 1474-1479, 2007.

[21]   R. Guntupalli, R. S. Lakshmanan, J. Hu, T. S. Huang, J. M. Barbaree, V. Vodyanoy, and B. A. Chin, "Rapid and sensitive magnetoelastic biosensors for the detection of Salmonella typhimurium in a mixed microbial population," *J. Microbiological Methods*, vol. 70, pp. 112-118, 2007.

[22]   R. S. Lakshmanan, R. Guntupalli, J. Hu, D.-J. Kim, V. A. Petrenko, J. M. Barbaree, and B. A. Chin, "Phage immobilized magnetoelastic sensor for the detection of salmonella typhimurium," *J. Microbiological Methods*, Submitted to publish.

[23]   R. S. Lakshmanan, R. Guntupalli, J. Hu, V. A. Petrenko, J. M. Barbaree, and B. A. Chin, "Detection of salmonella typhimurium in fat free milk using a phage immobilized magnetoelastic sensor," *Sensors Actuators B: Chemical*, Submitted to publish.

[24]   J. Wan, M. L. Johnson, R. Guntupalli, V. A. Petrenko, and B. A. Chin, "Detection of bacillus anthracis spores in liquid using phage-based magnetoelastic micro-resonators," *Sensors Actuators B: Chemical*, submitted to publish.

[25]   S. Li, L. Orona, Z. Li, and Z.-Y. Cheng, "Biosensor based on magnetostrictive microcantilever," *Appl. Phys. Lett*., vol. 88, pp. 073507, 2006.

[26]   R. C. O'Handley, "Magnetic materials for EAS sensors," *J. Materials Engineering and Performance*, vol. 2, pp. 211-218, 1993.

[27]   SIEMENS, "To catch a thief", Research and Innovation, vol. 1, 1999. [Online] available:

http://w4.siemens.de/FuI/en/archiv/zeitschrift/heft1_99/artikel10/index.html,"

[28]   S. Timoshenko and D. H. Young, Vibration Problems in Eng., 3rd ed. New York: D. Van Nostrand Company, Inc., 1955.

[29]   K. N. Tong, Theory of Mechanical Vibration. New york: John Wiley & Sons Inc., 1960.

[30]   L. D. Landau and E. M. Lifshitz, Theory of Elasticity, vol. 7, 3rd ed. Pergamon Press, 1986.

[31]   S. Schmidt and C. A. Grimes, "Elastic modulus measurement of thin films coated onto magnetoelastic ribbons," *IEEE Trans., Magnetics*, vol. 37, pp. 2731-2733, 2001.

[32] S. Schmidt and C. A. Grimes, "Characterization of nano-dimensional thin-film elastic moduli using magnetoelastic sensors," *Sensors Actuators A*: *Physical*, vol. 94, pp. 189-196, 2001.

[33] C. Liang and B. C. Prorok, "Measuring the thin film elastic modulus with a magnetostrictive sensor," *J. Micromech. and Microeng.* vol. 17, pp. 709-716, 2007.

[34] HP 8571A Network Anayzer Operation Manual, 2000. Hewlett. Packard.

[35] V. Ferrari, D. Marioli, A. Taroni, E. Ranucci, and P. Ferruti, "Development and application of mass sensors based on flexural resonances in alumina beams", *IEEE Trans. Ultrason. Ferroelectr. and Freq. Control.* vol. 43, pp. 601-608, 1996.

[36] T. Thundat, E. A. Wachter, S. L. Sharp, and R. J. Warmack, "Detection of mercury vapor using resonating microcantilevers," *Appl.Phys. Lette.*, vol. 66, pp. 1695-1697, 1995.

[37] H. P. Lang , R. Berger , F. Battiston, J. P. Ramseyer, E. Meyer, C. Andreoli, J. Brugger, P. Vettiger, M. Despont, T. Mezzacasa , L. Scandella, H. J. G, Therodt, C. Gerber, and J. K. Gimzewski, "A chemical sensor based on a micromechanical cantilever array for the identification of gases and vapors," *Appl. Physics. A: Materials Science & Processing*, vol. 66, pp. S61-64, 1998.

[38] G. Y. Chen, T. Thundat, E. A. Wachter, and R. J. Warmack, "Adsorption-induced surface stress and its effects on resonance frequency of microcantilevers," *J. Appl. Physics*, vol. 77, pp. 3618-3622, 1995.

[39] S.-J. Kim, T. Ono, and M. Esashi, "Capacitive resonant mass sensor with LC resonant circuit for use in atmosphere," presented at 13th International

Conference on Solid-State Sensors, Actuators and Microsystems, 2005. Digest of Technical Papers. Transducers, 2005.

[40]   Z. J. Davis, G. Abadal, E. Forsen, O. Hansen, F. Campabadal, E. Figueras, J. Esteve, J. Verd, F. Perez-Murano, X. Borrise, S. G. Nilsson, I. Maximov, L. Montelius, N. Barniol, and A. Boisen, "Nanocantilever based mass sensor integrated with CMOS circuitry," presented at 12th International Conference on Solid-State Sensors, Actuators and Microsystems, Transducers, 2003.

[41]   J. H. Lee, K. S. Hwang, J. Park, K. H. Yoon, D. S. Yoon, and T. S. Kim, "Immunoassay of prostate-specific antigen (PSA) using resonant frequency shift of piezoelectric nanomechanical microcantilever," *Biosensors Bioelectronics* Selected Papers from the Eighth World Congress on Biosensors, Part II, vol. 20, pp. 2157-2162, 2005.

[42]   R. Raiteri, H.-J. Butt, and M. Grattarola, "Changes in surface stress at the liquid/solid interface measured with a microcantilever," *Electrochimica Acta*, vol. 46, pp. 157-163, 2000.

[43]   L. A. Pinnaduwage, T. Thundat, J. E. Hawk, D. L. Hedden, P. F. Britt, E. J. Houser, S. Stepnowski, R. A. McGill, and D. Bubb, "Detection of 2,4-dinitrotoluene using microcantilever sensors," *Sensors Actuators B: Chemical*, vol. 99, pp. 223-229, 2004.

[44]   J. Pei, F. Tian, and T. Thundat, "Glucose Biosensor Based on the Microcantilever," *Anal. Chem.*, vol. 76, pp. 292-297, 2004.

[45] D. Rugar, H. J. Mamin, R. Erlandsson, J. E. Stern, and B. D. Terris, "Force microscope using a fiber-optic displacement sensor," *Rev. Sci. Instrum.*, vol. 59, pp. 2337-2340, 1988.

[46] L. A. Pinnaduwage, V. Boiadjiev, J. E. Hawk, and T. Thundat, "Sensitive detection of plastic explosives with self-assembled monolayer-coated microcantilevers," *Appl. Physics Lette.*, vol. 83, pp. 1471-1473, 2003.

[47] A. Passian, P. G. Evans, V. K. Varma, T. L. Ferrell, and T. Thundat, "Piezoresistive detection of acoustic waves," *Rev. Sci. Instrum.*, vol. 74, pp. 1031-1035, 2003.

[48] G. Shekhawat, S.-H. Tark, and V. P. Dravid, "MOSFET-Embedded microcantilevers for measuring deflection in biomolecular sensors," *Sci.*, vol. 311, pp. 1592-1595, 2006.

[49] G. S. Katranas, T. Meydan, A. Ovari, F. Borza, M. Yasin, C. Malvicino, H. Pfutzner, M. Vazquez, M. Rohn, and B. Marquardt, "Simulation and measurement of bilayer sensor characteristics," *Sensors Actuators A: Physical*, submitted to publish.

[50] S. H. Lim, S. H. Han, H. J. Kim, Y. S. Choi, J.-W. Choi, and C. H. Ahn, "Prototype microactuators driven by magnetostrictive thin films," *IEEE Trans. Magnetics*, vol. 34, pp. 2042-2044, 1998.

[51] E. Kaniusas, H. Pfutzner, L. Mehnen, J. Kosel, J. C. Tellez-Blanco, E. Mulasalihovic, T. Meydan, M. Vazquez, M. Rohn, C. Malvicino, and B. Marquardt, "Optimisation of sensitivity and time constant of thermal sensors based on magnetoelastic amorphous bilayers," *J. Alloys and Compounds*

Proceedings of the VI Latin American Workshop on Magnetism, Magnetic
Materials and their Applications, vol. 369, pp. 198-201, 2004.

[52]   C. M. Harris, "Shock and Vibration Handbook," in Vibration of systems having
distributed mass and elasticity, vol. chapter 7, W. F. Stokey, Ed. New York:
McGRAW-HILL.

[53]   L. G. Puckett, G. Barrett, D. Kouzoudis, C. Grimes, and L. G. Bachas,
"Monitoring blood coagulation with magnetoelastic sensors," *Biosensors
Bioelectronics*, vol. 18, pp. 675-681, 2003.

[54]   C. Mungle, C. A. Grimes, and W. R. Dreschel, "Magnetic field tuning of the
frequency-temperature response of a magnetoelastic sensor," *Sensors Actuators A:
Physical*, vol. 101, pp. 143-149, 2002.

[55]   K. Zeng, M. Paulose, K. G. Ong, and C. A. Grimes, "Frequency-domain
characterization of magnetoelastic sensors: a microcontroller-based instrument for
spectrum analysis using a threshold-crossing counting technique," *Sensors
Actuators A: Physical*, vol. 121, pp. 66-71, 2005.

[56]   C. Ruan, K. Zeng, O. K. Varghese, and C. A. Grimes, "A magnetoelastic
bioaffinity-based sensor for avidin," *Biosensors Bioelectronics*, vol. 19, pp. 1695-
1701, 2004.

[57]   O. K. Varghese, D. Gong, W. R. Dreschel, K. G. Ong, and C. A. Grimes,
"Ammonia detection using nanoporous alumina resistive and surface acoustic
wave sensors," *Sensors Actuators B: Chemical*, vol. 94, pp. 27-35, 2003.

[58]   C.-P. Chou, L. A. Davis, and R. Hasegawa, "Elastic constants of Fe(Ni,Co) -B
glasses," *J. Appl. Physics*, vol. 50, pp. 3334-3337, 1979.

[59]   W. D. Nix, "Mechanical properties of thin films," *Metallur. Trans. A*, vol. 20A, pp. 1989-2217, 1988.

[60]   Coventor. inc., 11/29/2007, [Online] available:"http://www.coventor.com/".

[61]   S. M. Spearing, "Materials issues in microelectromechanical systems (MEMS)," *Acta Materialia*, vol. 48, pp. 179-196, 2000.

[62]   W. Merlijn van Spengen, "MEMS reliability from a failure mechanisms perspective," *Microelec. Rel.*, vol. 43, pp. 1049-1060, 2003.

[63]   E. Arzt, "Size effects in materials due to microstructural and dimensional constraints: a comparative review," *Acta Materialia*, vol. 46, pp. 5611-5626, 1998.

[64]   L. H. Liang, J. C. Li, and Q. Jiang, "Size-dependent elastic modulus of Cu and Au thin films," *Solid State Commun.*, vol. 121, pp. 453-455, 2002.

[65]   J. W. Beams, *Structure and Properties of Thin Films*. New York: Wiley and Sons, 1959.

[66]   M. G. Allen, M. Mehregany, R. T. Howe, and S. D. Senturia, "Microfabricated structures for the in situ measurement of residual stress, Young's modulus, and ultimate strain of thin films," *Appl. Phys. Lett.,* vol. 51, pp. 241-243, 1987.

[67]   J. J. Vlassak and W. D. Nix, "new bulge test technique for the determination of Young's modulus and Poisson's ratio of thin films," *J. Mater. Research*, vol. 7, pp. 3242-3249, 1992.

[68]   J. S. Stolken and A. G. Evans, "A microbend test method for measuring the plasticity length scale," *Acta Materialia*, vol. 46, pp. 5109-5115, 1998.

[69] A. Rouzaud, E. Barbier, J. Ernoult, and E. Quesnel, "A method for elastic modulus measurements of magnetron sputtered thin films dedicated to mechanical applications," *Thin Solid Films*, vol. 270, pp. 270-274, 1995.

[70] H. Huang and F. Spaepen, "Tensile testing of free-standing Cu, Ag and Al thin films and Ag/Cu multilayers," *Acta Materialia*, vol. 48, pp. 3261-3269, 2000.

[71] P. M. Osterberg and S. D. Senturia, "M-TEST: A Test Chip for MEMS Material Property Measurement Using Electrostatically Actuated Test Structures," *J. Microelectromechanical Systems*, vol. 6, pp. 107-118, 1997.

[72] H. D. Espinosa and B. C. Prorok, "Effects of film thickness on the yielding behavior of polycrystalline gold films," *Mater. Research Soc. Symp. Proc.*, vol. 695, 2001.

[73] R. Schwaiger and O. Kraft, "Analyzing the mechanical behavior of thin films using nanoindentation, cantilever microbeam deflection, and finite element modeling," *J. Mater. Research,* vol. 19, pp. 315-324, 2004.

[74] J. N. Florando and W. D. Nix, "A microbeam bending method for studying stress-strain relations for metal thin films on silicon substrates," *J. Mechanics and Physics of Solids*, vol. 53, pp. 619-638, 2005.

[75] Z. M. Zhou, Y. Zhou, C. S. Yang, J. A. Chen, W. Ding, and G. F. Ding, "The evaluation of Young's modulus and residual stress of copper films by microbridge testing," *Sensors Actuators A: Physical*, vol. 127, pp. 392-397, 2006.

[76] D. Son, J.-h. Jeong, and D. Kwon, "Film-thickness considerations in microcantilever-beam test in measuring mechanical properties of metal thin film," *Thin Solid Films*, vol. 437, pp. 182-187, 2003.

[77] K. E. Petersen and C. R. Guarnieri, "Young's modulus measurements of thin films using micromechanics," *J. Appl. Physics*, vol. 50, pp. 6761-6766, 1979.

[78] L. Kiesewetter, J.-M. Zhang, D. Houdeau, and A. Steckenborn, "Determination of Young's moduli of micromechanical thin films using the resonance method," *Sensors Actuators A: Physical*, vol. 35, pp. 153-159, 1992.

[79] X. Y. Ye, Z. Y. Zhou, Y. Yang, J. H. Zhang, and J. Yao, "Determination of the mechanical properties of microstructures," *Sensors Actuators A: Physical*, vol. 54, pp. 750-754, 1996.

[80] C. Yu, C. Hsu, and W. Fang, "Comments on determining the elastic modulus of a thin film using the micromachined free/free beam," *J. Micromech. Microeng.*, vol. 15, pp. 351-357, 2005.

[81] H. Biehl and H. H. Mende, "Determination of the elastic constants of copper on copper-whiskers by the flexural vibration method," *J. Physics and Chemistry of Solids*, vol. 35, pp. 37-41, 1974.

[82] C.-L. Dai and Y.-M. Chang, "A resonant method for determining mechanical properties of Si3N4 and SiO2 thin films," *Mater. Lette.*, submitted to publish

[83] J. P. Cleveland and S. Manne, "A nondestructive method for determining the spring constant of cantilevers for scanning force microscopy," *Rev. Sci. Instrum.*, vol. 64, pp. 403-405, 1993.

[84] S. Lee, C. Cho, J. Kim, S. Park, S. Yi, J. Kim, and D.-i. D. Cho, "The effects of post-deposition processes on polysilicon Youngs modulus," *J. Micromech. Microeng.*, vol. 8, pp. 330-337, 1998.

[85]   K. Kang, K. Kim, and H. Lee, "Evaluation of elastic modulus of cantilever beam by TA-ESPI," *Optics & Laser Technology*, vol. 39, pp. 449-452, 2007.

[86]   D. Schneider and M. D. Tucker, "Non-destructive characterization and evaluation of thin films by laser-induced ultrasonic surface waves," *Thin Solid Films*, vol. 290-291, pp. 305-311, 1996.

[87]   B. Cros, E. Gat, and J. M. Saurel, "Characterization of the elastic properties of amorphous silicon carbide thin films by acoustic microscopy," *J. Non-Crystalline Solids*, vol. 209, pp. 273-282, 1997.

[88]   S. Peraud, S. Pautrot, P. Villechaise, P. Mazot, and J. Mendez, "Determination of young's modulus by a resonant technique applied to two dynamically ion mixed thin films," *Thin Solid Films*, vol. 292, pp. 55-60, 1997.

[89]   X. Xiao and X. You, "Numerical study on surface acoustic wave method for determining Young's modulus of low-k films involved in multi-layered structures," *Appl. Surface Sci.*, vol. 253, pp. 2958-2963, 2006.

[90]   G. F. Dirras, P. Djemia, Y. Roussigne, and K. M. Jackson, "Investigating the elastic properties of [beta]-SiC films," *Materials Sci. Eng. A*, vol. 387-389, pp. 302-306, 2004.

[91]   C. Bellan and J. Dhers, "Evaluation of Young modulus of CVD coatings by different techniques," *Thin Solid Films*, vol. 469-470, pp. 214-220, 2004.

[92]   H. Ogi, M. Hirao, T. Tada, and J. Tian, "Elastic-stiffness distribution on polycrystalline Cu studied by resonance ultrasound microscopy: Young's modulus microscopy," *Physical Rev. B* (Condensed Matter and Materials Physics), vol. 73, pp. 174107, 2006.

[93]   N. Nakamura, H. Nitta, H. Ogi, T. Yasui, and M. Hirao, "Anisotropic elastic

         constants of copper thin films: RUS/Laser and Picosecond-Laser Ultrasound,"

         presented at Quantitative nondestructive Evolution, 2006.

[94]   N. Nakamura, H. Ogi, and M. Hirao, "Resonance Ultrasound Spectroscopy for

         Measuring Elastic Constants of Thin Films," *Japanese J. Appl. Phys.*, Part 1:

         Regular Papers, Short Notes & Review Papers, vol. 43, pp. 3115-3118, 2004.

[95]   H. Ogi, M. L. Dunn, K. Takashima, and H. Ledbetter, "Elastic properties of a

         unidirectional SiC[sub f]/Ti composite: Acoustic-resonance measurements and

         micromechanics predictions," *J. Appl. Phys.*, vol. 87, pp. 2769-2774, 2000.

[96]   J. Tian, H. Ogi, and M. Hirao, "Effect of elastic anisotropy on contact stiffness in

         resonance ultrasound microscopy," *Appl. Phys. Lette.*, vol. 87, pp. 204107, 2005.

[97]   W. C. Oliver and G. M. Pharr, "An improved technique for determining hardness

         and elastic modulus using load and displacement sensing indentation

         experiments," *J. Mater. Research*, vol. 7, pp. 1564-1583, 1992.

[98]   B. Bhushan, B. K. Gupta, and M. H. Azarian, "Nanoindentation, microscratch,

         friction and wear studies of coatings for contact recording applications," *Wear*,

         vol. 181-183, pp. 743-758, 1995.

[99]   R. Saha and W. D. Nix, "Effects of the substrate on the determination of thin film

         mechanical properties by nanoindentation," *Acta Materialia*, vol. 50, pp. 23-38,

         2002.

[100]   W. C. Oliver and G. M. Pharr, "Measurement of hardness and elastic modulus by

         instrumented indentation: Advances in understanding and refinements to

methodology," *J. Mater. Research*, Vol. 19, No. 1, Jan 2004, vol. 19, pp. 3-20, 2003.

[101] Y.-G. Jung, B. R. Lawn, M. Martyniuk, H. Huang, and X. Z. Hu, "Evaluation of elastic modulus and hardness of thin films by nanoindentation," *J. Mater. Research*, vol. 19, pp. 3076-3080, 2004.

[102] Y. Wei, X. Wang, and M. Zhao, "Size effect measurement and characterization in nanoindentation test," *J. Mater. Research,* vol. 19, pp. 208-216, 2004.

[103] Y. T. Pei, D. Galvan, and J. T. M. De Hosson, "Nanostructure and properties of TiC/a-C:H composite coatings," *Acta Materialia*, vol. 53, pp. 4505-4521, 2005.

[104] Z. Q. Qi and E. I. Meletis, "Mechanical and tribological behavior of nanocomposite multilayered Cr/a-C thin films," *Thin Solid Films*, vol. 479, pp. 174-181, 2005.

[105] S. M. Han, R. Shah, R. Banerjee, G. B. Viswanathan, B. M. Clemens, and W. D. Nix, "Combinatorial studies of mechanical properties of Ti/Al thin films using nanoindentation," *Acta Materialia* 53 (2005) 2059?067, vol. 53, pp. 2059-2067, 2005.

[106] F. Zeng, Y. Gao, L. Li, D. M. Li, and F. Pan, "Elastic modulus and hardness of Cu-Ta amorphous films," *J. Alloys Compounds*, vol. 389, pp. 75-79, 2005.

[107] X. Li, B. Bhushan, K. Takashima, C.-W. Baek, and Y.-K. Kim, "Mechanical characterization of micro/nanoscale structures for MEMS/NEMS applications using nanoindentation techniques," *Ultramicroscopy*, vol. 97, pp. 481-494, 2003.

[108] A. A. Volinsky and W. W. Gerberich, "Nanoindentaion techniques for assessing mechanical reliability at the nanoscale," *Microelec. Eng.*, vol. 69, pp. 519-527, 2003.

[109] S. H. Hong, K. S. Kim, Y.-M. Kim, J.-H. Hahn, C.-S. Lee, and J.-H. Park, "Characterization of elastic moduli of Cu thin films using nanoindentation technique," *Composites Sci. Technology*, vol. 65, pp. 1401-1408, 2005.

[110] C. Liang, B. C. Prorok, P. Gupta, M. Tlustochovicz, R. Zhu, and M. McNallan, "Conversion of metal carbides to carbide derived carbon by reactive ion reactive etching in halogen gas," presented at Defense & Security Symposium 2006, Orlando, FL, 2006.

[111] J. Lintymer, J. Gavoille, N. Martin, and H. Takadoum, "Glancing angle deposition to modify microstructure and properties of sputter deposited chromium thin films," *Surf. Coat. Technol.*, vol. 174-175, pp. 316-323, 2003.

[112] J. P. Winterstein, J. B. LeBret, and M. G. Norton, "Characteristics of tin whiskers formed on sputter-deposited films-an aging study," *J. Mater. Research,*, vol. 19, pp. 689-692, 2004.

[113] C. V. Thompson, "Structure evolution during processing of polycrystalline films," *Annual Review of Materials Science*, vol. 30, pp. 159-190, 2000.

[114] B. Djurfors and D. G. Ivey, "Microstructure characterization of pulsed electrodeposited AuSn alloy thin films," *Mater. Sci.Eng. B*, vol. 90, pp. 309-320, 2002.

[115] J. M. Barandiaran, J. Gutierrez, and C. Gomez-Polo, "New sensors based on the magnetoelastic resonance of metallic glasses," *Sensors Actuators A: Physical*, vol. 81, pp. 154-157, 2000.

[116] C. ziegler, "Cantilever-based biosensors," *Anal Bioanal Chem*, vol. 379, pp. 946-959, 2004.

[117] N. V. Lavrik, M. J. Sepaniak, and P. G. Datskos, "Cantilever transducers as a platform for chemical and biological sensors," Rev. Sci. Instrum., vol. 75, pp. 2229-2253, 2004.

[118] H. D. Hubbard, *Key to the Periodic Chart of the Atoms*. Buffalo Grove, IL: VWR/Sargent-Welch Scientific Products, 1982.

[119] T. H. Courtney, *Mechanical Behavior of Materials*. New York: MeGraw-Hill, 2000.

[120] J. Lintymer, N. Martin, J.-M. Chapper, J. Takadoum, and P. Delobelle, "Modeling of Young's modulus, hardness and stiffness of chromium zigzag multilayers sputter deposited," *Thin Solid Films*, vol. 503, pp. 177, 2006.

[121] M. A. El Khakani, M. Chaker, A. Jean, S. Boily, and J. C. Kieffer, "Hardness and Young 担 modulus of amorphous a SiC thin films determined by nanoindentation and bulge tests," *J. Mater. Research*, vol. 9, pp. 96, 1994.

[122] H. D. Espinosa, B. C. Prorok, and M. Fischer, "A methodology for determining mechanical properties of freestanding thin films and MEMS materials," *J. Mech. Phys. Sol.*, vol. 51, pp. 47-67, 2003.

[123] S.-H. Lee, J. W. Evans, Y. E. Pak, J. U. Jeon, and D. Kwon, "Evaluation of elastic modulus and yield strength of Al film using an electrostatically actuated test device," *Thin Solid Films*, vol. 408, pp. 223-229, 2002.

[124] L. Wang, C. Liang, and B. C. Prorok, "A Comparison of Testing Methods in Assessing the Elastic Properties of Sputter Deposited Gold Films," *Thin Solid Films*, vol. 515, pp. 7911-7918, 2007.

[125] A. J. Kalkman, A. H. Verbruggen, and G. C. A. M. Janssen, "Young's modulus measurements and grain boundary sliding in free-standing thin metal films," *Appl. Phys. Lett.* vol 78, pp. 2673-2675, 2001.

[126] J. Lintymer, N. Martin, J.-M. Chappe, J. Takadoum, and P. Delobelle, "Modeling of Young's modulus, hardness and stiffness of chromium zigzag multilayers sputter deposited," *Thin Solid Films*, vol. 503, pp. 177-189, 2006.

[127] H. D. Espinosa, B. C. Prorok, and B. Peng, "Plasticity size effects in free-standing submicron polycrystalline FCC -lms subjected to pure tension," *J. the Mech. Phys. Sol.*, vol. 52, pp. 667 ?689, 2004.

[128] M. Chinmulgund, R. B. Inturi, and J. A. Barnard, "Effect of Ar gas pressure on growth, structure, and mechanical properties of sputtered Ti, Al, TiAl, and Ti3Al films," *Thin Solid Films*, vol. 270, pp. 260-263, 1995.

[129] A. K. Jamting, J. M. Bell, M. V. Swain, and N. Schwarzer, "Investigation of the elastic modulus of thin films using simple biaxial bending techniques," *Thin Solid Films*, vol. 308-309, pp. 304-309, 1997.

[130] L. Wang, C. Liang, and B. C. Prorok, "A Comparison of Testing Methods in Assessing the Elastic Properties of Sputter Deposited Gold Films," *Thin Solid Films*, vol. 515, pp. 7911-7918, 2007.

[131] C. Liang and B. C. Prorok, "Measuring thin film elastic modulus with a magnetostrictive sensor," *J. Micromech. and Microeng.* vol. 17, pp. 709-716, 2007.

[132] C. K. Ho, M. T. Itamura, M. Kelley, and R. C. Hughes, "Review of chemical sensors for in situ monitoring of volatile contaminants," SNADIA 2001.

[133] K. H. Behrndt, "Long term operation of crystal oscillators in thin-film deposition," *J. Vac. Sci. Technol.*, vol. 8, pp. 622-625, 1971.

[134] C.-s. Lu, "Mass determination with piezoelectric quartz crystal resonators," *J. Vac. Sci Technol.*, vol. 12, pp. 578, 1975.

[135] M. Muratsugu and e. al., "Quartz Crystal Microbalance for the Detection of microgram quantities of Human Serum Albumin: Relationship between the frequency change and the mass of protein adsorbed," *Anal. Chem.*, vol. 65, pp. 2933-2937, 1993.

[136] E. V. Olsen, S. T. Pathirana, A. M. Samoylov, J. M. Barbaree, B. A. Chin, W. C. Neely, and V. Vodyanoy, "Specific and selective biosensor for salmonella and its detection in the environment," *J. Microbiological Methods*, vol. 53, pp. 273-285, 2003.

[137] R. M. White, "Surface elastic waves," *Proc. IEEE*, vol. 58, pp. 1238-1276, 1970.

[138]   T. Moriizumi, A. Saitou, and T. Nomura, "Multi-channel SAW chemical sensor using 90 MHz SAW resonator and partial casting molecular films," presented at Ultrasonics Symp., 1994. *Proc., IEEE*, 1994.

[139]   G. Fischerauer, F. Dickert, P. Forth, and U. Knauer, "Chemical sensors based on SAW resonators working at up to 1 GHz," presented at Ultrasonics Symp., 1996. *Proc. IEEE*, 1996.

[140]   M. Benetti, D. Cannata, A. D'Amico, F. Di Pietrantonio, A. Macagnano, and E. Verona, "SAW sensors on Al/diamond/Si structures," presented at Sensors, 2004. *Proc. IEEE*, 2004.

[141]   R. G. Kryshtal, A. V. Medved, V. V. Shemet, and V. E. Zemlyakov, "Electronically tunable SAW chemosensors," *Electron. Lett.*, vol. 35, pp. 676-678, 1999.

[142]   L. Rufer, A. Torres, S. Mir, M. O. Alam, T. Lalinsky, and Y. C. Chan, "SAW chemical sensors based on AlGaN/GaN piezoelectric material system: acoustic design and packaging considerations," presented at Electronics Materials and Packaging, 2005.

[143]   J. D. Galipeau, R. S. Falconer, J. F. Vetelino, J. J. Caron, E. L. Wittman, M. G. Schweyer, and J. C. Andle, "Theory, design and operation of a surface acoustic wave hydrogen sulfide microsensor," *Sensors Actuators B: Chemical*, vol. 24, pp. 49-53, 1995.

[144]   J. P. Black, B. Chen, R. Quinn, M. Madou, and R. M. White, "Comparison of the performance of flexural plate wave and surface acoustic wave devices as the

detector in a gas chromatograph," presented at Ultrasonics Symposium, 2000 *Proce. IEEE*, 2000.

[145] R. Mukhopadhyay, M. Lorentzen, J. Kjems, and F. Besenbacher, "Nanomechanical sensing of DNA sequences using piezoresistive cantilevers," *Langmuir*, vol. 21, pp. 8400-8408, 2005.

[146] K. Y. Gfeller, N. Nugaeva, and M. Hegner, "Rapid biosensor for detection of antibiotic-selective growth of escherichia coli.," *Appl. Environmental Microbiology*, vol. 71, pp. 2626-2631, 2005.

[147] J. K. Gimzewski, C. Gerber, E. Meyer, and R. R. Schlittler, "Observation of a chemical reaction using a micromechanical sensor," *Chem. Phys. Lett.*, vol. 217, pp. 589-594, 1994.

[148] A. N. Cleland and M. L. Roukes, "Fabrication of high frequency nanometer scale mechanical resonators from bulk Si crystals," *Appl. Phys. Lett.*, vol. 69, pp. 2653-2655, 1996.

[149] T. Bachels and R. Schafer, "Microfabricated cantilever-based detector for molecular beam experiments," *Rev. Sci. Instrum.* vol. 69, pp. 3794, 1998.

[150] J.-J. Ho, Y. K. Fang, K. H. Wu, W. T. Hsieh, C. H. Chen, G. S. Chen, M. S. Ju, J.-J. Lin, and S. B. Hwang, "High sensitivity ethanol gas sensor integrated with a solid-state heater and thermal isolation improvement structure for legal drink-drive limit detecting," *Sensors Actuators B: Chemical*, vol. 50, pp. 227-233, 1998.

[151] C. Serre, P. Gorostiza, A. Perez-Rodriguez, F. Sanz, and J. R. Morante, "Measurement of micromechanical properties of polysilicon microstructures with

an atomic force microscope," *Sensors Actuators A: Physic*al, vol. 67, pp. 215-219, 1998.

[152]   J. E. Sader, "Frequency response of cantilever beams immersed in viscous fluids with applications to the atomic force microscope," *J. Appl. Phys.*, vol. 84, pp. 64-76, 1998.

[153]   Z. J. Davis, G. Abadal, O. Kuhn, O. Hansen, F. Grey, and A. Boisen, "Fabrication and characterization of nanoresonating devices for mass detection," *J. Vac. Sci. Technol*. B, vol. 18, pp. 612, 2000.

[154]   B. Ilic, D. Czaplewski, H. G. Craighead, H. G. Craighead, P. Neuzil, C. Campagnolo, and C. Batt, "Mechanical resonant immunospecific biological detector.," *Appl. Phys. Lett.*, vol. 77, pp. 450?52, 2000.

[155]   J. Tamayo, A. D. L. Humphris, A. M. Malloy, and M. J. Miles, "Chemical sensors and biosensors in liquid environment based on microcantilevers with amplified quality factor," *Ultramicroscopy*, vol. 86, pp. 167-173, 2001.

[156]   H. P. Lang , R. Berger , F. Battiston, J. P. Ramseyer, E. Meyer, C. Andreoli, J. Brugger, P. Vettiger, M. Despont, T. Mezzacasa , L. Scandella, H. J. Guntherodt, C. Gerber, and J. K. Gimzewski, "A chemical sensor based on a micromechanical cantilever array for the identification of gases and vapors," *Appl.ied Phys. A: Materials Science and Processing*, vol. 66, pp. S61-64, 1998.

[157]   R. Raiteri, M. Grattarola, H.-J. Butt, and P. Skladal, "Micromechanical cantilever-based biosensors," *Sensors Actuators B: Chemical*, vol. 79, pp. 115-126, 2001.

[158] G. Wu, R. H. Datar, K. M. Hansen, T. Thundat, R. J. Cote, and A. Majumdar, "Bioassay of prostate-specific antigen (PSA) using microcantilevers," *Nature biotechnol.*, vol. 19, pp. 856-860, 2001.

[159] K. M. Hansen and T. Thundat, "Microcantilever biosensors," *Methods*, vol. 37, pp. 57-64, 2005.

[160] H. G. Craighead, "nanoelectromechanical systems," *Sci.*, vol. 290, pp. 1532-1535, 2000.

[161] H. Sone, Y. Fujinuma, T. Hieida, T. Chiyyoma, H. Okano, and S. Hosaka, "Picogarm mass sensor using microcantilever," presented at SICE Annual Conference in Singapore, Singapore, 2004.

[162] D. A. Skoog, H. F. James, and T. A. Nieman, *Principles of Instrumental Analysis*, 5th ed. BROOKS/COLE, 1998.

[163] P. I. Oden, "Gravimetric sensing of metallic deposits using an end-loaded microfabricated beam structure," *Sensors Actuators B: Chemical*, vol. 53, pp. 191-196, 1998.

[164] P. G. Stoyanov, S. A. Doherty, C. A. Grimes, and W. R. Seitz, "A remotely interrogatable sensor for chemical monitoring," *IEEE Trans. Magn.*, vol. 34, pp. 1315-1317, 1998.

[165] C. A. Grimes, K. G. Ong, K. Loiselle, P. Q. Stoyanov, D. Kouzoudis, Y. Liu, C. Tong, and F. Tefiku, "Magnetoelastic sensors for remote query environmental monitoring," *Smart Mater. Struct.*, vol. 8, pp. 639?46, 1999.

[166] C. A. Grimes, P. G. Stoyanov, Y. Liu, C. Tong, K. G. Ong, K. Loiselle, M. Shaw, S. A. Doherty, and W. R. Seitz, "A magnetostatic-coupling based remote query

sensor for environmental monitoring," *J. Phys. D: Appl. Phys.*, vol. 32, pp. 1329-1335, 1999.

[167]   C. A. Grimes and D. Kouzoudis, "Remote query measurement of pressure, fluid-flow velocity, and humidity using magnetoelastic thick-film sensors," *Sensors Actuators A: Physical*, vol. 84, pp. 205-212, 2000.

[168]   M. K. Jain, S. Schmidt, K. G. Ong, C. Mungle, and C. A. Grimes, "Magnetoacoustic remote query temperature and humidity sensors," *Smart Mater. Struct.*, vol. 9, pp. 502-510, 2000.

[169]   D. Kouzoudis and C. A. Grimes, "The frequency response of magnetoelastic sensors to stress and atmospheric pressure," *Smart Mater. Struct.*, vol. 9, pp. 885-889, 2000.

[170]   P. G. Stoyanov and C. A. Grimes, "A remote query magnetostrictive viscosity sensor," *Sensors Actuators. A: Physical*, vol. 80, pp. 8-14, 2000.

[171]   K. G. Ong and C. A. Grimes, "A resonant printed-circuit sensor for remote query monitoring of environmental parameters," *Smart Mater. Struct.*, vol. 9, pp. 421-428, 2000.

[172]   M. K. Jain, S. Schmidt, and C. A. Grimes, "Magneto-acoustic sensors for measurement of liquid temperature, viscosity and density," *Appl. Acoustics*, vol. 62, pp. 1001-1011, 2001.

[173]   Q. C. a. C. A. G. Mahaveer K Jain, "A wireless micro-sensor for simultaneous measurement of pH, temperature, and pressure," *Smart Mater. Struct.*, vol. 10, pp. 347-353, 2001.

224

[174] K. G. Ong, J. Wang, R. S. Singh, L. G. Bachas, and C. A. Grimes, "Monitoring of bacteria growth using a wireless, remote query resonant-circuit sensor: application to environmental sensing," *Biosensors Bioelectronics*, vol. 16, pp. 305-312, 2001.

[175] K. G. Ong and C. A. Grimes, "Tracking the harmonic response of magnetically-soft sensors for wireless temperature, stress, and corrosive monitoring," *Sensors Actuators A: Physical*, vol. 101, pp. 49-61, 2002.

[176] Q. Y. Cai and C. A. Grimes, "A salt-independent pH sensor," *Sensors Actuators B: Chemical*, vol. 79, pp. 144-149, 2001.

[177] C. Ruan, K. G. Ong, C. Mungle, M. Paulose, N. J. Nickl, and C. A. Grimes, "A wireless pH sensor based on the use of salt-independent micro-scale polymer spheres," *Sensors Actuators B: Chemical*, vol. 96, pp. 61-69, 2003.

[178] C. Ruan, K. Zeng, and C. A. Grimes, "A mass-sensitive pH sensor based on a stimuli-responsive polymer," *Analytica Chimica Acta*, vol. 497, pp. 123-131, 2003.

[179] O. K. Varghese, D. Gong, M. Paulose, K. G. Ong, and C. A. Grimes, "Hydrogen sensing using titania nanotubes," *Sensors Actuators B: Chemical*, vol. 93, pp. 338-344, 2003.

[180] O. K. Varghese, P. D. Kichambre, D. Gong, K. G. Ong, E. C. Dickey, and C. A. Grimes, "Gas sensing characteristics of multi-wall carbon nanotubes," *Sensors Actuators B: Chemical*, vol. 81, pp. 32-41, 2001.

[181] I. G. Giannakopoulos, D. Kouzoudis, C. A. Grimes, and N. Nikolakis, "Synthesis and Characterization of a Composite Zeolite-Metglas Carbon Dioxide Sensor," *Advanced Functional Materials*, vol. 15, pp. 1165-1170, 2005.

[182] C. Ruan, K. Zeng, O. K. Varghese, and C. A. Grimes, "A staphylococcal enterotoxin B magnetoelastic immunosensor," *Biosensors Bioelectronics*, vol. 20, pp. 585-591, 2004.

[183] K. Shankar, K. Zeng, C. Ruan, and C. A. Grimes, "Quantification of ricin concentrations in aqueous media," *Sensors Actuators B: Chemical*, vol. 107, pp. 640-648, 2005.

[184] N. Bouropoulos, D. Kouzoudis, and C. Grimes, "The real-time, in situ monitoring of calcium oxalate and brushite precipitation using magnetoelastic sensors," *Sensors Actuators B: Chemical*, vol. 109, pp. 227-232, 2005.

[185] S. Wu, X. Gao, Q. Cai, and C. A. Grimes, "A wireless magnetoelastic biosensor for convenient and sensitive detection of acid phosphatase," *Sensors Actuators B: Chemical*, vol. In Press, Corrected Proof, 2006.

[186] Sigma-aldrich, "glass bead", 11/29/2007, [Online] available: http://www.sigmaaldrich.com/Area_of_Interest/The_Americas/United_States.htm l.

[187] B. Ilic, D. Czaplewski, M. Zalalutdinov, H. G. Craighead, P. Neuzil, C. Campagnolo, and C. Batt, "Single cell detection with micromechanical oscillators," presented at The 45th Int. conf. on Electron, Ion, and Photon Beam Technology and Nanofabrication, Washington, DC (USA), 2001.

[188] H. Foell, 11/29/2007, [Online] available:"http://www.tf.uni-kiel.de/matwis/amat/elmat_en/index.html".

[189] Y. Torii, H. Wakiwaka, T. Kiyomiya, Y. Matsuo, Y. Yamada, and M. Makimura, "Tb-Fe-Co giant magnetostrictive thin film and its application to force sensor," *J. Magnetism Magnetic Mater*. vol. 290-291, pp. 861-864, 2005.

[190] N. Tiercelin, P. Pernod, V. Preobrazhensky, H. Le Gall, J. Ben Youssef, P. Mounaix, and D. Lippens, "Giant magnetostriction thin films for multi-cantilever micro-structures driving," *Sensors Actuators A: Physical*, vol. 81, pp. 162-165, 2000.

[191] M. Frommberger, S. Glasmachers, C. Schmutz, J. McCord, and E. Quandt, "Microscopic magnetic and high-frequency properties of a stress sensor using FeCoBSi magnetostrictive thin films," *IEEE Trans. Magn*. ol. 41, pp. 3691-3693, 2005.

[192] M. Frommberger, C. Zanke, A. Ludwig, M. Tewes, and E. Quandt, "Processing and application of magnetoelastic thin films in high-frequency devices," Microelectronic Engineering Proceedings of the 28th International Conference on Micro- and Nano-Engineering, vol. 67-68, pp. 588-594, 2003.

[193] A. Speliotis and D. Niarchos, "Magnetostrictive properties of amorphous and crystalline TbDyFe thin films," *Sensors Actuators A: Physical*, vol. 106, pp. 298-301, 2003.

[194] M. Frommberger, A. Ludwig, A. Sehrbrock, and E. Quandt, "High-frequency magnetic properties of FeCoBSi/SiO/sub 2/ and (FeCo/CoB)/SiO/sub 2/ multilayer thin films," *IEEE Trans. Magn*., vol. 39, pp. 3166-3168, 2003.

[195] Y. M. Kim, D. Choi, K. H. Kim, J. Kim, S. H. Han, and H. J. Kim, "Thickness effects on magnetic properties and ferromagnetic resonance of Co-Ni-Fe soft

magnetic thin films," *J. Magnetism Magnetic Mater.* vol. 254-255, pp. 419-423, 2003.

[196] C. Petridis, P. Dimitropoulos, and E. Hristoforou, "A new magnetoelastic device for sensing applications," *Sensors Actuators A: Physical*, vol. 129, pp. 131-137, 2006.

[197] E. Quandt, A. Ludwig, J. Mencik, and E. Nold, "Giant magnetostrictive TbFe/Fe multilayers," *J. Alloys Compounds*, vol. 258, pp. 133-137, 1997.

[198] K. S. Chan, H. Ji, X. Wang, J. Hudak, S.J., and B. R. Lanning, "Mechanical properties and interface toughness of FeCo thin films on Ti-6Al-4V," *Mater. Sci. Eng. A: NANOAM*, vol. 422, pp. 298-308, 2006.

[199] I. Carabias, A. Martinez, M. A. Garcia, E. Pina, J. M. Gonzalez, A. Hernando, and P. Crespo, "Magnetostrictive thin films prepared by RF sputtering," *J. Magnetism Magnetic Mater.*, vol. 290-291, pp. 823-825, 2005.

[200] M. L. Johnson, J. Hu, J. Wan, R. S. Lakshmanan, V. A. Petrenko, and B. A. Chin, "A remote biosensor platform using sputtered magnetostrictive particles," presented at MS&T 2006, CT, OH, 2006.

[201] H. Chiriac, M. Pletea, and E. Hristoforou, "Magnetoelastic characterization of thin films dedicated to magnetomechanical microsensor applications," *Sensors Actuators A: Physical*, vol. 68, pp. 414-418, 1998.

[202] H. Uchida, Y. Matsumura, H. Uchida, and H. Kaneko, "Progress in thin films of giant magnetostrictive alloys," *J. Magnetism Magnetic Mater.*, vol. 239, pp. 540-545, 2002.

[203] J. H. Hsieh, C. Liang, C. H. Yu, and W. Wu, "Deposition and characterization of multi-layered TiN/TiAlN coating by unbalanced magnetron," *Surf..Coat. Technol.*, vol. 108/109, pp. 132-137, 1998.

[204] S. Zhang, X. T. Zeng, P. Hing, C. Liang, and J. Sun, "Dependence of micrstructural growth of DLC coating on processing parameters," presented at The 6th Conf. on Processing and Fabrication of Advanced Materials, Singapore, 1997.

[205] R. C. Jaeger, *Introduction to Microelectronic Fabrication*, vol. v, 2nd ed. Prentice Hall, 2002.

[206] M. J. Madou, Fundamentials of Microfabrication-The Science and Miniaturization, 2nd ed. New York: CRC Press, 2002.

[207] S. M. SZE, VLSI Technology, 2nd ed: McGraw-Hill Book Company, 1988.

[208] R. W. Berry, P. M. Hall, and M. T. Harris, *Thin Film Technology*: Van Nostrand Reinhold Company, 1968.

[209] A. D. Mattingley, C. Shearwood, and M. R. J. Gibbs, "Magnetic and Magnetoelastic Properties of Amorphous Fe-Si-B-C Films," *IEEE Trans Magn.*, vol. 30, pp. 4806-4808, 1994.

[210] R. F. Bunshah, Handbook of Deposition Technologies for Film and Coatings-Science, Technology and Applications: Noyes Publications, 1993.

[211] S. M. Rossnagel, J. Cuomo, and W. D. Westwood, Handbook of Plasma Processing Technology-Fundamentals, Etching, Deposition, and Surface Interactions: Noyes Publications, 1989.

[212] C. Liang, C. Ellis, L. C. Mathison, and B. C. Prorok, "Mechanical Property Measurement of Interconnection materials by Magnetostrictive Sensors," presented at MRS 2006 Fall Meeting, Boston, MA, 2006.

[213] J. H. Hsieh, B. H. Tan, C. Liang, and P. Hing, "Synthesis of carbon nitride thin films by unbalanced magnetron sputtering," presented at The 6th conf. on Processing and fabrication of Advanced Materials, Singapore, 1997.

[214] J. Wei, P. Hing, S. Zhang, X. H., C. Q. Sun, and C. Liang, "Formation of carbon nitride thin film by radio frequency magnetron sputtering," presented at the 4Th National Symposium on Progress in material Research, Singapore, 1998.

[215] G. Taguchi, *TAGUCHI METHODS, Design of Experiments*, vol. 4. ASI Press, 1993.

[216] J. L. Vossen and W. Kern, *Thin Film Processes*. New York: Academic Press, 1978.

[217] B. D. Cullity and S. R. Stock, *Elements of X-Ray Diffraction*. New Jersey: Prentice hall, 2001.

[218] S. Saiseng, P. Winotai, S. Nilpairuch, P. Limsuwan, and I. M. Tang, "Nanocrystallization in amorphous Fe40Ni40(Si+B)19Mo1-2 ribbons," *J. Magnetism Magnetic Mater.*, vol. 278, pp. 172-178, 2004.

[219] S. A. Kostyrya and B. Idzikowski, "Curie temperatures and crystallization behavior of amorphous Fe81-xNixZr7B12 (x=10, 20, 30, 40, 50, 60) alloys," *J. Magnetism Magnetic Mater.* vol. 304, pp. e537-e539, 2006.

[220] G. Herzer, "Grain size dependence of coercivity and permeability in nanocrystalline ferromagnets," *IEEE Trans. Magn.*, vol. 26, pp. 1397-1402, 1990.

[221] M. C. Chi and R. Alben, "Hysteresis curves and magnetization processes in a model for an amorphous magnet with random uniaxial anisotropy," *J. Appl. Phys.*, vol. 48, pp. 2987-2991, 1977.

[222] K. Mandal, M. Vazquez, D. Garcia, F. J. Castano, C. Prados, and A. Hernando, "Development of a tensile-stress-induced anisotropy in amorphous magnetic thin films," *J. Magnetism Magnetic Mater.*, vol. 220, pp. 152-160, 2000.

[223] R. Alben, J. J. Becker, and M. C. Chi, "Random anisotropy in amorphous ferromagnets," *J. Appl. Phys.*, vol. 49, pp. 1653-1658, 1978.

[224] X. K. Sun, J. Zhang, Y. Chu, W. Liu, B. Cui, and Z. Zhang, "Dependence of magnetic properties on grain size of alpha-Fe in nanocomposite (Nd, Dy)(Fe, Co, Nb, B)[sub 5.5]/alpha-Fe magnets," *Appl. Phys. Lett.*, vol. 74, pp. 1740-1742, 1999.

[225] F. Ott and C. Fermon, "Magnetic depth profiles in strained nickel thin films measured by polarized neutron reflectometry," *J. Magnetism Magnetic Mater.* vol. 165, pp. 475-478, 1997.